

DIEGO D.J. CORONA-LOPEZ

EIT FOR ROOT SYSTEM ANALYSIS

A STUDY INTO DESIGN-ORIENTED
PLANT ROOT PHENOTYPING SYSTEMS
FOR AGRICULTURAL PRACTICES

A THESIS SUBMITTED TO THE UNIVERSITY OF MANCHESTER
FOR THE DEGREE OF DOCTOR OF PHILOSOPHY IN THE
FACULTY OF SCIENCE AND ENGINEERING (2021)

THE UNIVERSITY OF MANCHESTER

Root system analysis using EIT

A study into design-oriented plant root phenotyping systems for agricultural practices

Copyright © 2021 Diego D.J. Corona-Lopez

Published by The University of Manchester

Supervision: Bruce Grieve

Co-supervision: Frank Podd

Typeset in LATEX

CONTENTS

Figures 12

Tables 14

Acronyms 15

Abstract 17

Declaration 19

Copyright statement 21

1.0 Background and motivation 27

1.1 The current state of affairs 27

1.1.1 The effects of careless food production 28

1.2 Phenotyping as a vessel for sustainable agriculture 29

1.3 Proposed approach 30

1.4 Nota bene 31

2.0 Root research 33

2.1 The elusive half of plants 33

2.1.1 Traits linked to crop productivity 34

2.2 Imaging roots 38

2.3 Electrical characteristics of plants 42

3.0 Direct problems	49
3.1 Electrical Imaging (<i>Can one hear the shape of a drum?</i>)	49
3.1.1 Foundations of Electromagnetic theory	50
3.1.2 Analytical approach	52
3.1.3 Numerical approach	56
3.2 Contribution: Improving EIT's vertical resolution	61
4.0 Inverse problems	69
4.1 Types of EIT inverse problems	69
4.2 Ill-behaviour	70
4.2.1 SVD Pseudo-inverse	72
4.2.2 Numerical example	74
4.3 Regularization	75
4.4 Selection methods for the optimal hyperparameter	77
4.5 Iterative descent methods	78
4.5.1 Newton algorithms	79
4.5.2 Conjugate Gradient	81
4.5.3 Comparison between regularization schemes	82
4.6 Graz consensus Reconstruction algorithm for EIT	83
4.7 Contribution: Noise performance evaluation of Stimulation patterns	86
4.7.1 Methodology	87
4.7.2 Discussion	88
5.0 Smart rhizotron	97
5.1 Measuring impedance: two v. four points	97
5.2 Analogue front-end	99
5.3 pEIT: Portable EIT System	102
5.4 SpEIT: Spectral EIT system	104
5.4.1 Signal integrity	106

5.5 <i>SpEIT Rhizotron</i>	110
5.6 <i>SpEIT's shell</i>	114
5.7 <i>SpEIT's IoT solution</i>	117
5.7.1 <i>SpEIT network</i>	119
6.0 <i>Empirical findings and discussion</i>	123
6.1 <i>Growth Materials</i>	124
6.2 <i>Substrate water characterisation</i>	124
6.3 <i>Substrate preparation</i>	135
6.3.1 <i>Packing protocol</i>	135
6.4 <i>Air drying experiment</i>	136
6.4.1 <i>Results</i>	140
6.4.2 <i>Discussion</i>	152
6.5 <i>Raphanus sativus</i>	154
6.5.1 <i>Results</i>	154
6.5.2 <i>Discussion</i>	166
6.6 <i>Brassica oleracea var. acephala</i>	168
6.6.1 <i>Results</i>	168
6.7 <i>Discussion</i>	178
7.0 <i>Concluding remarks</i>	181
7.1 <i>Limitations</i>	182
7.2 <i>Future work</i>	183
<i>Appendix</i>	185
<i>Bibliography</i>	189

THIS PAGE INTENTIONALLY LEFT BLANK

FIGURES

- 1 People experiencing acute hunger and in need of assistance (Integrated Food Security Phase 3, i.e. in crisis) 27
- 2 Percentage of the global population with severe food insecurity and how it divides across regions 28
- 3 Visual representation of the rhizosphere 30
- 4 Example of a Root System Architecture (RSA) (Tsutsumi, 2003). 33
- 5 Root growth adaptations to enhance plant's nutrient and water capabilities [Illustrative example based on Goff and Mayne's work (1904)]. 35
- 6 **A.** Effects of gravity on roots. Root tips are known to reorient once they are gravitationally stimulated [Illustrative example based on Beach's work (1914)]. **B.** Effects of gravitropism on *Pinus taeda* after 0.0, 1.0, 3.0, 6.0, and 12.0hrs (Zhang et al. 2019). 36
- 7 **A.** Anatomy of root hairs [based on the work of Stevens (1916)]. Comparison of maize RSAs between a hairless mutant(**B**) and a normal maize variant (**C**).[based on the findings of Hochholdinger et al. (2004) and the drawings of Miwa Kojima (Iowa State University)] 37
- 8 Illustrative example of earlier shovelomic approaches. The figure shows a 20 feet deep root excavation to study a variety of prairie plants [Extract from the work of Dix and Weaver (1969) used under CC0 licence]. 39
- 9 Illustrative example of a rhizotron. Rhizotrons do not have a standard shape, but the fundamental idea is to be able to visualise the RSA through a transparent window. 40
- 10 3D CT image of a *Lupinus* root system in a soil column [Aylmore (1993)]. 40
- 11 Dalton's Capacitor-root analogy. **A.** Cross-sectional anatomy of a single root tip. **B.** Capacitor equivalence of the root tip. 43
- 12 Typical EIS setup for root studies. 44
- 13 Typical electrode array for electrical sounding and electrical surveys. 46
- 14 Illustrative example between tap-root systems and fibrous RSAs. 47

- 15 Magic box analogy. 49
- 16 Electric potential field of three changes in vacuum. Two of the charges are positive (sources) and one is negative (drain). 50
- 17 Magnetic field generated from a 1 A current running through a loop of wire. 51
- 18 Normalised magnetic field around a wire, illustrating the right-hand rule. 52
- 19 Large conductive region R_b having radius r_b with an embedded small conductivity region R_a of radius r_a . 53
- 20 Sensitivity versus resolution plot as α approaches unity. 54
- 21 Sensitivity versus contrast plot for $r_a = 0.2mm$ and a non-fixed r_b . 55
- 22 Discretised two-dimensional plane for voltage calculation. 56
- 23 Five point stencil for the discretised Laplace's equation. 57
- 24 Solution to Laplace's equation for two sinusoidal boundaries. 57
- 25 **A.** 3D model of the EIT pot. **B.** Pot Tetrahedral FEM Model. The lighter coloured element indicates the first numbered electrode. 59
- 26 Nodal voltages in a mesh stimulating opposite electrodes for a 2D ring. 60
- 27 **A.** Adjacent or Sheffield S/M protocol. **B.** S3/M5 protocol. 61
- 28 Representation of the square electrode arrangement. Here s represents the distance between electrode rings. 61
- 29 Violin plot corresponding to the condition numbers obtained from all possible S/M combinations in both planar and square methods, tested in seven vertical electrode ring positions. 63
- 30 Vertical sensitivity across the vessel's centre for S5 at different positions for **A.** planar, and **B.** square protocols. 66
- 31 Planar protocols' sensitivity values at the middle of the vessel for position 4. 67
- 32 Square protocols' sensitivity values at the middle of the vessel for position 4. 68
- 33 Transformation induced by matrix A on a 3D spherical shape. The transformation is equivalent to the fundamental transformations: rotation, scaling, and another rotation. 72
- 34 Basic numerical example of solving EIT's inverse problem with Moore-Penrose Pseudo-inverse. **A.** Original VOI to be reconstructed with a homogeneous conductivity background, and a low conductivity spherical intrusion. **B.** 3D Reconstruction without noise considerations. **C.** Surface plot of a 2D slice taken at the middle of the electrode plane. The z-axis represents the amplitude of the reconstruction at that z-level. 74

- 35 Optimal solution for the least-squares problem using **A.** L2 and **B.** L2 norms. The outer elliptical plot represents the least-squares residuals, and the central plot represents the cost of the norm. The optimal solutions are found wherever there is an intersection between the contour plots. The β_n are the model parameters, and the small red dots represent the solution for different values of λ . 76
- 36 Ideal representation of **A.** L-curve and **B.** GCV methods for different λ . The optimal value $\lambda_{optimal}$ can be found at the L-corner in (**A**), and at the minimum of the GCV plot (**B**) 78
- 37 Illustrative example of Newton descent methods. The figure represents the Rosenbrock function, where the minimum is located in a banana shaped region. Given an initial guess, the algorithm gets closer to finding the minimum upon each iteration. 79
- 38 Comparison between regularization schemes for solving the inverse problem using a time-difference One-step GN algorithm. **A1.** & **A2.** Isometric and top view of the VOI to be reconstructed with a homogeneous conductivity background, and two orthotope intrusions of high and low conductivity. Reconstructions of the change in conductivity obtained using **B1.** & **B2.** Tikhonov, **C1.** & **C2.** Laplace, and **D1.** & **D2.** NOSER regularization schemes. 82
- 39 Image reconstructions for the evaluation of a one-step GN algorithm using GREIT's framework. The figure shows the reconstruction of the intrusions travelling from edge to edge every 10 steps. 84
- 40 GREIT figures of merit for a central inclusion moving horizontally across a cylindrical vessel with a single 16-electrodes ring. All metrics are presented using Arbitrary Units. 85
- 41 Higher electrode spacing geometry and its training targets. 88
- 42 Planar S1/M1 NP characterisation. 90
- 43 Planar S3/M7 NP characterisation. 91
- 44 Planar S5/M7 NP characterisation. 92
- 45 Comparison of the vertical resolution of **A.** an oval target at a 45° for a **B.** planar S3/M7 and a **C.** square S5/M6 protocol. 93
- 46 Square S1/M1 NP characterisation. 94
- 47 Square S5/M6 NP characterisation. 95
- 48 Square S7/M7 NP characterisation. 96
- 49 **A.** Two terminal impedance measurement method, and **B.** Kelvin measurement technique 98
- 50 AFE main excitation loop. 100
- 51 pEIT block diagram. 102
- 52 SpEIT improved excitation loop. 104
- 53 SpEIT block diagram. 105

54	On-resistance of a bilateral switch with respect of the input signal.	106
55	Equivalent circuit of a single CMOS bilateral switch.	107
56	Output voltage across a 50Ω at 1 kHz using the spectral and MUX output.	109
57	Power spectrum analysis for both A . Spectral, and B . MUX outputs.	110
58	Flexible electrode strip. The strip consists of eight impedance controlled electrodes.	111
59	A . SpEIT rhizotron, and B . its isometric view showcasing the sensor strips.	112
60	SpEIT mainboard A . Front face B . Bottom face. C . SpEIT feeder board.	113
61	SpEIT initialisation process.	115
62	Basic IoT architecture.	118
63	Physical representation of the SpEIT network	120
64	SpEIT network workflow.	121
65	spmqt hierarchy.	122
66	Soil three-phase diagram. The diagram shows what elements are considered part of the total volume (V_t), as well as for the total mass (M_t).	124
67	S-01 TDR characterisation. The figure shows the change in permittivity and electrical pore conductivity as a function of water content.	126
68	S-02 TDR characterisation. The figure shows the change in permittivity and electrical pore conductivity as a function of water content.	127
69	Cubical vessel used for the EIS characterisation in the present work.	127
70	S-01 substrate EIS curves for different water contents. The right side of each curve corresponds to the lower frequencies of the spectral profile.	128
71	S-02 EIS curves for different water contents. The right side of each curve corresponds to the lower frequencies of the spectral profile.	128
72	S-01 individual frequency response, where A . shows the resistance and B . displays the reactance at different water levels.	129
73	S-02 individual frequency response, where A . shows the resistance and B . displays the reactance at different water levels.	130
74	Proposed circuit analogue model for peat substrates	130
75	Changes in the fluid components of the analogue circuit model representing the fluid as water content increases in S-01.	131
76	Changes in the fluid components of the analogue circuit model representing the fluid as water content increases in S-02.	132
77	Changes in the Warburg and charge-transfer resistance as the water content increases in S-01.	132
78	Changes in the Warburg and charge-transfer resistance as the water content increases in S-02.	133

- 79 Changes in the CPE characteristics as water content increases in S-
01. 134
- 80 Changes in the CPE characteristics as water content increases in S-
02. 134
- 81 Wet pot packing protocol used in experiments. 136
- 82 Multi-ring stimulation and measurement protocols considered for both
planar and square arrangements. The figure exemplifies a S1/M1 con-
figuration for both arrangements. 138
- 83 Evolution of S-01's weight across the duration of the experiment. 140
- 84 De-trended weight response. 140
- 85 Air-drying experiment reconstructions showing conductivity changes
of all protocols using a 1 kHz stimulation. Images presented as slices
taken at the centre of the vessel in its y-planes. All slices represent the
first frame at the beginning of the day cycle. 141
- 86 Pseudo-section representing the difference in voltage magnitude be-
tween the reference and the electrode fault time-point. The detected
fault is circled in red. 142
- 87 S-01's conductivity and susceptance changes at 10 kHz presented as
3D iso-volumes for the most representative days. 143
- 88 S-01's conductivity changes at different frequencies. Slice views at spe-
cific axes. 144
- 89 S-01's susceptance changes at different frequencies. Slice views at spe-
cific axes. 145
- 90 Histograms of the admittance change magnitude of all FEM elements.
The histograms correspond to three different instances in time. N=25
and 5577 elements 147
- 91 S-01's average admittance magnitude and phase changes for **A.** 1 kHz,
B. 10 kHz, and **C.** 50 kHz. 149
- 92 Model fitting for weight loss versus total conductivity change across
the vessel for a 1 kHz stimulation signal. 151
- 93 Logged processor temperature changes for the duration of the exper-
iment. 152
- 94 Mass evolution for the *Raphanus sativus* subject. 155
- 95 *Raphanus sativus* mass decrease fitted model. 156
- 96 **A.** *Raphanus sativus* at the end of the experiment, **B.** and its main RSA. 156
- 97 *Raphanus sativus* conductivity and susceptance changes at 10 kHz pre-
sented as iso-volumes. 157
- 98 *Raphanus sativus* conductivity changes at different frequencies. Slice
views at specific axes. 159
- 99 *Raphanus sativus* susceptance changes at different frequencies. Slice
views at specific axes. 160

- 100 *Raphanus sativus* average admittance magnitude and phase changes over the time period 00:00–220:00 at **A.** 500 Hz, **B.** 10 kHz, and **C.** 40 kHz. 162
- 101 *Raphanus sativus* average admittance magnitude and phase changes over the time period 220:00–480:00 at **A.** 500 Hz, **B.** 10 kHz, and **C.** 40 kHz. 163
- 102 *Raphanus sativus* average admittance magnitude and phase changes over the time period 480:00–672:00 at **A.** 500 Hz, **B.** 10 kHz, and **C.** 40 kHz. 164
- 103 *Brassica oleracea* mass changes during a 43 day period. 169
- 104 Logged processor temperature changes for the *Brassica oleracea* experiment. 169
- 105 *Brassica oleracea* mass losses fitted model. 170
- 106 **A** *Brassica oleracea* at the end of the experiment, and **B** its main RSA. 170
- 107 *Brassica oleracea* conductivity changes at different frequencies. Slice views at specific axes. 172
- 108 *Brassica oleracea* susceptance changes at different frequencies. Slice views at specific axes. 173
- 109 Silhouette coefficients to find the optimal number of clusters. 174
- 110 *Brassica oleracea* clustered conductivity changes at 10 kHz presented as iso-volumes. 174
- 111 *Brassica oleracea* average conductivity and phase changes over **A.** 500 Hz, **B.** 10 kHz, and **C.** 40 kHz. 176
- 112 *Brassica oleracea* relationship between normalised weight and conductivity changes, and its fitted model. 178

TABLES

1	Summary of the most studied root traits in agriculture.	38
2	Root study methodologies.	42
3	Electrical methods in plant studies.	45
4	Vertical separation data-set description.	63
5	Relevant Pearson correlation coefficients for the planar protocol.	64
6	Relevant Pearson correlation coefficients for the square protocol.	65
7	Insertion loss across multiple frequencies.	108
8	SNR across multiple frequencies for both Spectral and MUX outputs.	109
9	Substrates' volumetric characterisation required to fill 2.5 cm of the smart rhizotron.	125
10	Substrate conditions to calibrate the moisture sensor.	126
11	Substrates' characterisation models for water content and EC pore as a function of permittivity change.	127
12	Computed hyperparameters for all S/M protocols.	139
13	Estimation results for S-01's SARIMA model	140
14	Seasonal moving average intensity ratios for individual admittance's components between reconstruction's frequencies at different stages of the experiment.	147
15	Coefficient estimation for S-01's SARIMA model for admittance magnitude changes	150
16	Distance correlation between VOI admittances changes and water content loss over different frequencies. C = complete, T = top, M = middle, and B = bottom.	151
17	Computed hyperparameters used to reconstruct images of the <i>Raphanus sativus</i> subject.	154
18	Irrigation events for the <i>Raphanus sativus</i> subject.	155
19	Coefficient estimation for <i>Raphanus sativus</i> mass changes SARIMA model.	155
20	Volumes computed from the reconstructions selected at 10 kHz	157
21	Linear relationship between mass losses and admittance magnitude changes at 10 kHz for the first two irrigation events.	165

- 22 Power-law between mass losses and admittance magnitude changes
at 10 kHz for eleven irrigation events. 166
- 23 Computed hyperparameters used to reconstruct images of the *Bras-*
soca oleracea subject. 168
- 24 *Brassica oleracea* experiment irrigation events. 169
- 25 Estimation results for the SARIMA models of the *Brassica oleracea* ex-
periment. 170
- 26 Distance correlation between mass losses and admittance magnitude
changes at 10 kHz for all irrigation events. Admittance changes are
presented as conductivity and phase changes. 177
- 27 Methods available to the SpEIT class. 185
- 28 Methods available to the DataLogger class. 188
- 29 Methods available to the SpAutomata class. 188

ACRONYMS

AC Alternate-Current.

ADC Analog-to-Digital Converter.

ADF Augmented Dickey-Fuller.

AFE Analog Front-End.

API Application Programming Interface.

BD Bulk Density.

BLE Bluetooth Low-Energy.

CEM Complete Electrode Model.

CG Conjugate Gradient.

CLI Command-Line Interface.

CMSIS Cortex Micro-controller Software Interface standard.

CoG Center of Gravity.

CPE Constant Phase Element.

CRC Cyclic Redundancy Check.

CT Computed Tomography.

DAC Digital-to-Analog Converter.

DC Direct-Current.

DFT Discrete Fourier Transform.

DRO1 DEEP ROOTING 1.

EIS Electrical Impedance Spectroscopy.

EIT Electrical impedance tomography.

ERT Electrical Resistivity Tomography.

EZ Evaluation Zone.

FAO Food and Agriculture Organization of the United Nations.

FEM Finite Element Method.

FFT Fast Fourier Transform.

GCV Generalized Cross-Validation.

GPR Ground Penetrating Radar.

GREIT Graz consensus Reconstruction algorithm for EIT.

GRFC Global Report on Food Crises.

IC Integrated Circuit.

IL Insertion Loss.

IoT Internet-of-Things.

MAC Medium Access Control.

MQTT Message Queue Telemetry Transport.

MRI Magnetic Resonance Imaging.

MUX Multiplexer.

NF Noise Figure.

NOSER Newton One-Step Error Reconstructor.

NP Noise Performance.

OSI Open System Interconnections.

PCG Preconditioned Conjugate Gradient.

PET Positron Emission Tomography.

PID Proportional-Integral-Derivative.

RMSA Root Mean Squared Amplitude.

RSA Root System Architecture.

RSSI Received Signal Strength Indicator.

S/M Stimulation & Measurement pattern.

SARIMA Seasonal Autoregressive Integrated Moving Average.

SNR Signal-to-Noise Ratio.

SS Solid-State.

STDIN Standard Input.

SUS Substrate Under Study.

SVD Singular Value Decomposition.

TIA Transimpedance Amplifier.

UART Universal Asynchronous Receiver-Transmitter.

VOI Volume of Interest.

THIS PAGE INTENTIONALLY LEFT BLANK

ABSTRACT

Considering that agriculture is the primary source of income to approximately 750 million people, the implication of climate change in agriculture will inevitably threaten food security around the globe. This thesis focuses on further developing a technology that could enhance a crucial part of the global food system, plant phenotyping. Plant roots are complex structures that explore the soil, serving numerous adaptive purposes that are direct responses to abiotic stresses such as drought, salinity stress, and flooding. Roots are, therefore, essential targets for plant breeders, particularly concerning responses to biotic and abiotic stresses. However, visualising the root system architecture (RSA) and associated root functions in plants grown in natural substrates is inherently difficult due to the opaqueness of soil, which has impacted breeding efforts. Significant advances have been made in using tomographic imaging techniques to visualise the RSA of soil-grown plants, including magnetic resonance imaging and high-resolution X-ray computed tomography. Nevertheless, due to practical and economic reasons, access to these types of systems is limited across the plant breeding community.

The work's original contribution to knowledge is the development of an electrical impedance tomography (EIT) system optimised for high-throughput root studies, and a methodology that enhances the interpretation of the images reconstructed. Modern phenotyping requires the evaluation of the RSA to be accurately characterised. Not only that, but any root phenotyping methodology should also be high-throughput in nature, in order to test multiple genotypes routinely. This project explores the use of EIT as a non-invasive, non-destructive method for continuous monitoring of root development and root-soil interactions.

The development of the EIT system, involves the study of non-traditional stimulation/measurement protocols to enhance the vertical resolution of 3D EIT images. The use of protocols using vertically optimised strategies with different "skips", do not only present an enhancement on the sensitivity of the measurement procedure, but also improves the ability of the technique to adequately reconstruct the vertical location of volumes-of-interest. These improvements, together with the characteristics of modern phenotyping techniques, were used to develop a high-throughput IoT enabled EIT system. The capabilities of the system and reconstruction methodology are demonstrated through three experiments under controlled conditions. The experiments explore the evolution soil moisture in an air-drying process, the monitoring of a tap-root based root system, and the root development of an herbaceous plant. The findings show that the high temporal resolution of the system can measure small changes that can lead to a better understanding of plant-soil interactions.

The results presented in this study are of relevance to the plant breeding community, who can enhance their ability to detect and select root focused traits through continuous monitoring of plant roots. The inclusion of this technology in phenotyping studies can help underpin efforts to develop plant varieties with roots better suited to the inevitable effects of climate change.

THIS PAGE INTENTIONALLY LEFT BLANK

DECLARATION

No portion of the work referred to in the thesis has been submitted in support of an application for another degree or qualification of this or any other university or institute of learning.

A handwritten signature in black ink, appearing to read "Diego Corona López". The signature is fluid and cursive, with a large, stylized 'D' at the beginning.

Diego Corona López

THIS PAGE INTENTIONALLY LEFT BLANK

COPYRIGHT STATEMENT

The author of this thesis (including any appendices and/or schedules to this thesis) owns certain copyright or related rights in it (the "Copyright") and he has given the University of Manchester certain rights to use such Copyright, including for administrative purposes.

Copies of this thesis, either in full or in extracts and whether in hard or electronic copy, may be made only in accordance with the Copyright, Designs and Patents Act 1988 (as amended) and regulations issued under it or, where appropriate, in accordance with licensing agreements which the University has from time to time. This page must form part of any such copies made.

Further information on the conditions under which disclosure, publication and commercialisation of this thesis, the Copyright and any Intellectual Property and/or Reproductions described in it may take place is available in the University IP Policy, in any relevant Thesis restriction declarations deposited in the University Library, the University Library's regulations in the University's policy on Presentation of Theses.

A handwritten signature in black ink, appearing to read "Diego Corona López".

Diego Corona López

THIS PAGE INTENTIONALLY LEFT BLANK

ACKNOWLEDGEMENTS

Many thanks to everyone who made this work such a rewarding experience:

- *Sarah Sommer* formerly part of the department of Animal and Plant Sciences, University of Sheffield, United Kingdom, for her friendship, assistance and advice at early stages of this project.
- *Stephen Rolfe* from the department of Animal and Plant Sciences, University of Sheffield, United Kingdom, for his continuous feedback, openness to collaborate, and enlightening discussions.
- *Saba Mohammed* from the Institute of Agricultural Research, Ahmadu Bello University, Nigeria, for the warm invitation to collaborate, which helped in the direction of this project.
- *Paul Shaw, Derrick Bradshaw, and Danny Vale* from the School of Electrical & Electronic Engineering, University of Manchester, for their support in the mechanical construction and PCB manufacturing of the early prototypes.
- *The Gentlemen of B37*, now the Fotenix team, who offered me their camaraderie, friendship and encouragement; making me feel welcome at all times.
- *Bruce Grieve and Frank Podd*, School of Electrical and Electronic Engineering, University of Manchester. For the initial guidance and help during the early stages of this project conception. Their guidance was integral to the scientific relevance of this study.
- *Andrea Ruiz*, for her continuous support building the early prototypes, and the consistent brainstorming which helped shape the final system, and for her patience and friendship which made my stay at the University of Manchester all the more enjoyable.
- *Angeles López Tlahuiz* for her time, continuous support and neverending encouragement.
- *Rayo and Daniel* for all their love, patience and support.
- To all my friends and family that even when there is an ocean between us, they would encourage me in tough times.
- To anyone who took the time to read through this work and helped me to correct it.
- I would also like to acknowledge CONACYT for its support.

Thank you all

THIS PAGE INTENTIONALLY LEFT BLANK

*To my father,
who nurtured my love of science through wonderful stories
throughout my life. This work, as with the last, would not
have been possible without his love and support.*

THIS PAGE INTENTIONALLY LEFT BLANK

BACKGROUND AND MOTIVATION

LIVING IN THE ANTHROPOCENE has put us, humans, in a peculiar position, in which we have to steer the path towards global sustainability. Before this, intensive agriculture was continuously promoted as the only solution to feed our burgeoning population. Focus on improving the supply chain, and on obtaining higher crop yields has enhanced the way of living across the globe; bringing poverty reduction, higher life expectancy, and lower child mortality rates¹. However, these practices may be the very reason of our current global food security predicaments.

1.1 The current state of affairs

Recent figures, from the Food and Agriculture Organization of the United Nations (FAO), show that severe global food insecurity was on the rise between 2014 and 2017; with significant increases in Africa and Latin America². During 2018 more than 113 million people suffered food insecurity requiring urgent assistance (Fig. 1).

“Civilisation is in crisis. We can no longer feed our population a healthy diet while balancing planetary resources. For the first time in 200,000 years of human history, we are severely out of synchronisation with the planet and nature”
Lucas and Horton, 2019

¹ Sarah Whitmee et al. *Safeguarding human health in the Anthropocene epoch: Report of the Rockefeller Foundation-Lancet Commission on planetary health*. 2015.

² Neil Bradford and David A. Wolfe. *Governing regional economic development: Innovation challenges and policy learning in Canada*. Vol. 6. 2. 2013.



Figure 1: People experiencing acute hunger and in need of assistance (Integrated Food Security Phase 3, i.e. in crisis)

In 2017 approximately 10% of the world population (around 770 million people) faced severe food insecurity scenarios (Fig. 2). These figures are alarming when considering that by 2050, the global urban population is expected to grow by at least 60%, and thus, food demand will inherently increase. This means that approximately 80% of the demand should be satisfied by increasing crop yields³. However, the current climate instability requires agriculture to transition to more productive and sustainable practices.

According to Willett et al.⁴ (2019) food production is one of the primary causative agents of global environmental change. In particular, the global food system is estimated to generate up to 30% of the total greenhouse gas emissions⁵. Agriculture is responsible for the conversion of natural ecosystems into croplands and pastures, and in most countries, it employs approximately 70% of the freshwater resources available⁶. The continuous increase in land degradation and future water scarcity issues will not only hinder yield capability but also compromise our ability to ensure access to adequate quantities of food in most countries.

Climate change will aggravate the aforementioned adverse effects as food production is inextricably tied to weather and climate conditions. Considering that agriculture is the primary source of income to approximately 750 million people, the implication of climate change in agriculture will inevitably strike already vulnerable populations, further threatening their food security. All of this put agriculture at the centre of the greatest health and environmental challenge of the century: “*adapting to climate change by creating practices that minimise its environmental impact while increasing its productivity.*”

1.1.1 The effects of careless food production

The effects of climate change are already affecting agriculture and food security, making the previously mentioned challenge more difficult to overcome. Climate variations (e.g. in rainfalls and temperature) keep undermining crop yields around the globe. For instance, tropical and temperate regions have seen a significant yield decrease in major crops (such as rice, maize and wheat) due to extreme temperature changes and precipitation. Zampieri et al.⁷ have measured the impact of heat, drought and water excess showing that these effects significantly increase the global inter-annual variability of yields for wheat and maize. The study estimates that climate factors cause between 32% and 39% of yield variability.

The extent to which communities are negatively impacted by climate variability is defined mainly by their exposure to climate shocks. According to the Global Report on Food Crises (GRFC), the intensity and occurrence of climate shocks have increased in the last decade; worsening the livelihoods of communities with high dependence on agriculture that are already threatened by food insecurity. Plants are under constant threat of countless attackers. Plant pests and diseases

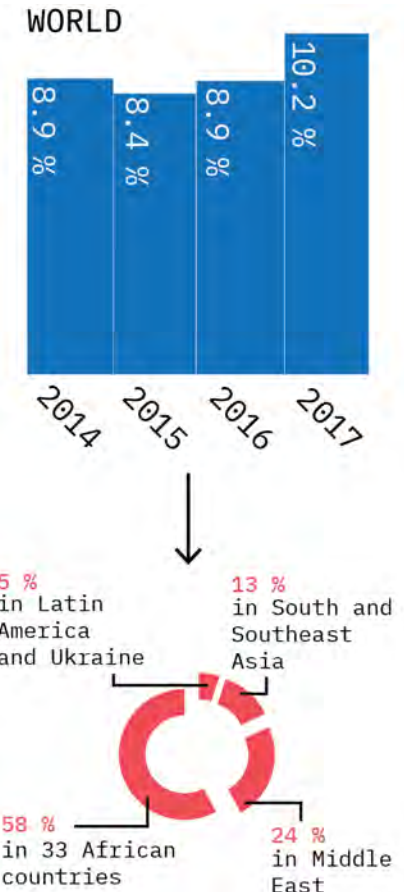


Figure 2: Percentage of the global population with severe food insecurity and how it divides across regions

³ J Alexandratos, N. and Bruinsma. “World Agriculture Towards 2030/2015: The 2012 Revision”. In: *World Agriculture* (2012).

⁴ Walter Willett et al. “Food in the Anthropocene: the EAT–Lancet Commission on healthy diets from sustainable food systems”. In: *The Lancet* 393.10170 (2019).

⁵ Sonja J. Vermeulen et al. “Climate Change and Food Systems”. In: *Annual Review of Environment and Resources* 37.1 (2012).

⁶ David Molden. *Water for food water for life: A Comprehensive assessment of water management in agriculture*. Routledge, 2013.

⁷ M. Zampieri et al. “Wheat yield loss attributable to heat waves, drought and water excess at the global, national and subnational scales”. In: *Environmental Research Letters* 12.6 (2017).

are considered as a key contributor in overall crop yield losses⁸. At least \$60 billion losses are attributed to fungal and oomycete pathogens. This represents approximately 23% of the total yield loss⁹. Bebber et al.¹⁰ show that there is a link between the individual crop production of a country and the likelihood of pathogen development. Climate change is contributing to the previous fact, as fungal and oomycete pathogens can adapt faster than plants to the environment; overcoming most plant resistances and evolving into multi-host pathogens. This can lead to disease epidemics that will further undermine crop productivity.

The challenge of food security is a massive multivariate problem that requires the involvement of different disciplines. This thesis focuses on further developing a technology that could enhance a crucial part of the global food system, plant phenotyping.

1.2 Phenotyping as a vessel for sustainable agriculture

One of the critical aspects needed to achieve sustainable food productions is adequate crop and resource management. Phenotyping offers approaches to enhance our understanding of plants in their environment, thus is easy to see why it is one pillar of sustainable agriculture. Modern phenotyping provides essential measurements related to complex plant processes such as environmental pressure, stress adaptation, growth and yield genetics, from small organs to large canopies¹¹. Therefore, phenotyping can be used as a breeding guide towards the efficient selection of plant traits suited for the oncoming environmental changes.

As proposed by Costa et al.¹², any plant phenotyping technique should have the following characteristics:

- **Non-destructive measurement acquisition:** to allow trait tracking over time
- **High-throughput analysis:** to enable screening for various genotypes under similar test conditions.

Furthermore, advanced phenotyping technologies act not only as breeding vessels but also as disease diagnosis techniques. As mentioned in the previous subsection (1.1), plant diseases portray more than a direct threat. The indirect repercussion of plant diseases to farmers may be far worse than the direct ones, as infections and infestations have long-term consequences that put at risk food security¹³.

A common practice in the farming community to diagnose plant diseases is through optical observation of leaves performed by a scouting specialist. Current disease diagnosis technologies take inspiration from the previous approach using optical hardware combined with data analysis algorithms to enhance the accuracy and repeatability of the technique¹⁴. Plant disease identification is hard, but when trying to automate the process, it becomes even more challenging. For

⁸ Serge Savary et al. "The global burden of pathogens and pests on major food crops". In: *Nature Ecology and Evolution* 3.3 (2019).

⁹ Matthew C. Fisher et al. "Emerging fungal threats to animal, plant and ecosystem health". In: *Nature* 484.7393 (2012).

¹⁰ Daniel P. Bebber et al. "Economic and physical determinants of the global distributions of crop pests and pathogens". In: *New Phytologist* 202.3 (2014).

¹¹ Corrado Costa et al. *Plant phenotyping research trends, a science mapping approach*. 2019.

¹² Costa et al., *Plant phenotyping research trends, a science mapping approach*.

¹³ E. C. Oerke. "Crop losses to pests". In: *Journal of Agricultural Science* 144.1 (2006).

¹⁴ X. E. Pantazi et al. "Automated leaf disease detection in different crop species through image features analysis and One Class Classifiers". In: *Computers and Electronics in Agriculture* 156 (2019).

this reason, modern plant phenotyping tends to lean more and more towards the use of big data and machine learning analysis.

Today's plant monitoring and phenotyping technologies focus predominantly on assessing the foliar canopy; yet, significant and complementary benefits can be obtained by analysing subsoil processes across different crop growth stages. These processes take place in the *rhizosphere* (Fig. 3). The term is derived from its Greek basis, '*rhiza*' meaning root, and '*sphere*', interpreted as an area of influence. The rhizosphere refers both to the volume of soil shaped by the root and the micro-organisms surrounding root tissues¹⁵. The rhizosphere is a nutrient-rich zone inhabited by numerous beneficial and pathogenic organisms^{16,17}. Having a better understanding of the rhizosphere is essential for agriculture, as a better perspective of the subsoil growth dynamics can enhance crop productivity¹⁸.

The study of the rhizosphere is a challenging task. Traditional research methods are monotonous, time-consuming, often destructive and require *in situ* sampling. As a result, our understanding of how root structures develop and interact with soil nutrients is still fractured, since no method offers an accurate description of these complex systems under 'real-life' conditions.

1.3 Proposed approach

The present project aims to adapt existing technologies based on the concept of bio-electrical impedance to help address the current limitations of plant-soil studies. The study of bio-electrical impedance inherently satisfies the requirements of modern plant phenotyping techniques, as it is non-destructive and can be implemented as a high-throughput solution.

HYPOTHESIS

"Electrical Impedance Tomography (EIT) and Electrical Impedance Spectroscopy (EIS) can act as plant phenotyping methods. EIT and EIS can deliver below-ground phenotypic data in a non-invasive and high-throughput manner."

The research objectives planned to validate the hypothesis are:

- Revise the state-of-art of plant-soil studies.
- Compare EIT/EIS to current root study technologies to have a bigger scope of the limitations in electrical impedance methods.
- Compare current reconstruction algorithms and stimulation patterns to find the adequate parameters for the end application.
- Engineer an EIT/EIS rhizotron capable to monitor root system interactions.
- Demonstrate the system capabilities in a research growing environment.

¹⁵ Roberto Pinton et al. *The Rhizosphere: Biochemistry and Organic Substances at the Soil-Plant Interface*. 2nd. Crc Press, 2019.

¹⁶ Anton Hartmann et al. "Lorenz Hiltner, a pioneer in rhizosphere microbial ecology and soil bacteriology research". In: *Plant and Soil*. Vol. 312, 1-2. Springer Netherlands, 2008.

¹⁷ James M Lynch et al. "Rhizosphere". In: *eLS*. Chichester, UK: John Wiley & Sons, Ltd, 2001.

¹⁸ E. W. Tollner. "X-ray computed tomography applications in soil ecology studies". In: *Agriculture, Ecosystems and Environment* 34.1-4 (1991).

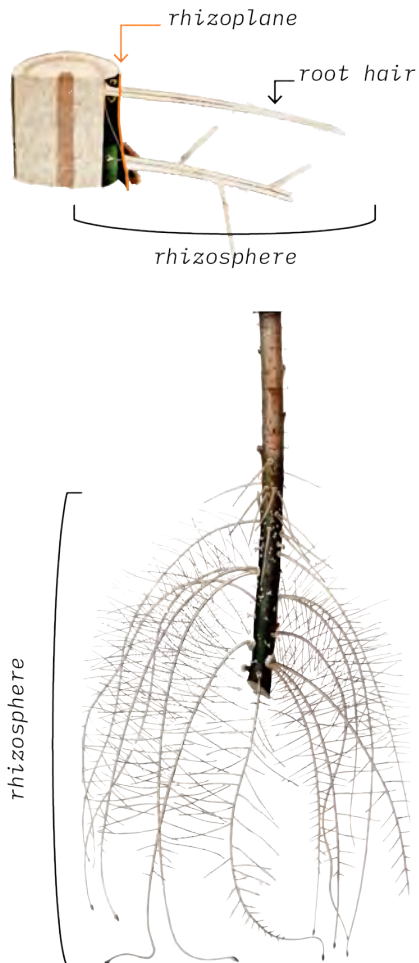


Figure 3: Visual representation of the rhizosphere

The present work encompasses seven chapters, each building on a significant aspect of the research.

- *Chapter 1 Background and motivation*: Overview of Current food security challenges presented, setting the context for this research.
- *Chapter 2 Root research*: Overview of traditional and modern root study methods. The chapter highlights the importance of root phenotyping.
- *Chapter 3 Direct problems*: Introduction to electrical imaging and modelling the electromagnetic nature of the imaging problem. Furthermore, it describes the research undertaken to improve the vertical resolution of 3D imaging beyond the use of single electrode planes.
- *Chapter 4 Inverse Problems*: Review of image reconstruction algorithms for electrical imaging. The chapter complements the contribution presented in Chapter 3 by analysing the effects of enhanced stimulation/measurement protocols in 3D reconstructions by using adequate metrics and expanding on current evaluation metrics.
- *Chapter 5 Smart rhizotron*: Describes the design of an electrical imaging system and platform for root studies. The Chapter not only describes the design of an IoT enabled EIT system but also the development of a previous iteration that led to the final design. Moreover, a detailed explanation of the firmware developed is presented.
- *Chapter 6 Empirical findings and discussion*: Demonstrates the capabilities of the EIT system through three experiments. It presents the profiling of growth substrates through EIS to enhance the understanding of EIT images. The chapter presents expands on the soil-preparation protocol developed previously by the author. Moreover, a new multi-ring stimulation/measurement protocol that enhances the vertical resolution of the system while maintaining its high-temporal resolution is demonstrated. The chapter explores multiple approaches to the analysis of volumes-of-interest.
- *Chapter 7 Concluding remarks*: Describes the implications of the research and advice for future work.

The current work builds on the author's prior contributions regarding the use of EIT as a tool for subsoil plant pathogen detection.

- Diego D.J. Corona-Lopez et al. "Electrical impedance tomography as a tool for phenotyping plant roots". In: *Plant Methods* 15.1 (2019)

1.4 Nota bene

The layout of the present work is inspired on Tufte's work^{19,20}, thus, references are placed alongside their citations in the form of sidenotes. Furthermore, when referring to a previous citation, the reference only includes the authors and title of the work, for instance repeating this citation will appear with a different style²¹.

¹⁹ Edward R. Tufte. *Visual Explanations*. Cheshire, Connecticut: Graphics Press, 1997.

²⁰ Edward R. Tufte. *Beautiful Evidence*. 1st Editio. Lcc: Graphics Press, 2006.

²¹ Tufte, *Beautiful Evidence*.

THIS PAGE INTENTIONALLY LEFT BLANK

ROOT RESEARCH

MUCH HAS BEEN SAID about the 2050 food security challenge and the needed increase in food production. Tackling this challenge involves acquiring significant vast yields using existing crop fields, but without extending the use of water, fertilizers, and pesticides. Improving humanity's resource management is related to our understanding of plant interactions with its environment. For this very reason, modern plant phenotyping will be at the forefront of future crop management. However, most phenotyping technologies focus predominantly on above-ground characteristics, leaving two critical aspects of crop management understudied, root water and nutrient uptake.

The present chapter offers a perspective on the importance of root phenotyping, as well as the existing root study methodologies. After considering the current panorama on root studies, a unique approach to root phenotyping is then proposed. The latter method is based on a characteristic present in all material, electrical impedance.

2.1 *The elusive half of plants*

Plant roots supply not only anchorage to plants but also mine essential resources from soil, such as water and nutrient uptake/storage. As the root system continues to explore its environment, it grows and expands; this process is known as Root System Architecture (RSA) development (Fig. 4). The RSA's plasticity depends entirely on their environment conditions (e.g. moisture changes, nutrient depletion, pH). Thus, exploring the RSA response to natural variation gives us the opportunity to identify advantageous root traits to enhance our agricultural systems.

The importance of roots does not only pertain to a production point-of-view, but also to the soil health; which corresponds to the soil's ability to act as a nurturer of plants, animals and, by proxy, humans¹. For instance, plant roots aid in the processes of soil phytoremediation. Phytoremediation uses the ability of some plant roots to extract certain toxic compounds from the soil, and store them in the plant's aboveground organs that can be easily gathered for disposal². But perhaps the most common way that agriculture use roots to improve soil health is through crop rotation. Crop rotation helps growers break pest and disease cycles, and enhance soil health by changing its nutrient availability³. Studies show that the interplay between roots and soil bacteria create nitrogen reservoirs available to subsequent

"Root research under natural field conditions is a step-child of science. The known methods are tedious, time-consuming, and the accuracy of their results is often not very great" Böhm, 1979

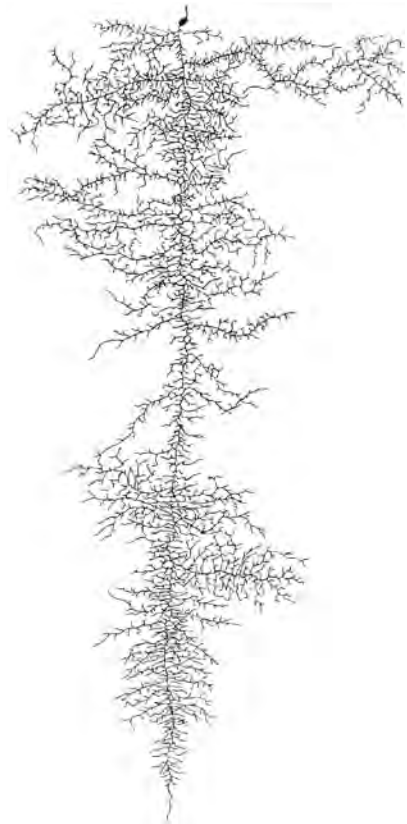


Figure 4: Example of a Root System Architecture (RSA) (Tsutsumi, 2003).

¹ John W. Doran and Michael R. Zeiss. "Soil health and sustainability: Managing the biotic component of soil quality". In: *Applied Soil Ecology* (2000).

² Bernard R. Glick. "Phytoremediation: Synergistic use of plants and bacteria to clean up the environment". In: *Biotechnology Advances* (2003).

³ Teresa Dias et al. "Accounting for soil biotic effects on soil health and crop productivity in the design of crop rotations". In: *Journal of the Science of Food and Agriculture* (2014).

crops⁴. This eliminates the necessity of chemically enhancing soils using a more sustainable farming practice.

As noted above, the RSA is a crucial part of plant adaptation under biotic/abiotic stresses. Roots' architectural features respond and adjust according to the plant needs. For example, under suboptimal nutrient conditions, plants prioritise root biomass allocation while inhibiting shoot growth. This adaptation is key for breeders that look to enhance their cultivars to tolerate stress conditions such as droughts. Therefore, as pointed out by Lynch⁵ (2007), crop production enhancement should also focus on improving RSA traits under a variety of environmental stresses.

RSA breeding requires us to identify specific root traits that enable plants to use resources efficiently in a variety of environments. Identifying these beneficial traits has proven to enhance crop productivity and its performance under abiotic stresses^{6,7}. Breeders can benefit greatly from identifying root phenes that lead to higher yields and increased tolerance to external stress factors. Nevertheless, as the RSA is a complex system with a variety of traits (described in the next subsection) any breeding program should consider: the farming system employed, soil conditions and its nature, and the heritability of the trait⁸. Despite the importance of root systems, at present, breeding methods for root traits are still limited. Breeding programs could benefit from understanding the root traits that lead to improvements in plant performance. Thus, a deeper understanding of what kind of root phenes should be crucial for agriculture is needed.

2.1.1 Traits linked to crop productivity

Roots do not only nurture plants, but they also perceive and respond to biotic and abiotic stresses sending signals to the aboveground organs. These functions influence the growth and development of plants, specifically through root-to-shoot signalling which determines plant's water use when soil conditions change. A considerable amount of literature has been published on the effect of root-to-shoot signalling. For example, Lynch (2007) points out that plant roots' plasticity adapts to the soil moisture content, particularly under low water stress, which results in a significant inhibition of shoot development.

Much of the current research on root traits pay particular attention to the practical value of these, such as increased foraging capacity under drought conditions. This subsection briefly describes the key root traits that are of practical significance for crop and forage production systems.

ROOT GROWTH

While the importance of root growth might be obvious from a resource acquisition point-of-view, it is key to not overlook its role in immobile nutrients' acquisition. By way of illustration, Barber (1995)⁹ describes two primary nutrient transportation processes. One is via

⁴ Guntur Venkata Subbarao et al. *Suppression of soil nitrification by plants*. 2015.

⁵ Jonathan P. Lynch. "Roots of the Second Green Revolution". In: *Australian Journal of Botany* 55.5 (2007).

⁶ K. Hassouni et al. "Root System Architecture and Its Association with Yield under Different Water Regimes in Durum Wheat". In: *Crop Science* 58.6 (2018).

⁷ Yusaku Uga et al. "Control of root system architecture by DEEPER ROOTING 1 increases rice yield under drought conditions". In: *Nature Genetics* 45.9 (2013).

⁸ Robert Meister et al. *Challenges of modifying root traits in crops for agriculture*. 2014.

⁹ Stanley A. Barber. *Soil nutrient bioavailability : a mechanistic approach*. Wiley, 1995.

transpiration-driven flow, in which water-soluble nutrients get closer to roots due to water movement caused by pressure or temperature gradients. The second process, is the acquisition of limited-diffusion nutrients by direct proximity. A plant that can have greater access to water and nutrients is a desirable characteristic for most growers, making root growth one of the most commonly evaluated root traits (Fig. 5).

Unsurprisingly, root depth is predominantly determined by the soil's physical and chemical characteristics¹⁰, with a dominant response to phosphorus availability. There are multiple studies that show how low-phosphorus availability change the root growth pattern of plants. Robinson (2005)¹¹, discusses the literature on how plants interact with nutrient patch supplies; this review explains how lateral root growth increases when a phosphorus-deficient plant finds a particular patch with higher nutrient concentration. The findings discussed indicate that root growth responds to poor nutrient availability by increasing the allocation of biomass to roots, which inhibits shoot growth. Typically, root growth declines during the normal plant life span, but for plants in infertile conditions the decline process is slower. Nevertheless, plants with phosphorus-efficient genotypes can overcome unfavourable phosphorus conditions maintaining a greater root-to-shoot ratio under low phosphorus. The latter emphasises how the selection of specific genotypes can enhance crop breeding.

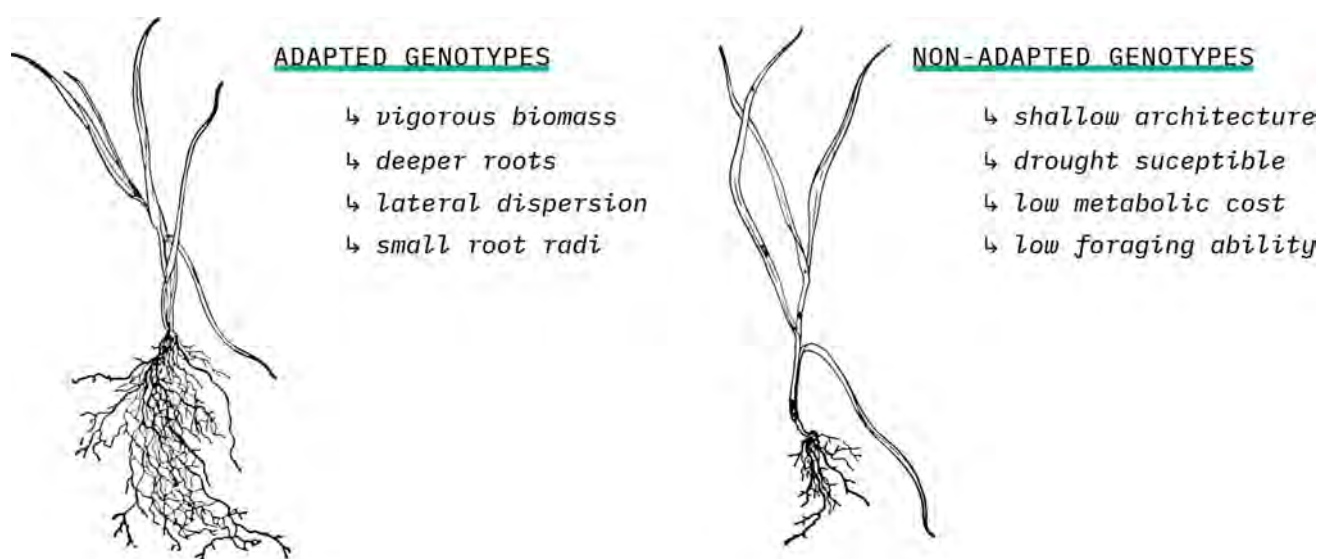
In spite of the previous facts, current root research has pointed out that there are complementary factors that shape the way roots grow other than soil's conditions. Lynch and Wojciechowski (2015), performed a study on maize root crowns to explore the benefits of anatomical traits under stress conditions¹². But, in order to fully comprehend the RSA's development breeders should also pay attention to the effects of gravitropism.

¹⁰ Jonathan P. Lynch and Tobias Wojciechowski. *Opportunities and challenges in the subsoil: Pathways to deeper rooted crops*. 2015.

¹¹ D. Robinson. "Integrated Root Responses to Variations in Nutrient Supply". In: *Nutrient Acquisition by Plants*. 2005.

¹² Jonathan P. Lynch. *Root phenes that reduce the metabolic costs of soil exploration: Opportunities for 21st century agriculture*. 2015.

Figure 5: Root growth adaptations to enhance plant's nutrient and water capabilities [Illustrative example based on Goff and Mayne's work (1904)].



GRAVITROPISM

Gravitropism describes the physiological response of plants organs to gravity. This response can be either towards (positive) or away (negative) the gravity vector (Fig. 6). The trait heavily related to gravitropism is known as DEEP ROOTING 1 (DRO1), which is a quantitatively localised trait that controls root growth angle. Uga et al. (2013)¹³ demonstrated that sharper root angles lead to strong gravitropic responses from rice seedling. In other words, a robust response to gravitropic effect inherently lead to plants with an enhanced tolerance to drought. The enhancement is thought to be occasioned by a deeper root system with better forage opportunities. Uga, explains that DRO1 is regulated by plant hormones called auxin, which are still not well understood. Nevertheless, the practical use of DRO1 breeding is clear, and is the subject of other studies¹⁴.

ROOT ARCHITECTURE

As previously discussed at the beginning of this section, the RSA refers to the spatial distribution of roots at a given time in the plant's life cycle. How the RSA develops is critical for the plant's soil resource acquisition as it defines root foraging for different soil conditions. Not only it dictates this resource exploration, but it also mediates the resource acquisition competition between neighbouring roots of the same plant. Most studies have explored the importance of RSA traits for phosphorus foraging (an immobile nutrient), however, less is known about the acquisition of other nutrients (e.g. nitrate, calcium). Lynch (2007) proposes the idea that nutrients with greater mobility would depend more on the structure of the RSA rather than the direct proximity of roots. He supports this idea using the findings of Fitter et al. (2002)¹⁵, where it was shown that *Arabidopsis* plants (with a mutation that impacts its lateral root development) with reduced architectural traits performed worse when trying to acquire immobile nutrients; this could mean that a less fine RSA with greater lateral and depth spread would benefit of an enhanced acquisition ability of soluble nutrients. Passioura (2012)¹⁶ discusses the effects of subsoil water availability in conjunction with periodic rainfall on both the above- and under-ground plant organs; further establishing the importance of deeper RSAs, that enhance crop yield under limited rainfall conditions, for breeding.

One of the biggest challenges that root studies face, is the RSA optimisation focused on improving the acquisition of nutrients distributed stochastically while at the same time addressing interplant competition (i.e. growth field conditions). A clear example of this is the research of Bolaños and Edmeades (1993)¹⁷, where they describe the inefficiency of drought tolerance trait selection and how its recurrence lead to suboptimal root systems. Thus, the importance of adequate RSA optimisation cannot be stressed enough. However, in breeding, growers also need to consider the metabolic cost of selecting genotypes with vigorous RSA. As an illustration, an abundant RSA im-

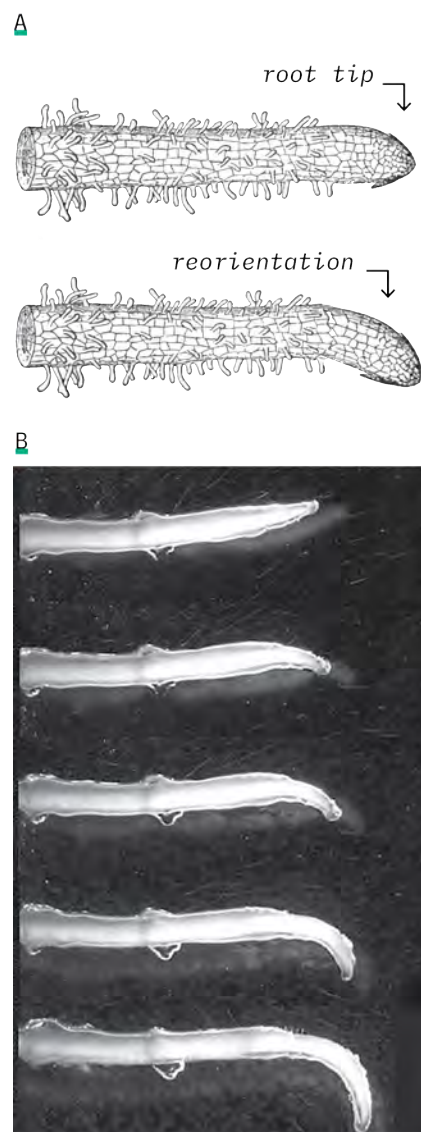


Figure 6: A. Effects of gravity on roots. Root tips are known to reorient once they are gravitationally stimulated [Illustrative example based on Beach's work (1914)]. B. Effects of gravitropism on *Pinus taeda* after 0.0, 1.0, 3.0, 6.0, and 12.0hrs (Zhang et al. 2019).

¹³ Uga et al., "Control of root system architecture by DEEPER ROOTING 1 increases rice yield under drought conditions".

¹⁴ Elison B. Blancaflor. "Regulation of plant gravity sensing and signaling by the actin cytoskeleton". In: *American Journal of Botany* 99.13 (2013).

¹⁵ Alastair Fitter et al. "Root system architecture determines fitness in an <i>Arabidopsis</i> mutant in competition for immobile phosphate ions but not for nitrate ions". In: *Proceedings of the Royal Society of London. Series B: Biological Sciences* 269.1504 (2002).

¹⁶ J. B. Passioura. "Phenotyping for drought tolerance in grain crops: when is it useful to breeders?" In: *Functional Plant Biology* 39.11 (2012).

¹⁷ J. Bolaños and G O Edmeades. "Eight cycles of selection for drought tolerance in lowland tropical maize. II. Responses in reproductive behavior". In: *Field Crops Research* 31.3-4 (1993).

ply, in some cases, an increased maintenance cost that could negatively impact the output yield. The higher metabolic cost of root foraging in soil is well documented, and it often exceeds the daily nutrient income from the photosynthetic process.

ROOT HAIRS

These delicate cylindrical root extensions, emerge from the root epidermal cells (Fig. 7). They are key to the nutrient acquisition process and microbe exchanges. It is estimated that they contribute to at least 50% of the total water absorption, since they make up most of the total RSA surface area. In studies where plant with root hair-less mutations were observed, plants exhibited a proclivity to poor performance under temperature and drought stress as their water absorption ability was impacted due to this mutation¹⁸. Several studies have demonstrated the impact of these traits in crop production. Research made on *Phaseolus vulgaris* (or common bean) showed that shallow basal roots with long root hairs enhance substantially (approx. 300% more) the plant's ability to acquire phosphorus¹⁹. Moreover, research made in barley showed that higher root hair concentration enhance the RSA ability to penetrate compact soils, and thus improve its establishment cycle and nutrient absorption²⁰.

While there are well-known methods to modify plants' gene expressions to modify the root hair anatomy, it is yet to be proved that crops can benefit from such morphological changes²¹. Root development dynamics, and roots in general, are complex mechanisms that involve diverse gene variables. Although complicated, the current research has demonstrated the importance of breeding these traits, specially to combat the coming food security challenges.

The aim of this section is to briefly describe the key traits that have been proven to significantly impact agriculture, however, it is important to note that root traits are not limited to the above mentioned ones. Table 1 gives a quick overview of other common root traits that have been under study and their benefits to crop production.

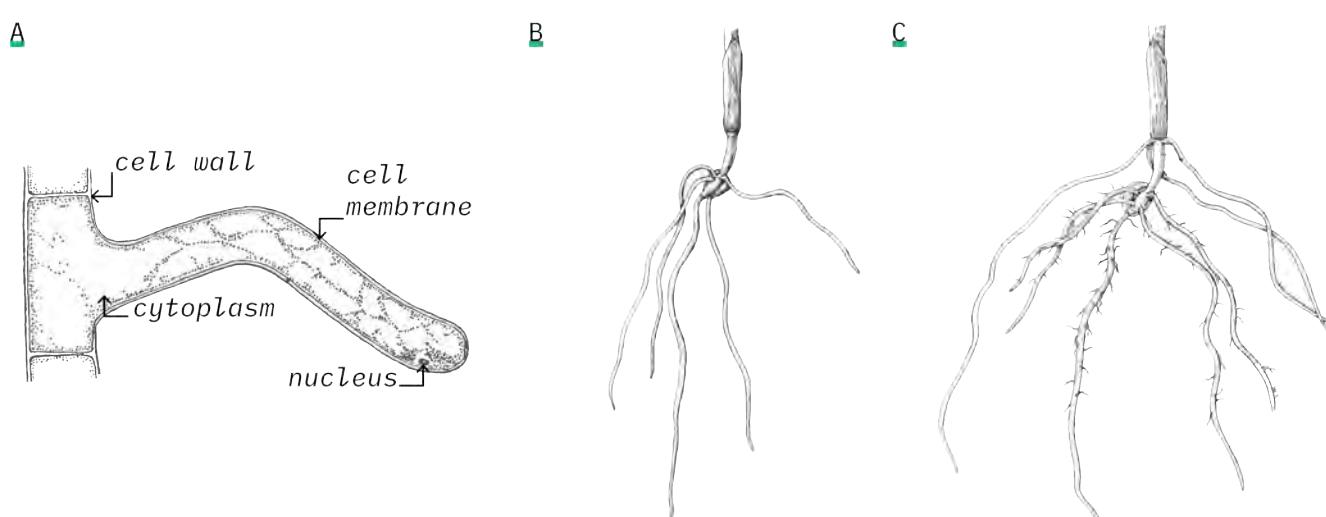
¹⁸ Natsuki Tanaka et al. "Characteristics of a root hair-less line of *Arabidopsis thaliana* under physiological stresses". In: *Journal of Experimental Botany* 65.6 (2014).

¹⁹ Magalhaes Amade Miguel et al. "Phene Synergism between Root Hair Length and Basal Root Growth Angle for Phosphorus Acquisition". In: *Plant Physiology* 167.4 (2015).

²⁰ Rebecca E. Haling et al. "Root hairs improve root penetration, root-soil contact, and phosphorus acquisition in soils of different strength". In: *Journal of Experimental Botany* (2013).

²¹ Amelie Mendrinna and Staffan Persson. "Root hair growth: It's a one way street". In: *F1000Prime Reports* 7 (2015).

Figure 7: A. Anatomy of root hairs [based on the work of Stevens (1916)]. Comparison of maize RSAs between a hairless mutant (B) and a normal maize variant (C), [based on the findings of Hochholdinger et al. (2004) and the drawings of Miwa Kojima (Iowa State University)]



ROOT TRAIT	AGRICULTURAL BENEFITS	REFERENCES
Root length (primary roots)	Potential for enhanced water and nutrient forage/absorption.	Wasson et al. (2012), Zhu et al. (2011)
Gravitropism	Enhanced gravitropic responses in seedling, leading to deeper root systems.	Uga et al. (2013), Bolaños and Edmeades (1993),
Root diameter	Regulation of drought stress, growth potential, mycorrhizal development. Improved root penetration in dry soils.	Arifuzzaman et al. (2019), Brown and Lynch (2006)
Crown roots	The number of this type of root is associated with the plant's nitrogen capture ability.	Saengwilai et al. (2014)
Root branching	A higher lateral branching implies a greater surface area, and thus, enhanced soil exploitation capabilities.	Postma et al. (2014)
Hair density	Enhanced root penetration and phosphorus acquisition.	Mendrinna and Persson (2015)
Cell walls	Improved water retention in mature roots.	Sato et al. (2015)
Transpiration	Optimisation of metabolic costs during soil exploration.	Cassiani et al. (2015)

2.2 Imaging roots

Understandably, today's phenotyping efforts have been centred mainly on shoot traits, whereas root phenotyping has received limited regard. Phenotyping roots in an opaque medium such as soil poses many technical challenges (in particular for non-destructive methods), which have made the study of plant root traits mostly unattractive. Most field-based approaches are known to be laborious, time-consuming, and destructive. In-field techniques are more challenging since researchers need to consider the soil structure, composition and its heterogeneity. Today's phenotyping requires the evaluation of the RSA to be accurately characterised. That is to say that the RSA assessment method should take into consideration procedures to reduce confounding effects that might impact the RSA development, while being able to easily translate the root phenotypes between controlled and in-field scenarios. Not only that, but any root phenotyping methodology should also be high-throughput in nature, in order to test multiple genotypes routinely. For these reasons, it is hard to consider any traditional root study technique as a viable phenotyping method. As noted by Harper et al. (1991)²² “...more energy has been spent on developing technologies than on studying roots”.

Traditionally, root study methodologies have been divided into two groups: one involving ‘shovelomics’ approaches, and the second relating to the use of rhizotrons. Both groups work in a two-dimensional context, however, that is not to say that here are no three-dimensional solutions, but certainly there are fewer. Shovelomics, as the name implies, revolves around excavating the RSA (Fig. 8) using a shovel, washing it and measuring its traits utilising a phenotyping board or a combination of imaging technologies²³. These approaches are not limited to plant excavation; they also involve soil core sampling, profile wall methods, and resin embedded techniques. Most of these methods are well documented through literature. For instance, Böhm (1979)²⁴ dedicates a whole book describing in detail the range of methods available to measure roots in-field. Atkinson et al. (2019)²⁵ revised methods that could link soil properties to root traits.

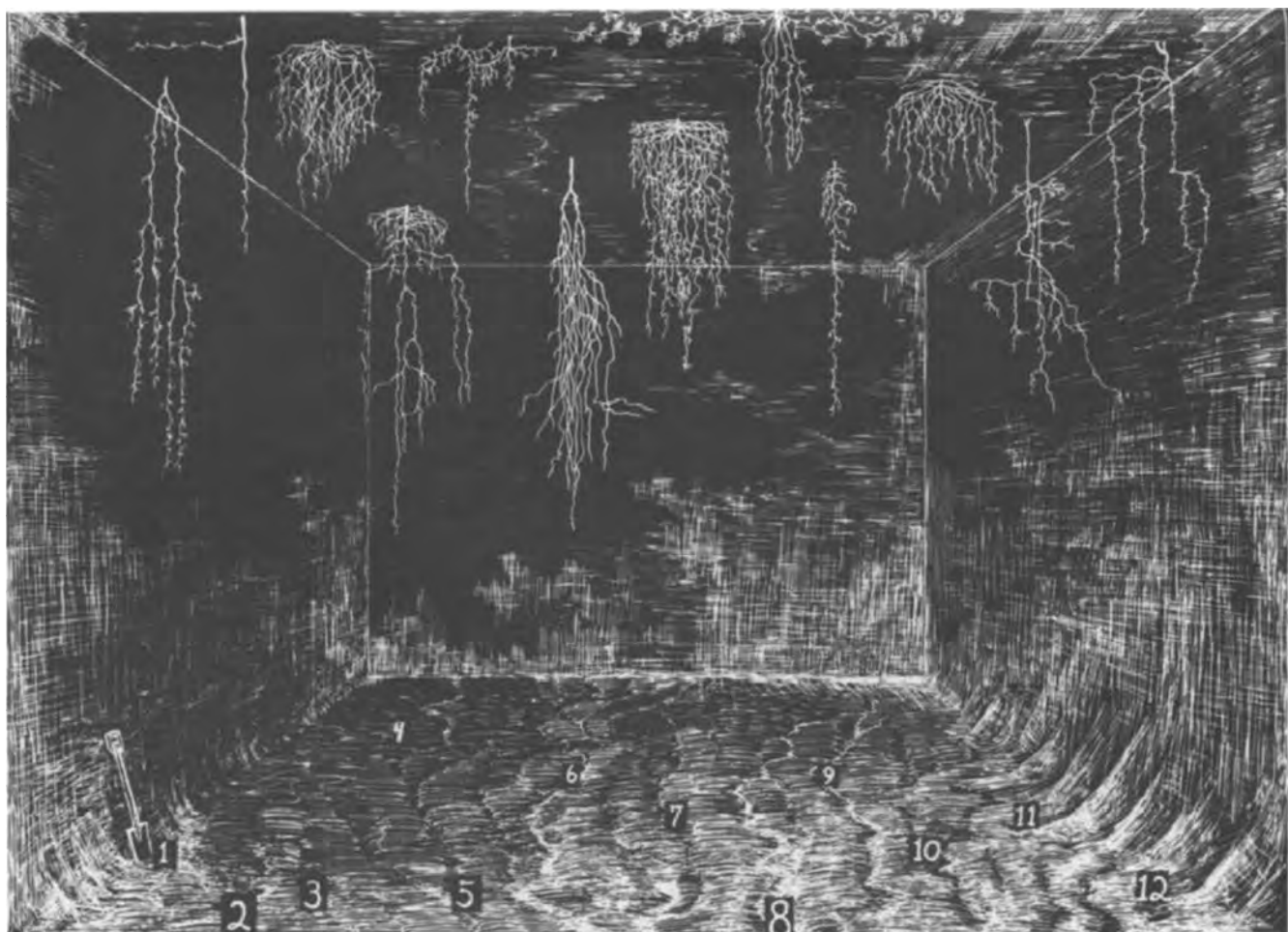
Table 1: Summary of the most studied root traits in agriculture.

²² J. L. Harper et al. “The evolution of roots and the problems of analysing their behaviour”. In: *Plant root growth* (1991).

²³ Muhammad Arifuzzaman et al. “Shovelomics for phenotyping root architectural traits of rapeseed/canola (*Brassica napus* L.) and genome-wide association mapping”. In: *Molecular Genetics and Genomics* 294.4 (2019).

²⁴ Wolfgang Böhm. *Methods of studying root systems*. Vol. 33. New York: Springer-Verlag, 1979.

²⁵ Jonathan A. Atkinson et al. “Uncovering the hidden half of plants using new advances in root phenotyping”. In: *Current Opinion in Biotechnology* 55 (2019).



More recently, Smit et al. (2000)²⁶ compendium of root methods describes classical and modern trends in root studies. Shovelomics remains the most common approach for root phenotyping, considered by some to be a high-throughput method, nevertheless, it still suffers from the limitations of being time-laborious and highly dependent on the user's skill-set. The before mentioned methods remain prevalent within every RSA study. Notwithstanding all the limitations of these methods, their ease of implementation alongside imaging systems makes them a popular choice for RSA studies.

Modern techniques under controlled conditions rely heavily on variations of the rhizotron concept (a plant vessel with translucent or detachable analysis windows) (Fig. 9). Common ways to automate this technique are through camera arrays or robotic imaging systems that track root growth. By combining these systems with segmentation algorithms, we can identify the unique parts of the RSA²⁷. The resolution of these types of methods is often enhanced by combining rhizotron images with luminescence-based reporters that track gene expression patterns²⁸. Soil-free techniques encompass hydroponics²⁹, aeroponics³⁰, gellan gum³¹, growth pouches³², and transparent soil³³. As mentioned earlier, images obtained through these approaches are mostly two-dimensional and often fail to image the complete RSA.

Figure 8: Illustrative example of earlier shovelomic approaches. The figure shows a 20 feet deep root excavation to study a variety of prairie plants [Extract from the work of Dix and Weaver (1969) used under CC0 licence].

²⁶ D. Tepfer. *Root methods, a handbook*. Vol. 160. 4. Springer, 2001.

²⁷ Achim Walter et al. "Dynamics of seedling growth acclimation towards altered light conditions can be quantified via GROWSCREEN: A setup and procedure designed for rapid optical phenotyping of different plant species". In: *New Phytologist* 174.2 (2007).

²⁸ Rubén Rellán-Álvarez et al. "GLO-Roots: An imaging platform enabling multidimensional characterization of soil-grown root systems". In: *eLife* 4.August2015 (2015).

²⁹ Laura Mathieu et al. "Rhizoponics": A novel hydroponic rhizotron for root system analyses on mature *Arabidopsis thaliana* plants". In: *Plant Methods* 11.1 (2015).

³⁰ C. B. Christie and M. A. Nichols. "Aeroponics - A production system and research tool". In: *Acta Horticulturae* 648.648 (2004).

³¹ J. T. Oliveira et al. "Gellan gum: A new biomaterial for cartilage tissue engineering applications". In: *Journal of Biomedical Materials Research - Part A* 93.3 (2010).

³² Cecile A.I. Richard et al. "High-throughput phenotyping of seminal root traits in wheat". In: *Plant Methods* 11.1 (2015).

³³ Helen Downie et al. "Transparent Soil for Imaging the Rhizosphere". In: *PLoS ONE* 7.9 (2012). Ed. by Malcolm Bennett.

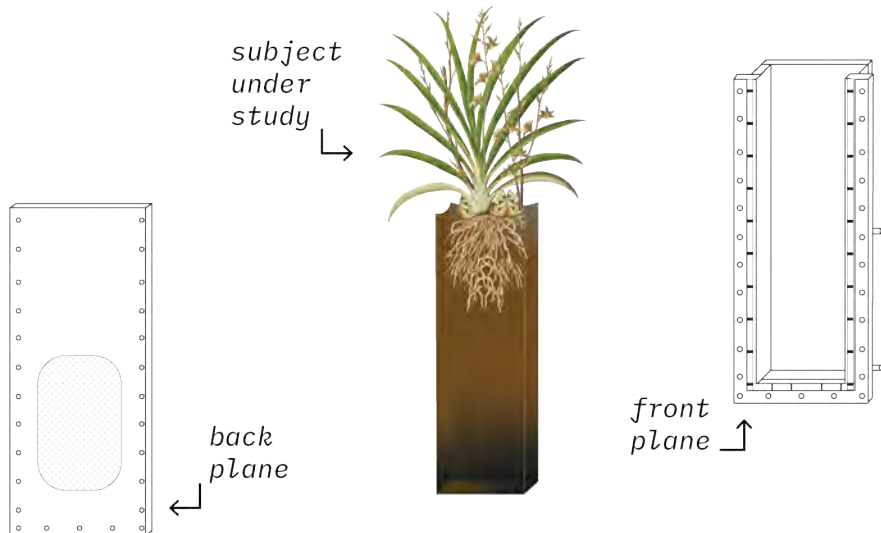


Figure 9: Illustrative example of a rhizotron. Rhizotrons do not have a standard shape, but the fundamental idea is to be able to visualise the RSA through a transparent window.

The complexity of imaging root systems not only comes from its inherent three-dimensional nature, but also from the vast amount of features that it contains. To illustrate, roots from certain cereal plants are known to grow in asymmetrical manner near their root crown, making it difficult if not impossible to quantify the number of roots and their insertion angles when using 'x-y' methods. Thus, 2D solutions cannot tell the whole story behind soil-plant interactions.

Soil-free techniques in conjunction with multi-view imaging systems have been used to study the three-dimensionality of root traits³⁴. The utility of such an approach is documented in Rellán-Álvarez et al. (2015)³⁵ research, where they uncover the genetic basis for 3D architectural traits of *Arabidopsis* plants. On the other hand, 3D root phenotyping studies in soil are only possible, at the current time, through tomographic technologies.

The prevalent application of tomographic methods is in medical research, since these methods offer a non-invasive/non-destructive solution to image internal organs. The nature of these techniques makes them good root candidates for root phenotyping. The most well known tomographic technology across the industry is X-Ray Computed Tomography (CT). X-ray CT measures the attenuation of X-rays through the Volume of Interest (VOI). These differential measurements are then used to create a 3D image (Fig. 10).

The use of this technique in root studies has gained greater traction, as there have been technological advancements in this area, e.g. resolution, scan and reconstruction times, and imaging segmentation algorithms. The use of such technology in root studies was demonstrated in the past century by Aylmore (1993)³⁶, but it is only now, when the limitations of the method have been enhanced, that it is worth considering as a viable root phenotyping technology. X-ray has been used for studying water processes³⁷, root responses to growth medium textures³⁸, lateral root development³⁹, and quantification of roots⁴⁰. However, one of the practical limitations of the X-ray technology is the choice of substrate. For instance, to ease the image segmentation process experiments need to consider the use of well-defined

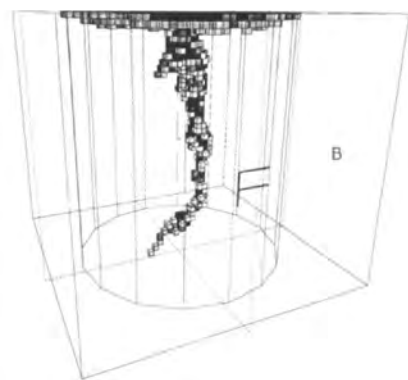


Figure 10: 3D CT image of a *Lupinus* root system in a soil column [Aylmore (1993)].

³⁴ S. J. Mooney et al. *Developing X-ray computed tomography to non-invasively image 3-D root systems architecture in soil*. 2012.

³⁵ Rellán-Álvarez et al., “GLO-Roots: An imaging platform enabling multidimensional characterization of soil-grown root systems”.

³⁶ L. A.G. Aylmore. “Use of Computer-Assisted Tomography in Studying Water Movement Around Plant Roots”. In: *Advances in Agronomy* 49.C (1993).

³⁷ Aylmore, “Use of Computer-Assisted Tomography in Studying Water Movement Around Plant Roots”.

³⁸ Susan Zappala et al. “Quantifying the effect of soil moisture content on segmenting root system architecture in X-ray computed tomography images”. In: *Plant and Soil* 370.1-2 (2013).

³⁹ Yun Bao et al. “Plant roots use a patterning mechanism to position lateral root branches toward available water”. In: *Proceedings of the National Academy of Sciences of the United States of America* (2014).

⁴⁰ Alexander M. Paya et al. “X-ray computed tomography uncovers root–root interactions: Quantifying spatial relationships between interacting root systems in three dimensions”. In: *Frontiers in Plant Science* (2015).

moisture profiles or even the use of artificial substrates. Therefore, the impact of substrate choice might impose a limitation for certain trait studies.

Magnetic Resonance Imaging (MRI) is another tomographic technique that uses magnetic fields in conjunction with radio-frequency waves to stimulate atoms and measure the energy released by them to create a 3D distribution map. In agricultural studies, MRI has been employed similarly to that of X-ray CT, using it mainly to image complete RSAs over time, and study water uptake processes⁴¹. In the case of MRI, the choice of substrate also has an impact on the process of image analysis. Additionally, the soil used might suppress soil-water interactions, leaving only the root-water signals; thus, making the segmentation of the roots and soil a part of the image acquisition process. But perhaps the most important thing researchers using MRI should consider, is the presence of ferromagnetic particles in soil. The latter has been proven to be detrimental to the quality of MRI root imaging⁴².

Positron Emission Tomography (PET) is a non-destructive imaging technology used to map the location of transitory radioactive substances inserted into a living organism. The main difference of PET scans with the above-mentioned techniques is its spatial resolution in the range of 1-5 mm. The use of PET in root studies is still limited and is often used as a complementary technique to the other CT methods when studying water dynamics⁴³ and root metabolic processes⁴⁴.

Most of these methods are difficult or even impossible to translate to in-field applications. Ground Penetrating Radar (GPR), on the other hand, is a geophysical method that can sense object boundaries by using high-frequency radio waves to measure the electric permittivity of the materials under study. In root studies, GPR has been used to quantify tree roots in a non-invasive manner⁴⁵ directly in-field. The limitation of GPR comes from its inability to detect small roots (around 2 mm thick)⁴⁶. However, when combined with other method, GPR could be considered as another important root phenotyping tool.

While the scientific and plant breeding community acknowledge the importance of studying root-soil interactions, there are still knowledge gaps in critical aspects of root development. Undoubtedly, there have been different attempts to tackle this problem, and even with their limitations, they offer new perspectives of this micro-universe. Nevertheless, we still require an effective root study methodology or a combination of methods that will allow us to enhance our understanding of plant-soil interactions. To that end, the next section explores another predominantly medical technique that could provide new insights into the hidden half of plants. Table 2 summarises both traditional and modern methods commonly used for root phenotyping.

⁴¹ Dagmar van Dusschoten et al. "Quantitative 3D analysis of plant roots growing in soil using magnetic resonance imaging". In: *Plant Physiology* 170.3 (2016).

⁴² Daniel Pflugfelder et al. "Non-invasive imaging of plant roots in different soils using magnetic resonance imaging (MRI)". in: *Plant Methods* (2017).

⁴³ Siegfried Jahnke et al. "Combined MRI-PET dissects dynamic changes in plant structures and functions". In: *Plant Journal* (2009).

⁴⁴ Amin Garbout et al. "The use of PET/CT scanning technique for 3D visualization and quantification of real-time soil/plant interactions". In: *Plant Soil* 352 (2012).

⁴⁵ Li Guo et al. *Application of ground penetrating radar for coarse root detection and quantification: A review*. 2013.

⁴⁶ Xiuwei Liu et al. *Ground penetrating radar for underground sensing in agriculture: A review*. 2016.

TYPE	TECHNIQUE	LIMITATIONS	EXAMPLES (REF)
Traditional	Rhizotrons	-High cost -Aberrant root growth along edges	Taylor et al. (1990), López et al. (1996), Johnson et al. (2001), Judd et al. (2015)
	Glass windows	-Static images -Aberrant root growth -Limited 2D area -Trench digging process	McMichael et al. (1992), Smit et al. (2000)
	Soil cores	-Requires a high number of samples -Limited sampling depth -Labour-intensive	Schuurman and Goedewaagen (1965), Yin et al. (2004), Böhm (1979)
	Root washing	-Large losses of fine roots -Destruction of natural root architecture -Labour-intensive	Pallant et al. (1993), Gregory and Hinsinger (1999), Yin et al. (2004), Trachsel et al. (2011)
Modern	GPR	-Water content dependency -Limited depth	Hruska et al. (1999), Stover et al. (2007), Cui et al. (2011), Guo et al. (2013), Isaac and Anglaere (2013), Zhu et al. (2014)
	Hydro/Aero-ponic	-Unnatural growth medium -Requires a root tracking system	Burgess et al. (1998), Neumann et al. (2009), Thompson (2004), Vaughan et al. (2011)
	Transparent soil	-Considerable user interaction -Unnatural growth medium -High cost	Downie et al. (2012)
	Digital imaging using computer analysis	-Root overlap harvested roots -Small resolution	Pound et al. (2013), Lobet et al. (2013), Wang et al. (2015)
	X-ray/NMR/MRI	-Limited to container studies -High cost instrumentation	Köckenberger (2001), Metzner et al. (2015)

Table 2: Root study methodologies.

2.3 Electrical characteristics of plants

The most common technique used to measure electromagnetic interactions, in many fields of science and technology, is Electrical Impedance Spectroscopy (EIS) which is a method to characterise the electrical properties of electrical systems, materials, or even biological tissues. When correctly modelled, EIS characterisation can describe composition, geometry and interfaces of complex biological systems. Electrical impedance refers to the electrical properties of a material, measured when an electrical current flows through it; in other words, electrical impedance measures the material's opposition to current flow when a potential is applied.

Impedance refers to both direct-current (DC, i.e. no variability across time) and alternate current (AC, varies according to a frequency). Thus, impedance can be represented mathematically as a vector of magnitude Z and a phase angle θ that determines its direction. The key elements representing the before-mentioned vector are resistance R , and reactance X . The former corresponds to the DC contribution (known as the real part), and the latter is related to the AC contribution (often referred to as the imaginary part).

The following equations describe such relationships:

$$(1) \quad Z = R + jX$$

$$|Z| = \sqrt{R^2 + X^2}$$

$$\theta = \operatorname{tg}^{-1}\left(\frac{X}{R}\right)$$

Both resistance and reactance are determined by the geometry of the material under study described by its length (L), surface area (A), and its conductivity according to the material type (ρ). In particular, reactance describes the inertia against the flow of current; its effect is observed as a voltage drop that is 90° out of phase in respect of the current. Depending on the direction of the phase change (positive or negative) reactance can be interpreted as capacitive, inductive or both. In biological systems, the reactance is mainly capacitive due to the energy storage effect of cell membranes. This effect is inversely proportional to frequency (f) and capacitance (C), thus:

$$(2) \quad R = \rho \frac{L}{A}$$

$$X_c = \frac{1}{2\pi f C}$$

The study and modelling of these properties over a range of frequencies is called spectroscopy. The first registered attempt to use impedance measurements as an indicator of mass and root size was made by Chloupek (1972)⁴⁷. The measurement procedure consists of inserting two electrodes⁴⁸, one at the base of the plant stem and the other directly into the soil (Fig. 12), measurements were obtained using a capacitance bridge at 1 kHz for different plant species (corn, sunflower, oat, onion, oilseed rape). While the previous study could find significant correlations between the RSA size and electrical capacitance, the effects of soil and root media were not considered. A second study⁴⁹ investigated the sensitivity of the method to soil characteristics and concluded that not only is capacitance very sensitive to soil electrical conductivity (affected by its ionic content), but also the response varies depending on the frequency and voltage applied.

The next step was to model the root-soil-electrode continuum, first developed by Dalton⁵⁰. Dalton's model describes the plant stem (mainly the xylem, r_1) as a highly conductive conduit, separated by isolating root membranes (r_2) from a low resistance medium (soil or nutrient solution).

It interprets the interface as a capacitor (Eq. 3) that is proportional to the electrical charges that accumulate between the xylem sap and the root media, where the root membranes represent the dielectric material (ϵ) between the plates of a capacitor (Fig. 11).

$$(3) \quad C = \frac{\epsilon A}{4\pi r_2 \ln\left[\frac{r_2}{r_1}\right]}$$

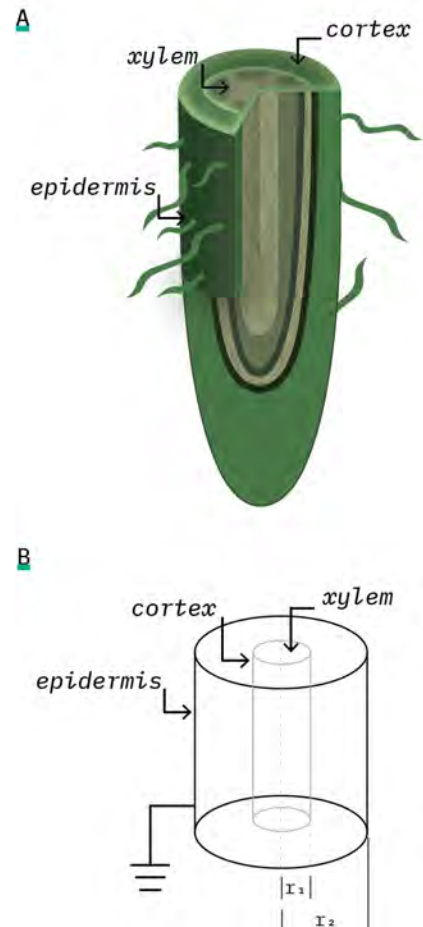


Figure 11: Dalton's Capacitor-root analogy. A. Cross-sectional anatomy of a single root tip. B. Capacitor equivalence of the root tip.

⁴⁷ O. Chloupek. "The relationship between electric capacitance and some other parameters of plant roots". In: *Biologia Plantarum* 14.3 (1972).

⁴⁸ Special consideration should be taken when selecting the electrodes. Typically, these studies use AgCl electrodes. The reason is to prevent the polarisation of the electrodes (the chloride ions of AgCl are exchanged with the same ions in biological tissues and electrolytes, avoiding charge accumulation at the surface of the electrodes) which can cause erroneous capacitance measurements.

⁴⁹ Oldrich Chloupek. "Evaluation of the size of a plant's root system using its electrical capacitance". In: *Plant and Soil* 48.2 (1977).

⁵⁰ F. N. Dalton. "In-situ root extent measurements by electrical capacitance methods". In: *Plant and Soil* 173.1 (1995).

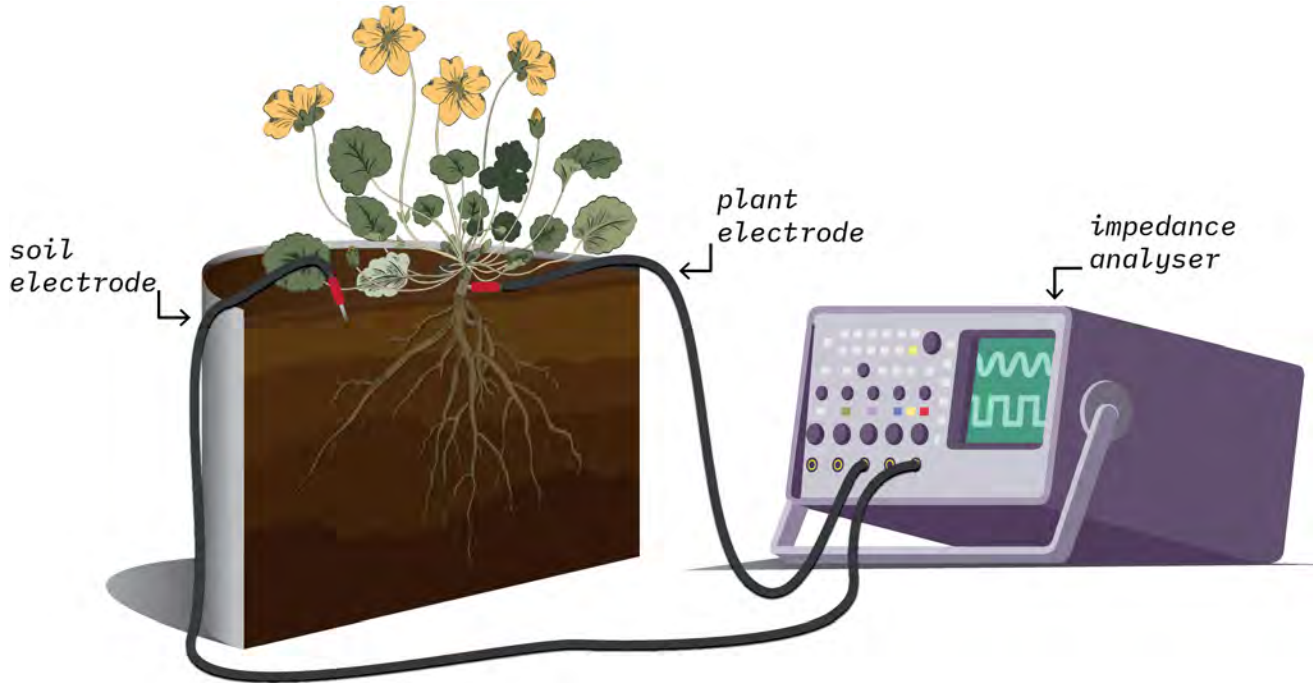


Figure 12: Typical EIS setup for root studies.

This means that a complete root system can be interpreted as a series of capacitors connected in parallel that are proportionally related to its size. In his observations, Dalton mentions that the total capacitance measured exponentially decreases with the distance between the measuring electrodes. However, this initial model does not fully consider the interfacing media surrounding roots.

Recent revised models proposed by Rajkai (2005)⁵¹ & Cao et al. (2011)⁵², acknowledge the contribution of the interfacing substrate, which is reflected in the capacitance measured. The latter defines one of the limitations of EIS, since the system can be seen as two capacitors in series (representing the RSA and the substrate respectively). This means that EIS requires the user to either fully characterise the capacitance of the interfacing medium, or ensure that its capacitance contribution is considerably higher than that of the RSA. The total capacitance of multiple capacitors in series is calculated using:

$$(4) \quad \frac{1}{C_{total}} = \frac{1}{C_1} + \frac{1}{C_2} + \dots + \frac{1}{C_n}$$

Eq. 4 shows that the total capacitive contribution is going to be dominated by the smallest capacitor. The prior method, along with Dalton's analogy for the root-media electrode network, has been applied with mixed success in root studies and breeding experiments (Table 3).

Recently, Dietrich et al. (2012)⁵³ revised the relevance of Dalton's model. Dietrich et al. noted that Dalton's model holds true when linearly relating total fresh root mass (i.e. measured without a substrate) to the measured capacitance. But the model fails when the system is submerged in substrate, partially or totally. Therefore, the revised model proposed by Dietrich et al., considers that while individual roots follow Dalton's original analogy (a capacitor directly propor-

⁵¹ K Rajkai. "Electrical capacitance of roots in relation to plant electrodes, measuring frequency and root media". In: *Acta Agronomica Hungarica* 53.2 (2005).

⁵² Yang Cao et al. "Analysis of the willow root system by electrical impedance spectroscopy". In: *Journal of Experimental Botany* 62.1 (2011).

⁵³ Ralf C Dietrich et al. "A new physical interpretation of plant root capacitance". In: *Journal of Experimental Botany* 63.17 (2012).

TECHNIQUE	PLANT CHARACTERISTICS STUDIED	PLANT STUDIED	EXAMPLES (REF)
Capacitance	Temperature stress, root biomass, tissue density, extent, diameter and activity	Alfalfa, Bean, Maize, Tomato, Willow	Stout et al. (1987), Kendall et al. (1982), Dalton (1995), Ellis et al. (2013), Dietrich et al. (2012)
Resistance	Frost resistance, water uptake, tissue density, metabolism	Maize, Pine tree, Willow	Walker (1965), Čermák et al. (2006), Urban et al. (2011), Cao et al. (2010)
Impedance Spectroscopy (EIS)	Leaf tissue damage, root biomass and water absorption area, Plant-soil interface Electrical models	Acalypha, Alfalfa, Tomato, Willow	Repo et al. (1994), Ozier-Lafontaine and Bajazet (2005), Repo et al. (2005), Repo et al. (2008), Cao et al. (2011), Postic and Doussan (2016)
Electrical Imaging	Single root quantification, root/soil spatial variability in-field, root water/nutrient uptake, root biomass, tillage effects	Alfalfa, Maize, Zea mays	Amato et al. (2008), Amato et al. (2009), Basso et al. (2010), Celano et al. (2011), Rossi et al. (2015), Fan et al. (2015)

tional to the cross-sectional area of the root), it might depend on the root anatomy of the particular plant species; root branches act as capacitors in parallel and thus can be interpreted as a single capacitor. Furthermore, they complement the contribution of the substrate, as well as the contribution of root hairs and other tissues, by modelling the interface as an RC circuit in series with each of the Root System Architecture (RSA) branches.

The model does not overcome the limitation above-mentioned, but Dietrich et al. note that EIS could be a viable RSA study technique as soils at field capacity appear to have a greater capacitance than plant tissue in most situations. However, when implementing the technique, researchers should characterise the interfacing substrate to avoid misleading results where the substrate dominates the response. Therefore, the practical application of EIS in root phenotyping is still not a straightforward process. The need for a specific calibration system alongside the lack of a standard measurement procedure has limited the generalisation of the method. Nevertheless, the advantages of characterising biophysical features through the injection of electrical current at different frequencies in a rapid non-destructive mode have sparked considerable interest in developing and perfecting EIS for root studies. This interest is further strengthened by the success of EIS in areas like food science⁵⁴, geology⁵⁵ and clinical medicine⁵⁶.

While electrical methods for root studies are gaining track among the scientific community, the geophysics community has been using a modality of EIS since 1913⁵⁷ to explore mineral deposits and other soil characteristics. Historically, this geophysics method is known as electrical sounding, which later would help develop electrical imaging. In geophysics, electrical imaging or Electrical Resistivity Tomography (ERT) is a survey technique to map the electrical characteristics of complex geology. The continuous development of electrical imaging over the past decades has made this technique the basis for a diverse set of semi/non-invasive approaches that map the electrical distribution inside a medium. Thus, it has also been used in medical studies, and

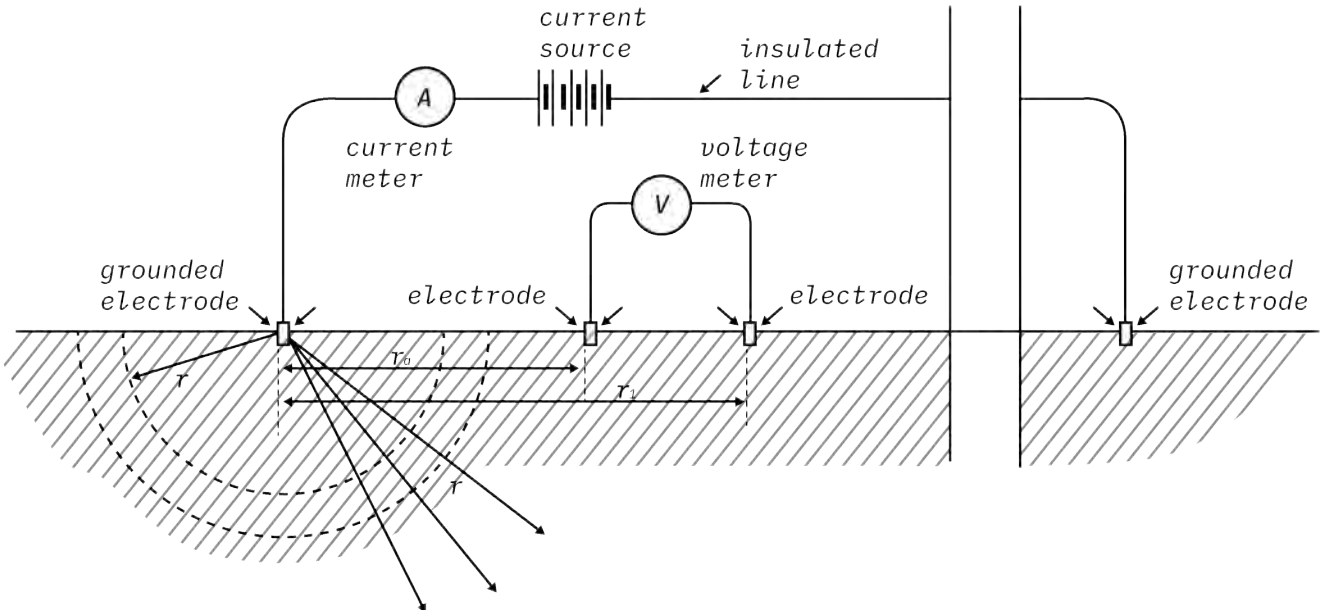
Table 3: Electrical methods in plant studies.

⁵⁴ Uwe Pliquett. "Bioimpedance: A review for food processing". In: *Food Engineering Reviews* 2.2 (2010).

⁵⁵ Dominique Gibert et al. "Electrical tomography monitoring of the excavation damaged zone of the Gallery 04 in the Mont Terri rock laboratory: Field experiments, modelling, and relationship with structural geology". In: *Applied Clay Science* 33.1 (2006).

⁵⁶ Tushar Kanti Bera et al. "Studying the Variations of Complex Electrical Bio-Impedance of Plant Tissues During Boiling". In: *Procedia Technology* 23 (2016).

⁵⁷ Don H. Heimer and Steven L. De Vore. "Near-Surface, High Resolution Geophysical Methods for Cultural Resource Management and Archaeological Investigations". In: *Science and Technology in Historic Preservation*. 2000.



in industrial process monitoring⁵⁸. The method typically employs an array of electrodes (25 or more) evenly placed on the surface under study to acquire resistivity measurements. A control system is used to select the set of active electrodes (carrying/injecting electrical current), while another set is used to measure the response (Fig. 13). The data acquired is then correlated to a pseudo-section to create an approximate image of the subsurface distribution. The measurements are then used to estimate the subsurface resistivity distribution. Since the resistivity is related to geological parameters, electrical surveys are used to determine soil porosity, mineral contents, as well as soil and rock water content.

The data acquisition procedure might be simple on its own, nevertheless, the complexity of this area arises in the mathematical procedures needed to obtain an image. Since 1990 there has been substantial progress in reconstruction algorithms for electrical imaging, but—as further explored in the next chapters—obtaining an adequate representation of the electrical distribution of a VOI depends on much more than the algorithm employed.

Agriculture and plant-soil studies have used electrical imaging, relating the previously mentioned geophysical variables to crop productivity⁵⁹, soil compaction⁶⁰, water content and flow in soil⁶¹, soil cracks⁶², tillage effects⁶³, moisture content in the root zone⁶⁴, water percolation⁶⁵, soil contamination⁶⁶, water uptake⁶⁷, and root biomass⁶⁸.

Most of these studies have been conducted using trees with associated high root biomass; herbaceous plants are more challenging, as their smaller root biomass makes it difficult to distinguish between roots and changes in soil moisture (Fig. 14). This is exemplified in the findings of Amato et al. (2009)⁶⁹. A key challenge for ERT is the variability of soil conditions (e.g. soil texture, compaction, particle

Figure 13: Typical electrode array for electrical sounding and electrical surveys.

⁵⁸ Andy Adler and Alistair Boyle. “Electrical Impedance Tomography”. In: *Wiley Encyclopedia of Electrical and Electronics Engineering*. Wiley, 2019.

⁵⁹ D. L. Corwin and S. M. Lesch. “Apparent soil electrical conductivity measurements in agriculture”. In: *Computers and Electronics in Agriculture* 46.1-3 Spec. Iss. (2005).

⁶⁰ A. Besson et al. “Structural heterogeneity of the soil tilled layer as characterized by 2D electrical resistivity surveying”. In: *Soil and Tillage Research* 79.2 (2004).

⁶¹ Ulrike Werban et al. “Monitoring of root-zone water content in the laboratory by 2D geoelectrical tomography”. In: *Journal of Plant Nutrition and Soil Science* 171.6 (2008).

⁶² A. Samouelian et al. “Electrical resistivity survey in soil science: A review”. In: *Soil and Tillage Research* 83.2 (2005).

⁶³ Bruno Basso et al. “Two-Dimensional Spatial and Temporal Variation of Soil Physical Properties in Tillage Systems Using Electrical Resistivity Tomography”. In: *Agronomy Journal* 102.2 (2010).

⁶⁴ G. Celano et al. “Evaluation of soil water content in tilled and cover-cropped olive orchards by the geoelectrical technique”. In: *Geoderma* 163.3-4 (2011).

⁶⁵ A. K. Greve et al. “3D cross-hole resistivity tomography to monitor water percolation during irrigation on cracking soil”. In: *Soil Research* 49.8 (2011).

⁶⁶ L. J. West et al. “Resistivity imaging of soil during electrokinetic transport”. In: *Engineering Geology* 53.2 (1999).

⁶⁷ Benjamin Mary et al. “Improvement of coarse root detection using time and frequency induced polarization: from laboratory to field experiments”. In: *Plant and Soil* 417.1-2 (2017).

⁶⁸ Roberta Rossi et al. “Soil bulk electrical resistivity and forage ground cover: Nonlinear models in an alfalfa (*Medicago sativa* L.) case study”. In: *Italian Journal of Agronomy* 10.4 (2015).

distribution, porosity), as this can lead to ambiguities when trying to explain the results obtained. These ambiguities are accentuated when the RSA impact on the growth-medium is ignored. As explained previously, it is difficult to identify the individual contribution of each root segment to bioelectrical measurements due to a high number of variables. To mediate this issue researchers have proposed the combination of multiple methods.

For instance Mary et al. (2017) propose the use of ERT with a mise-à-la-masse approach, which involves attaching a stationary electrode in the media of interest. Moreover, other researchers have used ERT in conjunction with electromagnetic inductance imaging⁷⁰, and also with a field-scale soil thermal profiling calibration method⁷¹ to overcome the issues presented above. Cassiani et al. (2016)⁷² and Vanella et al. (2018)⁷³ demonstrated how ERT in conjunction with other technologies, soil moisture sensors and eddy covariance systems respectively, can be used to characterise the spatial distribution of water content and nutrient uptake. While it might not be possible to detect individual root interactions through this technique, ERT can detect root related processes.

This field is still under continuous development, thus, new approaches and standards are being established. The next chapter presents the basics for electrical imaging, and the steps towards the design of an electrical imaging system for plant phenotyping.

⁶⁹ Mariana Amato et al. "Multi-electrode 3D resistivity imaging of alfalfa root zone". In: *European Journal of Agronomy* 31.4 (2009).

⁷⁰ W.R. R. Whalley et al. "Methods to estimate changes in soil water for phenotyping root activity in the field". In: *Plant and Soil* 415.1-2 (2017).

⁷¹ Didier Michot et al. "Spatial and temporal monitoring of soil water content with an irrigated corn crop cover using surface electrical resistivity tomography". In: *Water Resources Research* 39.5 (2003).

⁷² Giorgio Cassiani et al. "Soil-plant interaction monitoring: Small scale example of an apple orchard in Trentino, North-Eastern Italy". In: *Science of the Total Environment* 543 (2016).

⁷³ D. Vanella et al. "Use of small scale electrical resistivity tomography to identify soil-root interactions during deficit irrigation". In: *Journal of Hydrology* 556 (2018).

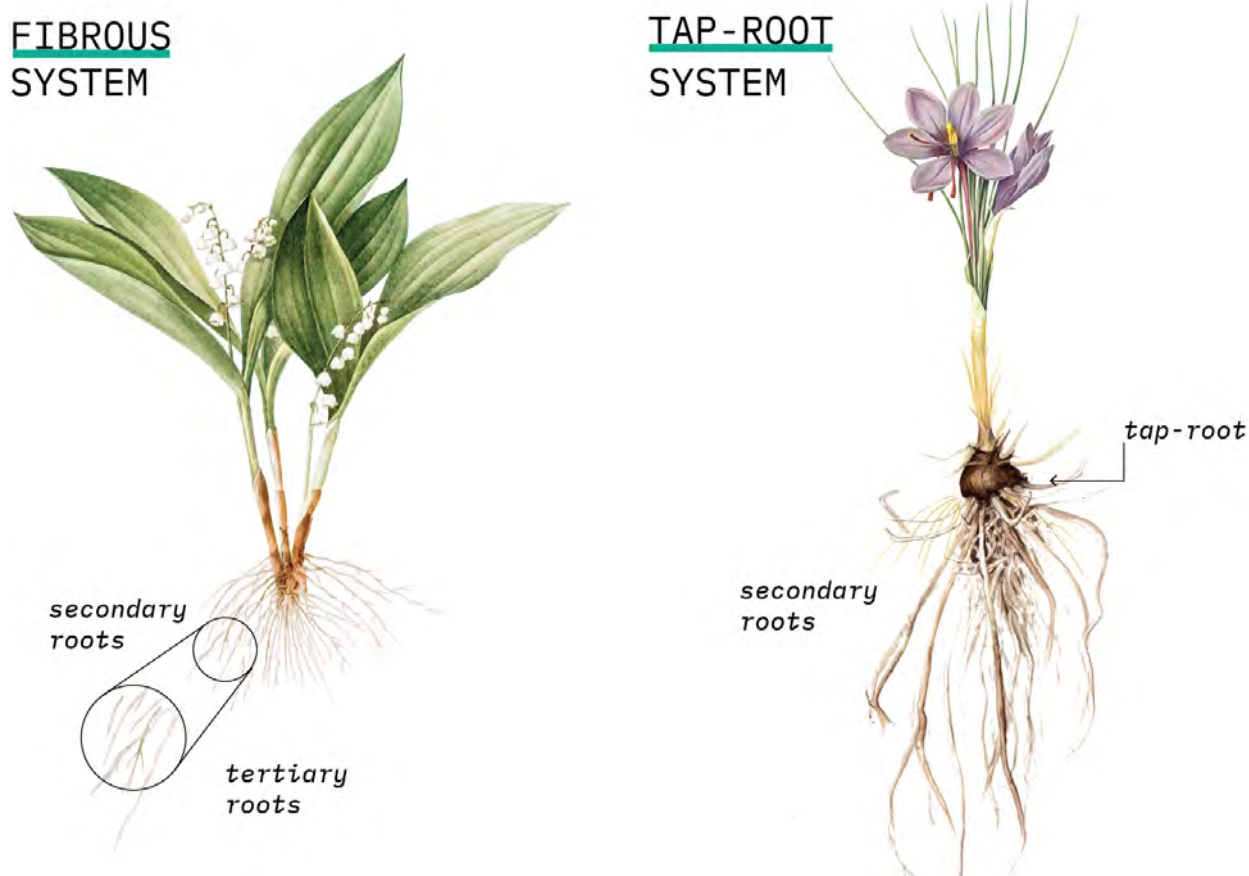


Figure 14: Illustrative example between tap-root systems and fibrous RSAs.

THIS PAGE INTENTIONALLY LEFT BLANK

DIRECT PROBLEMS

DESPITE THE GROWING efforts in plant breeding through root dynamics, the quantification and identification of root traits remains a challenging topic. Our understanding of root-soil interactions remains fragmented, and in dire need of an adequate phenotyping method that complies with modern-standards: non-invasiveness and high throughput. As previously discussed in Chapter 1.0, one such promising method could be electrical imaging. This method has been used for decades in geophysics explorations, and more recently in medical and industrial applications. Electrical imaging, most commonly known as Electrical Resistivity Tomography (ERT), is a non-invasive geo-electrical approach used to study soil characteristics based on their response to electrical stimuli. This chapter introduces the reader to the theory of electrical imaging. It assumes that the reader is familiar with some basic electrical concepts mentioned in the electrical methods section of the previous chapter. The chapter not only underlines the theory behind the method, but also presents the work towards the design of the electrical imaging system presented in this work.

3.1 Can one hear the shape of a drum?

Electrical imaging aims at identifying the spatial distribution of objects in a system from its response to electrical stimulation. Solving this type of problem is akin to answering the question posed in the title of this subsection. The question (asked by Kac (1966))¹ clearly illustrates the difference between direct and inverse problems where one consists of calculating the sound produced by a drum, and the other pertains to identify the shape of the drum. One can imagine the problem as having a “magic box” (Fig. 15) (*A*) that transforms an input (x) into a measurable output (y) i.e. $Ax = y$. In the case of electrical imaging, the main question can be formulated as ‘Can one determine the electrical conductivity distribution of a volume by measuring its response to electric stimuli; this is known as Calderon’s problem². To answer this question, first it is important to understand the dynamics of electromagnetism, or in other words, to solve the problem directly (otherwise known as solving the forward problem). Solving the forward problem is to find the electrical response to a certain stimulus given that the volume’s internal conductivity distribution is known. Maxwell’s equations are key to solving this problem as they describe all electromagnetic phenomena.

“In every branch of knowledge the progress is proportional to the amount of facts on which to build, and therefore to the facility of obtaining data” Maxwell, J.C. (1851)

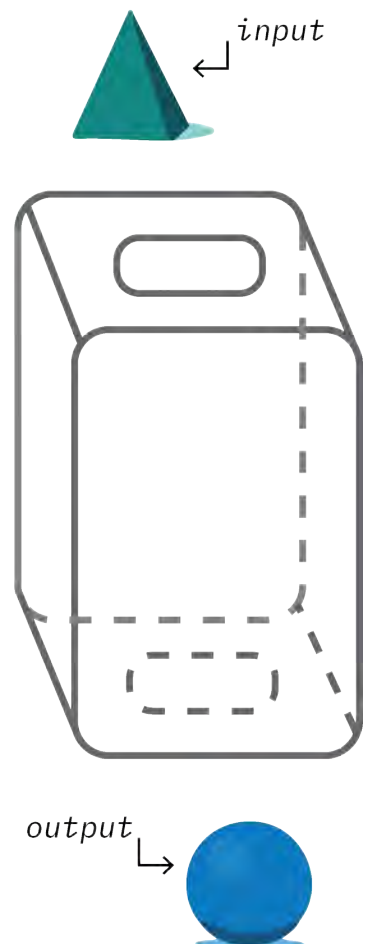


Figure 15: Magic box analogy.

¹ Mark Kac. “Can One Hear the Shape of a Drum?” In: *The American Mathematical Monthly* (1966).

² Alberto P Calderón. “On an inverse boundary value problem”. In: *Computational and Applied Mathematics* 25.2–3 (2006).

3.1.1 Foundations of Electromagnetic theory

Maxwell's equations are a set of mathematical expressions that describe how electric (\mathbf{E}) and magnetic (\mathbf{B}) fields behave in nature. Maxwell's equations are:

$$(5) \quad \nabla \cdot \mathbf{E} = \frac{\rho}{\epsilon}$$

$$(6) \quad \nabla \cdot \mathbf{B} = 0$$

$$(7) \quad \nabla \times \mathbf{E} = \frac{\delta \mathbf{B}}{\delta t}$$

$$(8) \quad \nabla \times \mathbf{E} = \mu \mathbf{J} + \frac{1}{c^2} \frac{\delta \mathbf{E}}{\delta t}$$

To anyone familiar with calculus, these differential equations describe the rate of change regarding an input (or multiple inputs in some cases). The inputs in this case are charge density (ρ) and electrical current density (\mathbf{J}). One can relate these functions to the physical medium conditions using the constants ϵ and μ that correspond to the permittivity and permeability of the material; these are further related to each other by the speed of light $c = 1/\sqrt{\epsilon_0 \mu_0}$ (where 0 refers to the free space/vacuum). The previous set of equations can be used to determine the electromagnetic fields inside a volume when the boundaries of such are defined.

In order to explain these equations, other key concepts need to be defined. When referring to electric and magnetic fields, in this work we specifically talk about vector fields. Thus, one can imagine a delimited space with many vectors assigned to specific points inside that area. Fig. 16 shows the electric field generated by three charges in space. Vectors describe the magnitude and direction of the fields. Here, Fig. 16 describes the nature of positive and negative charges; one acting as a source (vectors pointing away from positive charges) and the others acting as sinks (vectors points towards negative charges). With this basic explanation in mind, let us describe the first Maxwell equation, Gauss' Law (Eq. 5). Gauss' law has two representations, the differential (Eq. 5) and the integral form:

$$(9) \quad \int_S \mathbf{E} \cdot \hat{n} dS = \frac{Q}{\epsilon_0}$$

The integral form describes the total charge inside a closed surface S , which can be of any shape or form. In other words, Gauss' law states that the flux of electric field lines is defined by the total charge enclosed in S inversely proportional to the permittivity of space. While the integral form is a definition of the electric field in terms of a surface, the differential version uses the divergence operator, which is a way to describe the amount of flux entering and leaving a point³.

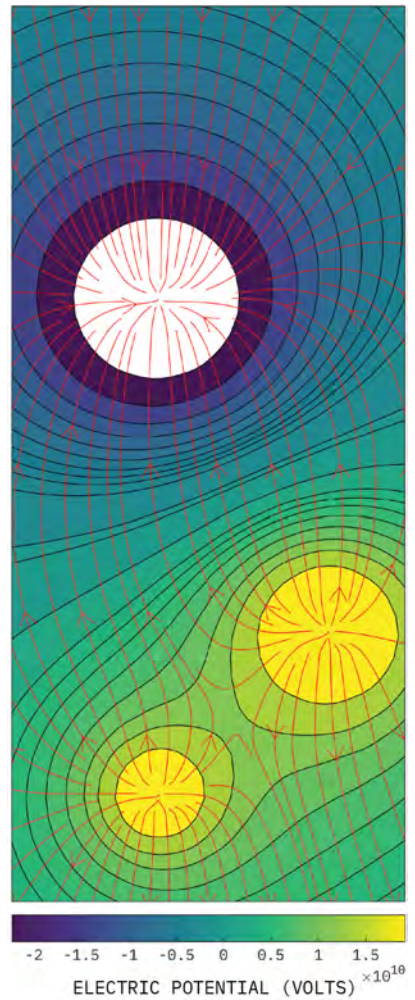


Figure 16: Electric potential field of three charges in vacuum. Two of the charges are positive (sources) and one is negative (drain).

³ One can apply the divergence theorem to Eq. 9 to obtain the differential version of Gauss' Law.

Eq. 6 is known as Gauss' law for magnetism. This equation states that the total flux entering or leaving a space is zero in the presence of a magnetic field. In mathematical terms, this means that magnetic fields are divergenceless. Moreover, this describes the nature of magnetic materials, in which there are no sources or sinks. In other words, magnetic monopoles do not exist (at least in classic electromagnetism theory).

The way in which magnetic and electric fields are related are described by the last two equations. The first is the Maxwell-Faraday equation (Eq. 7). The equation describes how in the absence of a magnetic field or if the field does not change in time, a particle does no work when moving in a closed loop. Thus, it can be said that \mathbf{E} is a conservative field in the absence of a magnetic field. This describes the nature of electromagnetic induction. For instance, a change in the magnetic field through the area of a wire coil causes electromagnetic fields across it (Fig. 17). Faraday's Law of induction is derived from the previous equation:

$$(10) \quad \mathcal{E} = \frac{d\phi_B}{dt}$$

where \mathcal{E} represents the electromotive force in a closed wire loop, and ϕ_B represents the flux of magnetic field through the area created by the loop. Thus, the electromotive force corresponding to the work done by a unit charge moving around a loop C is⁴:

$$(11) \quad \mathcal{E} = \oint_C \mathbf{E} \cdot \hat{\mathbf{e}}_t dl$$

Applying Stokes' theorem, which relates the line integral around a surface's boundary to the curl of a vector field along said surface, the following expression is attained:

$$(12) \quad \mathcal{E} = \int_S (\nabla \times \mathbf{E}) \cdot \hat{n} dS$$

then using the Maxwell-Faraday equation:

$$(13) \quad \mathcal{E} = -\frac{d}{dt} \int_S \mathbf{B} \cdot \hat{n} dS$$

The above equation describes the magnetic field flux through the area enclosed by the loop of wire, explaining why a change in magnetic field near a wire loop induces a current inside the wire and vice versa. The last equation is Ampere's law (Eq. 8). First let us consider that there is no time dependence involved. Thus, $\nabla \times \mathbf{B} = \mu_0 \mathbf{J}$ explains the direct proportionality of the magnetic field and the current at a given point. This equation takes the integral form:

$$(14) \quad \oint_C \mathbf{B} \cdot \hat{\mathbf{e}}_t dl = \mu_0 I$$

This is a way of describing how the total current running through an enclosed loop is proportional to the magnetic field around that loop. That is to say, this is the definition of the right-hand rule for magnetic fields around a wire (Fig. 18). For the time dependent case,

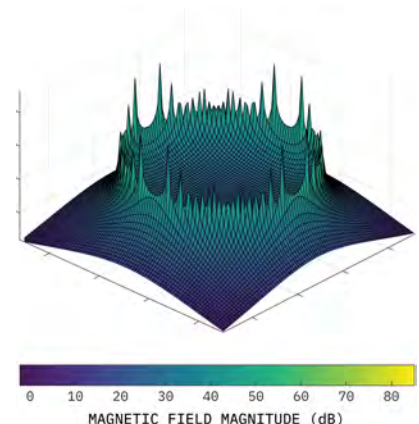


Figure 17: Magnetic field generated from a 1 A current running through a loop of wire.

⁴ Here $\hat{\mathbf{e}}_t$ is the unique vector tangent to the corresponding curve.

a second term is used and is known as displacement current or electric flux $D = \epsilon_0 \mathbf{E}$, which helps explain electromagnetic fields inside materials rather than free space. Faraday's original law did not consider D . It was Maxwell who found out its importance in demonstrating the existence of electromagnetic waves. Maxwell drew this conclusion by considering that all electric currents follow the continuity equation $\delta\rho/\delta t = \nabla \cdot \mathbf{J}$. Substituting in Eq. 8 this gives us:

$$(15) \quad \nabla \cdot (\nabla \times \mathbf{B}) = 0 = \mu_0 \nabla \cdot \mathbf{J} + \mu_0 \frac{\delta\rho}{\delta t}$$

When applying Gauss' Law, Maxwell's equations in vacuum are defined:

$$(16) \quad \begin{aligned} \nabla \cdot \mathbf{E} &= 0 \\ \nabla \cdot \mathbf{B} &= 0 \\ \nabla \times \mathbf{E} &= \frac{\delta \mathbf{B}}{\delta t} \\ \nabla \times \mathbf{B} &= \frac{1}{c^2} \frac{\delta \mathbf{E}}{\delta t} \end{aligned}$$

Like many partial differential equations, Maxwell's equations can be extremely difficult or impossible to solve directly even when having a defined set of boundary conditions. Thus, a diversity of mathematical tricks are needed to obtain an approximate solution. The next section presents two approaches to understanding the forward problem. One approach is the analytical method, which describes the intricate interrelationships between the variables that pertain to the problem, and the second is the numerical approach that is often used in practical applications.

3.1.2 Analytical approach

Let us consider the concentric conductivity distribution presented in Fig. 19. The body Ω is divided into two regions R_a and R_b with their respective conductivities σ_a and σ_b . Let us assume a current density distribution $J(\theta)$ is injected into the body at r_b with a frequency low enough to ignore any reactive effects. Moreover, Ohm's law, $J = \sigma E$, relates the current density $J(\theta)$ and the electric field E in Ω .

Thus, let us define the following conductivities:

$$(17) \quad \sigma(r, \theta) = \begin{cases} \sigma_a, & 0 \leq r \leq r_a \\ \sigma_b, & r_a \leq r \leq r_b \end{cases}$$

The voltage V can be expressed as a Fourier series in polar coordinates for some coefficients a_0 , $a_n^{(1,2,3)}$ and c_n , using:

$$(18) \quad V(r, \theta) = a_0 + \begin{cases} \sum_{n=1}^{\infty} \left(\frac{r}{r_a}\right)^n a_n^{(1)} \cos(\theta - \psi), & 0 \leq r \leq r_a \\ \sum_{n=1}^{\infty} (r^n + r^{-n} c_n) a_n^{(2)} \cos(\theta - \psi), & r_a \leq r \leq r_b \end{cases}$$

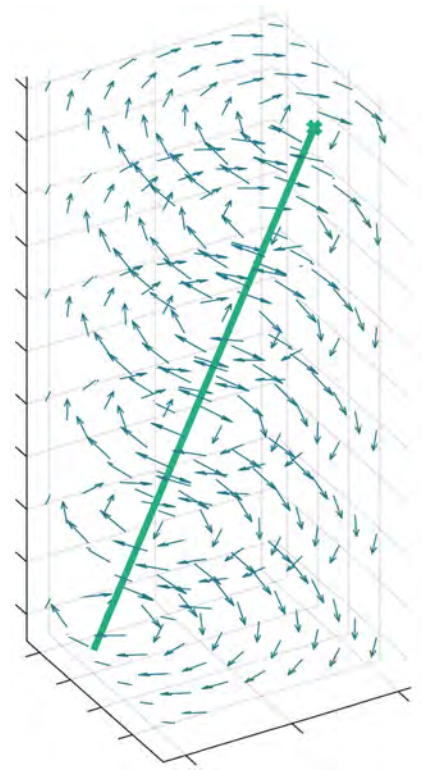


Figure 18: Normalised magnetic field around a wire, illustrating the right-hand rule.

From this expression, the current field in any radial direction is obtained through:

$$(19) \quad J(r, \theta) = -\sigma \begin{cases} \sum_{n=1}^{\infty} n \left(\frac{r}{r_a} \right)^{n-1} a_n^{(1)} \cos(\theta - \psi), & 0 \leq r \leq r_a \\ \sum_{n=1}^{\infty} n \left(r^{n-1} a_n^{(2)} - r^{-n-1} a_n^{(3)} \right) \cos(\theta - \psi), & r_a \leq r \leq r_b \end{cases}$$

Substituting the appropriate coefficients, the impedance in any unit disk's point for $\sigma_b = 1$ is found using:

$$(20) \quad z_n = V_n / J_n = -\frac{1}{n} \left[\frac{(1 + \sigma_a) + (1 - \sigma_a)r^{2n}}{(1 + \sigma_a) - (1 - \sigma_a)r^{2n}} \right]$$

Following the same steps, the driving point impedance for a disk of radius r_b is defined by:

$$(21) \quad z_n = -\left(\frac{r_b}{n\sigma_b} \right) \left[\frac{\left(1 + \frac{\sigma_a}{\sigma_b} \right) + \left(1 - \frac{\sigma_a}{\sigma_b} \right) \left(\frac{r_a}{r_b} \right)^{2n}}{\left(1 + \frac{\sigma_a}{\sigma_b} \right) - \left(1 - \frac{\sigma_a}{\sigma_b} \right) \left(\frac{r_a}{r_b} \right)^{2n}} \right]$$

From Eq. 21, it is clear that *priori* information is needed in order to infer the size and conductivity of the intrusion. Moreover, if Ω is uniform (i.e. $\sigma_a/\sigma_b = 1$):

$$(22) \quad z_n = -\left(\frac{r_b}{n\sigma_b} \right)$$

Eq. 22 tell us that most of the architectural information of the body is enclosed in the first term ($n = 1$), as n gets closer to ∞ the structural information starts to disappear. As with any subsurface imaging technology, one of the main goals is to produce an image that faithfully represents the inner contents of the subject under study. In EIT, the spatial and conductivity resolution often define the quality of the image obtained. The former describes the minimum identifiable region size for independent conductivity areas. For the present case, this parameter can be quantified with the ratio $Resolution = r_a/r_b$, since R_a is the smallest region present.

The conductivity resolution can be defined as the smallest conductivity change that can be detected. The previous analysis considers a

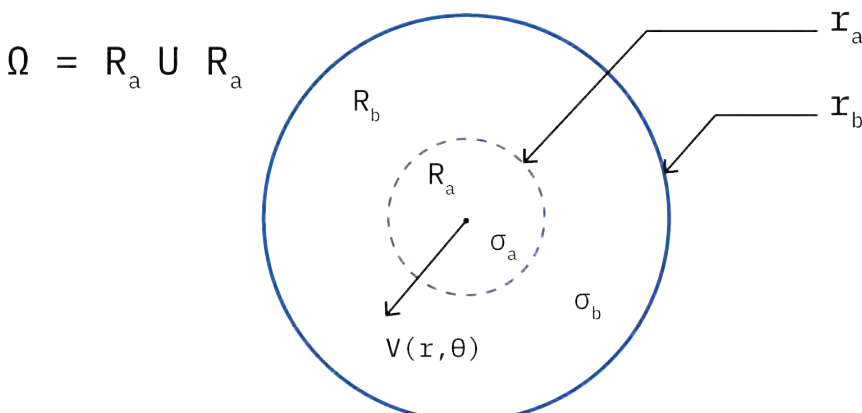


Figure 19: Large conductive region R_b having radius r_b with an embedded small conductive region R_a of radius r_a .

centred inclusion, for this reason, it is useful to define the conductivity contrast as $\alpha = \sigma_a / \sigma_b$. Thus, it is possible to quantify the conductivity resolution through $Accuracy = d\alpha / \alpha$. As proposed in diverse works, both resolution and accuracy are inherently related.

In the following section, a case study analysis is examined using a previously designed EIT pot, in order to understand how to achieve a good balance between *Resolution & Accuracy* by exploring the theoretical limitations of the approach.

THEORETICAL INTERRELATIONSHIPS

As described by Seagar (1983)⁵, the goal is to detect the smallest voltage change that a conductivity perturbation creates when Ω is non-uniform. Therefore, to attain the best resolution and conductivity contrast, the noise must equal this fractional change in voltage (dV / V). Hence, the sensitivity can be understood as the corresponding fractional change in voltage to a fractional change in contrast. In other words:

$$(23) \quad S_n(\alpha, \beta) = \frac{dV}{V} \frac{\alpha}{d\alpha} = -\frac{4\alpha\beta^n}{(1+\alpha)^2 - (1-\alpha)^2\beta^{2n}}$$

Where $\beta = (r_a / r_b)^2$. Eq. 23 is a pair-wise comparison between the most significant variables that can determine the quality of EIT images. In order to relate the parameters of interest to each other, some of the parameters must remain fixed. Fig. 20 shows the results of the relationship between resolution and sensitivity, first using ten contrast values linearly spaced for $n = 1$.

As expected, from Fig. 20 one can observe that for small values of β , sensitivity is always higher when the conductivity contrast approaches unity. Higher resolution values were not explored, since it would make no sense to have an intrusion bigger than the subject under study. The small argument approximation can be used to obtain the slopes for the sensitivity of a constant value of α :

$$(24) \quad \frac{d \ln \beta}{d \ln S} = \frac{d \beta S}{d S \beta} = \frac{-\alpha}{(1-\alpha)^2 S \beta n - 2n\alpha}$$

It is important to note that the distribution converges at all values, thus, the change in sensitivity is not oscillatory. As for small β values, the sensitivity slopes lean towards $1/2n$ despite α . Considering $n = 1$, the slope of the S - β curve approximates a value of $1/2$. Similar to the findings reported by Seagar (1983), this result means that an improvement in resolution by a factor K is obtained by enhancing the sensitivity with K^2 .

Next, let us explore the relationship between sensitivity and conductivity contrast. For the purpose of our application (aiming at imaging root systems), the analysis presented of this interrelationship, uses the typical minimum size for a *Brassica Napus L.*⁶ type-b lateral root ($r_a = 0.2mm$), and different outer radii to represent a variety of pot sizes. This behaviour is demonstrated in the graph below.

⁵ A D Seagar. "Probing With Low Frequency Electric Currents". In: *Electrical Engineering* PhD (1983).

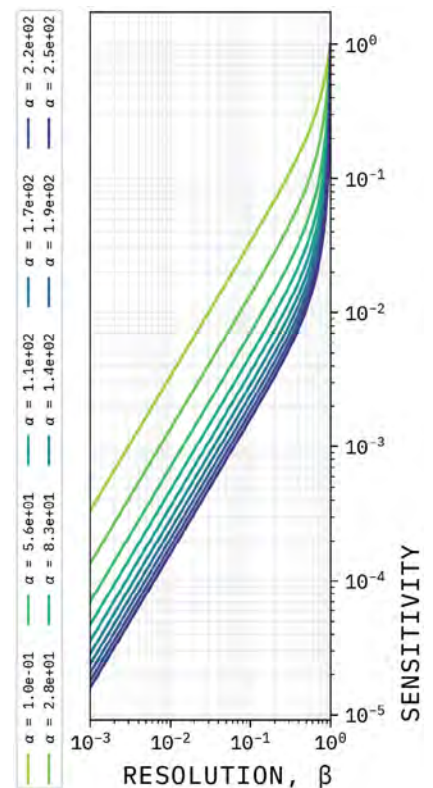


Figure 20: Sensitivity versus resolution plot as α approaches unity.

⁶ Oilseed rape is a particular case of a fibrous RSA.

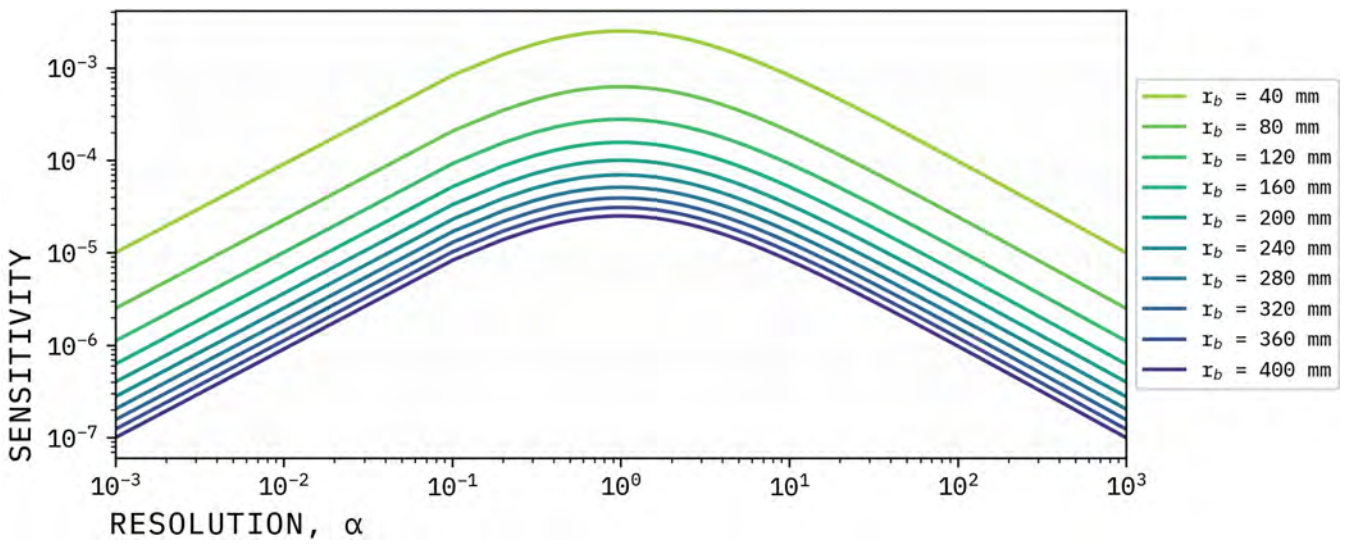


Fig. 21 shows that the maximum levels of sensitivity are achieved as the conductivity and resolution approach unity. Moreover, for small β values (compared to unity) the sensitivity is considerably smaller. This is further proven by obtaining the expression for its slopes:

$$(25) \quad \frac{d \ln S}{d \ln \alpha} = \frac{dS \alpha}{d\alpha S} = \frac{2\alpha ((\alpha + 1) + (1 - \alpha)\beta^{2n})}{(\alpha - 1)^2\beta^{2n} - (\alpha + 1)^2}$$

Considering $n = 1$ in Eq. 25 it can be observed that improving the contrast resolution by a K factor balances out any sensitivity enhancement by the same factor K . This is obvious since the slope's value is $+1$ or -1 as α leans towards zero or infinity respectively.

Finally, the slope of $\beta - \alpha$ is plotted for different sensitivity values using the following expression:

$$(26) \quad \frac{d \ln \beta}{d \ln \alpha} = \frac{d\beta \alpha}{d\alpha \beta} = -\frac{2\alpha^2 (\alpha - (\alpha - 1)\beta^{2n} + 1)}{((1 - \alpha)^2\beta^{2n} - (\alpha + 1)^2)((1 - \alpha)^2\beta n S - 2\alpha n)}$$

This expression can be obtained by multiplying Eqs. 24 & 25. With the same approach ($n = 1$) small resolutions, sensitivities approaching zero and contrast values close to zero or infinity, the curve's slope approaches $1/2$. Therefore, it can be deduced that expanding the contrast range by a factor K is going to impact the resolution by \sqrt{K} . The previous interrelationships can be summarised in the following:

- Improving noise by a factor K , improves accuracy by the same factor K .
- An enhancement in resolution by a factor K , balances out the sensitivity by a factor K^2 .
- Extending the range of the conductivity contrast reduces the sensitivity by the same factor, K .
- Enhancing the conductivity contrast by K^2 degrades the resolution by K .

Figure 21: Sensitivity versus contrast plot for $r_a = 0.2\text{mm}$ and a non-fixed r_b .

3.1.3 Numerical approach

The previous section presents an analytical solution to mapping the electrical conductivity distribution of a VOI. Unfortunately, an analytical solution is sometimes only possible for very simple models. This section presents a numerical approach, also referred to as discretisation. The process of discretisation helps frame a continuous differential equation into a matrix algebra problem, which can then be implemented as a computing algorithm. Let us start with the relationship between the electric field and electrical potential:

$$(27) \quad \mathbf{E} = -\nabla V$$

Substituting the previous relationship in Gauss' Law (Eq. 5) it is possible to obtain the potential related to the charge density represented by Poisson's equation:

$$(28) \quad \nabla^2 u = \nabla^2 V = -\frac{\rho}{\epsilon_0}$$

The operator $\nabla \cdot \nabla = \nabla^2$ is known as the Laplacian operator. In this case, Poisson's equation states that the electric potential field is related to a charge inside the domain of the problem. In the case of EIT, the source responsible for creating an electric field lies outside the domain. Therefore, this area can be considered free of charge, which simplifies Poisson's equation:

$$(29) \quad \nabla^2 V = 0$$

This is known as Laplace's equation. Both equations are key in solving a variety of physics problems that do not depend on time. To solve most differential equations, a set of boundary conditions need to be imposed on the system. Such boundary conditions help define the VOI and find a solution within it. The most common boundary conditions employed are Dirichlet's and Neumann's conditions respectively⁷:

$$(30) \quad \begin{aligned} u &= \text{constant on } \delta\Omega \\ \frac{\partial u}{\partial n} &= \text{constant on } \delta\Omega \end{aligned}$$

In practice, it is necessary to use a mixture of the previous conditions, as it defines a finite number to truncate the computing process. Once a boundary condition is defined, one can solve the problem numerically through relaxation methods that imply having an initial guess for V and then obtain an approximate solution through different iterations. First, let us start defining Laplace's equation in Cartesian coordinates for a two-dimensional case (Fig. 22):

$$(31) \quad \frac{\delta^2 V}{\delta x^2} + \frac{\delta^2 V}{\delta y^2} = 0$$

Eq. 31 describes the equilibrium state of our system under study within certain boundary conditions. To discretise Laplace's equation,

⁷ Dirichlet boundary conditions specify a value of the solution at the boundary. Neumann boundary conditions specify the normal derivative of the solution at the boundary.

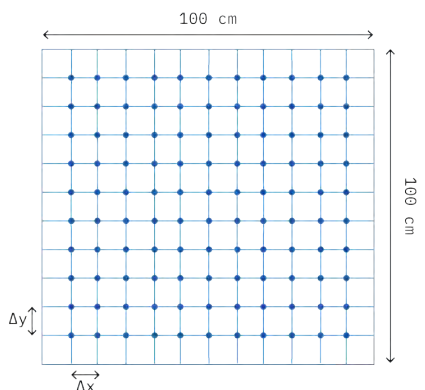


Figure 22: Discretised two-dimensional plane for voltage calculation.

let us use the second-order derivatives discretisation with a central difference method. For our two-dimensional case this yields:

$$(32) \quad \frac{V_{i+1,j} - 2V_{i,j} + V_{i-1,j}}{\Delta x^2} + \frac{V_{i,j+1} - 2V_{i,j} + V_{i,j-1}}{\Delta y^2} = 0$$

In this case $\Delta x = \Delta y$, thus, the final discrete equation is:

$$(33) \quad V_{i+1,j} + V_{i-1,j} + V_{i,j+1} + V_{i,j-1} - 4V_{i,j}$$

If a two-dimensional square (Fig. 22) is discretised, i.e. subdivided into smaller squares, Eq. 33 describes how to calculate the Laplacian operation at any point (i, j) in our discretised plane. Therefore, one can evaluate each point discretely using neighbouring points (Fig. 23). In this method, the starting point is to solve the problem using an initial guess for the solution, and then to update the solution through the previous equation, iterating until V^k . As the iterations (k) get closer to ∞ , the system will reach equilibrium, however, when computing the solution one can get close to equilibrium by iterating until the changes between iterations are non-significant. Thus, a simplified approach is to use the Jacobi method to convert Eq. 33 into an iterative solution that replaces the grid values with their respective weighted averages:

$$(34) \quad V_{i,j}^{k+1} = \frac{1}{4}(V_{i+1,j}^k + V_{i-1,j}^k + V_{i,j+1}^k + V_{i,j-1}^k)$$

Fig. 24 shows the numerical solution to two sinusoidal boundaries at two opposite edges of a square. The method presented is one of the simplest relaxation techniques to implement. Hence, it is useful for illustrative purposes on how to solve a forward problem and as a first introduction to discretisation of planes and volumes, which is known as the Finite Element Method (FEM). Now, let us describe how a typical EIT system works.

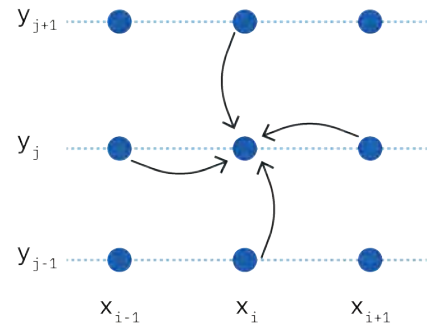


Figure 23: Five point stencil for the discretised Laplace's equation.

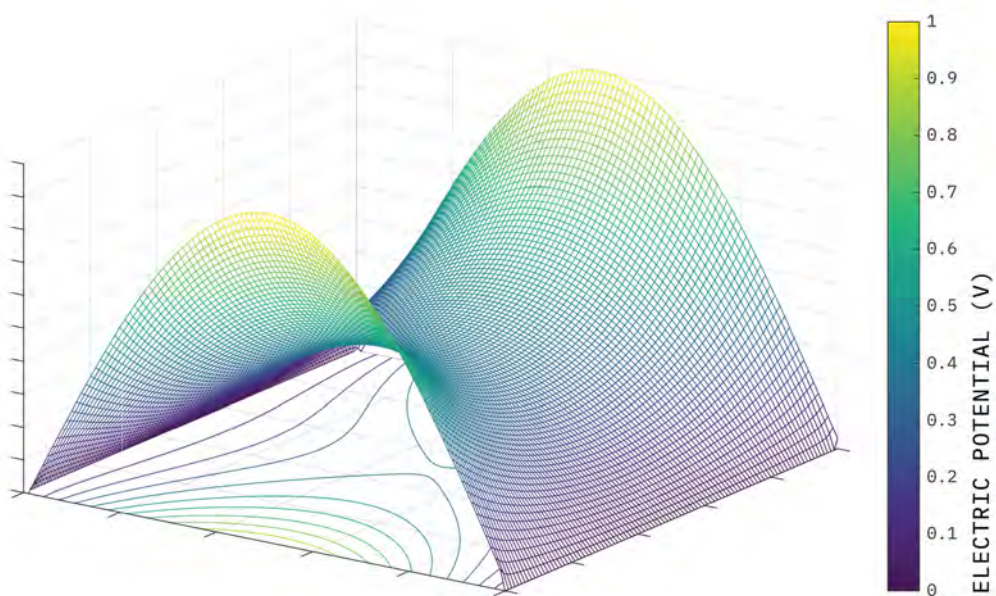


Figure 24: Solution to Laplace's equation for two sinusoidal boundaries.

Traditional EIT systems apply a sinusoidal current at the body's surface and perform voltage measurements. Typically, a pair-drive configuration is used. In other words, electrical current is injected across one pair of electrodes, while voltage is measured across all other pairs of electrodes. Without taking into consideration the modelling of the electrodes, the values calculated by the forward solution presented in Eq. 18 will decay towards $1/n$. For this reason, it is important to accurately depict the current distribution at the boundary by modelling the interface between the electrode and the medium.

Three electrode models are often considered when solving EIT's forward problem. The first one is the continuum model, in which the electrodes are assumed to be perfect conductors and assumes that the current is a continuous function that can be randomly set on the entire boundary (akin to the previous example). The second one is the gap-shunt model, the assumptions of which are that the electrode area is the only place where a constant current density exists, and that it varies according to:

$$(35) \quad \int_{E_l} \sigma \frac{\delta u}{\delta \mathbf{n}} ds = I_l$$

where E_l is the l -th electrode for L number of electrodes, and \mathbf{n} is the outward normal unit vector. Finally, the Complete Electrode Model (CEM) improves the gap shunt model by taking into consideration the contact impedance with the boundary, making it the most refined electrode model for EIT's forward problem⁸. The complete electrode model consists of the following boundary conditions and equations:

$$(36) \quad \int_{E_l} \sigma \frac{\delta u}{\delta \mathbf{n}} ds = I_l$$

$$(37) \quad \nabla \cdot (\sigma \nabla u) = 0 \quad \text{in } \Omega, \sigma > 0$$

$$(38) \quad u + Z_l \sigma \frac{\delta u}{\delta \mathbf{n}} = V_l$$

$$(39) \quad \sigma \frac{\delta u}{\delta \mathbf{n}} = 0$$

The CEM states that the current density on the electrode's surface is equal to the total current injected to that electrode (Eq. 35). Next, the CEM considers an absence of current sources or sinks within the domain Ω (Eq. 36). Eq. 37 states that the measured voltage on the electrode is the sum of the voltage underneath the electrode's surface and the voltage drop that results from the electrode impedance. Finally, the CEM considers that there are no currents leaving or entering the boundary on the electrode inner gap (Eq. 38). A selection of a ground point is needed to ensure the existence of the solution. Adding

⁸ Erkki Somersalo et al. "Existence and Uniqueness for Electrode Models for Electric Current Computed Tomography". In: *SIAM Journal on Applied Mathematics* 52.4 (1992).

these considerations to EIT's forward problem helps to improve the accuracy of the solutions during simulations, but similar to the example previously presented it is important to add the CEM to EIT's FEM. To continue explaining the EIT FEM solution, let us consider an EIT pot (used in preliminary studies) of 9 cm radius, 13 cm height, with two rings of 16 Ag plated electrodes (electrode radius = 0.75 cm). The pot model (Fig. 25 A) considers some suggestions presented by Passioura (2006)⁹. The pot's FEM model (Fig. 25 B) was created using an automatic 3D mesh generator software, Netgen v6.0¹⁰. Furthermore, the software allows the user to choose the amount of partitioning for the domain of interest. This means that Netgen can generate a coarse (less tetrahedra) or super fine (more tetrahedra) 3D mesh volume. Naturally, a more dense mesh will lead to better and more accurate results. However, a high number of elements inherently implies more calculations¹¹. Thus, it is imperative to find an adequate balance between solution accuracy and mesh density. One way to find the proper balance is through the mesh quality calculation. This can be computed using circumference approximations with the following equation^{12,13}:

$$(40) \quad Q = \frac{\sum_k Q_k}{Error} \quad \text{where} \quad Q_k = \frac{3r_{in}(T_k)}{r_{out}(T_k)}$$

where r_{in} and r_{out} is the radius of the inner-scribed and circumscribed sphere in the k 'th tetrahedron respectively. The *Error* is based on the approximation of such circumferences to the tetrahedron. The model used in section is composed of 48400 boundary components, 55305 nodes, and 400479 elements. Using such configuration, the quality factor calculated for this mesh volume is $Q = 0.8214$. Thus, a good equilibrium between the computing time and solution precision can be achieved through this mesh configuration.

Linear first-order FEM models offer an adequate solution accuracy with high tolerance to some mismatches between the model and the body's actual shape. In order to use the FEM, a reformulation of the basic set of equations is required. Since the model now considers electrodes in its boundary, it is important to add the electrodes' impedance contribution to each element using a set of linear basis functions¹⁴ $w_i(x, y, z)$. Thus, one can approximate the potential on each point with^{15,16}:

$$(41) \quad V_{FEM} = \sum_{i=1}^N v_i w_i$$

consequently, the FEM forward solution can be described as:

$$(42) \quad \begin{bmatrix} A_M + A_Z & A_w \\ A_w^T & A_D \end{bmatrix} \begin{bmatrix} \Phi \\ \mathbf{V} \end{bmatrix} = \begin{bmatrix} 0 \\ \mathbf{I} \end{bmatrix}$$

where Φ is a vector containing the discrete potential approximations for each mesh element, \mathbf{V} and \mathbf{I} represent the electrode potential and current vector respectively

⁹ John B Passioura. "Viewpoint: The perils of pot experiments". In: *Functional Plant Biology* 33.12 (2006).

¹⁰ Joachim Schöberl. "An advancing front 2D/3D-mesh generator based on abstract rules". In: *Computing and Visualization in Science* 1.1 (1997).

¹¹ Depending on the computational hardware could significantly impact the computing time.

¹² Päivi J. Vauhkonen et al. "Static three-dimensional electrical impedance tomography". In: *Annals of the New York Academy of Sciences*. Vol. 873. 1 Electrical Bi. Blackwell Publishing Ltd, 1999.

¹³ Jin Fa Lee and Romanus Dyczij-Edlinger. "Automatic mesh generation using a modified delaunay tessellation". In: *IEEE Antennas and Propagation Magazine* 39.1 (1997).

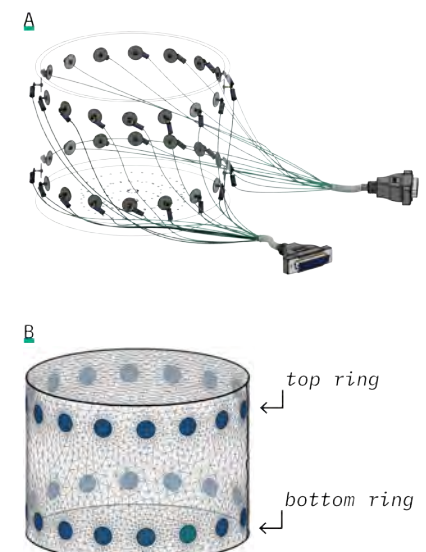


Figure 25: A. 3D model of the EIT pot. B. Pot Tetrahedral FEM Model. The lighter coloured element indicates the first numbered electrode.

¹⁴ Equal to unity on the i 'th vertex and zero for all others

¹⁵ Nicholas Polydorides. "Image reconstruction algorithms for soft field tomography". In: (2002).

¹⁶ David Holder. "Electrical Impedance Tomography: Methods, History and Applications". In: *Medical Physics* 32.8 (2005).

A_M, A_Z, A_w and A_D are calculated through:

$$(43) \quad A_{M_{i,j}} = \sum_{k=1}^K \sigma_k \int_{\Omega_k} \nabla w_i \cdot \nabla w_j dV$$

$$(44) \quad A_{Z_{i,j}} = \sum_{l=1}^L \int_{El_l} \frac{1}{Z_l} w_i w_j ds$$

$$(45) \quad A_{w_{i,j}} = -\frac{1}{Z_l} \int_{El_l} w_i w_j dS$$

$$(46) \quad A_D = \text{diag}\left(\frac{|El_l|}{Z_l}\right)$$

In this case, l represents the number of electrodes surrounding the pot, and Z_l represents the contact impedance of the l 'th electrode. Furthermore, to relate the changes in conductivity across Ω to the measurements' changes (v), the Jacobian (commonly known as sensitivity matrix) needs to be computed using:

$$(47) \quad \text{Jacobian}_{m,k} = \begin{bmatrix} \delta v_1 / \delta \sigma_1 & \dots & \delta v_1 / \delta \sigma_k \\ \delta v_1 / \delta \sigma_1 & \dots & \delta v_1 / \delta \sigma_k \\ \vdots & \ddots & \vdots \\ \delta v_m / \delta \sigma_1 & \dots & \delta v_m / \delta \sigma_k \end{bmatrix}$$

The sensitivity matrix can be computed through different approaches^{17,18}, but the most common methods are^{19,20,21}: direct differentiation using Eq. 43, and the adjoint field method. The latter consists of integrating the inner product of the electric fields produced by all stimulation patterns over each element of the FEM²².

One way to validate these methods is through the perturbation method, which relies on making subtle conductivity changes in each FEM region to reach an approximation of the Jacobian (this requires higher computation time)²³. Before solving the forward problem, one needs to consider the way EIT systems acquire data. Usually a stimulus (sinusoidal current) is applied across a pair of electrodes and the m -th measurement (voltage) is obtained through the difference of electrical potential across a different pair of electrodes caused by the stimulus. This is known as the pair-drive configuration and is the most widespread acquisition method in EIT. This resembles a Kelvin 4-point measurement configuration, which can eliminate errors caused by contact impedances. A whole data set comprises all the measurements taken with all possible combinations.

Next, one should calculate the nodal voltages for every stimulation and measurement pattern (Fig. 26). This allows us to further investigate several aspects of the EIT configuration using mainly the Jacobian.

Solving the forward problem means obtaining the Jacobian matrix. In the Jacobian matrix, each column represents the change in voltage due to a conductivity contrast for every element that composes the

¹⁷ Polydorides, "Image reconstruction algorithms for soft field tomography".

¹⁸ Holder, "Electrical Impedance Tomography: Methods, History and Applications".

¹⁹ Tadakuni Murai and Yukio Kagawa. "Electrical Impedance Computed Tomography Based on a Finite Element Model". In: *IEEE Transactions on Biomedical Engineering* Bme-32.3 (1985).

²⁰ T. J. Yorkey and J. G. Webster. "A comparison of impedance tomographic reconstruction algorithms". In: *Clinical Physics and Physiological Measurement* 8.4a (1987).

²¹ Margaret Cheney and David Isaacson. "Distinguishability in Impedance Imaging". In: *IEEE Transactions on Biomedical Engineering* 39.8 (1992).

²² If implemented correctly both can output the same solution.

²³ The FEM calculation in this project is obtained through the Electrical Impedance and Diffuse Optical tomography Reconstruction Software (EIDORSv3.10). EIDORS is a free-software that provides a set of MATLAB tools and algorithms for the EIT problem [Polydorides and Lionheart (2002)].

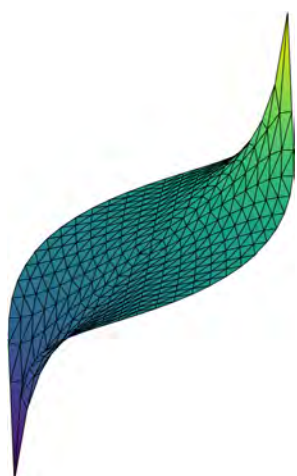


Figure 26: Nodal voltages in a mesh stimulating opposite electrodes for a 2D ring.

FEM model. The rows represent the contribution of each FEM element for every measurement. Therefore, one can calculate the total pot's sensitivity map. To compute the sensitivity maps, each FEM element contribution is normalised using its element or volume size (N_i):

$$(48) \quad \text{Sensitivity}_i = \frac{\sqrt{(\sum_m \text{ Jacobian}_{m,k}^2)}}{N_i}$$

CONTRIBUTION

3.2 Improving EIT's vertical resolution

Typically, EIT systems use the pair-driven method described in the previous section. While it is possible to take two-point measurements, this requires more rigorous design considerations for the EIT system, e.g. invariable contact impedance between electrodes. Thus, any combination of pair-driven measurements is referred to as a stimulation and measurement pattern (S/M pattern for short). The most common S/M pattern used in the EIT community is the Sheffield protocol (also known as adjacent protocol) (Fig. 27 A). This protocol continues to be commonly used as it is easy to implement, and in some cases the legacy hardware in studies is tailored to use this stim/meas pattern. Unfortunately, this acquisition pattern offers a poor sensitivity distribution, being considerably higher at the boundaries of the vessel.

Adler et al. (2011)²⁴ have highlighted the importance of S/M patterns, and studies have proposed steering away from the traditional adjacent pattern to 'skip' patterns that offer higher sensitivities²⁵. The term skip methodologies refer to having some separation between driving/measurement electrodes, i.e. skipping electrodes. For instance, the adjacent method corresponds to a skip-1 method; meaning that current is injected using Electrode 1 & 2 (E1 & E2) and the voltage response is measured using electrodes 2 & 3, 3 & 4 and so on (Fig. 27 A). Thus, one can use a stim-skip-3 with a meas-skip-5 (S3/M5); that is to say, stimulating in E1 & E4 and measuring on E2 & E7, E3 & E8 and so on (Fig. 27 B). Nevertheless, current literature does not fully explore the possibilities and implications of different skip configurations and electrode arrangements.

In Section 2.1.2 the theoretical implications of EIT systems for resolution pertaining to noise, contrast, and intrusion size were analysed. This section explores how certain design choices and S/M patterns can enhance the sensitivity, and thus, the overall performance of EIT systems. Before dealing with how to improve EIT systems, one needs to understand that some limitations come from the perpetual use of legacy hardware and techniques²⁶. The Sheffield protocol is a product of its time, corresponding to the hardware limitations and taking advantage of the ease of implementation. Considering the computing limitations of 1987, traditional EIT systems mainly aimed at solving 2D problems, thus, it makes sense to use a single measurement

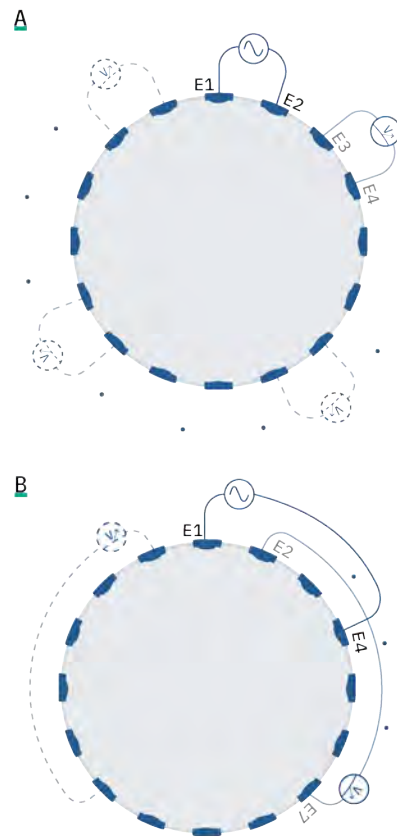


Figure 27: A. Adjacent or Sheffield S/M protocol. B. S3/M5 protocol.

²⁴ Andy Adler et al. "Adjacent stimulation and measurement patterns considered harmful". In: *Physiological Measurement* 32.7 (2011).

²⁵ Specially at centre of the vessel.

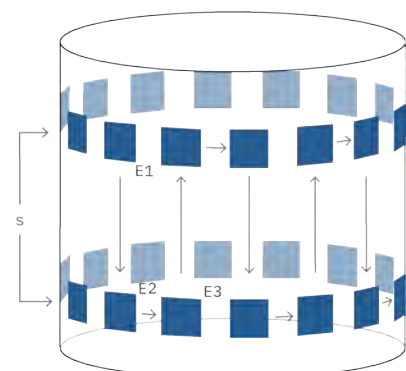


Figure 28: Representation of the square electrode arrangement. Here s represents the distance between electrode rings.

²⁶ Andy Adler and Alistair Boyle. "Electrical Impedance Tomography: Tissue Properties to Image Measures". In: *IEEE Transactions on Biomedical Engineering* 64.11 (2017).

ring. With recent advancements in both theory and technology, it is now possible to consider 3D electrical imaging using multiple rings. However, most studies still rely heavily on old methodologies. While there are some studies that use multiple electrode rings, most of them are driven individually; i.e. the S/M pattern runs on each ring and does not contain measurements between rings. In some cases, the reason for this is again the use of legacy hardware.

Currently, the EIT medical community is embracing the use of two electrode rings for 3D lung imaging. Due to this, Wagenaar and Adler (2016)²⁷ proposed the “square” method to overcome the difficulties presented of using old hardware by, rearranging the electrodes like, as its name implies, a square (Fig. 28). Therefore, one has to categorise the S/M patterns in traditional approaches fit for single ring electrode arrangements, called planar, and squared ring solutions for multiple rings. First, this work discusses the implications of using multiple rings, especially in terms of the vertical separation between them.

VERTICAL SEPARATION ANALYSIS

The following analysis uses an 18×16 cm cylindrical FEM with two electrode rings comprised of sixteen 2×2 cm electrodes. This study employs a fine mesh with 1.9×10^5 elements with a higher mesh density near the electrodes [as proposed by Grychtol and Adler (2013)²⁸]. The analysis starts with the rings in close proximity being positioned at the middle of the vessel (to be specific at 7 & 9 cm respectively), then the rings are separated one centimetre at a time²⁹, calculating the sensitivity for each new model using both planar and square S/M patterns with multiple skip configurations. The study presented in this section, analyses:³⁰

- Seven vertical positions.
- Eight injection skips.
- Eight measurement skips.
- Two protocols: planar and squared.

The analysis starts by creating eight cylindrical FEMs for the different electrode ring positions. All the models have roughly the same amount of elements with a higher mesh density near the electrodes. All the sensitivity maps calculated correspond to a 1A excitation source and are calculated using Eq. 48.

As explored in the previous sections, it is common for EIT to have lower sensitivity values near the VOI's centre. Therefore, this work focuses in achieving the maximum sensitivity possible in this region through the careful selection of both ‘s’ and S/M patterns. The present work further analyses the 3D sensitivity maps by sampling points across a vertical and horizontal line that run from top-to-bottom & left-to-right respectively. Additionally, this study explores the nature of the measurements generated by each S/M pattern through the Singular Value Decomposition (SVD) method.

²⁷ Justin Wagenaar and Andy Adler. “Electrical impedance tomography in 3D using two electrode planes: characterization and evaluation”. In: *Physiological Measurement* 37.6 (2016).

²⁸ Bartłomiej Grychtol and Andy Adler. “FEM electrode refinement for electrical impedance tomography”. In: *Proceedings of the Annual International Conference of the IEEE Engineering in Medicine and Biology Society, EMBS*. 2013.

²⁹ The distance between electrode rings is referred as s, as portrayed in Fig. 28.

³⁰ The corresponding dataset employed is available upon reasonable request.

	v_sensitivity	h_sensitivity	total_sensitivity	max_sensitivity	cond_n	injection	measurement
count	89600.000000	89600.000000	1.792000e+05	179200.000000	1.792000e+05	179200.000000	179200.000000
mean	17.741031	138.538844	3.727936e+07	11.502466	6.200448e+64	4.500000	4.500000
std	11.724960	1269.299387	1.209991e+07	7.260480	6.467149e+65	2.291294	2.291294
min	0.956454	0.000000	1.106095e+07	0.723296	1.065035e+15	1.000000	1.000000
25%	8.749195	13.869282	3.014836e+07	5.765510	8.127541e+15	2.750000	2.750000
50%	15.048698	25.172724	3.395274e+07	10.002300	3.243132e+16	4.500000	4.500000
75%	24.059691	46.357330	3.971577e+07	16.028715	1.595739e+17	6.250000	6.250000
max	76.940466	25765.556676	6.758822e+07	38.330645	1.340933e+67	8.000000	8.000000

Table 4: Vertical separation data-set description.

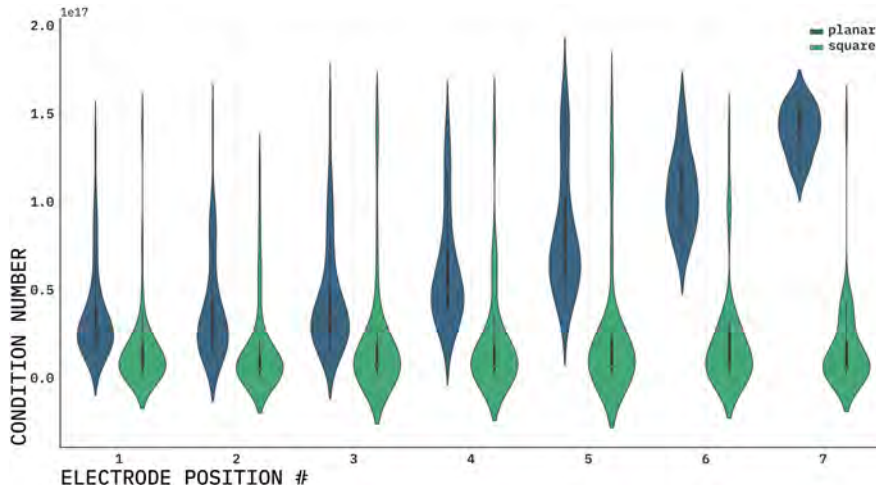
An SVD analysis allows us to have a clear understanding of how feasible it will be to reconstruct an image solely on our measurements³¹. The present analyses the condition number obtained from the SVD analysis, which refers to the ratio of the largest to the smallest singular value acquired. The larger this value is, the harder will it be to construct an image out of our measurements. A quick summary of the data-set obtained is presented in Table 4. There are columns omitted for simplicity's sake, as they are mainly used for indexing inside the data-set. From the data-set description, it is evident that there are condition numbers significantly higher than the average. Thus, the analysis filters such results by calculating the data-set quantiles using the 99th percentile, which corresponds to conditional numbers greater or equal to 2.0e+17. The S/M patterns with significantly large condition numbers relate to M8 for planar arrangements and S8/M8 in square arrangements. The particular case of S8/M8 is known to reconstruct 'mirrored' images, rendering the acquired image useless.

Fig. 29 shows the violin plot corresponding to the distribution of the condition number for both planar and square patterns across the seven ring positions tested³². Fig. 29 shows that it is possible to obtain lower condition numbers when using square patterns. Furthermore, it appears that square patterns offer what one can consider as a logarithmic normal distribution through all positions, being more bottom skewed when reaching the last two positions. On the other hand, the condition number pertaining to planar arrangements increases

³¹ The role of SVD in EIT is discussed in the next chapter

³² The higher the number the higher the separation between electrode planes.

Figure 29: Violin plot corresponding to the condition numbers obtained from all possible S/M combinations in both planar and square methods, tested in seven vertical electrode ring positions.



with the position, performing poorly on the last position, where the distribution is top skewed. This case shows that one can overcome the limitations imposed by certain design constraints, through the careful selection of S/M patterns. Moreover, it shows the enhanced stability of square patterns.

Additionally, multiple Pearson product-moment correlation coefficients were calculated to assess the relationship between the variables presented in this study. Table 5 summarises these relationships. First, analysing the planar protocols, a medium negative correlation between the position of electrodes and the total sensitivity ($r = -0.50$) is observed. Moreover, there is a substantial positive correlation between the condition number and the position of electrodes ($r = 0.60$). In other words, the position of the electrode rings is crucial in planar protocols, as higher separations decrease significantly the total sensitivity and worsen the condition number, making the reconstruction processes more difficult. As explored in the relaxation method, the solution to Laplace's equations is symmetrical. For instance, in the central sensitivity images from Fig. 30 one can observe from left-to-right high sensitivity levels that decrease towards the centre. Therefore, it is important to explore how the impact of the variables studied correspond to the central point of the vessel.

With the previous considerations in mind, the study found that there is a strong positive correlation between the central sensitivity and both skip variables of the S/M pattern ($r = 0.80$). Furthermore, there is a small positive correlation between the injection-skip selected and the condition number ($r = 0.21$). On the other hand, the measurement-skip selected does not appear to have a significant impact on the condition number. Interestingly, the vertical sensitivity has a strong positive correlation with the skip variables of S/M patterns ($r = 0.78$).

VARIABLES	r-VALUE	p-VALUE	SAMPLES
total sensitivity & position	-0.50	< 0.001	192
condition number & position	0.60	< 0.002	192
condition number & stimulation skip	0.21	< 0.001	192
central sensitivity & S/M skip	0.80	< 0.002	192
vertical sensitivity & S/M skip	0.78	< 0.002	192

Table 5: Relevant Pearson correlation coefficients for the planar protocol.

Next, let us explore the square protocol (Table 6). The separation between electrode planes appears to be beneficial to the vertical sensitivity with a strong positive correlation ($r = 0.61$). However, similar to the planar protocol, there is a negative correlation between position and total sensitivity, but in this case is considered small ($r = -0.30$).

In contrast with the planar strategy, there is an insignificant correlation between the condition number and the separation of electrode rings ($r = 0.045$). Moreover, there is a small correlation between injection S/M variables and the central sensitivity ($r = 0.15$). Individually,

both stimulation and measurement skip have a medium positive correlation with the vertical sensitivity ($r = 0.35$) in both cases.

VARIABLES	r-VALUE	p-VALUE	SAMPLES
total sensitivity & position	-0.30	< 0.001	242
vertical sensitivity & position	0.61	< 0.001	242
condition number & position	0.045	< 0.001	244
central sensitivity & S/M skip	0.15	< 0.001	242
vertical sensitivity & stimulation skip	0.35	< 0.002	242
vertical sensitivity & measurement skip	0.34	< 0.002	242

Table 6: Relevant Pearson correlation coefficients for the square protocol.

Overall planar strategies show a more linear relationship with the vertical separation between electrode rings. The linearity of planar protocols is illustrated³³ in Fig. 30 A., where one can observe how the vertical sensitivity response is affected with position. It is important to notice that under small electrode ring separations the planar protocols offer a significantly higher sensitivity than square patterns. Typically, since EIT presents a poor sensitivity at the centre, one desires to enhance the response in this area. Therefore, one can considerably improve this variable by using multi-ring planar methods with small vertical separations. An almost homogenous distribution can also be achieved if desired, as can be observed in position 3.

From Fig. 30 B in general one can conclude that reconstructions can benefit from square patterns more under greater distances between electrode rings. Furthermore, there are particular S/M cases in which the increase in electrode ring separation boosts the sensitivity at the centre of the vessel. The findings of the previous analysis are encompassed in the following design recommendations:

- An analysis of electrode position should be carried out to determine which position offers the best sensitivity for the application.
- The electrode separation should be determined depending on the application. If the application does not require the analysis of multiple z-axis levels, a multi-ring planar protocol with small electrode ring separation is preferred.
- For applications desiring to observe multiple z-axis levels, multi-ring planar protocols with small ring distances might be useful if the EIT hardware allows the control of a high number of electrodes. On the other hand, with larger vessels with a limited number of electrodes, a square pattern with higher electrode ring separation should be used.
- In planar protocols, M8 patterns should be avoided due to the high condition number. In square protocols, M8 patterns can be used except for S8/M8 since it generates the 'mirror' effect.
- When selecting the skip variable for S/M, if the EIT hardware is susceptible to noise, one should select the skips that offer greater sensitivity with low condition numbers.

³³ The horizontal sensitivity is also illustrated in Figs. 31 & 32 as central slices of the VOI, to give the reader a more visual representation of the topic at hand. Due to the considerable amount of information presented, Fig. 30 only shows the response to S5. The interactive visual representations are available from the author upon reasonable request.

This chapter began by describing the electromagnetic theory basics to solve EIT's forward problem and discussing multiple approaches to solve Laplace's problem to determine the voltage response from a conductivity distribution. It then suggested that one of the desirable characteristics from EIT systems is a high sensitivity distribution across the EIT vessel. The present chapter lays out the intricacy of the variables involved in solving the forward problem and concludes by presenting some practical recommendations for EIT designers. The next chapter builds upon the theory presented here to present a solution to the inverse problem, i.e., reconstructing an image from measured data.

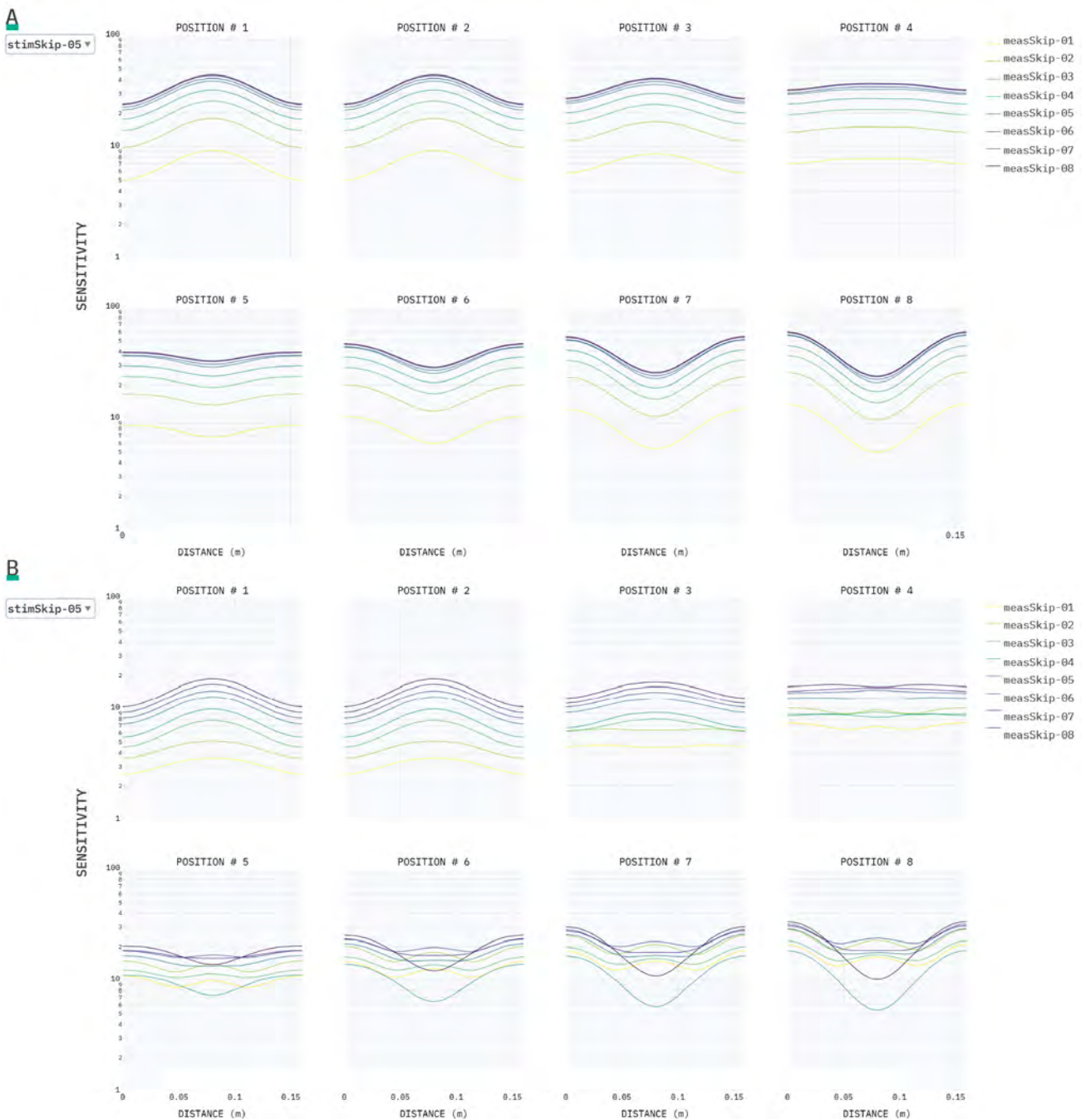


Figure 30: Vertical sensitivity across the vessel's centre for S5 at different positions for **A.** planar, and **B.** square protocols.

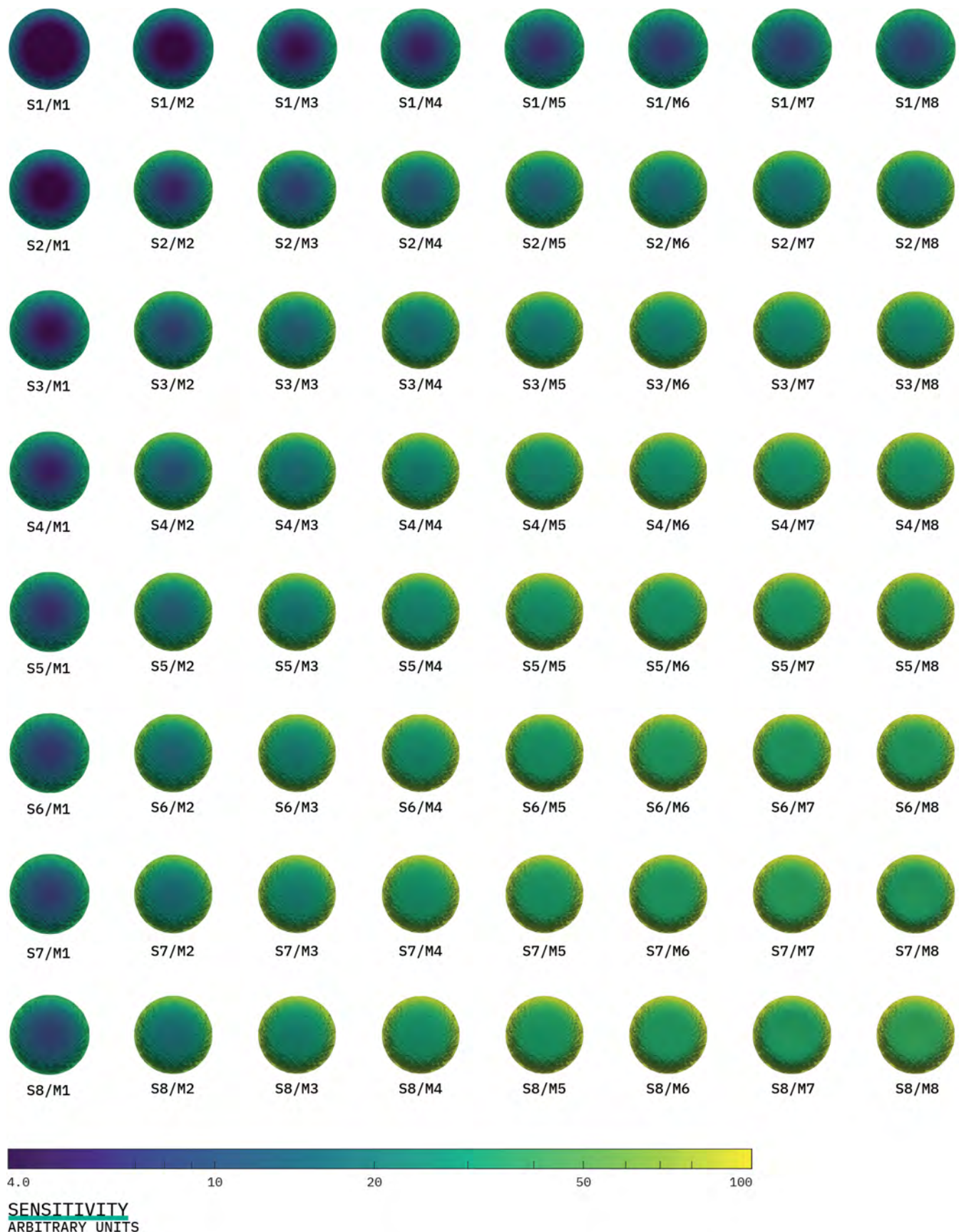


Figure 31: Planar protocols' sensitivity values at the middle of the vessel for position 4.

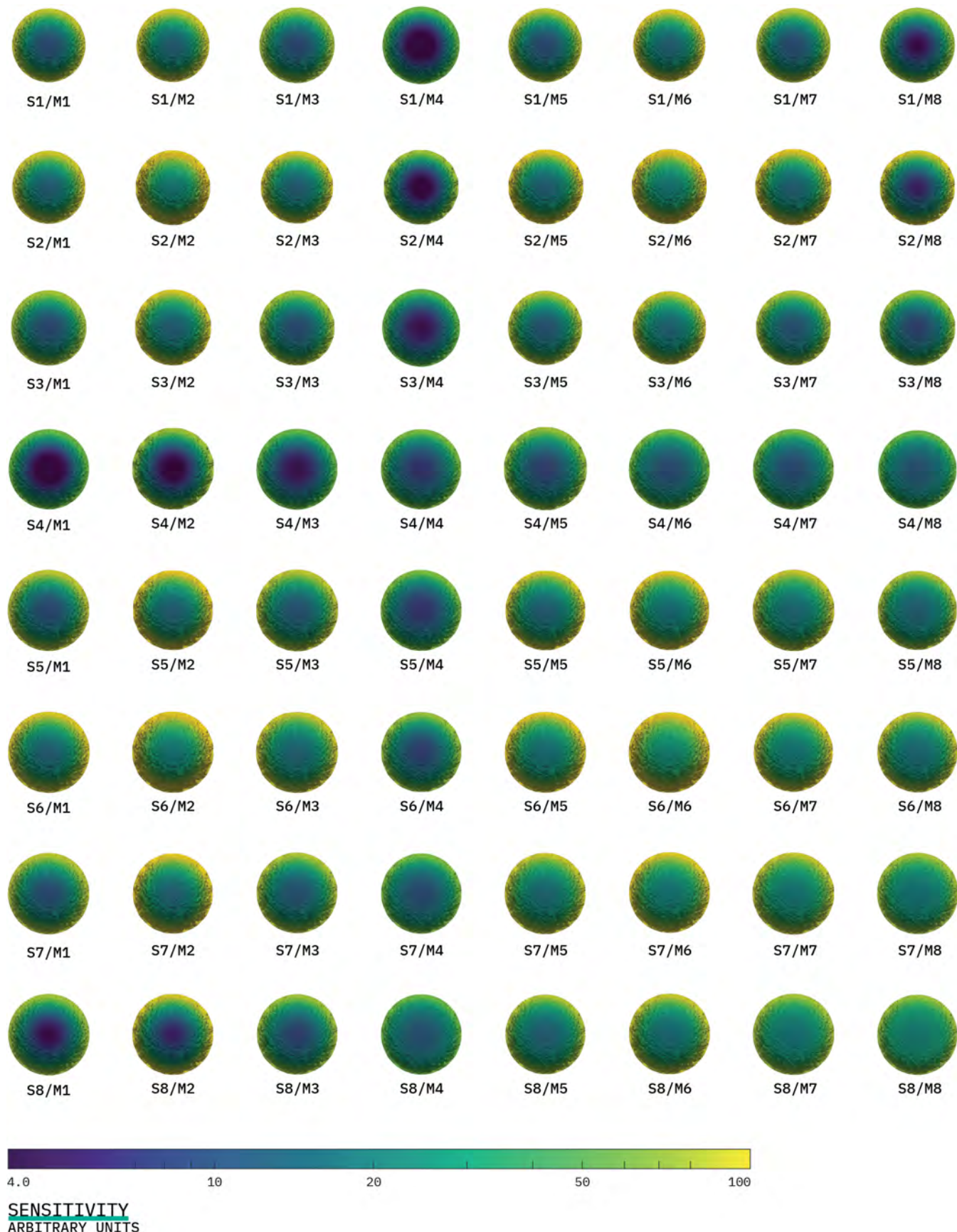


Figure 32: Square protocols' sensitivity values at the middle of the vessel for position 4.

INVERSE PROBLEMS

ROOT IMAGING in its purest form is a subsurface imaging problem similar to geophysical explorations. In most subsurface imaging problems there are at least three components: a source, a detector, and an object covered by some medium. The previous chapter discussed how EIT uses electrical currents that travel through the medium (non-invasively) and react to the object under study on its way back to the sensors. Modelling the aforementioned process is known as the forward problem, and in its simplest form it can be described mathematically¹ as $\sigma J = \phi$. The inverse problem is to convert the response from the sensors into a conductivity map that fits the data. Using the equation $\sigma = \phi J^{-1}$ might be considered as the intuitive way to solve the problem. While the problem might look like a straightforward equation, its complexity arises from the dynamics between inputs, outputs, and the nonlinear behaviour of the physical phenomena occurring in the system. Furthermore, under certain conditions different inputs can originate the same output within a system. Solving the inverse problem requires the use of approaches to deal with the uncertainty of mixing multiple parameters, e.g. geometry, electrode impedance, electrode position, the shape of the boundaries and the internal conductivity distribution. The modelling of the forward problem aids in removing some uncertainties from the system as the parameters previously mentioned are considered when creating the model. However, the linearization of the forward problem does not imply that the inverse problem is linear. The present chapter explains the processes involved in solving the inverse problem with the goal of reconstructing the conductivity distribution of a VOI.

“Root research under natural field conditions is a step-child of science. The known methods are tedious, time-consuming, and the accuracy of their results is often not very great.” Böhm, 1979

¹ In Chapter 2.0 the forward problem was introduced using the general formula $Ax = y$. The presented formula substitutes the general terms with the ones corresponding to Ohm’s law

4.1 Types of EIT inverse problems

The formulation of EIT’s inverse problem can be classified by the end-goal of the application; this could range from merely providing an image of the contents inside a VOI to serving as a process monitoring technique. Therefore, EIT can be classified into:

- *Absolute Imaging (aEIT)*. The goal is to produce an image of the conductivity inside a VOI using a single set of measurements. Ideally, this is the type of solution that all applications can benefit from since it provides absolute and quantitative information. Absolute imaging is extremely challenging as it is sensitive to model errors. In practice, this requires a high degree of precision in how the user describes the electrodes and the electronics used ².

² A. Nissinen et al. “Compensation of errors due to discretization, domain truncation and unknown contact impedances in electrical impedance tomography”. In: *Measurement Science and Technology* 20.10 (2009).

- *Time-Difference imaging (tdEIT)*. The time-difference method creates an image from the difference of two data sets obtained at two different time instances (t_1 and t_2). The approach is mainly used for functional imaging to track physical phenomena over time³. While the approach does not provide absolute values⁴, it is less susceptible to modelling errors, which in turn makes it a more feasible practical approach⁵.
- *Frequency-Difference imaging (fdEIT)*. In this approach an image is reconstructed from the two or more data sets acquired using different stimulation frequencies. The method can classify properties of biological tissues without the need for any previous data.

Before solving any of the above formulations of the inverse problem, it is important to understand the nature of the problem.

4.2 Ill-behaviour

Inverse problems are challenging to solve as the interactions between outputs and inputs are typically associated with complicated physical phenomena that cannot be described linearly. The implication of this behaviour could mean that under well-defined system parameters and measurement conditions, different inputs would generate the same output. The adequate modelling of the forward problem removes a certain degree of the uncertainty generated from this dynamic process (as explored in Chapter 2.0). As with most mathematical problems, solving the forward and inverse problem can be reduced to the evaluation of a function⁶. Evaluating the function ensures that a solution exists, which is the first criteria for solving inverse problems. But it is more challenging to ensure the second criteria, the uniqueness of the solution. The uniqueness of the solution poses both a theoretical and practical challenges that can be traced back to the modelling of the problems. Thus, it is crucial to define the concept of well-posed problems⁷:

1. *Existence: there is at least one solution to the problem.*
2. *Uniqueness: the problem has only one solution.*
3. *Stability: the solution changes continuously and slowly with the data.*

As with many physical systems, the EIT inverse problem can be represented as a linear system of equations $Ax = b$. Usually the system matrix or Jacobian⁸ (Eq. 47), A , and measurement vector b are known, and the x input vector is unknown. In EIT a known current is injected through the VOI and a response is measured, and while some system parameters are known, this does not guarantee that the system can be solved. Therefore, this means that the parameters involved in the forward model during the linearization of the problem are not the same parameters involved in the linearization of the inverse model. In EIT solving the inverse problem involves finding the model parameters that provide the best fit to the measurements acquired (i.e. it does not involve finding the input).

³ One of the main applications of tdEIT is the monitoring of heart activity and breathing.

⁴ The present work considers only time/frequency difference methods due to the practical challenges imposed by aEIT.

⁵ B H Brown. "Electrical impedance tomography (EIT): a review BH Brown Electrical impedance tomography (EIT): a review". In: () .

⁶ Such a process requires simplifying the problem, which sacrifices some details of the physical phenomena being studied. Therefore, it is expected that the formulation of both problems will suffer contain modelling errors. For instance, practical data will always contain sources of noise that the model will ignore.

⁷ J Hadamard. *Sur les problèmes aux dérivées partielles et leur signification physique*. Vol. 13. Princeton University, 1902.

⁸ The system matrix A encloses both the implicit and explicit model parameters. The parameters can be the internal conductivity distribution, electrode geometry along its locations, and geometry of the main vessel.

Considering our initial forward problem, finding b given A and x , Hadamard's conditions are inherently satisfied by writing the problem linearly. However, to satisfy the third condition, stability, the singular vectors of the system of equations need to have small values in the presence of random perturbations. Typically, small perturbations (e.g. from noise sources) in the acquired measurements from a system will generate an out of proportion variation in the estimation of the model characteristics. This lack of stability is problematic when considering that most numerical algorithms solve the problem through testing a variety of model parameters and expecting that when close to a solution, the solution-error decreases. Moreover, the FEM discretization process adds to the ill-posedness of the inverse problem as the approximation of a continuous physical phenomenon carries with it numerical or modelling errors.

A useful mathematical tool to understand the extent of the ill-condition of the problem is the SVD. The SVD method is a data driven tool that converts high-dimensional data into the key features that describe the data. Furthermore, the SVD method can also serve as an approximation method to find a solution to an ill-conditioned⁹ system of equations.

The SVD analysis decomposes matrix A into a product of three matrices. First, let us consider that A is an $m \times n$ matrix, and that $A^T A$ can be decomposed into:

$$(49) \quad A^T A = (v_1 \cdots v_n) \begin{pmatrix} \sigma_1^2 & & \\ & \ddots & \\ & & \sigma_n^2 \end{pmatrix} \begin{pmatrix} v_1^T \\ \vdots \\ v_n^T \end{pmatrix} = \mathbf{V} \Sigma \mathbf{V}^T$$

where $v_1 \cdots v_n$ are orthonormal eigenvectors and $\sigma_1 \cdots \sigma_n$ are the diagonal singular values. Then, considering $u_i = (1/\sigma_i) A v_i$:

$$(50) \quad A A^T u_i = \sigma_i A v_i$$

Since \mathbf{V} is an orthogonal matrix ($\mathbf{V}^T = \mathbf{V}^{-1}$) then:

$$(51) \quad \sigma_i u_i = A v_i \iff \mathbf{U} \Sigma = A \mathbf{V}$$

and thus:

$$(52) \quad A = \mathbf{U} \Sigma \mathbf{V}^T$$

where \mathbf{U} and \mathbf{V}^T represent the left and right singular vectors. The singular value diagonal matrix Σ is ranked, meaning that its values σ_n are ordered by importance (from top to bottom). Using the SVD analysis, one can divide the matrix A into pieces ranked by their weight:

$$(53) \quad A = \sigma_1 u_1 v_1^T + \cdots + \sigma_n u_n v_n^T$$

⁹ It can provide solutions to both underdetermined and overdetermined systems of equations.

σ tends to decrease when getting closer to the n th value, thus, the calculation can be truncated:

$$(54) \quad A = \sigma_1 u_1 v_1^T + \cdots + \sigma_t u_t v_t^T$$

this is known as truncated SVD where $t < n$. Therefore, coming back to the linear equation $Ax = b$, using SVD analysis the following linear transform is obtained:

$$(55) \quad b = Ax = \mathbf{U} \Sigma \mathbf{V}^T x$$

A visual representation of applying the SVD decomposition of matrix A to a matrix x (Eq. 55) is presented in Fig. 33. As previously mentioned in Chapter 2, to acquire an estimation of how probable it is that an image can be reconstructed from a set of measurements and its model (i.e. how ill-conditioned is the problem) the condition number must be calculated. For discrete problems, it can be estimated using:

$$(56) \quad \text{cond}(A) = \|A^{-1}\| \cdot \|A\| \geq 1$$

In terms of the SVD analysis, the condition number corresponds to the ratio between the largest and smallest singular value.

$$(57) \quad \text{cond}(A) = \frac{\max(\Sigma)}{\min(\Sigma)}$$

In physical terms, the condition number can be interpreted as the amplification factor related to the maximum relative change in the solution originated from a change in the right hand singular vector¹⁰. This implies that for large condition numbers the numerical calculations can become unstable as the condition number indicates an expected loss of n digits of precision, assuming that:

$$\text{cond}(A) = 10^n$$

The SVD analysis of inverse problems can help understand their ill-posedness, and while the decomposition process can be significantly expensive to calculate in terms of computational processing, it also provides a method to obtain the minimum norm least squares solution for the problem.

4.2.1 SVD Pseudo-inverse

EIT's inverse problem is to find the conductivity¹¹ change x . Before substituting the SVD expansion in the previously presented system of equations, it is important to consider the nature of the system. For instance, whenever A is a square matrix (i.e. it is an invertible matrix with non-zero determinant) then it means that the solution is

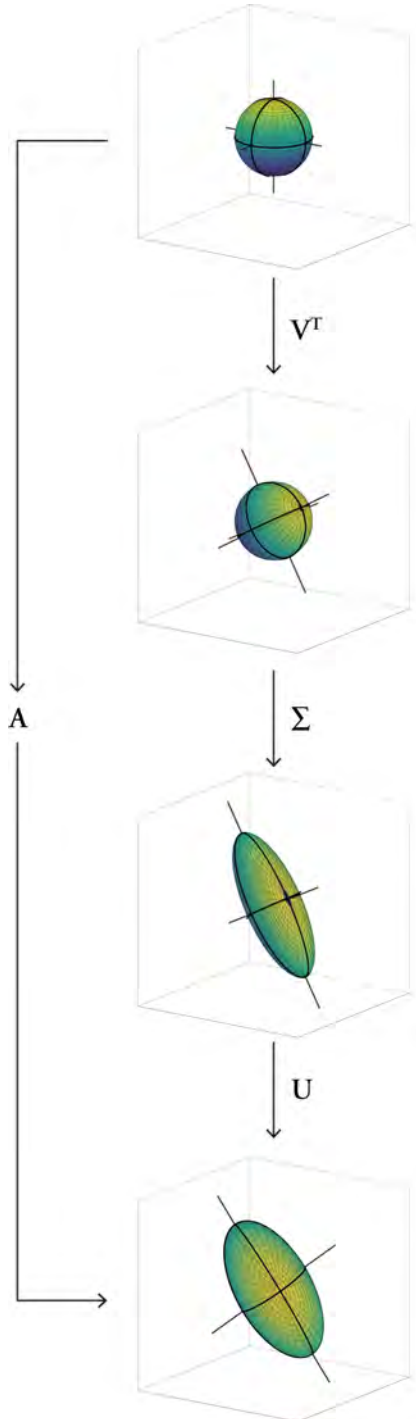


Figure 33: Transformation induced by matrix A on a 3D spherical shape. The transformation is equivalent to the fundamental transformations: rotation, scaling, and another rotation.

¹⁰ In simple terms, in ill-conditioned problems a small change in the input will produce a large change in the output.

¹¹ For simplicity's sake, this section discusses conductivity changes. However, as previously explored, impedance is a complex number, and as such there are specific mathematical definitions and symbols to indicate this.

unique. However, if A is non-invertible (i.e. singular or rectangular) it means that there might be an infinite number of solutions, depending on the shape of A and b . There are two main cases that need to be considered to understand how to solve the inverse problem. The first case to consider is when the system is underdetermined, i.e. where there are fewer equations (measurements) than unknowns (model parameters). In underdetermined systems, $A \in \mathbb{C}^{n \times m}$ where $n \ll m$, there are infinite solutions as there are insufficient measurements to uniquely determine the high-dimensional data of the model parameters.

The second case is when the system is overdetermined, i.e. when $n \gg m$. In this type of system there are more equations than unknowns. This means that there are more measurements than unknown model parameters. Typically, this type of system meets the criteria for well-posed problems. However, when a solution cannot be found, it is still possible to find an approximate solution that minimizes the sum-squared error, $\|Ax - b\|_2^2$, which corresponds to the least-squares solution:

$$(58) \quad \hat{x} = \arg \min_x \|Ax - b\|_2$$

The above equation is an example of how to calculate a best-fit solution to a homogeneous conductivity \hat{x} . On the other hand, for an undetermined system when an infinite number of solutions exist, a solution can be approached finding the minimum norm solution by employing the minimum norm $\|x\|_2$. An optimisation of the above problem is found using the SVD method. Thus, solving the linear system of equations $Ax = b$ through the SVD expansion results in the Moore-Penrose left pseudo-inverse¹², A^\dagger of A :

$$(59) \quad x = A^{-1}b = \mathbf{V}\Sigma^{-1}\mathbf{U}^*b \Rightarrow A^\dagger Ax = A^\dagger b$$

where:

$$A^\dagger := \mathbf{V}\Sigma^{-1}\mathbf{U}^* \Rightarrow A^\dagger A = \mathbf{I}$$

Therefore, substituting the solution from Eq. 59 back into the original system of equations:

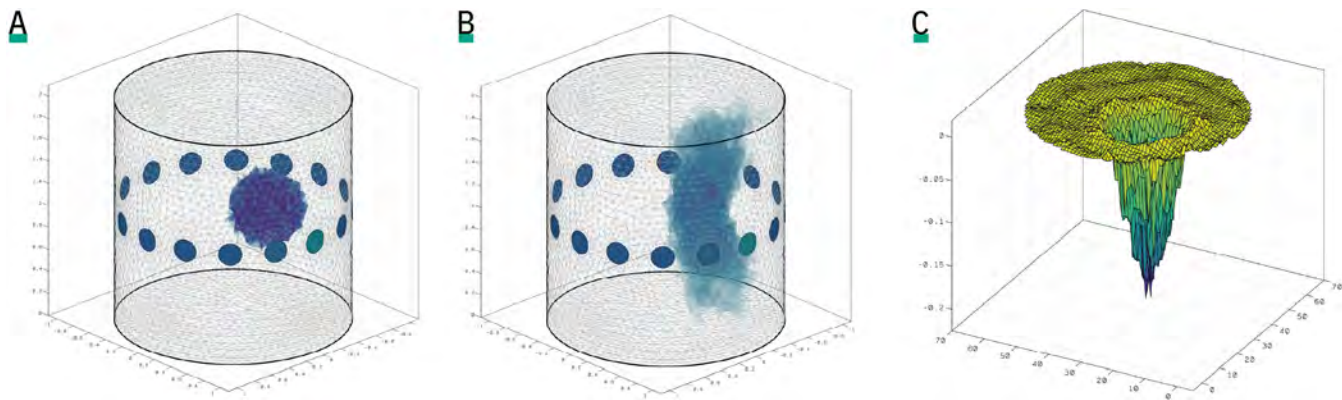
$$(60) \quad Ax = \mathbf{U}\Sigma\mathbf{V}^T\mathbf{V}\Sigma^{-1}\mathbf{U}^*b = \mathbf{U}\mathbf{U}^*b$$

In this context¹³, $\mathbf{U}\mathbf{U}^*$ is a projection in the column space of \mathbf{U} . While the computation of the SVD is rather expensive, the calculation of the pseudo-inverse A^\dagger is more efficient once the SVD expansion has been completed. However, even the least-squares approach can fail if A is badly conditioned. The singular values of severely ill-posed matrices make them decay significantly to values even below bit-precision.

¹² R. Penrose. "A generalized inverse for matrices". In: *Mathematical Proceedings of the Cambridge Philosophical Society* 51.3 (1955).

¹³ Here \mathbf{U}^* corresponds to the conjugate transpose (which implies the use of complex numbers), but it can be understood as \mathbf{U}^T .

¹⁴ B Murat Eyüboğlu. "An interleaved drive electrical impedance tomography image reconstruction algorithm". In: *Physiological Measurement* 17.4a (1996).



The inclusion of small singular values in the above equation create noisy images¹⁴. This is exemplified in the findings of Eyüboglu (1996), where even when using no-noise simulation measurements, images could not be recovered¹⁵. Therefore, a type of regularization is needed to obtain sensible images. One way of doing this is through the truncation of the diagonal Σ^{-1} , so that only the largest singular values are conserved. By removing singular values from the system matrix, a reduction in the sensitivity is expected. This drop in sensitivity is more prominent in the spatial resolution of the images, especially when some larger singular values are dropped.

4.2.2 Numerical example

A reconstruction example is presented in this subsection to illustrate the points made in the previous and present chapters. The simulations across the presented work take into consideration the guidelines and recommendations of Adler and Lionheart (2006)¹⁶ to avoid committing “*inverse crimes*”. In this first instance, the simulated data (acquired by solving the forward problem) has been obtained using a finer mesh than that of the reconstruction. A basic reconstruction of a test object¹⁷, located at $(x, y, z) = (0.2, 0.2, 1)$ with a radius corresponding to 30% of that of the main vessel and with a conductivity 75% less than the one from the background, inside a cylindrical vessel, comprised of 7×10^4 elements with a single ring of 16 electrodes with a unitary background conductivity, is carried out using the Moore-Penrose pseudo-inverse with a truncated SVD. In this example, an adjacent S/M pattern is used. The model used for the reconstruction was produced using a coarser mesh (1×10^4 elements). The result is presented in Fig. 34 B, where the reconstructed target extends beyond the imaging plane, and as previously stated, single plane stimulation patterns offer low vertical resolution. But as illustrated in Fig. 34 C, when taking a 2D slice of the reconstruction, a shape resembling the original distribution can be observed. This example shows a simple 3D case when there is no noise present to illustrate the initial steps of solving the EIT’s inverse problem. In practice, the presence of noise in the data will degrade the quality of the reconstruction due to the ill-posed nature of the problem.

Figure 34: Basic numerical example of solving EIT’s inverse problem with Moore-Penrose Pseudo-inverse. A. Original VOI to be reconstructed with a homogeneous conductivity background, and a low conductivity spherical intrusion. B. 3D Reconstruction without noise considerations. C. Surface plot of a 2D slice taken at the middle of the electrode plane. The z-axis represents the amplitude of the reconstruction at that z-level.

¹⁵ In practice finding convergence to a solution can be problematic when the measurements are noisy or have discrepancies. Therefore, to achieve convergence, the system needs to employ a form of regularization.

¹⁶ Andy Adler and William R B Lionheart. “Uses and abuses of EIDORS: an extensible software base for EIT”. In: *Physiological Measurement* 27.5 (2006).

¹⁷ Simulations use SI units.

4.3 Regularization

One of the biggest challenges of EIT is ensuring Hadamard's third condition, as small perturbations in the measurements lead to meaningful changes in the solution. Let us start by considering our linear set of equations $Ax = b$ using a notation more related to EIT:

$$(61) \quad \mathbf{J}\sigma = y + \epsilon$$

Here J represents the *Jacobian*¹⁸, σ is the internal conductivity distribution, y depicts the measurements taken¹⁹, and ϵ is the error vector in the measurements due to noise, and is considered to be additive. It is important to remember that this is a nonlinear problem as the measured data depends on the VOI internal conductivity distribution in a nonlinear manner²⁰. There are two main approaches to solve this nonlinear problem. The first is to replace the forward operator with a linear approximation (e.g. using the Jacobian) through an initial conductivity σ_0 and calculating only the differences in conductivity, $\Delta\sigma$. The second approach is through the use of iterative algorithms based on gradient descents. The general way to provide a stable solution to the inverse problem is to modify the approximation of Eq. 58 using penalty arguments:

$$(62) \quad \begin{aligned} \hat{\sigma} &= \arg \min_{\sigma} (\mathbf{F}(\sigma, \mathbf{B}, \mathbf{El}) + \lambda \mathbf{R}(\sigma_*)) \quad \text{or} \\ \hat{\sigma} &= \arg \min_{\sigma} (||\mathbf{J}\sigma - (y + \epsilon)||_2 + \lambda ||\mathbf{R}(\sigma_*)||_2) \end{aligned}$$

where $\mathbf{F}(\sigma, \mathbf{B}, \mathbf{El})$ is the forward operator related to equations 35-38, λ and $\mathbf{R}(\sigma_*)$ are the regularization term and matrix respectively; in which σ_* corresponds to the changes in σ with respect to a prior known value σ_0 (i.e. $\sigma_* = \sigma - \sigma_0$). The above equation shows the mathematical framework for both the nonlinear general regression and the one using the linear approximation of the forward operator $\mathbf{F}(\sigma, \mathbf{B}, v)$ (which corresponds to the Jacobian from Eq.47). In both cases, a regularization is needed to produce a solution. How much problem is regularised is given by the penalty parameter λ , also known as hyperparameter in the EIT community. The above solution can be understood as an optimisation problem for a quadratic equation that is guaranteed to have a unique solution when penalized.

Both the measurement residual and regularization terms of Eq. 62 can have a norm different from L2. By definition the L1-norm adds all errors, meaning that all differences have the same value. For the measurement residual the L1-norm would correspond to:

$$(63) \quad ||\mathbf{J}\sigma - y||_1 = \sum_k |J_k \sigma - y|$$

On the other hand, the L2-norm penalizes errors more heavily as they are sum-squared. However, it provides more robust error norms

¹⁸ Not to be confused with current density \mathbf{J} , presented in Chapter 2

¹⁹ Considering a set of voltage measurements v : for tdEIT $y = v_{t2} - v_{t1}$. And in the case of fdEIT $y = v_{f2} - kv_{f1}$, where k is a scaling factor.

²⁰ The Jacobian presents this nonlinear behaviour. When approximating an ill-posed problem using discrete methods, e.g. FEM, the linearization of the problem becomes ill-conditioned due to the unstable nature of the original problem.

on data mismatches as it treats each term as if it was independent. The L2-norm is calculated:

$$(64) \quad ||\mathbf{J}\sigma - y||_2^2 = \sum_k (\mathbf{J}_k \sigma - y)^2$$

The most common norm used in EIT regularization algorithms is the L2-norm. Solutions based on the L2-norm smooth the edges of reconstructed conductivity inhomogeneities. In contrast, the L1-norm algorithms preserve the edges of the different conductivity regions as it does not penalize sharp transitions between conductivities²¹. The type of application is what determines the choice of norm. For instance, an L1-norm is better suited for problems with strong conductivity discontinuities²². The geometric intuition of the norms is illustrated in Fig. 35. Additionally, the choice of the regularization matrix will impact the final solution. The most common method of regularization in EIT is the Tikhonov approach²³. The Tikhonov regularization scheme aims to obtain a balance between obtaining a small residual and being small in L2-norm to obtain a unique solution. Therefore, λ can be understood as the tuning parameter of such optimisation. The regularization matrix $\mathbf{R}(\sigma_*)$ is understood as imposing prior knowledge regarding the solution. In the standard Tikhonov method, the $\mathbf{R}(\sigma_*)$ is the identity matrix²⁴ \mathbf{I} . This type of regularization is similar to the solution obtained through the SVD truncation. The regularization penalizes large σ parameters, thus, the small singular values that introduce instability weigh less²⁵. The solution is obtained through:

$$(65) \quad \hat{\sigma} = (\mathbf{J}^T \mathbf{J} + \lambda \mathbf{R}^T \mathbf{R})^{-1} (\mathbf{J}^T y) = \mathbf{R}y$$

Tikhonov's regularization applies a homogeneous penalization to each image element, and thus, it weights the image amplitude; which implies that all targets are independent of each other. Overall, this type of regularization is simple to implement, but the resulting images will present boundary emphasis and small artefacts.

Sharper reconstructions can be obtained using Laplace's regularization. Similar to Tikhonov's \mathbf{R} , the Laplace regularization applies a non-smoothness weighting parameter using \mathbf{R} . Laplace's regularization is a second-derivative filter that responds to image edges in any direction. On a discrete matrix it takes the diagonal elements (i) of $\mathbf{R}_{i,i}$ and subtracts the adjacent elements (j) so that $\mathbf{R}_{i,j} = -1$. The direction of the non-smoothing penalization in FEMs is determined by the selection of discrete filter to be applied. For rectangular FEMs in two dimensions, the filter is a convolution with one of the following matrices:

$$(66) \quad \begin{pmatrix} -1 & -1 & -1 \\ -1 & -8 & -1 \\ -1 & -1 & -1 \end{pmatrix} \quad \text{or} \quad \begin{pmatrix} 0 & -1 & 0 \\ -1 & -4 & -1 \\ 0 & -1 & 0 \end{pmatrix}$$

²¹ The L1-norm is used for total variation (TV) algorithms that offer image reconstructions with less 'blur'

²² A. Borsig and A. Adler. "A primal-dual interior-point framework for using the L1 or L2 norm on the data and regularization terms of inverse problems". In: *Inverse Problems* (2012).

²³ Also known as ridge regularization in statistics.

²⁴ John B. Bell et al. "Solutions of Ill-Posed Problems." In: *Mathematics of Computation* 32.144 (1978).

²⁵ If $\lambda = 0$ the regularization is removed, and the solution corresponds to that of the traditional least squares method. Furthermore, if the prior σ_0 is removed, then it is implied that the previous conductivity was zero across the VOI.

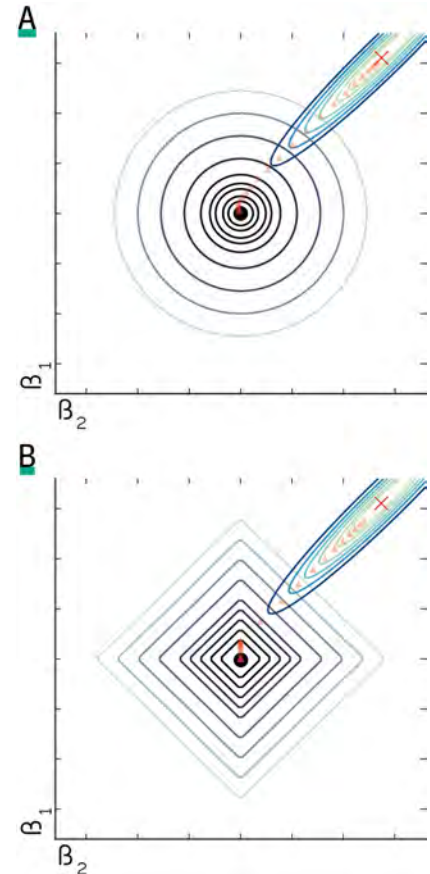


Figure 35: Optimal solution for the least-squares problem using A. L2 and B. L2 norms. The outer elliptical plot represents the least-squares residuals, and the central plot represents the cost of the norm. The optimal solutions are found wherever there is an intersection between the contour plots. The β_n are the model parameters, and the small red dots represent the solution for different values of λ .

Another typical choice of \mathbf{R} is through the Newton One-Step Error Reconstructor (NOSER)²⁶ method, which describes the regularization matrix as:

$$(67) \quad \mathbf{R} = \text{diag}(\mathbf{J}^t \mathbf{J})$$

In contrast with the previous regularization schemes, the NOSER method weights the image elements using their respective sensitivity to changes. As a result, the reconstructed images show less emphasis closer to the boundaries of the volume under study. All the previous regularization schemes depend on λ , and as such its selection will affect the reconstruction.

4.4 Selection methods for the optimal hyperparameter

The choice of how much a solution should be regularized is in itself another optimisation problem. In the previous regularization approaches, the use of a higher λ value reconstructs a smooth image closer to the original, however, the drawback is the introduction of more noticeable artefacts in the solution. On the other hand, when λ decreases, the reconstruction is less smooth with high amplitudes, which makes it difficult to discern the true shapes of internal conductivity distributions.

Typically, the selection of the penalty has been done heuristically in most EIT applications; meaning that often studies comparing algorithm performance do not compare them on a fair basis, as λ can be tuned to hide image ‘imperfections’. Furthermore, for practical applications a way to automatically choose λ is more important; this means that the selection method has to be robust, and thus, be able to handle the most common range of problems encountered for that specific application. For these reasons, the way to properly choose λ has been a subject of discussion in the EIT community²⁷. Currently, the most common methods to automatically choose λ are the Generalized Cross-Validation (GCV) and the L-curve methods.

The L-curve method consists of using different λ values as the main parameter to plot the solution norm to the mismatch data between the measurements obtained from the forward operator and the practical data, $||\mathbf{J}\sigma - y||$, against the residual norm $||\mathbf{R}(\sigma_*)||$. The results are then plotted using a logarithmic grid²⁸ (Fig. 36 A). In most applications the plot will resemble an ‘L’ shape, where the optimal λ value is located near the L-curve’s corner. If λ is located near the ‘steep’ part of the curve, the solution will be dominated by noise errors. On the other hand, if λ is located next to the ‘flat’ part of the plot, the reconstructions will be governed by regularization errors. Thus, the optimal ‘middle’ point between noise and regularization is the L-curve’s corner.

In the GCV method, λ is used as a predictor parameter for the missing elements in the measurement data set. The procedure in-

²⁶ M. Cheney et al. “NOSER: An algorithm for solving the inverse conductivity problem”. In: *International Journal of Imaging Systems and Technology* 2.2 (1990).

²⁷ B. M. Graham and A. Adler. “Objective selection of hyperparameter for EIT”. in: *Physiological Measurement* 27.5 (2006).

²⁸ Per Christian Hansen. “Analysis of Discrete Ill-Posed Problems by Means of the L-Curve”. In: *SIAM Review* (1992).

volves removing a single measurement and calculating the residual error for the inverse problem without that measurement²⁹. The GCV calculation is iterative, thus, the before-mentioned steps are repeated for each measurement. The goal is to find the λ that produces the smallest sum of residual errors. The GCV is calculated using $G(\lambda) = \|\mathbf{J}\sigma - y\|^2 / \text{trace}(\mathbf{I} - \mathbf{J}(\sigma_*)^2)$ and plotting the sum of residuals against different hyperparameter values (Fig. 36 B).

The above methods are highly related to the data, its noise, and thus, the application. In other words, λ can not be precomputed. Furthermore, both functions are computationally expensive as they are continuously solving the inverse problem to obtain an optimal fitting λ . Depending on the size of the problem, the computation of λ through these methods can take a long time³⁰ to compute depending on the resources available to the user. These methods provide a good first approach to the λ selection automation, but at this stage it is difficult to consider them for use in automated applications. In this work, both methods are employed. Both functions were implemented using the MATLAB regularization tools from Hansen (2007)³¹. The decision to use both is cemented in the fact that, occasionally, the L-curve (the method with better optimal values) fails to deliver λ values that produce interpretable images when the solution is significantly smooth. In comparison, the GCV function might not choose the optimal λ in terms of balancing noise and regularization, but it is a more robust method.

4.5 Iterative descent methods

The previously presented optimisation procedures rely on classic least-squared fitting methods, however, descent methods can be better suited to handle nonlinear systems of equations and to optimize over nonlinear spaces for parameter dependencies. These types of approaches are based on iterative searches for the global minimum of the objective function based on Eq. 62:

$$(68) \quad \Phi(\sigma) = \|\mathbf{J}\sigma - (y + \epsilon)\|_2 + \lambda \|\mathbf{R}(\sigma_*)\|$$

The aim is to start using a hypothesis for the minimum and at each iteration verify that the minimum has been reached. The simplest nonlinear solver is the gradient descent method, which aims to minimize the mismatch between data and model³²:

$$(69) \quad \sum_{k=1}^n (\Phi(\sigma_k, \beta) - y_k) \frac{\delta \Phi}{\delta \beta_j} = 0 \quad \text{for } j = 1, 2, 3, \dots, m$$

by taking steps towards minimization using the gradient:

$$(70) \quad \nabla \Phi(\sigma) = 0$$

²⁹ Grace Wahba and Yonghua Wang. "When is the optimal regularization parameter insensitive to the choice of the loss function?" In: *Communications in Statistics - Theory and Methods* 19.5 (1990).

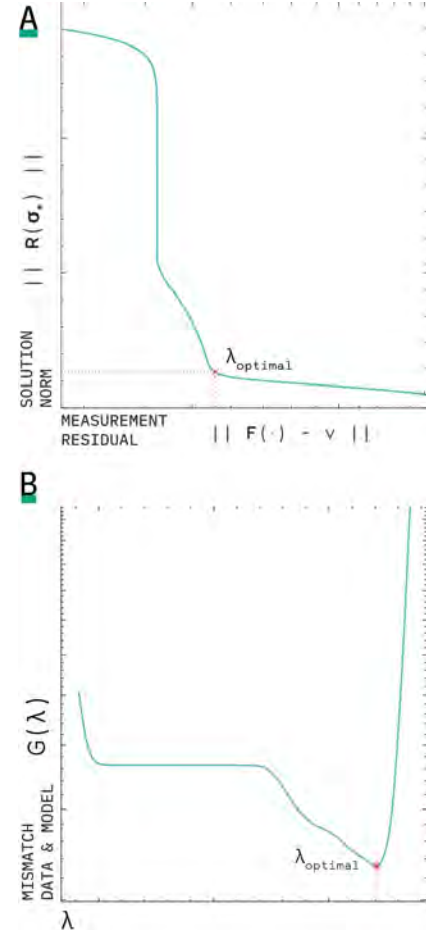


Figure 36: Ideal representation of A. L-curve and B. GCV methods for different λ . The optimal value $\lambda_{optimal}$ can be found at the L-corner in (A), and at the minimum of the GCV plot (B)

³⁰ Depending on the number of measurements, and the FEM's complexity, the time can vary from a couple of hours to entire days.

³¹ Per Christian Hansen. "Regularization Tools version 4.0 for Matlab 7.3". In: *Numerical Algorithms* 46.2 (2007).

³² In this case β is considered to be the forward operator $\mathbf{F}(\sigma_k, \mathbf{B}, \mathbf{El})$ presented earlier.

Descent methods begin by defining a starting point $k = 0$, and from that point they descend towards the minimum in the direction which decreases more rapidly³³ (Fig. 37). Mathematically, the process is described as follows:

$$(71) \quad \hat{\sigma}_{k+1}(\alpha) = \hat{\sigma}_k - \alpha \nabla \Phi(\hat{\sigma}_k)$$

where α is the step size³⁴. The gradient is calculated then using:

$$(72) \quad \nabla \Phi(\hat{\sigma}_k) = \mathbf{J}(\hat{\sigma}_k)^T \Sigma_{\epsilon}^{-1} (\mathbf{F}(\boldsymbol{\sigma}, \mathbf{B}, \mathbf{E}) - \mathbf{y}) + \lambda \mathbf{R}(\hat{\sigma}_k)$$

where Σ_{ϵ}^{-1} is the covariance of the noise which is assumed to be additive white Gaussian noise³⁵. One of the challenges of descent methods is to converge around the global minimum in the presence of multiple local minima. Typically, a one dimensional line search is used to determine an optimal step at each iteration:

$$(73) \quad \alpha_k = \arg \min_{\alpha_k > 0} \Phi(\hat{\sigma}_k - \alpha \nabla \Phi(\hat{\sigma}_k))$$

This general type of descent is known as Steepest descent, and while it might be simple to implement, it is often considered to be inefficient and computationally expensive³⁶.

4.5.1 Newton algorithms

Problems with multiple asymmetric minima require a different approach that is not restricted to minima that are linearly close to the initial guess. Newton-type methods provide a better solution by approximating the objective function $\Phi(\hat{\sigma})$ locally using:

$$(74) \quad \Phi(\sigma_k + d_t) \approx \Phi(\sigma_k) + \nabla \Phi(\sigma_k)^T d_k + \frac{1}{2} d_k^T \nabla^2 \Phi(\sigma_k) d_k$$

here the Hessian is represented by $\nabla^2 \Phi(\sigma_k)$, where $\nabla \Phi(\sigma_k)$ is the gradient of the objective function with search direction d_k . To calculate d_k the derivate of the objective function should be equal to zero, and thus the following equation is obtained:

$$(75) \quad d_k = -\nabla^2 \Phi(\sigma_k)^{-1} \nabla \Phi(\sigma_k)$$

the above calculation is known as Newton direction. Once an acceptable residual is reach, or if the iterations do not improve the residual, the process stops. For problems with a large amount of data (usually this is reflected by a complex FEM with a large quantity of elements) this method might not be appropriate, as the storing and inversion of the Hessian is computationally expensive. As such, this type of algorithm relies on an exact search, which sometimes is suboptimal for

³³ The choice of the size of the step and direction vary depending on the descent method.

³⁴ In simple problems, α is kept constant.

³⁵ Some solvers take into consideration the noise by applying a diagonal weighting matrix using an estimate of the noise variance, $\mathbf{W}_{i,i} = 1/\text{var}(v_i)$ for each i measurement, to the measurement residual L2-norm:

$$\begin{aligned} \|J\sigma - v\|_2 &\rightarrow \|J\sigma - v\|_W \\ \|J\sigma - v\|_W &= \sum_i \mathbf{W}_{i,i} (J\sigma - v_i) \end{aligned}$$

³⁶ Andrea Borsic. "Regularisation Methods for Imaging from Electrical Measurements by Andrea Borsic". In: July (2002).

³⁷ As with most optimisation methods, regularization is expected as the standard solutions offered by descent methods will not converge without it.

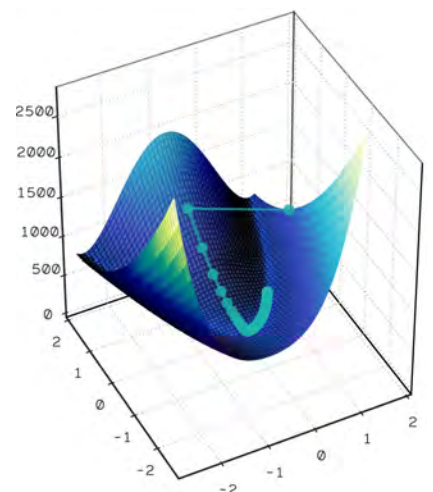


Figure 37: Illustrative example of Newton descent methods. The figure represents the Rosenbrock function, where the minimum is located in a banana shaped region. Given an initial guess, the algorithm gets closer to finding the minimum upon each iteration.

nonlinear optimisations. Therefore, a better approach can be found using the Gauss-Newton (GN) method³⁷.

The GN algorithm uses an inexact search to determine a step to ensure a good convergence rate. In general, a unitary homogeneous σ_0 is assumed for the initial case and can be calculated through using the forward operator. Then, an initial approximation to $\hat{\sigma}_0$ can be found by using Ohm's law and solving the L2-norm with the pseudo-inverse of the measurements v . For instance, considering $V_0 = I/\sigma_0$ and $V_1 = I/\sigma_1$, the initial approximation can be obtained through:

$$(76) \quad V_0 \times \sigma_0 = V_1 \times \sigma_1 = I \rightarrow \hat{\sigma}_0 = v^\dagger \mathbf{F}(1, \mathbf{B}, \mathbf{El})$$

In the GN method the residual error is considered to be inconsequential, thus, the Hessian can be calculated using:

$$(77) \quad \nabla^2 \Phi(\sigma_k) = \mathbf{J}^T \Sigma_h^{-1} \mathbf{J} + \lambda \nabla^2 \mathbf{R}(\sigma_k)$$

An efficient way to calculate Eq. 77 is to employ a finite number of iterations using a Krylov solver e.g. Preconditioned Conjugate Gradients (PCGs). These type of solver do not directly solve the matrix $\mathbf{J}^T \Sigma_h^{-1} \mathbf{J}$, and solve the gradient in two steps:

$$(78) \quad \begin{aligned} \nabla \Phi(\sigma_k) &= \\ \text{Step 1: } &\mathbf{J}^T \Sigma_h^{-1} \mathbf{J} + \lambda \nabla^2 \mathbf{R}(\sigma_k) \\ \text{Step 2: } &\text{Step 1} \times d_k \end{aligned}$$

the following update rule corresponds to the iterative formulation for the GN method:

$$(79) \quad \sigma_{k+1} = \sigma_k + \alpha_k d_k = \sigma_k - \alpha_k \nabla^2 \Phi(\sigma_k)^{-1} \nabla \Phi(\sigma_k)$$

The success rate of Newton's methods depends on information found inside the Hessian. For instance, if the Hessian is continuous and positive, the solution can be found in one step using an initial assumption of the VOI's conductivity distribution, σ_0 . In most reconstruction applications, the change in conductivity is reconstructed using a known baseline or reference point. Thus, one can get a solution for a known reference assuming that:

$$(80) \quad \begin{aligned} 1: \sigma &= \sigma_0 + \Delta\sigma \\ 2: v_0 &= \mathbf{F}(\sigma_0, \mathbf{B}, \mathbf{El}) \\ 3: v &= v_0 + \Delta v = v_0 + (v_{change} - v_{reference}) \end{aligned}$$

where σ_0 corresponds to the background conductivity map from the baseline, and in the same manner v_0 is the measurements obtained from the forward model using the estimated conductivity characteristics. Next, an estimation of conductivity changes can be calculated:

$$(81) \quad \Delta\hat{\sigma} = \arg \min_{\Delta\sigma} \|\mathbf{F}(\sigma_0 + \Delta\sigma, \mathbf{B}, \mathbf{El}) - (v_0 + \Delta v)\|_{\mathbf{W}}^2 + \|\lambda \mathbf{R}(\Delta\sigma - \Delta\sigma_*)\|^2$$

where the prior estimate of the conductivity change³⁸ is represented by $\Delta\sigma_*$. A common starting point³⁹ is to choose $\sigma_0 = 1 \text{ S/m}$. If the conductivity change is small enough (i.e. $\Delta\sigma \approx 0$), a one-step GN solution can be obtained without re-calculating d_k computing:

$$(82) \quad \Delta\sigma = -(\mathbf{J}^T \Sigma_\epsilon^{-1} \mathbf{J} + \lambda^2 \mathbf{R}^T \mathbf{R})^{-1} (\mathbf{J}^T \Sigma_\epsilon^{-1} \Delta v - \lambda^2 \mathbf{R}^T \mathbf{R} \Delta\sigma_*)$$

The GN algorithm achieves good approximations, however, depending on the Hessian the algorithm may not converge and its computation can take a significant amount of time to calculate. As mentioned previously, a better way of dealing with big computational problems is by using conjugate gradient methods.

4.5.2 Conjugate Gradient

Similar to the GN algorithm, the Conjugate Gradient (CG) finds a solution upon iterations. However, the advantage of the CG algorithm is that it does not directly compute the Hessian and its inverse, allowing for a faster convergence rate. Additionally, the CG method stores the previous search directions upon each iteration; meaning that the algorithm is able to change to an orthogonal direction when the search direction starts oscillating. How much the previous direction is used for the new direction is defined by the conjugate scalar⁴⁰ β_k .

There are multiple approaches to define the value of β . A robust method is the *Polak-Ribi  re* scheme, that guarantees convergence by ignoring the previous d_{k-1} and using a direction based on the steepest descent methodology⁴¹. In other words, this is equivalent to restarting the CG process when $\beta < 0$. The conjugate parameter is calculated:

$$(83) \quad \beta_k = \frac{d_k^T (d_k - d_{k-1})}{d_{k-1}^T d_{k-1}}$$

where initially $d_k = -\nabla\Phi(\sigma_k)$, and the subsequent search directions are determined by $s_n = d_k + \beta d_{k+1}$. The initial estimation of the VOI conductivity distribution can accelerate the convergence of the CG method⁴². The CG algorithm is described by the following steps:

```

1 setup number of iterations and residual tolerance
   calculate initial search direction  $d_0 = -\nabla\Phi(\sigma_0)$ 
2 repeat
   calculate  $\alpha_k$ 
   minimize  $\Phi(\sigma_k + \alpha_k d_k)$ 
   update  $\sigma_{k+1} = \sigma_k + \alpha_k d_k$ 
   calculate  $d_{k+1}$  and  $\beta_{k+1}$ 
   update search direction using  $d_{k+1} + \beta_{k+1} d_k$ 
    $k \leftarrow k + 1$ 
3 until  $\epsilon < \text{tolerance}$  or  $k = \text{iterations}$ 
```

³⁸ In most applications $\Delta\sigma_*$ is assumed to be zero.

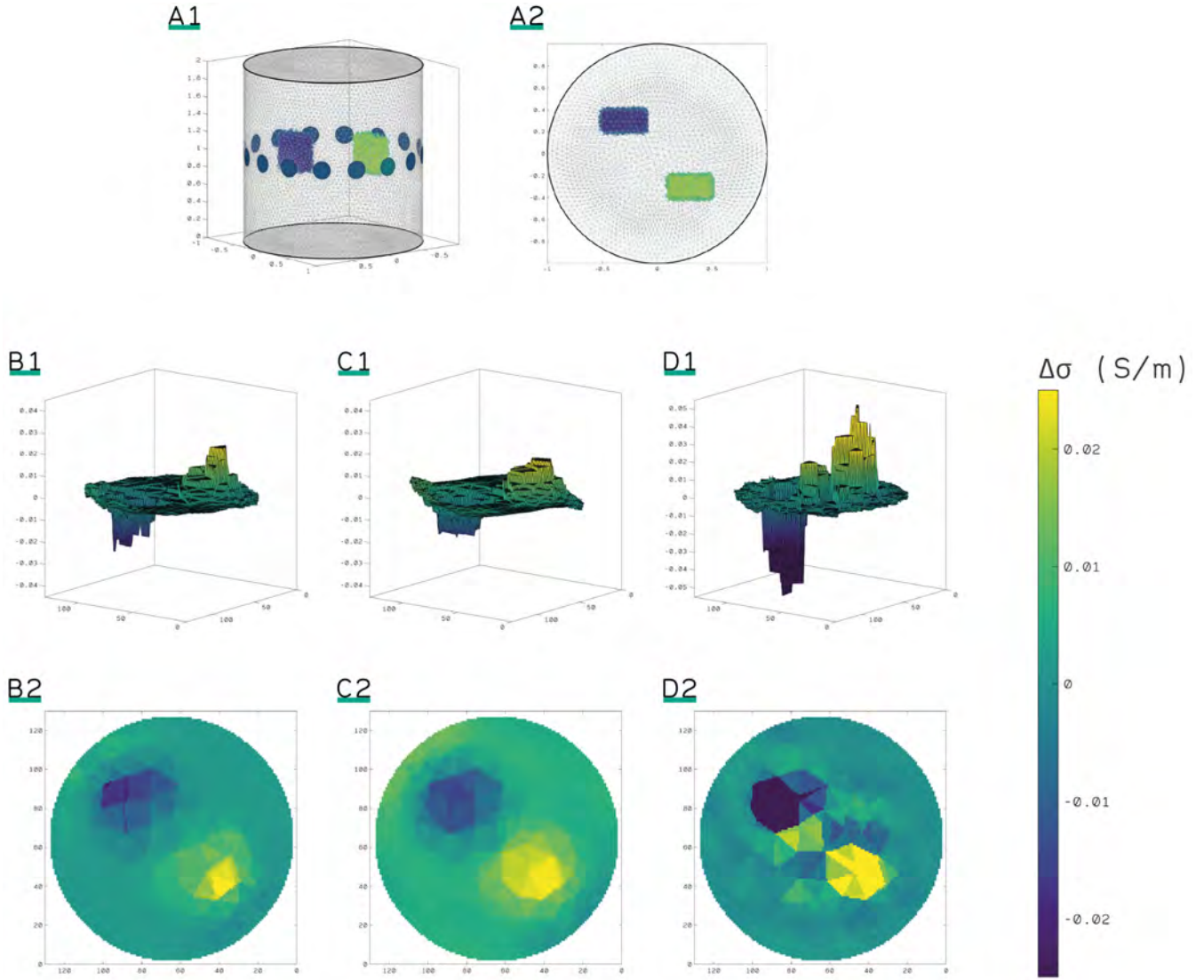
³⁹ Another good approach is to obtain a set of σ_0 parameters to best-fit Eq. 76

⁴⁰ The GN algorithm can be derived from the CG approach by defining $\beta = 0$

⁴¹ J Nocedal and S Wright. *Numerical optimization*. 2006.

⁴² As with many iterative method, the CG algorithm can be halted when the residual fails to improve or has reached an acceptable value.

Listing 1: Inverse problem solver based on the Conjugate Gradient method.



4.5.3 Comparison between regularization schemes

To illustrate the practical importance of the regularization scheme in the reconstruction process, a numerical example is presented. The VOI is a cylindrical vessel (Fig. 38 A) surrounded by a sixteen-electrodes ring, where the radius of each electrode is $r = 0.1$ m. The 2×2 VOI has a unitary homogeneous background. The FEM contains 7.5×10^3 points, 4.3×10^5 elements. A reference dataset is created by solving the forward model without inhomogeneities. Next, another dataset is calculated using the same model but considering two regions of different conductivity. The two orthotope regions are located at:

$$\begin{aligned} -0.4 < x_1 < -0.2 & \quad \& \quad +0.2 < x_2 < +0.4 \\ +0.1 < y_1 < +0.5 & \quad \& \quad -0.5 < y_2 < -0.1 \\ +0.8 < z_1 < +1.2 & \quad \& \quad +0.8 < z_2 < +1.2 \end{aligned}$$

The conductivity of such regions is 25% more or less than that of the background. In order to correctly evaluate the performance of different EIT algorithms, it is important to consider the case when noise is present. Thus, the dataset corresponding to the inhomogeneous case

Figure 38: Comparison between regularization schemes for solving the inverse problem using a time-difference One-step GN algorithm. A1. & A2. Isometric and top view of the VOI to be reconstructed with a homogeneous conductivity background, and two orthotope intrusions of high and low conductivity. Reconstructions of the change in conductivity obtained using B1. & B2. Tikhonov, C1. & C2. Laplace, and D1. & D2. NOSER regularization schemes.

Gaussian additive noise has been added, so that the Signal-to-Noise ratio is 20 dB. The algorithm employed to obtain all reconstructions is the one-step GN solver. The hyperparameter is selected empirically such that the Noise Figure (NF)⁴³ is equal to 0.5⁴⁴.

The results presented in Fig. 38 use a FEM reconstruction model of coarse resolution (3×10^3 points, 14.6×10^3 elements) and show the reconstructed conductivity changes using the three previously described regularization methods. The inverse problem is solved three-dimensionally, thus, similar to the previous numerical example, the resolution outside the ring plane is extremely poor. For this reason, the results presented show a slice taken at the middle of the sensing plane. A surface representation is useful in this case to understand how the regularization scheme affects the amplitude of the conductivity map.

As per the above theory, both Tikhonov (Fig. 38 B) and Laplace (Fig. 38 C) methods penalize the entire image, however, the latter method obtains smoother conductivity change transitions in which the inhomogeneity regions do not fluctuate. In contrast, the Tikhonov approach emphasizes the conductivity regions that are closer to the edges, making it harder to discern the true shape of the regions. In the case of the NOSER approach (Fig. 38 D), the conductivity regions are more clearly defined. However, with the NOSER scheme the presence of artefacts is more pronounced, and the amplitude of the conductivity change is twice the one from the original VOI.

In this example the resolution of the image obtained is also constrained by the reconstruction mesh. This case considers a 3D approach to reconstructions, thus, to obtain higher resolution reconstructions, it would require the use of extra computational resources to solve the inverse problem with a finer mesh. While not in the scope of this work, it is important to point out that there are different ways to circumvent this challenge, e.g. the use of backslash solvers through GPU arrays, or a dual models 3D-2D approach.

4.6 Graz consensus Reconstruction algorithm for EIT

In order to objectively evaluate the performance of different algorithms as well as its parameters, the EIT medical community developed the approach known as Graz consensus Reconstruction algorithm for EIT (GREIT)⁴⁵. GREIT aims to overcome ongoing problems in EIT lung imaging, which range from the use of out-of-date reconstruction algorithms to subjective parameter selection. Although the reconstruction procedure is successful, reconstructed images still show significant limitations in terms of resolution, contrast amplitude, and detectability, which may lead to erroneous diagnostics. Despite GREIT's main medical focus, the present work applies some of its evaluation principles.

The framework tests a reconstruction algorithm using multiple independent spherical inhomogeneities. The size of such intrusions

⁴³ Andy Adler and Robert Guardo. "Electrical impedance tomography: Regularized imaging and contrast detection". In: *IEEE Transactions on Medical Imaging* 15.2 (1996).

⁴⁴ This is a recommended value used in the EIT community to compare single ring configurations, which is comparable to the often reported values from the Sheffield Back-projection solver.

⁴⁵ Andy Adler et al. "GREIT: a unified approach to 2D linear EIT reconstruction of lung images". In: *Physiological Measurement* 30.6 (2009).

must be at least 5% of the vessel diameter. As an example, this section evaluates the horizontal performance of the previous vessel (Fig. 38 A). The evaluation consists of solving the inverse problem for 100 intrusions that travel from edge to edge of the vessel. The algorithm of choice is the one-step GN solver with a NOSER regularization scheme, and using an adjacent S/M pattern. Additive Gaussian noise corresponding to 20dB was added to all measurements. Fig. 39 shows the slices of the reconstructed images taken from the sensing mid-place.

GREIT considers the reconstructed image $\hat{x} = Ry$, where R is the linear reconstruction algorithm, and \hat{x} is a column vector representing the pixel grid of the images. The image reconstruction evaluation process starts by calculating an amplitude set \hat{x}_q that contains all image pixels greater than $\frac{1}{4}$. The threshold is chosen to detect most of the intrusion effects. Nevertheless, the threshold value does not impact the algorithm performance. Next, the Center of Gravity (CoG) is computed for both the original reconstruction \hat{x} and its amplitude threshold set to \hat{x}_q . In this case, \hat{x}_q contains all the pixels greater than $\frac{1}{4}$. The distance from their CoG to the vessel's centre is then computed, as r_t and r_q (for \hat{x} and \hat{x}_q respectively). Based on these definitions the following figures of merit for the GREIT framework are described:

- **Amplitude Response (AR).**- The pixel amplitudes ratio of the target and reconstructed image. It is defined as $AR = \frac{\sum_k [\hat{x}_k]}{V_t \frac{\Delta\sigma}{\sigma_r}}$ where V_t represents the target volume.
- **Position Error (Error).**- Position accuracy of the reconstruction. It is calculated through $PE = r_t - r_q$.
- **Resolution (RES).**- The ratio between the area of \hat{x} and the area of the whole reconstruction A_0 . Calculated as $RES = \sqrt{\frac{\sum_k [\hat{x}_q]_k}{A_0}}$.
- **Shape Deformation (SD).**- Defines the fraction of \hat{x}_q that does not fit within a circle of the same area. It is calculated with

$$SD = \sum_{k \notin C} [\hat{x}_q]_k / \sum_k [\hat{x}_q]_k$$

where C is a circle located at the CoG of \hat{x}_q .

- **Ringing (RNG).**- Corresponds to the ratio of the opposite sign image amplitude outside the C , to the image amplitude within C . The ratio is computed using $RNG = \sum_{k \notin C \& [\hat{x}_k] < 0} [\hat{x}]_k / \sum_k [\hat{x}]_k$.

The above definitions are used to compute the figures of merit for the corresponding example (Fig. 40). The desired behaviour of AR is for it to be constant for any target position. In this example, constant AR values are observed near the vessel's centre. This is expected since the areas closer to the electrodes suffer the most from ringing, which impacts the result. The ideal behaviour of PE is for it to present small

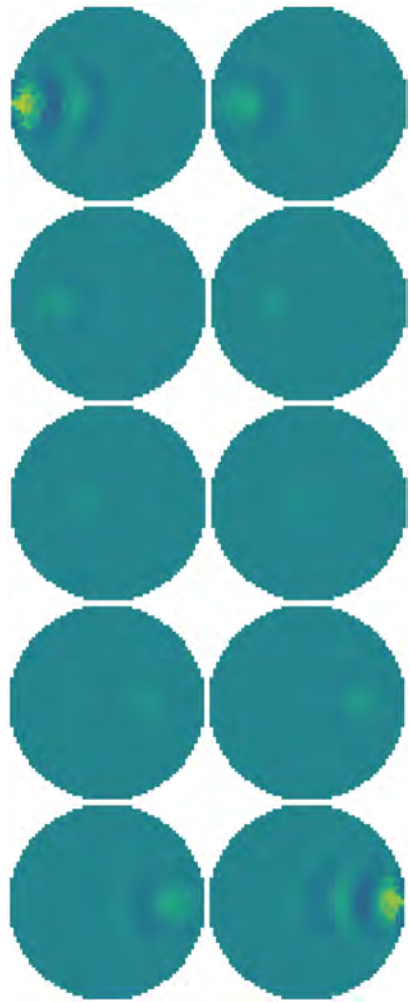


Figure 39: Image reconstructions for the evaluation of a one-step GN algorithm using GREIT's framework. The figure shows the reconstruction of the intrusions travelling from edge to edge every 10 steps.

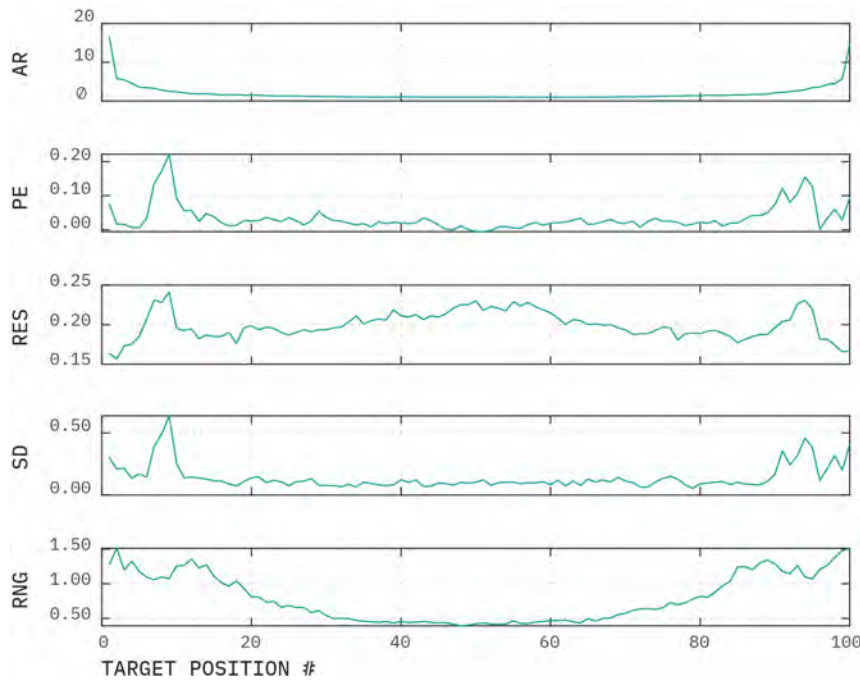


Figure 40: GREIT figures of merit for a central inclusion moving horizontally across a cylindrical vessel with a single 16-electrodes ring. All metrics are presented using Arbitrary Units.

values and variability for targets at any radial position. While the example's values PE are low, it still presents a higher variability when closer to the edges. For RES the desired figure of merit should show small and uniform values. Obtaining a uniform RES is a crucial task for any reconstruction algorithm, as a non-uniform RES leads to position errors for larger targets. Similarly, SD is expected to display small values and be mostly uniform. For the present example, the GN algorithm performs well except for the spikes near the vessel's edges. Large SD values should be avoided, as this can lead to misinterpretation of the reconstructions. Finally, the effects of ringing should always be low since high overshoot responses can create non/conductive patterns that often appear in the reconstructions as undesired artefacts. The RNG in this example is mostly uniform aside from the positions near the vessel's boundaries, where their closeness with the electrodes inherently increase the overshoot. The effect of ringing can be seen in Fig. 39 whenever the intrusion is close to the vessel's edges⁴⁶.

The aim of these figures of merit is to have criteria to characterize the optimal reconstruction algorithm. Undoubtedly, when considering all the factors that might affect the performance of a reconstruction algorithm, it is a challenging task to optimize all aspects. Nevertheless, it presents a general framework to objectively define the best parameters for certain scenarios; further avoiding subjective and heuristic parameter choice. The multi-variety complexity of the EIT inverse problem can disguise subtle implementation mistakes when creating reconstruction algorithms. Implementation errors are challenging to detect, thus, it is important to test reconstruction algorithms under both noise and noise-free scenarios, as implementation errors in a robust scheme usually lead to introducing undesired artefacts in the final images.

⁴⁶ Ringing near the edges is more pronounced when using the adjacent S/M pattern. Measurement strategies with increased skip values can show lower levels of RNG .

CONTRIBUTION

4.7 Noise performance evaluation of S/M patterns

The previous section introduced a scheme to evaluate the performance of EIT algorithms. However, to accurately compare different algorithms, it is important to carefully choose the hyperparameter which directly impacts the previously described accuracy parameters. In the presence of noise, the hyperparameter will reflect the robustness of the algorithm to noise at the cost of the resolution of the reconstructed image. For this reason, it is unreasonable to compare EIT algorithms using the same hyperparameter for all. When comparing regularization schemes, the GREIT scheme works well, nevertheless, if one desires to compare different setups, as in the case of the vertical separation of electrode rings and the different S/M patterns, the GREIT methodology does not amend for the Noise Performance (NP) characteristics of the different setups, leading to ‘unfair’ comparisons. Therefore, one approach is to select a hyperparameter based on the NP of the reconstructed images by measuring the amount of noise present in the final images.

A common approach for this type of comparison is the metric known NF, first introduced by Adler (1996)⁴⁷. The NF is analogous to a basic communications system block diagram; in essence NF corresponds to the relationship between both signal-to-noise-ratio (SNR) of the raw measurements (v) and that of the reconstructed image (img_r), thus:

$$(84) \quad \frac{SNR [img_r]}{SNR [v]}$$

where SNR is defined in terms of amplitude, thus, it is calculated as:

$$(85) \quad SNR[x] = \frac{mean[x]}{std[x]}$$

The GREIT framework uses the NF approach to test multiple λ to obtain a noise performance (NP) of the reconstructed images that matches a specific NF. Nevertheless, as further explored by Braun et al. (2017)⁴⁸, the NF metric is useful when comparing mathematical algorithms under the same S/M configuration since it fails to recreate a homogeneous NP in the presence of low noise levels which occur when using S/M patterns with skips higher than one. For this reason, it is difficult to replicate the same NP under different S/M patterns using the NF metric. Therefore, to accurately compare the S/M patterns’ NP the present work employs the \overline{SNR} presented by Braun et al. (2017). \overline{SNR} is an extension of the NF approach. It measures the SNR of various objects (n_t) within an area to obtain the average ratio:

$$(86) \quad \overline{SNR} = \frac{1}{n_t} \sum_{i=1}^{n_t} SNR_i$$

⁴⁷ Adler and Guardo, “Electrical impedance tomography: Regularized imaging and contrast detection”.

⁴⁸ Fabian Braun et al. “A Versatile Noise Performance Metric for Electrical Impedance Tomography Algorithms”. In: *IEEE Transactions on Biomedical Engineering* 64.10 (2017).

Braun's SNR calculation leads to results similar to Eq. 85. In this particular case, the signal level S is calculated from the reconstructed image without noise (\hat{x}) and the noise N in the image (img_{rn}) calculated at a specific Evaluation Zone (EZ) for k -th training targets t_k . The EZ defined by Braun et al. (2017) is the zone where changes in conductivity are expected to occur. Thus, the analysis is restricted to the EZ by using a weighting vector z , which acts as a Boolean filter that cleans the pixels/elements outside the EZ i.e. $z_k = V_{elem_k} * zone_{th}$, where V_{elem_k} is the volume of each element in the model and $zone_{th}$ is the threshold filter defining the EZ. Therefore, S is calculated using:

$$(87) \quad S = \frac{\sum(V_{elem_k} zone_{th})}{V_t} z^T \hat{x}$$

where V_t is the volume of the training target. Finally, N is the noise level that corresponds to the Root Mean Squared Amplitude (RMSA) of \hat{x}_N based on y for all t_k , which is calculated using the main diagonal of the covariance matrix filtered by z :

$$(88) \quad N = z^T diag(\mathbf{R}\Sigma_e\mathbf{R}^T)$$

One can implement the following steps to calculate \overline{SNR} :

1. Define the region of interest (ROI). The ROI should be located where there is the highest likelihood that the conductivity will change.
2. Distribute a desired number of training targets n_t with a predefined size and amplitude⁴⁹.
3. Solve the forward problem for each of the targets⁵⁰.
4. Reconstruct the images with the algorithm of choice.
5. The noise signal-to-noise level is computed for each target using an evaluation zone adapted to the position of the reconstructed object. The zone is defined from the centre of the target to the pixels that exceed one-fourth of the maximum amplitude of the reconstructed target⁵¹. The SNR is then calculated for each target in the evaluation zone using Eq. 85 depending on the desired noise characteristics.
6. Finally, \overline{SNR} is computed using Eq. 86.

Following the above definitions, the present work evaluates the noise performance of the most notable S/M patterns presented in chapter 3.0.

4.7.1 Methodology

The present study compares the traditional S/M adjacent pattern with the most representative S/M patterns presented in the previous chapter, which offer a good balance between higher sensitivity and low condition number. The compared patterns are:

- Planar protocols S1/M1, S3/M7, and S5/M7.
- Square protocols S1/M1, S5/M6, and S7/M7.

⁴⁹ The higher the number of targets the more accurate the calculation, however, this represents a greater computation time.

⁵⁰ Noise is assumed to be present in the data.

⁵¹ Adler et al., "GREIT: a unified approach to 2D linear EIT reconstruction of lung images".

For each pattern, the geometry presented in chapter 3.0 is considered under two scenarios for the distance between electrode rings: $s = 4$ cm and $s = 8$ cm. The reconstruction algorithm employed is the one-step Gauss-Newton with a Laplace regularization scheme. An adequate selection of the hyperparameter is obtained through the above described SNR approach. Therefore, first a typical NF value of 2.0 is considered⁵² to calculate the hyperparameter for this scenario. Next, the SNR of the reconstruction is calculated⁵³.

The original approach proposed by Braun et al. (2017) considers 2D geometries, and thus, the evaluation targets are placed in an EZ constrained to the height of the electrode plane. Here we expand the methodology to 3D by considering a volumetric EZ for the placement of the targets. The volumetric EZ considered corresponds to a scaling of the vessel's dimensions by 50% positioned at the core of the geometry. Since a higher resolution is expected at the vessel's edges, the area of interest explored here is the centre, where accurate imaging reconstruction is challenging. A total of 2,250 targets are introduced into the EZ of each reconstruction model to determine the adequate λ for the \overline{SNR} corresponding to S1/M1 NF. The target size employed is 5% of the main geometry radius, considering the resolution limitations explored in chapter 3.0.

As the purpose of this analysis is to evaluate the vertical enhancements from changes in electrode placement and S/M patterns, a unitary conductivity is used for the background, and a conductivity two times greater than the previous is set to all targets. Difference y data sets were generated using the homogeneous background, and using 100 targets to simulate a moving conductivity change that translates from the centre to edge of the vessel at a 30° for three z-axis positions⁵⁴ (Fig. 41) based on the vessel's height h : $h/2$, $h/4$, and $h/8$. In order to avoid committing an inverse crime, white Gaussian noise corresponding to -75 dB is added to each y data set. For each different target position 1,000 noise scenarios were created, thus, the total number of data sets generated were 30,000. The NP is evaluated by first calculating the temporal domain RMSA of the reconstructed images for each target position and their respective noise scenarios, and then obtaining the corresponding GREIT evaluation parameters. All reconstructions were conducted using a 3D pixel model of the forward model to ease the computation time. The reconstruction model is comprised of six blocks of 32×32 pixels, each reconstructing a different height of the forward model.

4.7.2 Discussion

The results (Figs. 42-48) show the evaluation of the NP for each S/M pattern for two different electrode vertical placements, and targets positioned at $h/2$, $h/4$, and $h/8$. The reconstructed slices presented⁵⁵ are located at $h/2$. The GREIT parameters are plotted for the 100 positions of the simulated moving target at the three z-axis heights for a fixed $\overline{SNR} = 2.98 \times 10^{-4}$ that correspond to $NF = 2.0$.

⁵² Value frequently selected for 3D reconstruction using S1/M1 and 32 electrodes (Adler et al. (2016)).

⁵³ This SNR is used to evaluate all the other patterns.

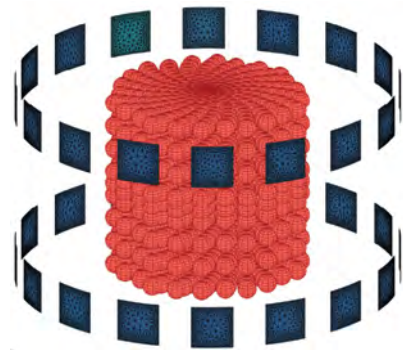


Figure 41: Higher electrode spacing geometry and its training targets.

⁵⁴ Conductivity changes at perpendicular angles are less prone to noise, thus, it can be harder to discern the effects of different configurations.

⁵⁵ As mentioned previously, all slices presented have been normalised to the maximum value of the temporal RMSA

Fig. 42 shows the traditional adjacent approach, which usually has an acceptable tolerance to noise and poor vertical resolution. The best NP case for this protocol is when the target of interest is located at the centre of the vessel with a vertical separation of $s = 2$ cm. In this case, the amplitude and resolution remains almost constant. However, the shape deformation parameter increases as the target gets close to the edges, and this is observed in the reconstructions where targets have a non-significant elongation at the sides. When positioning the target below the electrode plane ($h/4$ and $h/8$), the NP of the protocol decreases, especially in the centre of the vessel. The poor vertical resolution of the protocol can be observed in the high amplitude of the reconstructed images when the targets are located far from the electrode planes. Nevertheless, the performance starts improving at 60% of the target final destination (i.e. at the edges). For the case of $s = 8$ cm, the NP drops considerably (50 – 60%) especially for $h/2$, but this is expected as in this scenario the target is further away from the electrode planes. Similarly to $s = 2$, the NP improves when getting closer to the edge⁵⁶. In the case of low vertical target positions, the target is difficult to visualise from 80 – 91% of the trajectory. From the S1/M1 evaluation, one can observe that at lower electrode separations the system tends to overestimate the amplitude when the target is located below both electrode planes. Nevertheless, a higher electrode separation can help obtain a more accurate amplitude that represents adequately the vertical position of the target but with a low NP that can lead to artefacts around the centre of the VOI. Furthermore, while higher electrode separation can enhance the resolution of the system, the latter will start decreasing when getting closer to the edges.

⁵⁶ Improvements observed at 34% of the trajectory for $h/2$, 45% for $h/4$ and $h/8$

Figs. 43 & 44 show the NP for higher skip S/M patterns. As expected, the reconstruction algorithm performs better not only in terms of the noise present in the reconstruction, but also, an improvement in the amplitude response can be observed. Similar to the adjacent pattern, an overestimation of the target's amplitude is seen when close to the VOI's centre. Nevertheless, at $s = 4$ when reaching 39% of the target's trip, the estimation of the amplitude starts to improve. On the other hand, when the target gets closer to the edges, it becomes harder to identify, and in the case of $h/8$ the target cannot be distinguished from the noise. Moreover, at higher electrode separation ($s = 8$ cm) while the NP improves, the shape of the target suffers from deformation effects and its amplitude gets overestimated when closer to the edges. Overall, higher skips perform better than the traditional adjacent pattern, especially in the case of a low electrode vertical separation. If the vertical resolution is of no interest in a particular EIT application, the adjacent pattern is more capable of detecting targets independently of their location in the z-axis. This shows the impact in vertical resolution for planar protocols, and how larger electrode vertical separation can be detrimental to the final image reconstructions.

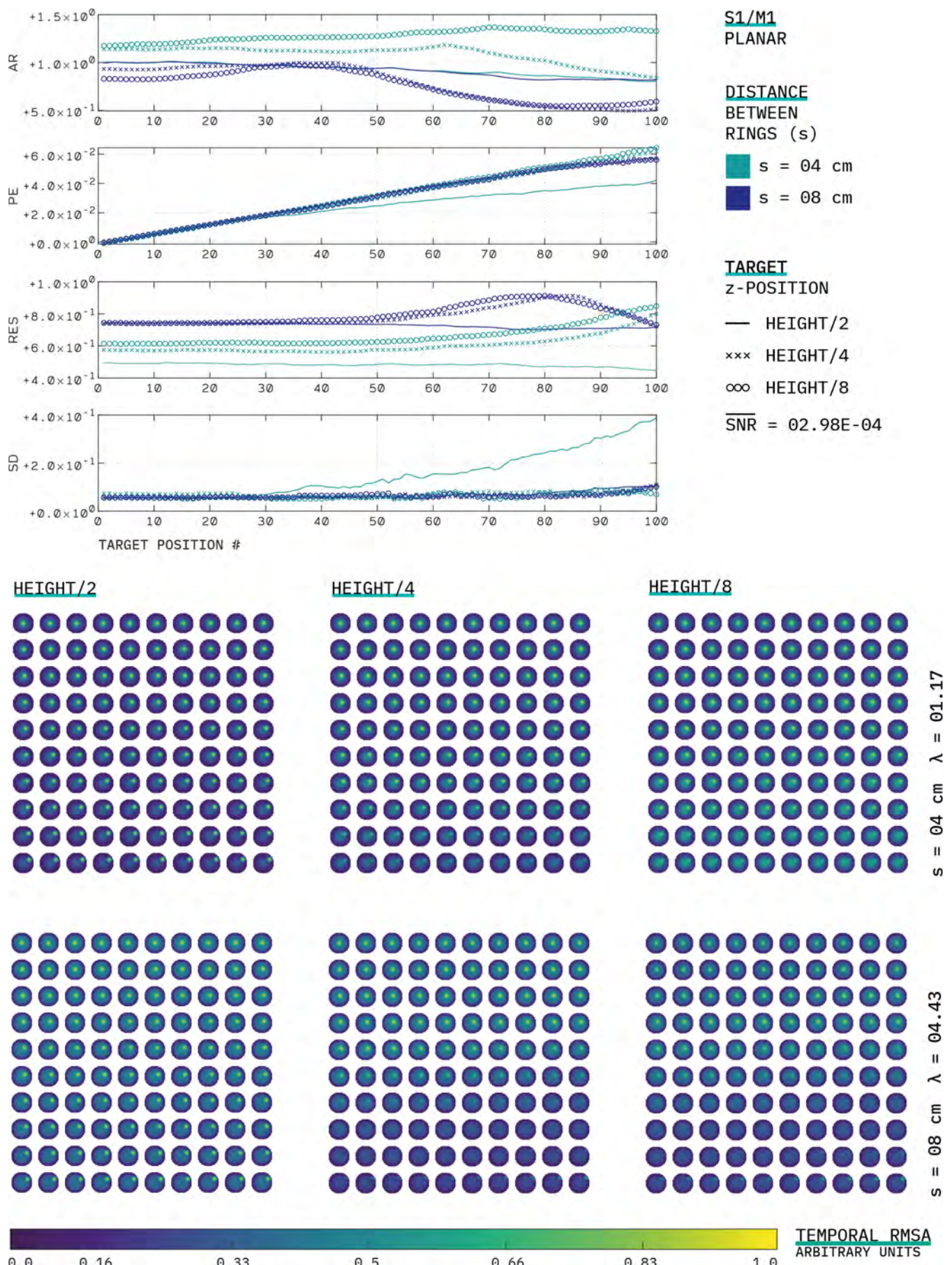


Figure 42: Planar S1/M1 NP characterisation.

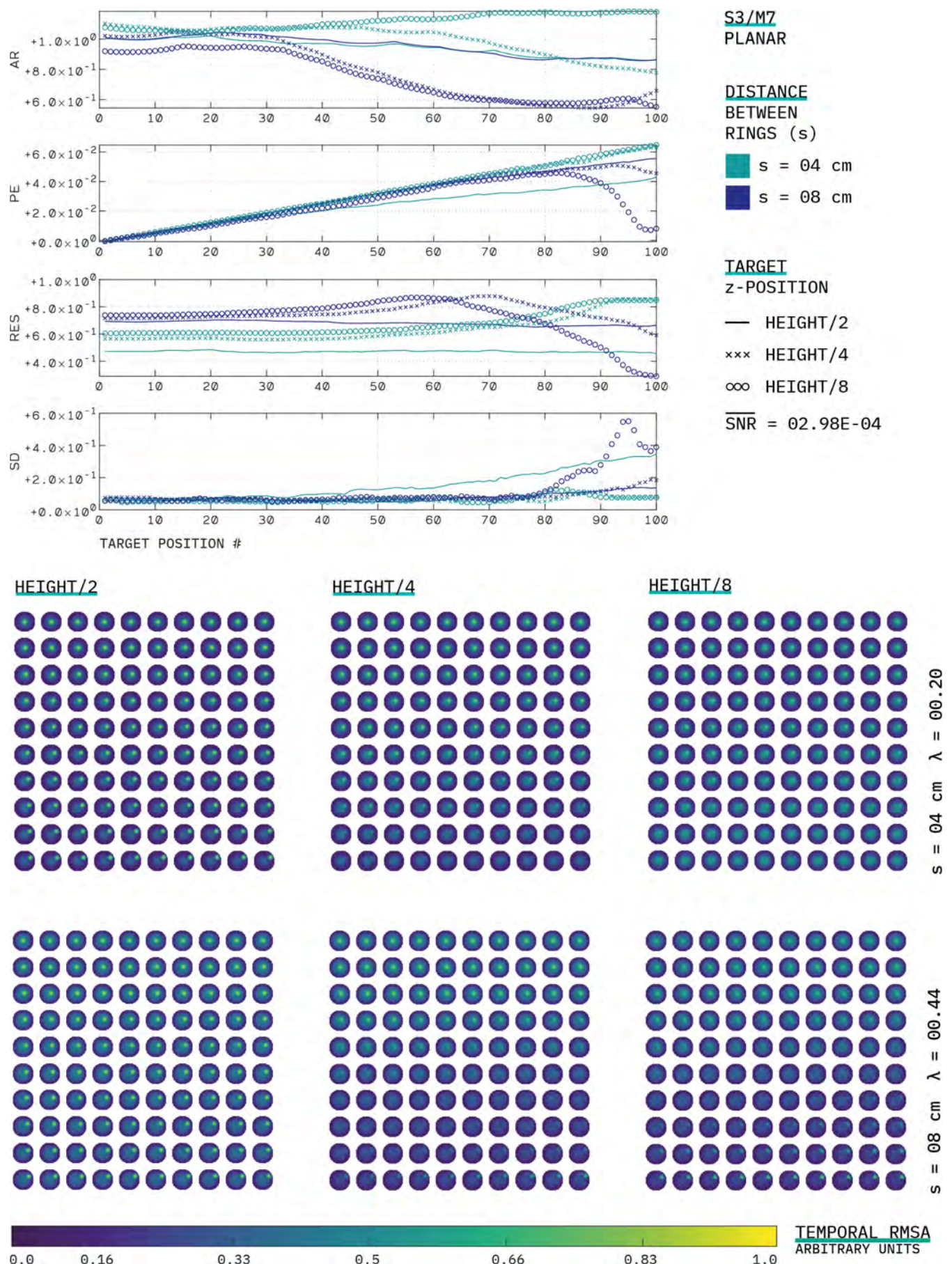


Figure 43: Planar S3/M7 NP characterisation.

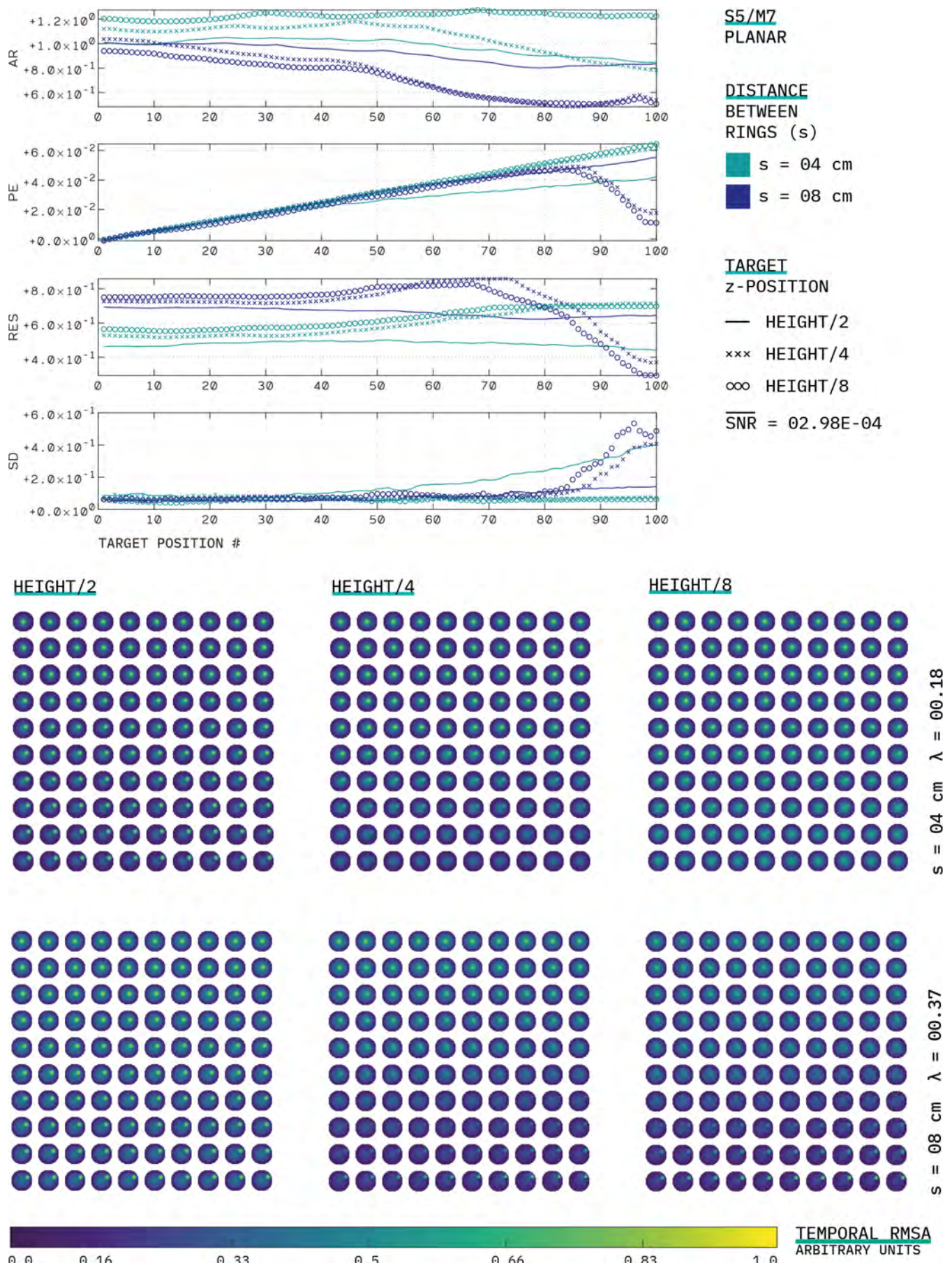


Figure 44: Planar S5/M7 NP characterisation.

The square pattern (Fig. 46-48) shows an improved amplitude estimation of the reconstructed target as the reconstructed images present a smaller amplitude when they are not located at $h/2$. However, if the target is too far away from the electrode planes (e.g., at $h/8$ with $s = 4$ cm) there is an overestimation of the target's amplitude when getting closer to the edge⁵⁷. Similar to the planar protocol when $s = 08$ cm, as the target gets closer to the edge the amplitude overshoots. In comparison with the traditional adjacent pattern, the S1/M1 square pattern provides a more continuous resolution during the target's journey. Nevertheless, when approaching the edges, the reconstructions start suffering from high shape deformation (starting at 85% – 90% of the total trajectory). With an increase in skip (e.g. S5/M6) there is an improvement in the amplitude response and the continuity of the resolution. While the resolution decreases when the separation of the electrodes is higher, and the target is at $h/4$ or $h/8$, the position error also decreases when getting closer to the edges. For the particular case of S7/M7, there is a clear difference between the reconstruction obtained with low and high electrode separation. For instance, with higher separation the amplitude response is almost constant during the target's journey toward the edge of the vessel. Furthermore, a more continuous resolution response can be observed, but like the previous patterns as it gets closer to the edge (around 80% of the trajectory) the resolution starts to drop for targets at $h/4$ & $h/8$, whereas the position error improves significantly at 85% of the total journey. Moreover, the fact that the λ values of the square pattern do not fluctuate significantly when using different electrode positions implies that there can be further enhancements to the noise performance of the system⁵⁸. While S1/M1 is more resilient to shape deformation, square patterns offer a better NP when used with higher skips.

From the previous analysis, one can conclude that the choice of S/M patterns and the location of the electrode rings is not a trivial choice and optimising this selection can drastically improve the final reconstruction. This section proposes a way to evaluate these geometrical parameters, considering a 3D approach that combines \overline{SNR} and GREIT metrics. For instance, Fig. 45 shows the reconstruction of an oval target at a 45° angle using a planar S3/M7 and a square S5/M6 with $s = 08$ cm where one can observe the overestimation of the target in the planar case, which can lead to incorrect interpretations of the reconstructed image⁵⁹. Overall, if verticality is of no use in an application, the planar protocol offers a robust solution that will detect intrusions independent of their z-axis location. On the other hand, square protocols can better distinguish the target z-location, however, they can be more prone to shape deformation and noise. In the latter case, a way to improve the noise is through the adequate positioning of the electrode rings. Furthermore, a better NP can be achieved with higher electrode ring distance when using square protocols. The results presented show the importance of considering the final application in order to optimise the geometric configuration of EIT systems.

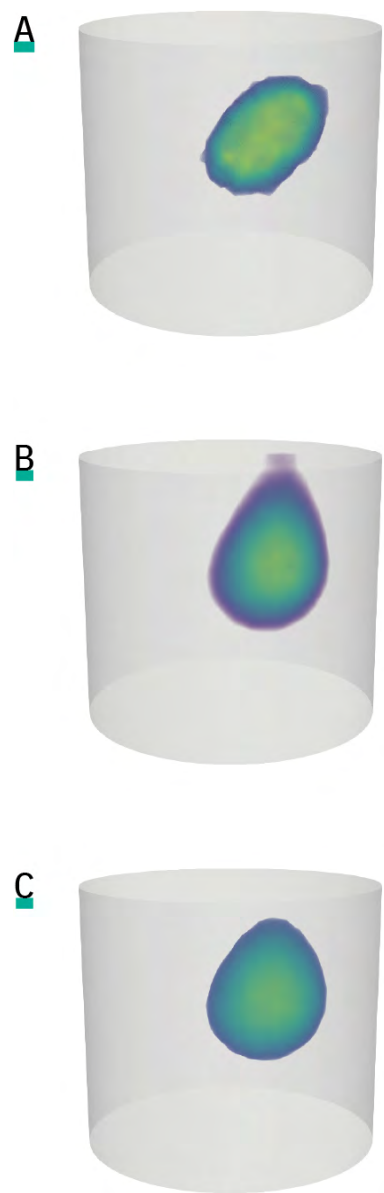


Figure 45: Comparison of the vertical resolution of **A.** an oval target at a 45° for a **B.** planar S3/M7 and a **C.** square S5/M6 protocol.

⁵⁷ At approximately 60% of the trajectory for S7/M7, and 30% for S1/M1 and S5/M6

⁵⁸ Typically, as λ increases one can observe improvements in the SNR at the cost of downgrading the resolution.

⁵⁹ The reconstructed images use the previously found λ values to ensure the same NP.

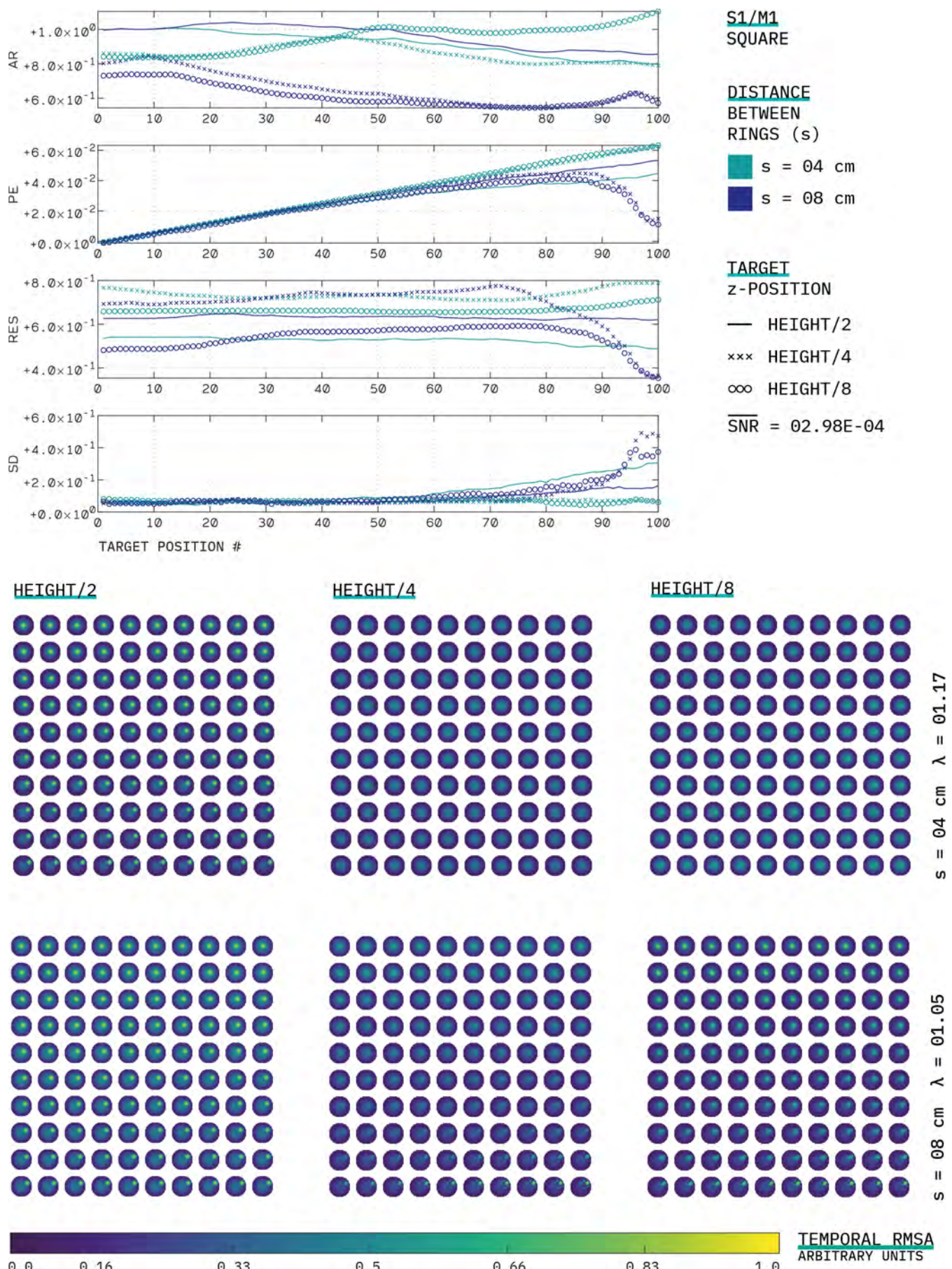


Figure 46: Square S1/M1 NP characterisation.

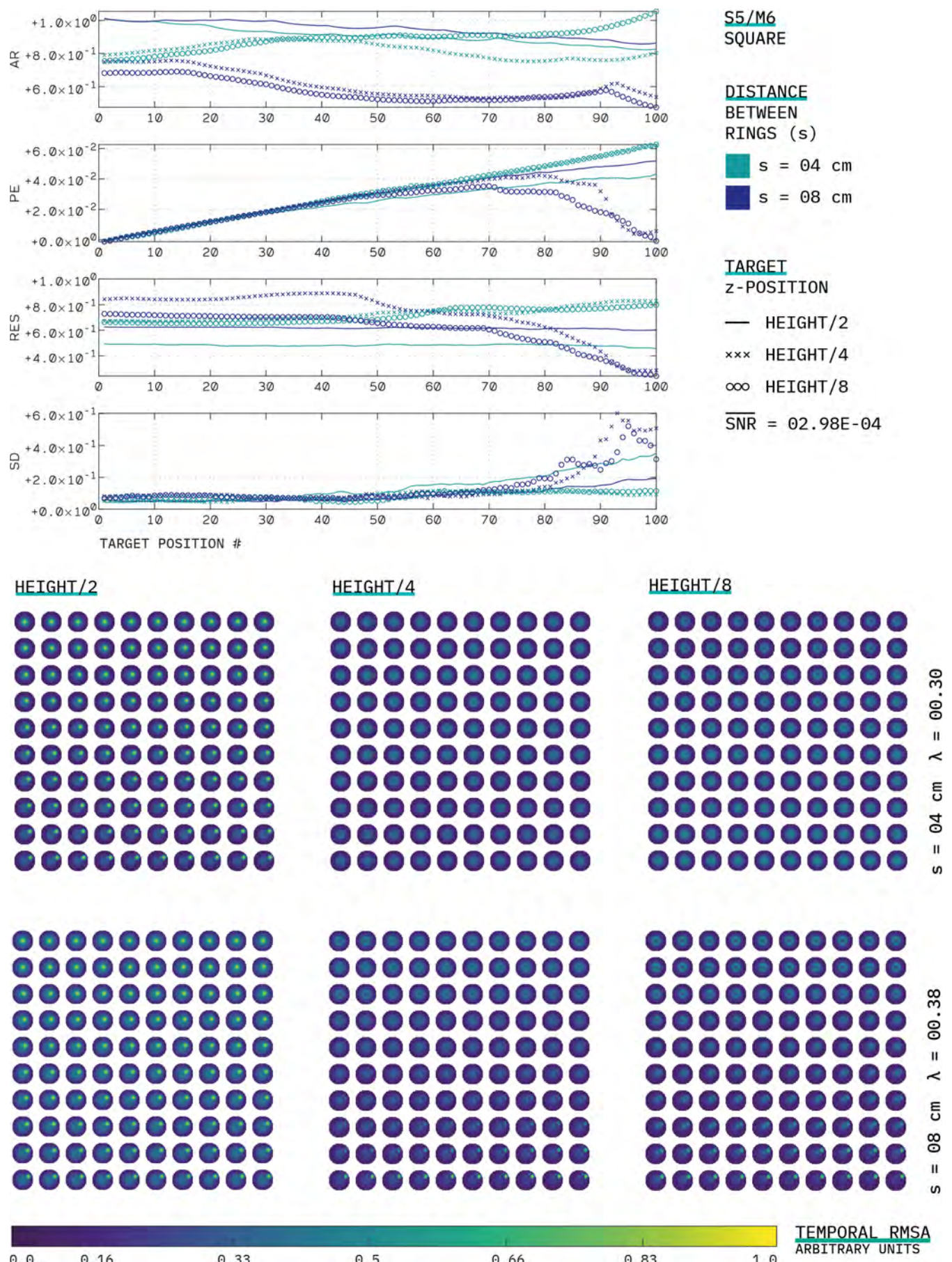


Figure 47: Square S5/M6 NP characterisation.

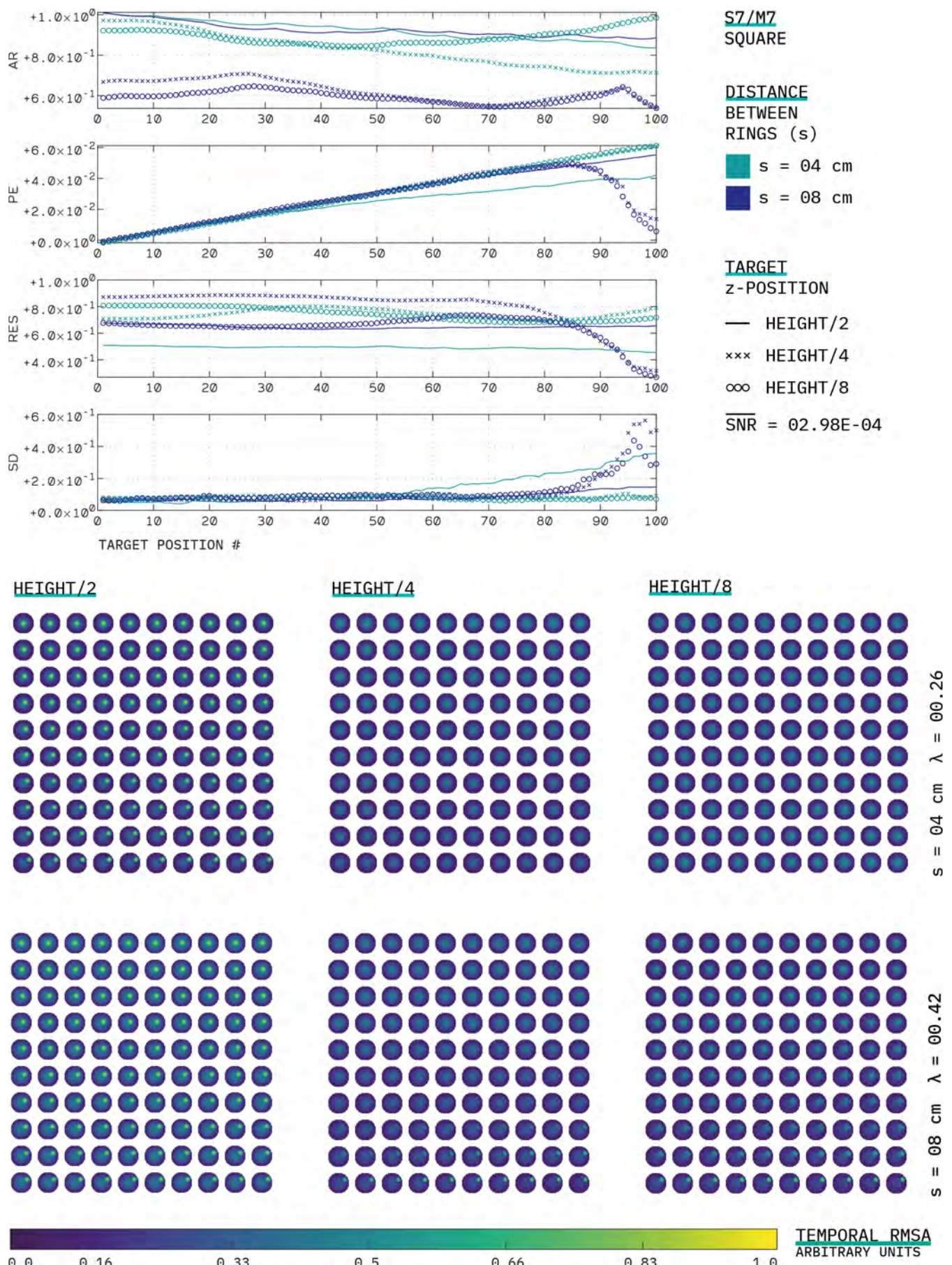


Figure 48: Square S7/M7 NP characterisation.

SMART RHIZOTRON

THE VALUE of incorporating root system traits into breeding programmes has been proved since the 1970s¹. However, despite understanding the value that these traits can provide to global productivity, we still have not fully overcome the challenges of measuring roots.

Therefore, we need to take advantage of the current technological advancements to ease and speed up root phenotyping. This chapter proposes the use of EIT as a phenotyping platform that fits the definition of a modern plant phenotyping methodology. While the technique is still used currently in a diverse range of areas (particularly in medicine), the literature corresponding to EIT design concepts is scattered into different topics and often relies on old hardware. In this chapter, a description of the steps taken to design a smart rhizotron is presented, from the analogue circuitry, electrodes design, to the software implementation. The chapter starts by explaining the most common impedance measurement techniques, followed by the evolution of the hardware presented in this work. Next, the chapter discusses the limitations of the first design, arguing that it requires adjustments to work under the low-impedance circumstances; therefore presenting an enhanced design. Afterwards, the inner workings of the system's shell is explained. The chapter concludes by describing the IoT scheme proposed for the system, thus creating a Smart Rhizotron.

"The challenge is to develop systems for non-destructive root phenotyping to accurately reflect and capture the RSA" Paez-Garcia et al., 2015

¹ Saoirse R. Tracy et al. *Crop Improvement from Phenotyping Roots: Highlights Reveal Expanding Opportunities*. 2020.

5.1 Measuring impedance: two v. four points

For simplicity's sake, let us start analysing the simple task of measuring resistance². The electronic devices used to calculate the electrical resistance of a material (or circuit) are called ohmmeters and are based on Ohm's law, $V = IZ$.

² $Z = R + iX$.

TWO-TERMINAL SENSING

The principle behind ohmmeters is the use of an internal current source to force a test current through the component under study, and then measure the voltage generated across the component (Fig. 49 A). Next, depending on the type of meter used, it can either move a measurement needle (analogue meter) or it will calculate the resistance and display the result on a screen (digital meter). This type of measurement can be performed by most DMMs, and is typically used with values above the milliohm range that do not require high-accuracy. The reason behind this lack of accuracy comes from the topology employed, as

observed in Fig. 49 A the voltage measured occurs across both its own terminals and the component's ends. As a consequence, there will be a voltage drop within the connection points (r_w) that will be present in the final resistance calculation. For instance, just considering the loop of the subject under study, Z_{unk} , the total impedance would be:

$$(89) \quad Z_{total} = r_w + Z_{unk} + r_w$$

Depending on the design of the meter and the value of r_w , their detrimental effect can be negligible. Typically, since r_w is considered to be in the milliohm range (10^{-3}), their effect can be ignored when measuring large resistances. However, when measuring low resistance values, the error that they introduce needs to be mitigated.

FOUR-TERMINAL / KELVIN SENSING

The Kelvin sensing strategy is more akin to how one would typically solve ohm's law. This approach involves three main elements (Fig. 49 B): an excitation source (e.g. battery), a voltmeter, and an ammeter. The excitation source, in series with the sample, generates a current flow, while the voltage generated is measured directly across the sample. Usually, voltmeters have high impedance inputs, which means that there is almost no current flowing through them. For this reason, a high degree of accuracy can be achieved during the calculation of the resistance, as the total measured resistance corresponds only to the sample and is independent of the leads' impedance. Consequently, the resistance is deduced by applying ohm's law directly.

Currently, there are single-chip solutions in the market that can measure impedance reasonably accurately. However, most single-chip network analysers (e.g. AD5933) employ the two-terminal ap-

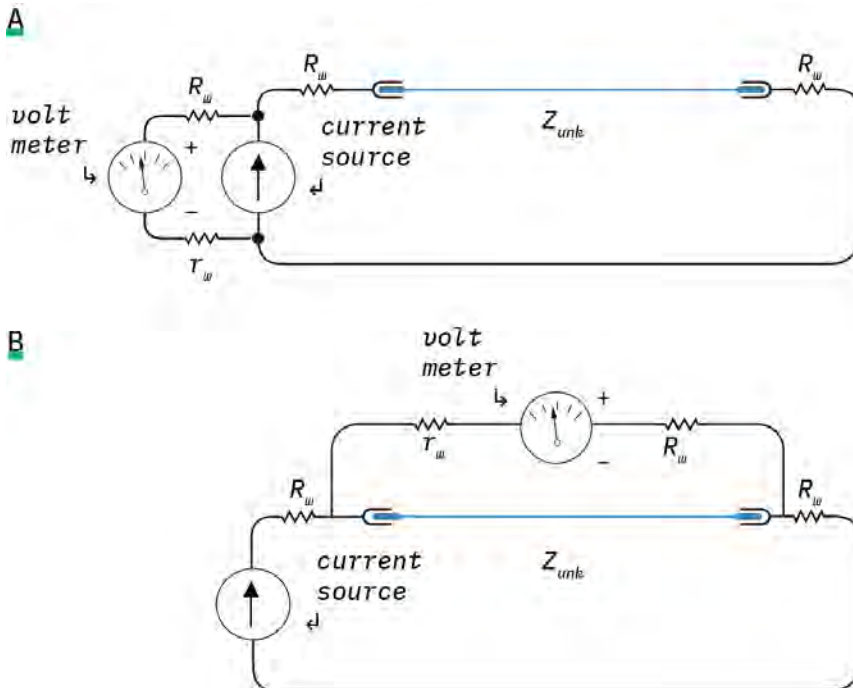


Figure 49: A. Two terminal impedance measurement method, and B. Kelvin measurement technique

proach to measure impedance. Similar to the approach previously mentioned, these chips measure impedance by exciting an unknown impedance (Z_{unk}) with a known voltage at a defined frequency, then measuring the current through Z_{unk} , and calculating both impedance components (real and imaginary) through the calculation of their respective Discrete Fourier Transform (DFT) coefficient. The previous operation can be repeated through different stimulation frequencies to generate a spectroscopic profile of the sample under study. However, most of the time, this excitation signal has a DC bias. While for typical application, this might not be a problem, it may electrochemically alter the measured medium at particular interfaces between metal electrodes and aqueous solutions³.

Researchers have developed solutions to acquire tetra polar measurements with the AD5933^{4,5,6,7}. Nevertheless, a better solution to this approach has been presented in the development of a new single-chip solution by Analog Devices Inc., the ADuCM350. The ADuCM350 is a high precision, meter-on-chip for portable, low-power system applications. It was designed for high precision potentiostat, current, voltage and impedance measurement capabilities. Thus, the characteristics mentioned above make the ADuCM350 a reasonable candidate for the EIT system presented in this work.

5.2 Analogue front-end

The core element of the system presented in this work is its Analog Front-End (AFE). Recapitulating the theory exposed before, the act of measuring impedance is a three-step process:

- Stimulate the object under study with an electrical current.
- Measure the response to the stimuli.
- Process the data to present a final impedance value.

STIMULATION

In the case of single-chip solutions, all of these actions are carried out by a single microcontroller, using what is known as the AFE. The ADuCM350 carries the first step, employing a waveform generator that can be programmed to create sine, trapezoid and custom shaped waves⁸. To output the actual waveform, the block uses a Digital-to-Analog Converter (DAC). The frequency can be adjusted using a 26 bits control word (*FCW*) that can be calculated using:

$$(90) \quad f_{out} = f_{clk} \times FCW / 2^{26}$$

this corresponds to a frequency resolution of approximately 0.25Hz using a 16MHz operating clock (f_{clk}). In terms of the amplitude, the DAC range is $-800mV / 800mV$ effectively reaching a maximum 1.6V amplitude swing. The system uses a 12-bit DAC with an amplitude resolution of $1.6V / 2^{12} = 390.63\mu V$.

³ Sverre Grimnes and Ørjan Grøttem Martinsen. *Bioimpedance and Bioelectricity Basics*. 2008.

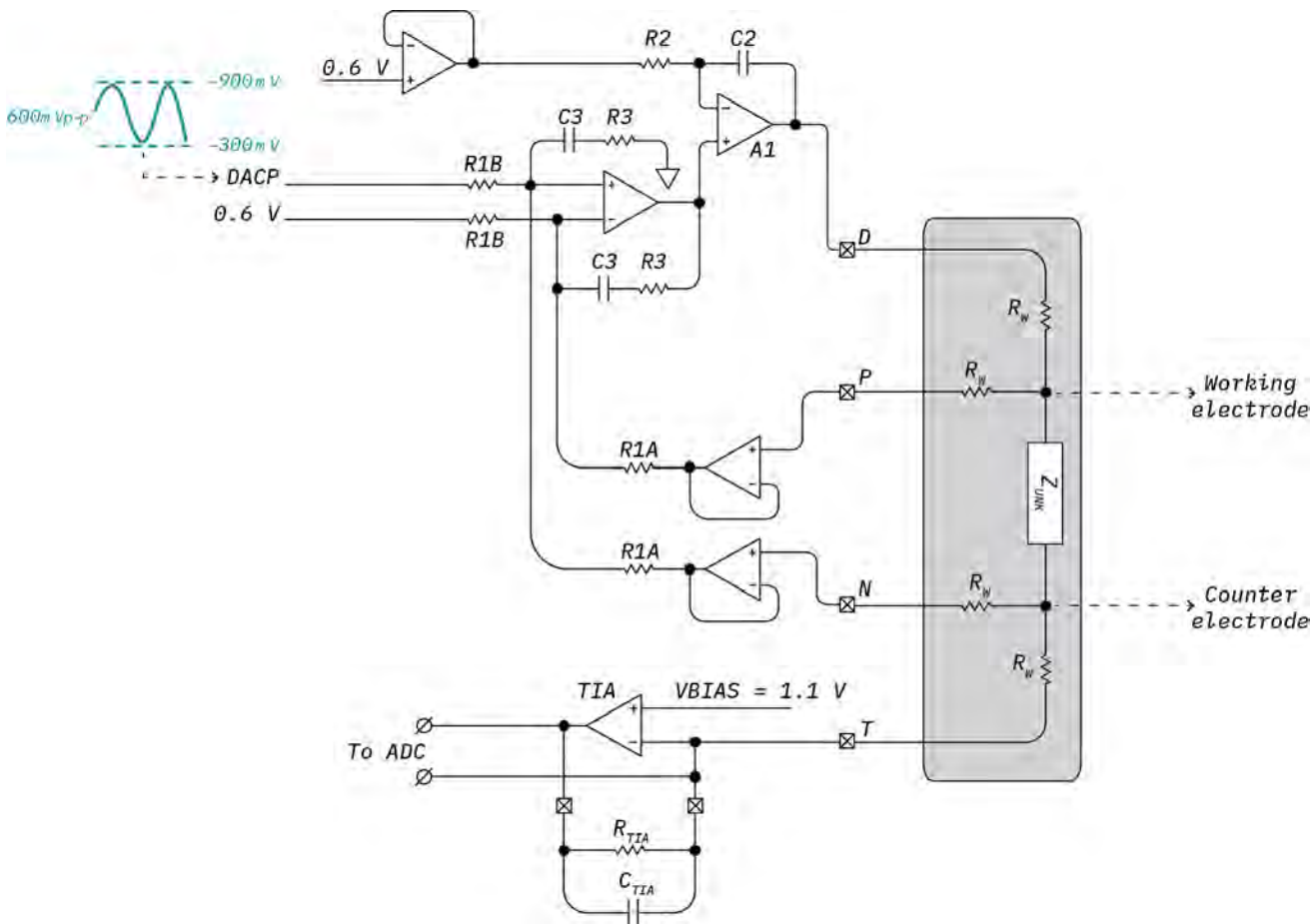
⁴ C. Margo et al. “A four-electrode low frequency impedance spectroscopy measurement system using the AD5933 measurement chip”. In: *Physiological Measurement* 34.4 (2013).

⁵ Antonio Ansede Pena. “Final Degree Thesis A Feasibility Study of the Suitability of an AD5933-based Spectrometer for EBI Applications”. In: *Analyzer* (2009).

⁶ Andreas Barthel et al. “Interfacing the AD5933 for bio-impedance measurements with front ends providing galvanostatic or potentiostatic excitation Related content Electrodes-the challenge in electrical characterization of biological material”. In: *Journal of Physics: Conference Series* 407 () .

⁷ Fernando Seoane et al. “An analog front-end enables electrical impedance spectroscopy system on-chip for biomedical applications”. In: *Physiological Measurement* 29.6 (2008).

⁸ The analogue front end can be run in parallel without blocking the data processing in the chip, allowing for asynchronous sampling.



MEASUREMENT

Figure 50: AFE main excitation loop.

To explain the AFE's stimulation loop (Fig. 50), let us express the following considerations:

- As per recommendation of the manufacturer, the final application should only use between 1/8 to 7/8 of the total DAC range; which means that the maximum swing is 1.2V.
- To enhance the performance of the system against noise, the system uses a common mode set by the positive input of the Transimpedance Amplifier (TIA) set at 1.1V internally. Therefore, the swing goes from 500 mV to 1.7V.

The impedance measurement process starts by setting an excitation voltage across Z_{unk} through the excitation nodes D & T. This particular voltage is set to be two times larger than the differential DAC output voltage. The gain required to increase this differential voltage is set by the ratio between $R1B$ and $R1A$. Moreover, the feedback capacitors and resistors, in conjunction with the gain from the stimulation buffer (A1 & A2), place complex zero in the loop to increase the gain excitation frequencies (representing the typical function of a Proportional-Integral-Derivative (PID) controller). As the stimulation and sense (nodes P & D) differ, it provides an accurate method of controlling the voltage across Z_{unk} through the wire resistances (R_w). In other words, Z_{unk} is sensed differentially by the P and N nodes. Both nodes are sent back into the feedback loop of the stimulation

stage through an instrumentation amplifier. The stimulation buffer forces the output voltage on D to be equal to the differential voltage across Z_{unk} . The sensing nodes present a very high input impedance that guarantees no current flow through these lines. The voltage across the sensor sets up an impedance dependent that flows through the TIA. Next, the TIA converts the electrical current to a voltage through an external resistor (R_{TIA}). Finally, the resulting voltage is measured by the ADuCM350's Analog-to-Digital Converter (ADC). Thus, the governing equations for the stimulation procedure are:

$$(91) \quad I_{TIA} = \frac{(V_P - V_N)}{Z_{unk}}$$

$$V_{ADC} = I_{TIA} \times R_{TIA}$$

PROCESSING

The measurement acquisition process ends at the ADC receiving end. The data going through the ADC can be obtained using three methods: raw data, through the supply rejection filter, and through the internal DFT engine⁹. The present work employs the on-chip DFT engine, which performs a 2048 point single frequency DFT. In essence, the engine takes the ADC input and returns a complex number corresponding to the real and imaginary parts of the measurements. To be more specific, both the sinusoid generator and the DFT engine are based on the same phase accumulator, which allows the DFT to start at any given time n , generating a magnitude and phase shifted from the current sinusoid generator phase in the process. The ADC data is first windowed using a Hann function. These processes ensure that the system is coherent by minimising the spectral leakage¹⁰ of the DFT process. Then, the DFT equation is applied to the windowed data with the following format:

$$(92) \quad R = \sum_n^{n+2047} x(i) \cos\left(2 \pi i \frac{f_{out}}{f_{ADC}}\right)$$

$$I = \sum_n^{n+2047} x(i) \sin\left(2 \pi i \frac{f_{out}}{f_{ADC}}\right)$$

here R & I correspond to the real and imaginary components of the measurement taken. Therefore, the magnitude and phase of the measurement can be calculated through the basics of complex analysis and vector calculus:

$$(93) \quad \text{Magnitude} = \sqrt{(R^2 + I^2)}$$

$$\text{Phase} = \text{atan}(I/R)$$

The whole measurement process is operated using a binary sequence, which controls: the wave generation, the switching of sensor channels (D, P, N, T), and the evaluation of impedance. The

⁹ The essence of the Fourier transform (both in its continuous and discrete form) is to decompose a signal into its pure frequencies to have a better understanding of its composition. The DFT takes discrete time domain data and converts it to the frequency domain.

¹⁰ Having a defined frequency resolution (which is the minimum change in frequency that the DFT can detect and is equal to $f_{sampling} / N_{samples}$) it is possible to encounter the effect of spectral leakage when the input signal is not an exact multiple of the system's frequency resolution. When this happens, the Fourier analysis can be inaccurate as it can introduce frequency elements that are indistinguishable from those corresponding to noise.

ADuCM350 has an internal switching matrix that enables the nodes to connect to a calibration resistor channel, and to an auxiliary channel. Using the former channel, one can measure the impedance of a precision resistor to use as a reference for subsequent measurements.

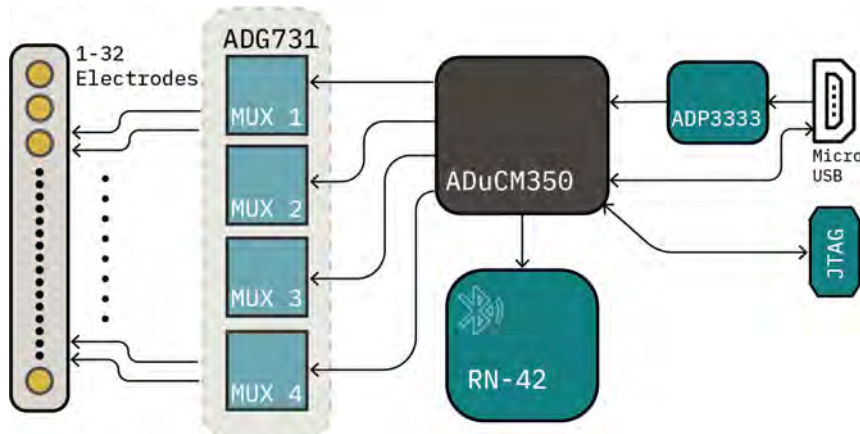
To guarantee stability, high accuracy and repeatability, it is important to optimise the selection of C_{TIA} , R_{TIA} and the calibration resistor R_{CAL} . The goal is to maximise the usage of the 16-bit ADC range. The present work considers that there are no electrical current limitations^{11,12}. The maximum allowable swing for the DAC output and ADC input is $600mVp$ and $750mVp$ respectively. Therefore, the following steps were followed to calculate the appropriate values for the previously mentioned variables:

- R_{CAL} should be close to the expected minimum value of Z_{unk} . In turn, a larger signal will go through the DFT engine during the calibration stage, hence, improving accuracy and repeatability.
- R_{TIA} is calculated by estimating the highest current that can go through the TIA: $I_{TIA} = 600mVp/R_{CAL}$, and therefore one can calculate: $R_{TIA} = 750mVp/I_{TIA}$.
- Finally, to prevent the TIA from oscillating and improve its anti-aliasing performance C_{TIA} must be optimised, using the maximum working frequency of the system: $C_{TIA} = 1/2\pi f R_{TIA}$.

The above process is a summary of the essential impedance acquisition through the main excitation loop. Nevertheless, to ensure the quality of the data acquired there are additional steps that the system takes into consideration. The latter will be discussed in the next sections.

5.3 pEIT: Portable EIT System

The ADuCM350 by itself provides a single on-chip impedance measurement system that could be used as a single EIT system. As mentioned in the previous section, the chip has a switching matrix that can redirect the nodes to eight different positions with certain limitations. Meaning that by itself, the ADuCM350 could work as an 8 electrode EIT system¹³.



¹¹ For medical applications this might be critical, as there are guidelines to ensure that the stimulation injected is not harmful.

¹² This consideration also means that a higher signal-to-noise ratio is attainable by increasing the amount of swing into the ADC from the TIA.

¹³ For most applications this number of electrodes does not offer the best resolution possible for the intended purpose.

Figure 51: pEIT block diagram.

Traditional EIT systems achieve the control of multiple electrodes through relay arrays or cross-point switches that enable the system to achieve different S/M patterns. One of the biggest advantages of this type of switching methodology, is that the signal going through them remains almost unaltered. The effect is due to the switch mainly being a conductive component with a low ohmic value. On the other hand, their size can be a significant disadvantage for portability.

Often, these types of switches rely on a type of mechanical action that ultimately adds to the time the switch takes to change its state. When trying to reach the aim of using EIT as a phenotyping technique, scalability and portability must be taken into consideration. Therefore, to reach the previous purpose and to expand on the amount of electrodes that the system can use, the present work employs an array of Solid-State (SS) Multiplexer (MUX) Integrated Circuit (IC)s in the design of the EIT system for the present work.

The first iteration of this endeavour was the portable EIT (pEIT) system. The central core of pEIT's design is the ADuCM350, using four SS multiplexing through four ADG731. Each SS MUX is in charge of redirecting one of the sense nodes to one of the 32 available electrodes (Fig. 51). In terms of communicating with the system, the user can choose between a traditional JTAG interface and a classic Bluetooth module that handles data transmission wirelessly. The PCB was manually routed in two layers (with dimensions 92×76 mm), considering the in-house rules for production at The University of Manchester. In turn, the design had some limitations. Ideally, the ADuCM350 requires separate analogue and digital ground planes¹⁴.

Despite the limitations in the design, the pEIT system helped to understand the pitfalls of the early concept. As per the description of the excitation loop, pEIT uses a PID controller that regulates the voltage between two terminals of the object under study. This turned out to be one of the drawbacks of the early system. Assuming that the impedance under study is completely unknown to the user, this would mean that under low impedance conditions the system could go out of range, performing badly at the task of maintaining a certain voltage within the object under study. In other words, the ADC would saturate under considerable low resistance loads. The user could easily mitigate this effect by stimulating the target with an attenuated voltage signal. While this process is simple to execute when having one single impedance under study, it can be a more difficult task when dealing with multiple measurements from different S/M patterns. Furthermore, this approach would require the main measurement algorithm to detect the status of the ADC and attempt to adjust the driving voltage automatically. An alternative approach is to fix the maximum current that can go through the system, to ensure that even under low impedances the system's ADC would not reach saturation. The before-mentioned approach led to the creation of the second version of the system, SpEIT.

¹⁴ Most signal traces were placed on the top, and the bottom layer was mainly used as a general ground plane.

5.4 SpEIT: Spectral EIT system

Instead of using the ADuCM350 high precision excitation loop, SpEIT differentially senses the voltage across Z_{unk} with an instrumentation amplifier, and its output is fed back to the central core using one of its auxiliary channels (Fig. 52). The core's 160 kSPS (samples per second) DAC then reads the measurement. As described previously, the obtained data goes through a 2048 sample point DFT to obtain the real and imaginary components of both voltage and current.

The in-amp used for the next iteration of pEIT is a general purpose amplifier that can change its gain with a single resistance. The AD8226 employs the typical three operational amplifiers' topology, which preamplifies the differential signals and then removes the common-mode voltage with a difference amplifier. The amplifiers use the TIA V_{bias} voltage as reference to the common mode of the system to level-shift the output.

SpEIT's AFE has been optimised to supply approximately $900\mu A$ using a current limiting resistor. The TIA feedback resistor is calculated by making an assumption of the minimum resistance that the system can measure; this ensures that the TIA's full range is used, thus, it can be calculated through:

$$R_{TIA} = TIA_{range} / I_{TIA}$$

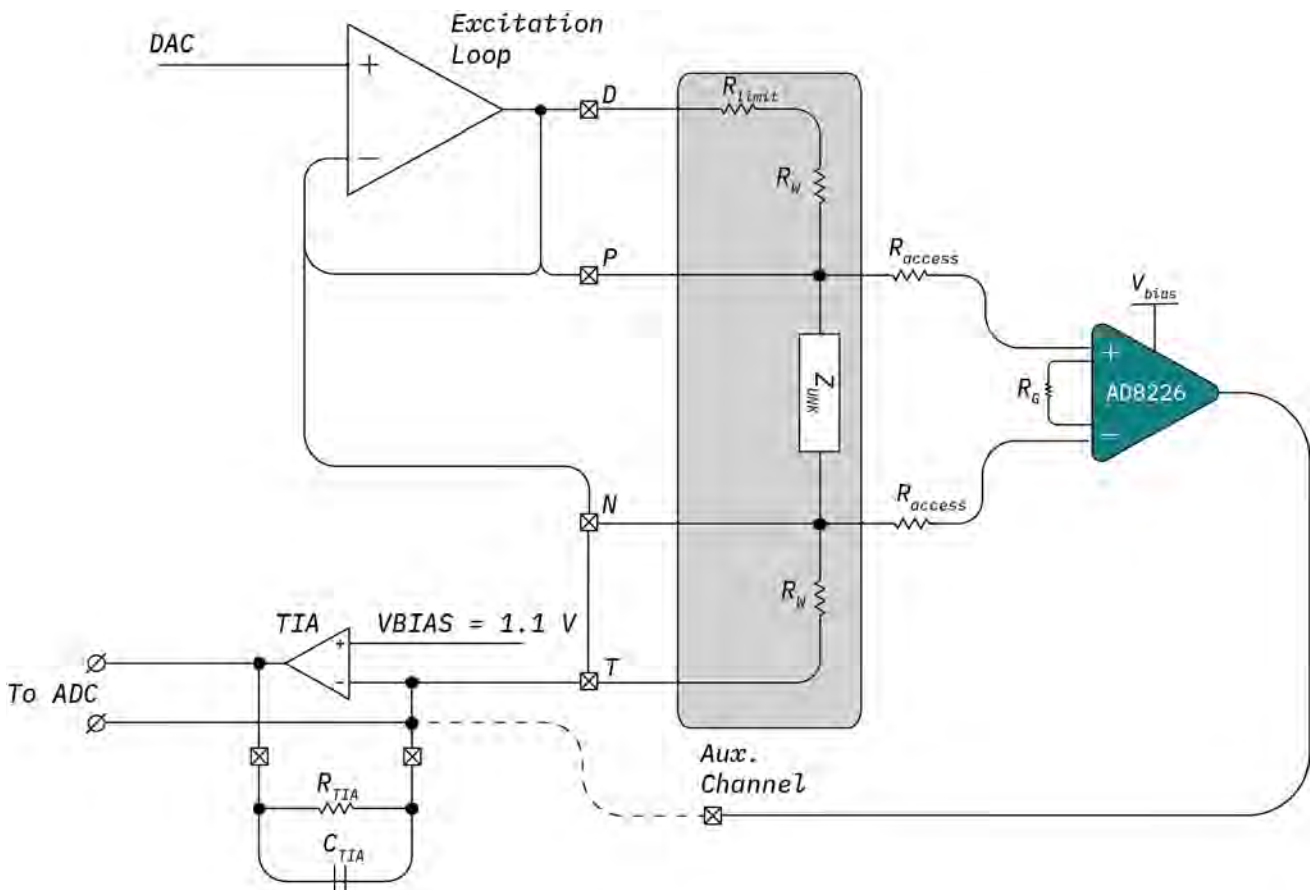


Figure 52: SpEIT improved excitation loop.

A safety factor, SF , is used to ensure the ADC does not overrange. The safety factor must be applied to the maximum peak current seen by the AD8226:

$$I_{AD8226\ pk} = I_{out}/SF$$

thus, the maximum measurable impedance will be:

$$Z_{unkMAX} = I_{AD8226\ pk} \times (750mv/SF)$$

Based on SF , the AD8226's gain can be determined by identifying the amplifier's V_{in} , thus, RG can be calculated through:

$$RG = 49.4k\Omega/(G - 1)$$

The gain going through the system must be considered when calibrating the auxiliary and TIA channels. In this way, the difference between the voltage and current gain corresponds with that of the SF .

Alongside the aforementioned improvement of the excitation loop, SpEIT's design (Fig. 53) allows users extra flexibility. The six-layer board (dimensions 70×36 mm) provides a spectroscopy output, which means that users can take EIS measurements without the extra circuitry of the multiplexers. Moreover, the board has four expansion connectors that can add multiplexing capability (up to 64 electrodes). The communication can be done now through USB-type C and using a Bluetooth low energy module (RN-4871)¹⁵. Protection diodes (SP3004) have been added to all measurement outputs, and an I²C interface for status reports (or for other interfacing purposes) is available on board. The board also provides selection resistors, so the user can choose between ADuCM350's standard and the improved measurement scheme. If needed, DC isolation capacitors can be added on board to facilitate bioimpedance measurements (e.g. for use in medical applications). SpEIT provides a low-cost solution and flexibility for not only plant phenotyping, but also diverse applications. This extra flexibility allows the user to use the spectral output for high precision impedance measurements, and the MUX output for EIT measure-

¹⁵ pEIT used the RN-42 Bluetooth module, which uses the classic Bluetooth communication protocol. The RN-4871 is better suited for the internet-of-things applications, as the data transmission is optimised to work using low energy.

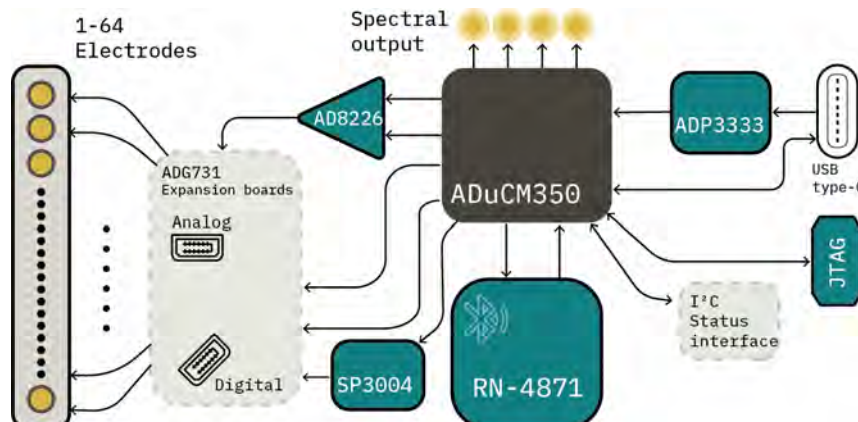


Figure 53: SpEIT block diagram.

ments with a high degree of precision too. However, passing the signal through the MUXes does have some effects.

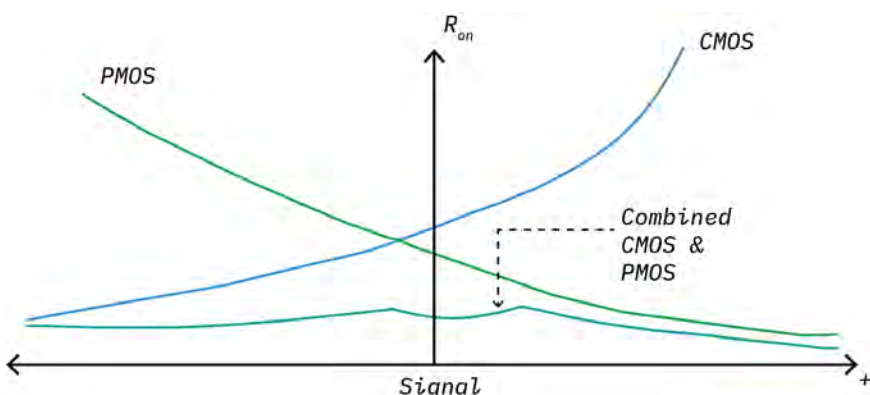
5.4.1 Signal integrity

As mentioned above, the choice between passive (electromagnetic switches, relays) and active switches (CMOS, MOSFET switches) is going to affect the behaviour of the signal going through the excitation loop. Ideally, the characteristics of any switch should be: no switching delay, capable of handling small and large signals, infinite off-resistance and no on-resistance. As one can expect, neither the passive nor active switches have all of these characteristics; but despite this, both have an effective combination of attributes suitable for specific applications. SpEIT uses monolithic CMOS technology. The biggest advantages of SS technology are its small on-impedance and fast switching capabilities. On the other hand, because it is composed of active elements, the impedance when the MUX is on will change depending on its input. To mitigate this effect, most SS MUXes employ bilateral CMOS switches¹⁶.

The use of bilateral switches not only reduces the on-impedance, but also lessens the variation due to the input signal (Fig. 54). The before mentioned figure shows the advantage of bilateral switches, which make the variation of the on-resistance more linear; this effect is also known as the on-resistance flatness¹⁷. The on-resistance is also heavily related to distortion, and therefore, an MUX with low values of on-resistance should be preferred. This distortion can be understood as the effect that the resistance has at the output of the MUX.

The present work considers the equivalent circuit of a single bilateral switch (Fig. 55). Examining the DC conditions when the switch turns on attenuation of the input signal will be observed as the wire resistance in both the source and drain, R_W , will be in series with¹⁸ R_{ON} . Furthermore, the leakage current, I_{LKG} , will flow through the before mentioned resistance that is in parallel with a load¹⁹.

Therefore, the voltage measured at the load can be expressed as:



¹⁶ A bilateral switch is composed of both PMOS and NMOS devices.

¹⁷ This can also be defined as the minimum and maximum value of the on-resistance during operation. In the case of the ADG731, the on-resistance flatness is 0.5Ω .

¹⁸ The drain and source are interchangeable, meaning that both can act as input or output. Thus, the diagram does not directly state the location of the output signal.

¹⁹ For simplicity's sake, the analysis considers a resistive load, R_{load}

Figure 54: On-resistance of a bilateral switch with respect of the input signal.

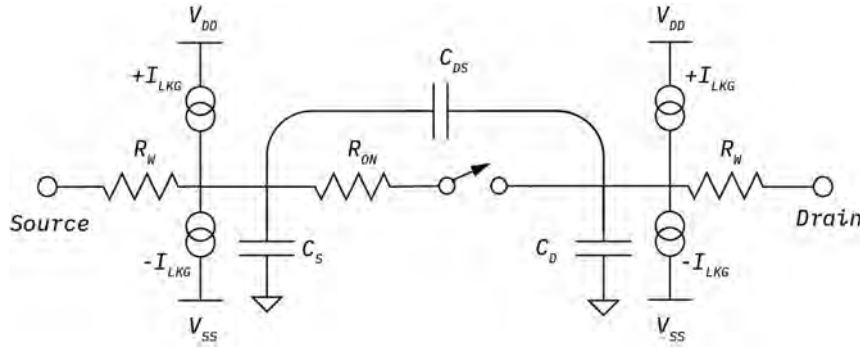


Figure 55: Equivalent circuit of a single CMOS bilateral switch.

(94)

$$V_{out} = V_{in} \left(\frac{R_{load}}{2R_w + R_{on} + R_{load}} \right) + I_{LKG} \left[\frac{R_{load}(2R_w + R_{on})}{2R_w + R_{on} + R_{load}} \right]$$

In terms of the AC performance, the presence of parasitic capacitances can affect the system's bandwidth and crosstalk. To simplify the analysis, let us consider the wire resistances as part of the on-resistance and the load respectively (R_{on_w} and R_{load_w}). Analysing Fig. 55's loop with an AC signal with a purely resistive load:

$$(95) \quad \left[\frac{R_{load_w}}{R_{load_w} + R_{on_w}} \right] \left[\frac{1 + R_{on_w} C_{DS} S}{1 + \frac{(C_D C_{DS})}{R_{load_w} + R_{on_w}} S} \right]$$

In the same manner, taking into consideration the case of an RC load, the transfer function of the system is calculated through:

$$(96) \quad \frac{R_{load_w}}{R_{load_w} + R_{on_w}} \left[\frac{1 + C_{DS} R_{on} S}{1 + (C_D R_{on} + C_{DS} R_{on} + C_{load} R_{on}) S} \right]$$

As can be observed in Eq. 96, the total bandwidth of the system will be dictated by the capacitances of the multiplexer along the load capacitance. In simple terms, Eq. 96 shows the behaviour of an RC filter that attenuates the signal at certain frequencies. The pole related to C_d dominates the frequency roll-off (i.e. once the attenuation of the signal is noticeable). C_{DS} introduces a zero that will affect the signal only at high frequencies since R_{ON} is considerably small. Moreover, this analysis shows the importance of implementing electrodes with matched impedance and similar parasitic capacitances. For instance, if there is an impedance mismatch between the electrodes at node P and N, the voltage seen at the instrumental amplifier will lead to a voltage error. Furthermore, this means that the effects of parasitic elements will vary depending on the measurement nodes.

In the case of the D node, the effect of R_{on_w} limits the current injected to Z_{unk} , but this does not translate directly into a measurement error. In the P node, C_{DS} and R_{on_w} act as a low pass filter that ultimately degrades the measured voltage signal, introducing attenuation and phase shifting. The PID controller depends strongly on

the N node to control the output signal, thus R_{on_w} can cause the PID controller to be unstable, but due to its small value the effect is insignificant. Finally, an effect is presented on the T node which is similar to that of node P, but in this case the effect will be observed in the measured current. Therefore, the dissipation factor²⁰ is used to estimate the measurement error, which is proportional to the frequency, i.e. as the frequency increases the error rises too. In general, one can calculate the error introduced by parasitic elements, using the following formulas:

$$(97) \quad \begin{aligned} \text{Magnitude}_{\text{error}} &= \frac{1}{\sqrt{1 + (wC_pR_p)^2}} - 1 \\ \text{Phase}_{\text{error}} &= \tan^{-1}(-wC_pR_p) \end{aligned}$$

where $w = 2\pi f$, and both C_p & R_p represent the parasitic elements of any measuring channel.

Using the above equations, one can estimate the error introduced by the ADG731, and not only mitigate through best practice measurement techniques (e.g. the use of controlled impedance connections), but also add the contribution of this effect to the final impedance calculation as a compensation factor. Another useful metric used to estimate the error introduced by the MUXes, is the concept of Insertion Loss (IL). IL is related to the amount of attenuation that a signal suffers when going through a switch in its on state using a purely resistive load of 50Ω . To enable the maximum power transfer IL must be small. IL is defined as:

$$(98) \quad IL = 20\log_{10}\left(\frac{V_{\text{out}} \text{ through MUX}}{V_{\text{out}} \text{ without MUX}}\right)$$

Table 7 shows IL across several frequencies. Moreover, the results from the table show that as the frequency increases the degradation of the signal is more noticeable. The effect of IL can be seen in the attenuation of the output signal in Fig. 56. As mentioned before, the signal going through the MUX is not only attenuated, but is also more susceptible to noise.

FREQUENCY (Hz)	INSERTION LOSS (dB)
100	-1.5892
1000	-1.6225
10,000	-1.6396
20,000	-1.7541
40,000	-1.8362
60,000	-2.9321
80,000	-3.8256

²⁰ The dissipation factor describes the tendency of dielectric materials to retain energy when an AC signal is present.

To conclude this section, the analysis of the Signal-to-Noise Ratio (SNR) is presented to fully characterise the hardware aspects that will affect the quality of the image reconstruction. SNR has a different definition, depending on the area of study. In our case it represents, as its

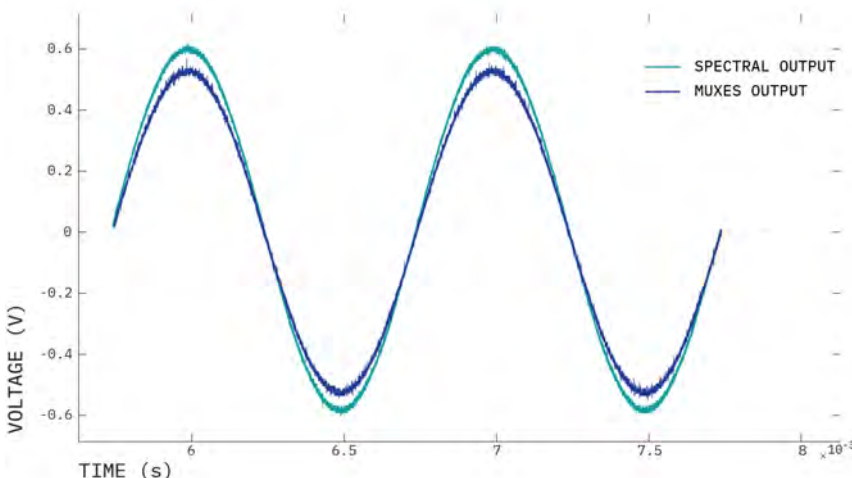
Table 7: Insertion loss across multiple frequencies.

name implies, the amount of signal in respect of the background noise. Electronic components are all subject to noise coming from diverse sources, for instance, electromagnetic noise, or noise due to coupling and crosstalk introduced by parasitic elements. While certain design consideration can help improve the SNR, one must acknowledge that a certain degree of noise will be present in the system.

The output signal²¹ was measured with a digital oscilloscope connected to a $1\text{ k}\Omega$ high precision resistance (tolerance $\pm 0.01\%$) through a testing fixture that allows the user to connect the SpEIT's spectral output²², and also connects the MUXes output to a through-hole impedance. Next, a Fast Fourier Transform (FFT) analysis was conducted on the signals to measure the power spectrum corresponding to the signal and the noise present in it. To be more specific, a periodogram was obtained to estimate the spectral density of the signal using a Kaiser window²³ with $\beta = 38$ to provide a balanced solution between side-lobe level and main-lobe width²⁴. Fig. 57 shows the results achieved using the periodogram process. The results are summarized in Table 8.

FREQUENCY (Hz)	SPECTRAL OUTPUT (dB)	MUX OUTPUT (dB)
100	40.2809	36.3344
1000	39.8099	36.5837
10,000	39.9797	36.5468
20,000	39.5005	36.3609
40,000	35.9201	32.2904
60,000	32.4082	29.7851
80,000	28.4255	25.5179

Similar to IL, the SNR is calculated using the same frequencies. The SNR does not vary greatly between outputs, and as expected, the spectral output performs better than the MUX output in that the SMB connectors offer an extra layer of noise protection with their coaxial type cabling.



²¹ The measurements were taken using the full swing of the AFE

²² The spectral output uses 50Ω SMB female connectors.

²³ This is often referred to as the optimal window as it has a simple representation of Bessel functions, having maximum amplitude attenuation close to frequency zero.

²⁴ The lobes refer to the areas seen in the visual representation of a Fourier transform. The main lobe represents the frequencies where most of the energy is stored, and the side-lobes depict the left-over energy due to noise

Table 8: SNR across multiple frequencies for both Spectral and MUX outputs.

Figure 56: Output voltage across a 50Ω at 1 kHz using the spectral and MUX output.

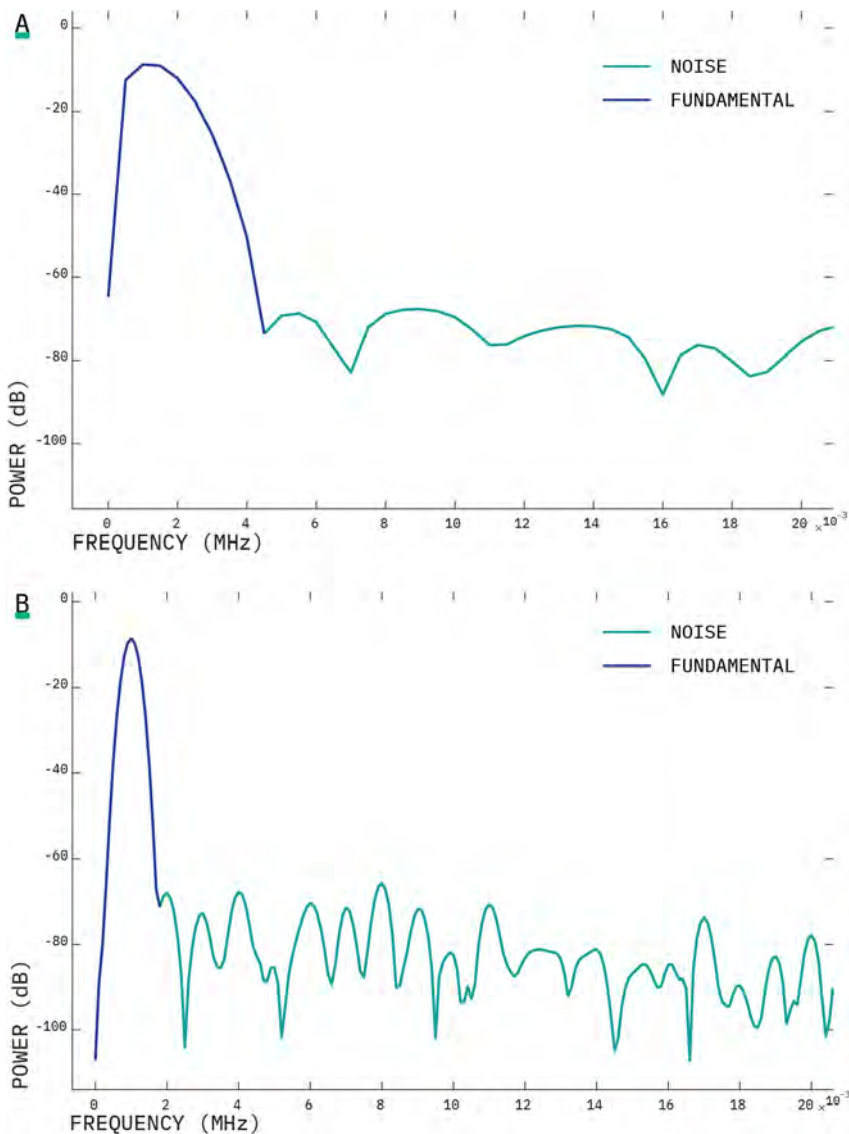


Figure 57: Power spectrum analysis for both A. Spectral, and B. MUX outputs.

The inclusion of both outputs in SpEIT was intended to provide users with a system not only capable of obtaining EIT measurements, but also adequate for EIS studies, which are common for root biomass estimation. In turn, this offers root researchers the ability to carry out both types of experiments using one system. It is now necessary to explain the final hardware design aspects that allow the creation of a smart rhizotron.

5.5 SpEIT Rhizotron

One of the common pitfalls of root experiments under controlled environments is the extreme disparity between the field and the lab. Realistic scenarios mean working under great variability of multiple environmental factors. On the other hand, working in controlled conditions allows us to understand the impact of one variable at a time, thus, making experiments more repeatable. Failing to consider some important factors when working with plants growing in pots can make it difficult or even impossible to extrapolate the results to field conditions.

Passioura (2006)²⁵ discusses the sources of “noise” or artefacts when conducting pot experiments. In the project’s case most of these were considered due to our collaboration with The University of Sheffield, and a subsequent plan to validate the whole technology using the X-Ray facilities at The University of Nottingham. Therefore, the choices made when designing the system took into consideration the mechanical constraints of the X-Ray system in Nottingham.

As with any pot system that wants to reflect a realistic scenario, the vessel must enable plant roots to grow with the minimum amount of constraints possible. The first obvious constraint is the diameter. Typical rhizotrons force the plant to grow on a 2D window or a small box, in which the roots can only explore in a downward manner. Thus, the SpEIT rhizotron is designed to be a cylindrical pot of 20 cm diameter. Since the system is mainly intended to monitor herbaceous plants, it is expected that this size will allow the plant to have a considerably long growth process before its roots reach the wall²⁶. In terms of length, the system has a 40 cm height, considering the X-ray system at Nottingham.

The physical dimension of the presented vessel posed a challenge in terms of implementation. For instance, a vessel with such height implies the use of more than one ring of electrodes to track root development alongside the whole vessel. Another critical obstacle to overcome is the positioning of multiple electrodes and their respective cabling. To overcome the discussed implementation challenges, keeping in mind that for any phenotyping experiment would require more than one smart rhizotron, the electrodes were manufactured with flex-PCB technology to ease the assembly process. Not only do flexible PCBs present a cost-effective solution, but makes maintenance of the system easier. The electrodes’ PCB were designed with modularity in mind. This means that whenever an electrode or set of electrodes fails, it can be easily replaced.

Fig. 58 illustrates the design of the flexible electrode strip. Each strip contains eight electrodes that can be accessed through a connector at the end of the strip. The strip is impedance controlled, thus, each electrode has a conductivity of 4Ω . The electrodes are gold-plated using the electroless nickel immersion gold (ENIG) process, to protect the electrodes from oxidation processes and offer excellent protection against corrosion. At the moment of writing, there is no study discussing the potential drawbacks of using ENIG electrodes. This work assumes that there will be a degree of electrode polarisation since they contain gold. Gold is considered to be a polarizable material as with most metals, but it presents lower polarisation effects at high frequencies²⁷.

Electrode polarisation is a phenomenon that affects the way current travels to the target under study, thus, this will influence any impedance measurements. The effect occurs when an electrical charge accumulates in the immediate vicinity of a metal in contact with a biomaterial²⁸. As most conductive media contains free ions, the ions will

²⁵ Passioura, “Viewpoint: The perils of pot experiments”.

²⁶ Chapter 2 presents the limitations of EIT when discerning targets in the centre of the vessel, as well as a mitigation technique involving the S/M patterns; thus, in theory, the vessel could have a greater diameter with some resolution compromises.

²⁷ Peyman Mirtaheri et al. “Electrode polarization impedance in weak NaCl aqueous solutions”. In: *IEEE Transactions on Biomedical Engineering* 52.12 (2005).

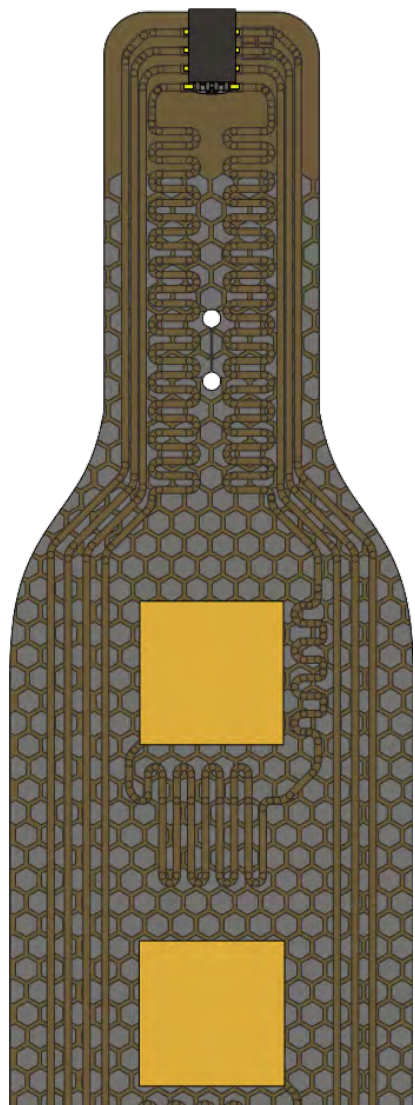


Figure 58: Flexible electrode strip. The strip consists of eight impedance controlled electrodes.
²⁸ Tapani Repo et al. “Electrical Impedance Spectroscopy and Roots”. In: *Measuring Roots*. Berlin, Heidelberg: Springer Berlin Heidelberg, 2012.

lean towards the electrodes when an electric field is present. In turn, a high degree of ions will create what is known as a double ionic layer. The double layers lead to measurement errors since they will generate a dielectric response at low frequencies, masking the true impedance of the subject under study. In this application, electrode polarisation is not of concern due to four design choices:

1. *High-surface-area electrodes*²⁹.
2. *A high injection current density*³⁰.
3. *Considerable electrode separation*³¹.
4. *The use of a kelvin measurement technique*³².

Having impedance controlled electrodes is of crucial importance, as this allows us to eradicate any point of uncertainty that could make the excitation loop unstable. Furthermore, controlling the impedance of the electrodes allows the user to carry two-point EIT sweeps as this removes errors introduced by the resistance of different electrodes. The controlled impedance helps avoid any latency issues and phase discrepancies between the signal reaching the subject and acquiring the measurement. The strip is a two layer flexible PCB; while the top side contains the routing of the electrodes, the bottom layer is a hexagonal copper pattern that can be connected to ground to decrease electromagnetic noise (similar to a twisted pair of cables), and could be used for turning the electrodes to capacitive probes. The main role of the hexagonal mesh at the back of each strip is to relieve the bending stress on the electrode copper. A full description of the system follows, as a conclusion to this section.

The SpEIT rhizotron encompasses two major components: the rhizotron sensing area, and the central processing unit. The rhizotron sensing area comprises 128 electrodes arranged in eight horizontal

²⁹ H. P. Schwan et al. "On the low-frequency dielectric dispersion of colloidal particles in electrolyte solution". In: *Journal of Physical Chemistry* 66.12 (1962).

³⁰ H. P. Schwan. "Electrode polarization impedance and measurements in biological materials." In: *Annals of the New York Academy of Sciences* 148.1 (1968).

³¹ H. P. Schwan. "Linear and nonlinear electrode polarization and biological materials". In: *Annals of Biomedical Engineering* 20.3 (1992).

³² Constantino Grosse and Mónica Cecilia Tirado. "Low-frequency dielectric spectroscopy of colloidal suspensions". In: *Journal of Non-Crystalline Solids*. Vol. 305. 1-3. 2002.

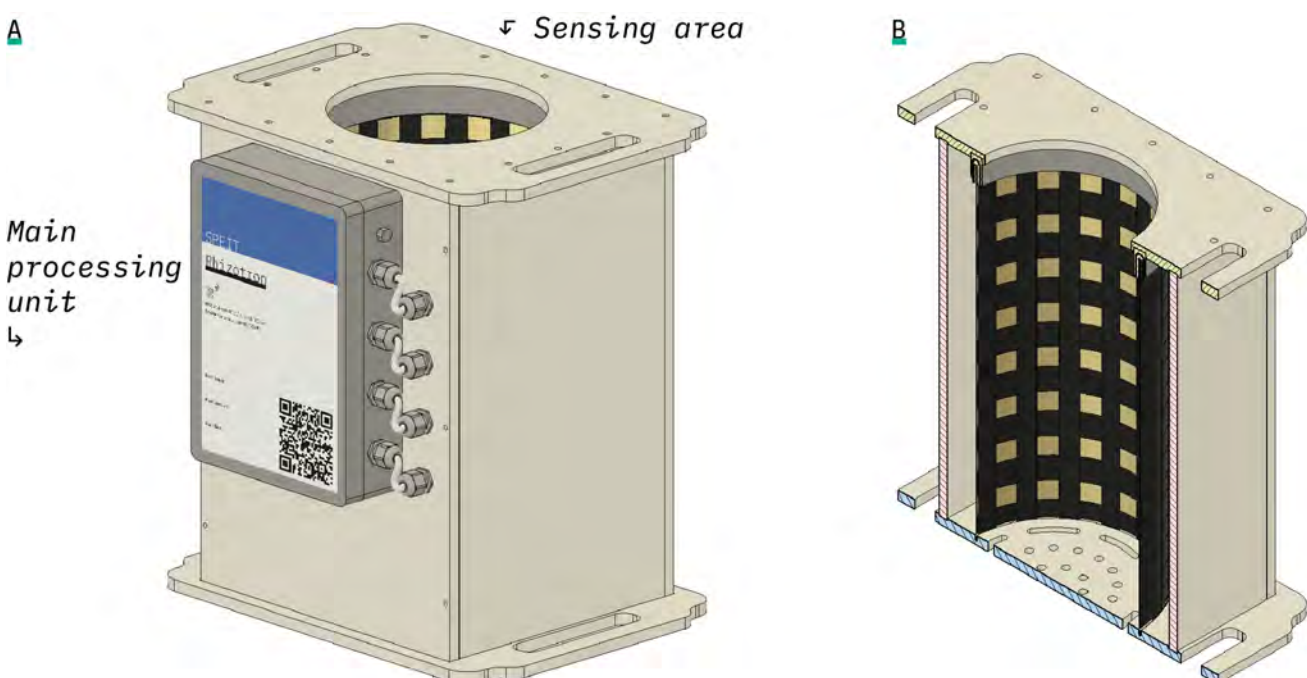
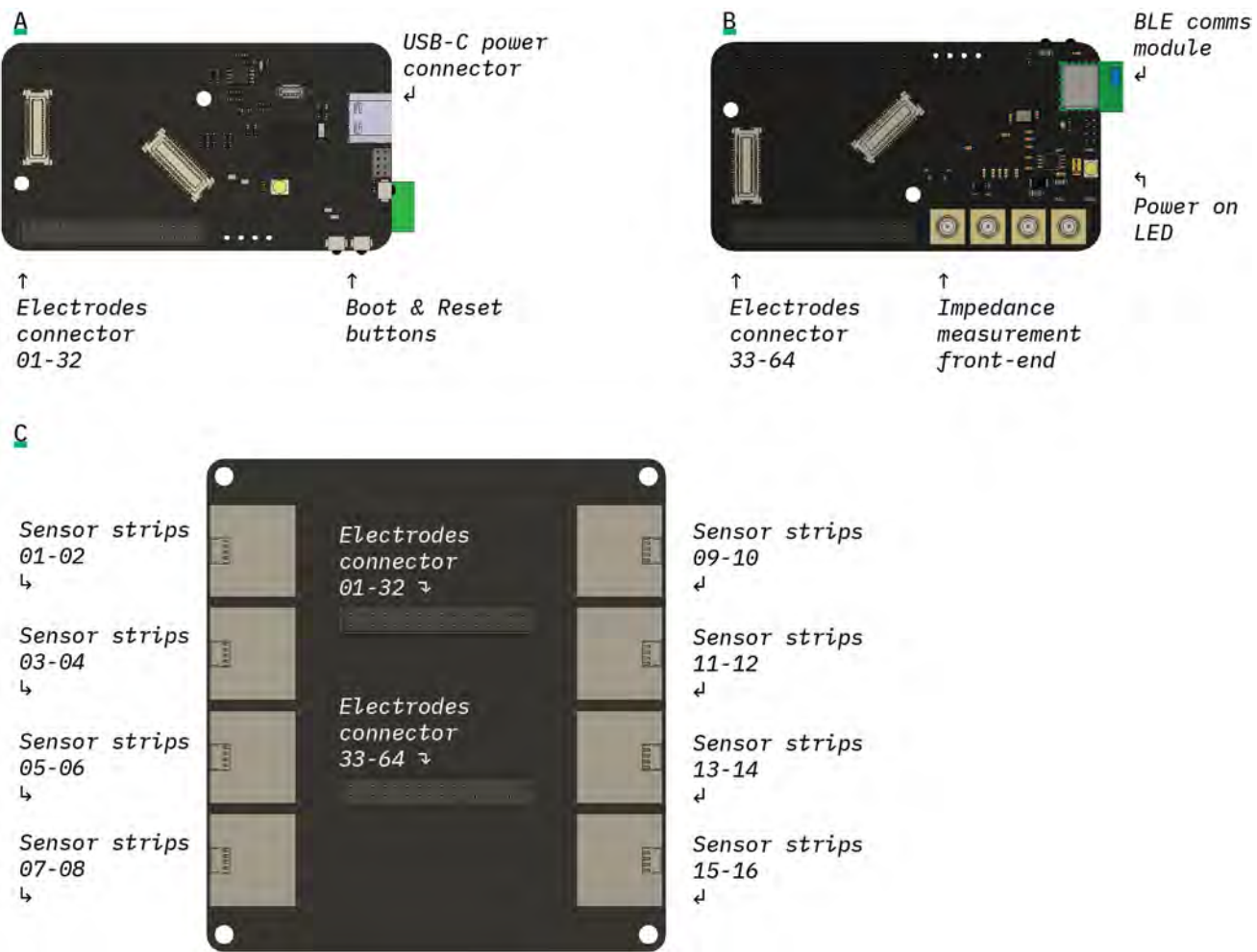


Figure 59: A. SpEIT rhizotron, and B. its isometric view showcasing the sensor strips.



rings of sixteen electrode planes (Fig. 59). The sensing area is 20×40 cm. The vessel dimensions are $28 \times 39 \times 42.5$ cm. The bottom of the vessel contains several draining holes, and mechanical slots that ease the watering procedure from the bottom. The outer shell was designed and manufactured in collaboration with Glideology LTD³³.

The SpEIT main board (Fig. 60) is located inside the processing unit (using four expansion boards to control 64 electrodes) and a feeder board³⁴. The SpEIT rhizotron can only control 64 electrodes at one time, thus, the connections allow the control of four electrode rings per measurement cycle. The feeder board enables the user to swap between odd and even numbered rings (starting at the top of the vessel). Therefore, if the user desires to use the 128 electrodes to explore the complete vessel, they can do it using one SpEIT board. The choice of placing the electrode configuration as odd and even, was made to attain a suitable compromise between vertical resolution and the practicability of the system. In this way, the user can explore the whole vessel without the need to swap strips, but if needed, the user can get extra resolution by taking two measurements that use the 128 electrodes. Each cable hose provides two RJ45 connectors; for instance, to use the odd-numbered bank, the user should connect only the connectors with the odd-colour combination.

Figure 60: SpEIT mainboard A. Front face B. Back face. C. SpEIT feeder board.

³³ The CAD file supplied by Glideology LTD was used to create the composite Fig. 59.

³⁴ The feeder board allows the user to swap between sensor strips.

5.6 SpEIT's shell

The ADuCM350 core is based on an ARM Cortex M3 32-bit processor intended for low-cost platforms that require high-performance. By itself, the Cortex M3 is a typical micro-controller with a rich instruction set and debug-and-trace abilities that allows SpEIT to handle complex tasks faster. While SpEIT has its debugging and programming interface exposed so that different programs can be uploaded, a shell was developed to allow users to access the services offered by the system. The user can get access to the Command-Line Interface (CLI) through the Universal Asynchronous Receiver-Transmitter (UART) port or via Bluetooth Low-Energy (BLE). The CLI follows the traditional implementation, in which the user provides commands and the CLI passes them to the shell to be executed. Therefore, the shell is in charge of the following three tasks:

- *Initialisation*: The shell loads any configuration files that can change its behaviour.
- *Interpretation*: The shell reads any Standard Input (STDIN) commands and executes them.
- *Termination*: Once the command is executed, the shell frees up memory and runs any available shutdown commands.

An implementation of the shell is summarized in the pseudo-code:

```

int main(int argc, char **argv){
    // initialisation and loading config files
    ...
    // call shell1
    shell_loop();
    // perform any shutdown/cleanup
    return EXIT_SUCCESS;
}

10 void shell_looop(){
    char* command;
    char** args;
    do{
        printf(">_"); // print cursor
        15 line = shell_read();
        args = shell_parse();
        status = shell_execute(args);

        free(command);
        free(args);
    }
    20 while(status);
}

```

In order to use SpEIT as both an accurate metering solution and as an IoT device, the system undergoes a rigorous initialisation process. During initialisation, the system calibrates the different measuring channels and enables all the communication peripherals³⁵. The initialisation process is summarised on the next page.

Listing 2: Pseudo-code describing SpEIT's main loop.

³⁵ To use the system as a dynamic IoT solution, the device retrieves the characteristics of the BLE module to determine if a new name for the device needs to be generated; and if so, it starts the entropy system to generate a unique ID.

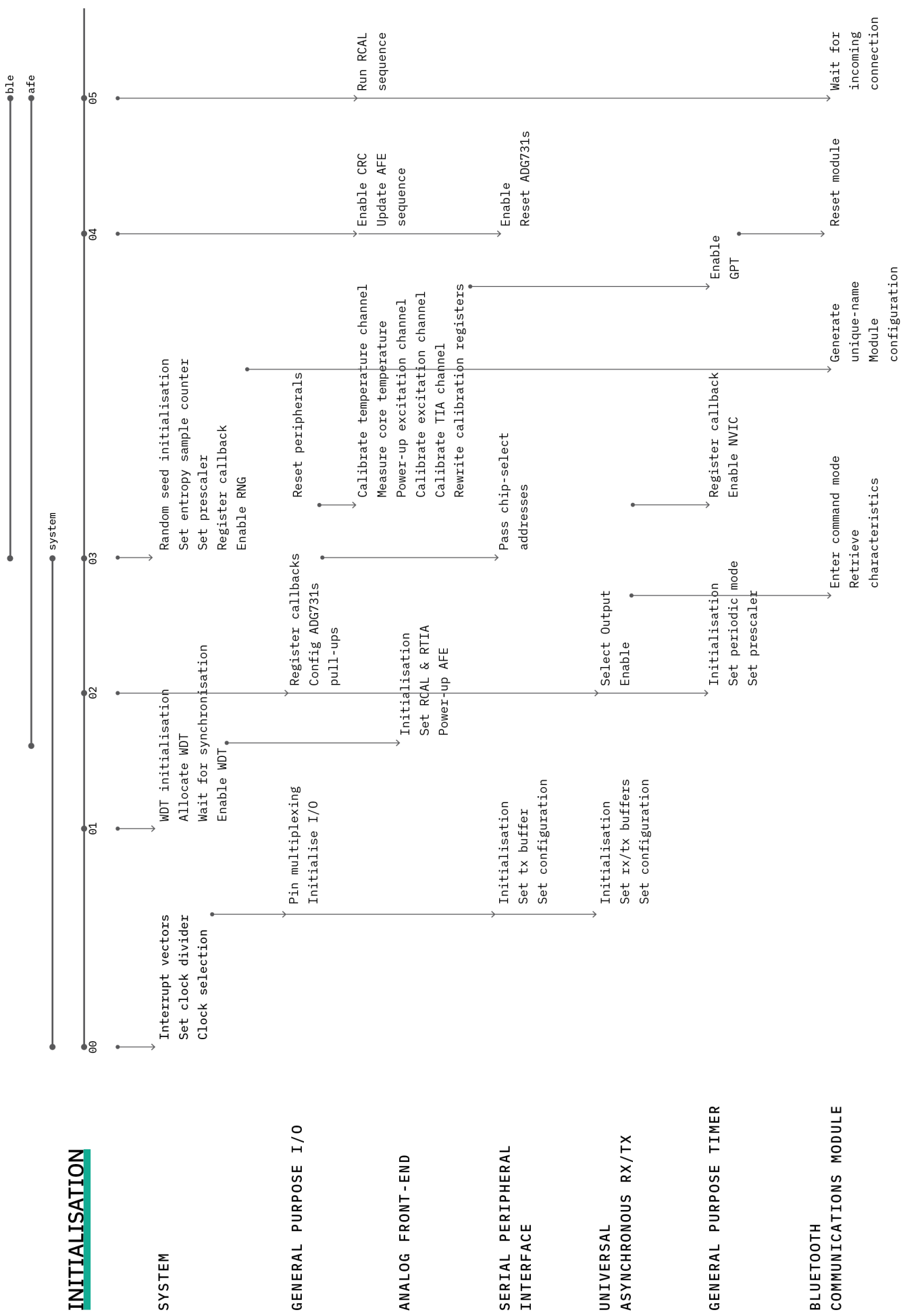


Figure 61: SpEIT initialisation process.

After the initialisation process is completed, the system waits for any incoming connection request through the BLE module. If the connection is successful, the BLE central (i.e. the device connecting to the system) will establish the connection parameters, and open the transparent UART service. Once this three-step process is complete, the system will call the CLI and initiate the main loop. Once in the CLI, the user can provide any command followed by specific or optional parameters. SpEIT offers a streamlined set of commands intended to ease the interaction with the user. As a consequence, the user does not need to know how the AFE works internally, or the complexities of the measuring sequence³⁶. Moreover, as the Cortex M3 does not possess a floating point engine, the processing of the raw data provided by the DFT engine when measuring impedance is done using a mix of fixed point arithmetic and instruction sets provided in the Cortex Micro-controller Software Interface standard (CMSIS). Therefore, being a 32-bit resolution micro-controller, some accuracy will be lost in the processing of the data³⁷. The commands provided in SpEIT's firmware are:

- > **help**. Presents information on how to use the SpEIT's shell. When passing a specific command alongside help, the user can obtain a specific description of such command.
- > **mux**. Allows the user to manipulate the MUXes directly.
- > **sleep**. Disables all peripherals and resets the MUXes to their initial state. This command sets the core to hibernation mode to save power.
- > **reset**. When called, it goes through the reset process, which involves disabling the system peripherals. The BLE client needs to handle the disconnection to the peripheral.
- > **temp**. Measures the temperature inside the core. If the temperature has changed, it recalibrates the AFE accordingly.
- > **meas**. Takes a single measurement at a desired frequency and amplitude. The user can choose between the spectral and MUX output.
- > **kelvin**. Takes a single measurement using the spectral, front-end measuring current and voltage directly. The measurement is carried at 600mV, thus, the user can only select the stimulation frequency.
- > **spec**. Runs a spectral sweep through the spectral output across a range of frequencies using a selected amplitude. The user can define the range of the sweep and the number of steps needed.
- > **eit**. This command allows the user to create an EIT sweep at a desired frequency with a custom S/M pattern. The S/M pattern can be configured to be planar or square. The algorithm continuously monitors any temperature changes to recalibrate when appropriate.

This suite of commands allows the user full control of the system without dealing with the complexities of the AFE sequencer, calibration sequences, and processing maths. The code implementation of the system is done in embedded C. While this is a comprehensive set of functions, for most EIT applications the 'eit' command will meet their needs. The algorithm employed in this command allows

³⁶ Internally the AFE uses a hexadecimal sequencer that determines its functionality. The measuring commands provided have direct access to the sequencer and can modify any present sequence. The sequence needs to be checked through the Cyclic Redundancy Check (CRC) engine, which in turn can make the measuring process more difficult to carry out for inexperienced users.

³⁷ One could further mitigate the precision issue by processing the raw data outside the Cortex M3 processor.

the user to create their own S/M pattern with the chance to choose between planar and square arrangements. The implementation relies on creating a multidimensional array, containing a combination set for each pair of stimulating and measuring electrodes. Moreover, the system carries out this process each time the command is called. Thus, the time taken to acquire subsequent frames of data will not be fully optimised; meaning that if a certain study requires a higher frame rate, the user could possibly opt to generate its own S/M pattern externally and control the device with the 'mux' and 'meas' commands. In a phenotyping environment, a two-minutes frame rate is acceptable since the system is acquiring approximately 3500 measurements using 64 electrodes, and the subject under study has a slow rate of change. Therefore, the aim of the 'eit' command is to serve as a high accuracy data acquisition algorithm that offers a wide degree of flexibility to the user. The pseudo-code of the algorithm previously described follows:

```

void cmd_eit{
    // Set the full AFE swing, rewrite sequencer
    SEQ_MMR_WRITE( REG_AFE_WG_AMPLITUDE, 600mV);
    if (user_frequency > 20 &lt; 80k)
        SEQ_MMR_WRITE(REG_AFE_WG_FCW, user_frequency);
    else return;

    // Recalibrate system before measurements
    AFE_TempSensChanCal();
    // Run the CRC engine for the modified sequence
    AFE_EnableSoftwareCRC();

    if planar
        // Create sequence using skip values
    else if square
        // Create sequence using left-rotation
        // Modify sequence using skip values

    for counter < user_n_electrodes{
        // select corresponding MUX for injection
        mux_change(I);
        for inner_counter < user_n_electrodes{
            // select corresponding MUX for measurement
            if I & V are different
                mux_change(V);
            else
                continue;
            // Run measurement sequence and calculate results
            printf(results);
        }
    }
    return;
}

```

Listing 3: Pseudo-code describing the behaviour of the eit command.

5.7 SpEIT's IoT solution

According to the definition of a modern phenotyping platform, the system needs to be able to analyse thousands of subjects in a small amount of time (i.e. be high-throughput). Therefore, this work also considers the scenario where thousands of SpEIT rhizotrons are ac-

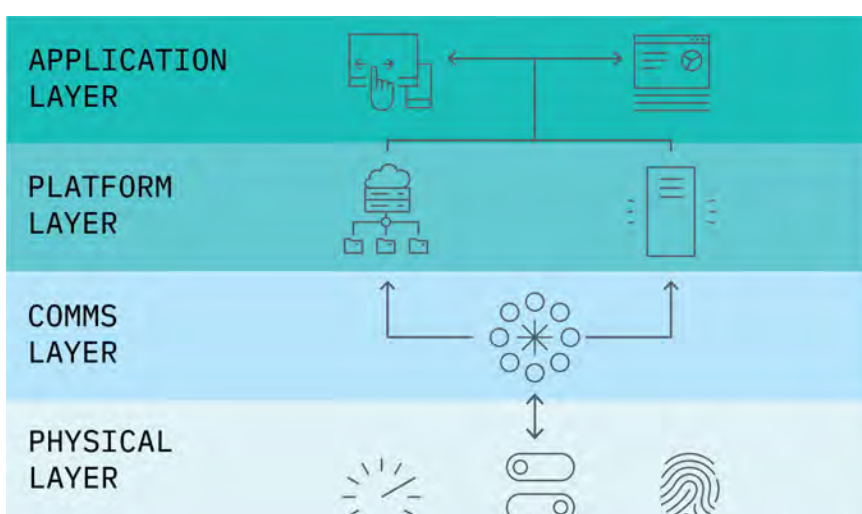
tively tracking the development of multiple plants in a root breeding program. To achieve this objective, this section discusses the common communication protocol of the fourth industrial revolution³⁸.

Industry 4.0 refers to the automation of industry processes using smart electronics. In particular, the technological framework in charge of leading this revolution is the Internet-of-Things (IoT). IoT involves connecting multiple interrelated devices to the Internet using unique IDs, and without requiring human interaction. The devices connected to the IoT network can share information about their current status and their environment. The value of IoT is not only the automation, but the handling of significant quantities of data (Big Data) to make informed decisions. Implementing a network of connected devices and cloud services is a complex endeavour, which poses challenges in areas such as wireless communications, volume of data, real-time analytics, and security.

In order to remove some inherent complexity of IoT solutions, it is important to have a reference-architecture for IoT implementations. Using standard architectures significantly reduces the implementation risks while at the same time defining standards, best practices and patterns. A simple architecture is presented in Fig. 62. As with any IoT architecture, it encompasses all the components of IoT ecosystems: electronic devices, networking protocols, services, and security. The objective is to retrieve the data generated by the devices to create insights for the final user or help make a decision in an automated environment. To better understand the components of any IoT solution, let us start by describing the layers in Fig. 62:

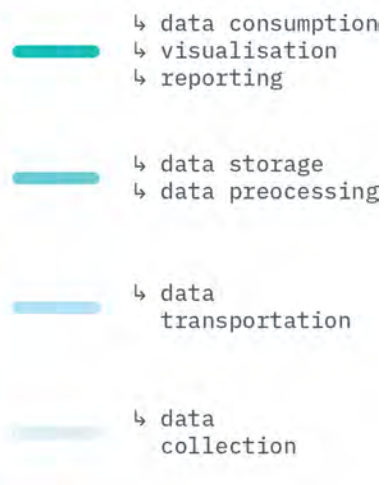
- **Physical layer:** This is where the IoT life-cycle starts. It relates to the data collection from various sensors. This layer involves understanding the source of the data. For instance, if the data comes from different sensors there needs to be a standard to format the data for it to be usable at higher layers. Furthermore, if the sensors come from different manufacturers, the designer needs to consider protocols to unify the data³⁹. Devices in this layer need to provide remote monitoring & calibration, address management, and security.

³⁸ Klaus Schwab. "The Fourth Industrial Revolution: what it means and how to respond". In: *World Economic Forum* (2016).



³⁹ The main sensing device is the SpEIT system for the present application, which internally preprocess the data using a basic CSV formatting.

Figure 62: Basic IoT architecture.



- **Communication layer:** *For the data to be fully processed, it needs to be first transmitted through the internet. The complexity of this layer depends on how many steps are needed to make the data available on the IoT platform securely. For instance, sensors that communicate wirelessly through Bluetooth require an extra device to transmit the data over the internet. This layer is crucial to operate each sensor remotely.*
- **Platform layer:** *Once the control of the sensors has been established, useful data can be acquired from them. The system needs to manage the collection of information from a large volume of sensors, and all of this in near-real-time conditions. The main application implements predictive analytics to process the incoming data at very high rates. Moreover, it also needs to apply a level of data security, particularly related to the access of the data.*
- **Application layer:** *After processing the raw data and getting some valuable insight from it, the data needs to be formatted for user consumption. Thus, this layer deals with the enrichment, cleansing and visualisation of data. Using a defined set of usage consumption policies that grant secure access to the data either publicly or privately.*

The end-goal of any application is what defines the type of IoT network required. For instance, in real-time or near-real-time operations there is a need for frameworks that enable quick data evaluation. For root phenotyping, real-time analytics is not crucial as roots do not change in small-time intervals. While moisture changes occur frequently in a span of minutes, the framework would not be necessarily a real-time application as the application must track slow changes in the subject under study. Therefore, the most important challenge to overcome to use SpEIT as an IoT solution is the communication with multiple devices at one time.

5.7.1 SpEIT network

Let us start with the physical layer of the system. SpEIT systems can communicate wirelessly via their Bluetooth Low-Energy (BLE) modules (RN4871). BLE is one of the technologies developed to enable IoT applications, as it is intended to work with low power at intermittent periods of time. Therefore, BLE is optimised to work in burst mode, i.e. send moderate amounts of data at intervals. It retains the traditional radio band of 2.4 GHz from traditional Bluetooth, but its operation is different. BLE has been designed for short-range operation (typically less than 10 meters, but under special conditions can reach 100 meters) using a star configuration⁴⁰. Another differentiating factor between traditional and Low-energy Bluetooth is that BLE operates in the physical and the Medium Access Control (MAC)⁴¹ layer of the Open System Interconnections (OSI) model⁴².

The BLE module in SpEIT acts primarily as a peripheral, thus, it will broadcast its presence regularly to be found by a central BLE device. The central device is in charge of sending and receiving data to each SpEIT node. Depending on the BLE central (e.g. cellphone, laptop, BLE board), the acquired data can be processed, stored, or pushed to a cloud service. The system presented in this work uses a

⁴⁰ A primary device, called central, controls secondary devices, known as peripherals.

⁴¹ It is in reality a sub-layer of the data link layer in the OSI model.

⁴² The OSI model is a communication standardisation protocol created to enable the communication between diverse communication devices.

BLE plus Wi-Fi module to connect to the SpEIT devices and send the data through Wi-Fi to a server. The module used is the WiPy 3.0, an IoT device based on the popular ESP32 boards⁴³. The WiPy 3.0 offers reliable data stream service, secure data transmission, and ease of implementation of IoT protocols. Therefore, the WiPy 3.0 module acts as a primary gateway for SpEIT systems. Fig. 63 shows the multi-star configuration of both BLE centrals and peripherals.

In order to create an IoT network with the previously mentioned devices, each one of the devices needs a unique identifier. The ID creation process takes place in both the SpEIT nodes and the gateway modules. In the case of SpEIT systems, the main core of the system retrieves the configuration data from the BLE module. Depending on the information retrieved, the core will determine if the BLE module has been configured previously and if it needs a unique ID. If the module has not been assigned a unique ID, the core starts its entropy generator module to create a five digit random number to succeed the prefix “SpEIT_”⁴⁴. The ID creation process is unique for the gateway modules. The gateways first connect to the network and scan for other gateways connected within the network. With this knowledge they generate a unique ID that does not clash with any existing gateways. The reason the process is different is that the control of the gateways, and thus the modules, is done using the Message Queue Telemetry Transport (MQTT) protocol.

The MQTT protocol is a light-weight messaging protocol focused on IoT applications. The protocol is useful in low-bandwidth applications, where network data transmission might be unreliable. The base of all MQTT applications is their publish/subscribe methodology, which allows the control of multiple devices with small-footprint code. For this reason, the unique ID of the gateways is more important on this side, as it is a lightweight protocol. However, the simplicity of MQTT does not mean that it lacks security. MQTT provides security mechanisms at the application level. Depending on the requirements of the application, MQTT can be used in conjunction with other

⁴³ The key difference between WiPy 3.0 and a single ESP32 board is that WiPy modules have installed the firmware that enables the use of MicroPython on the system. However, this module was selected due to its enhanced Flash & RAM size, certifications and availability. Thus, this project uses the WiPy modules as enhanced ESP32 systems programmed with C++.

⁴⁴ While all BLE modules have a specific MAC address, the intention of having a “verbal” ID is to ease the control at user level.

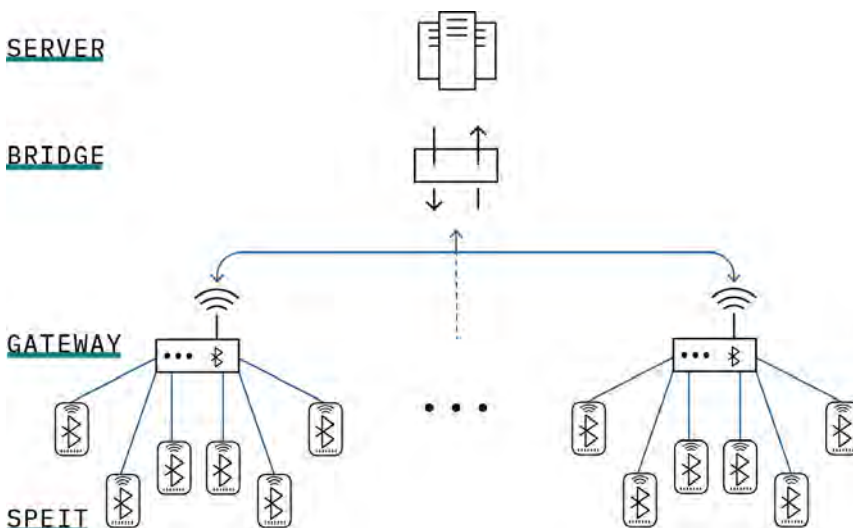


Figure 63: Physical representation of the SpEIT network

state-of-art security solutions such as a Virtual Private Network. In the case of the SpEIT network, a message encryption and client authentication is implemented using the OAuth protocol.

As mentioned previously, the publish/subscription model of MQTT means that this kind of protocol follows a star topology with a central node known as the broker. The broker manages the incoming messages and makes sure that they reach the correct client. Afterwards, it re-routes messages according to topics, thus, clients can subscribe to topics to wait for incoming data, and they can also send data to the same topic or different ones. The broker deals with all the interactions involved in this process.

The SpEIT network employs Mosquitto™; an open-source broker developed by the Eclipse Foundation⁴⁵. The broker is mounted on a Raspberry Pi 3 B+ to demonstrate the level of readiness of the system to integrate with industry systems. The gateways and broker were configured to use Transport Layer Security (TLS) with the appropriate certificates.

The workflow of the SpEIT IoT network is illustrated in Fig 64. First, the gateways connect to the MQTT broker using a generic name and establish a connection. Once connected, they scan for other devices connected within the network and then proceed to rename themselves according to the scan. Next, the gateways will scan for nearby SpEIT devices. Depending on the Received Signal Strength Indicator (RSSI) measured, the gateways will determine which devices ensure connection stability and will store a list of these devices. The gateway creates a topic with its unique ID, and another two subtopics: one for receiving commands from the broker, and the other one to publish the list of connectable devices. This represents the first control layer of the network. The user can connect to any SpEIT available through a custom Application Programming Interface (API), the 'spmqt'⁴⁶.

The API allows the user to control, acquire and format data from each SpEIT system without the need to directly interact with the communications layer. The hierarchy of the spmqt package is illustrated in Fig. 65.

⁴⁵ <https://mosquitto.org>

⁴⁶ Developed in Python 3.6 and based on the Paho project.

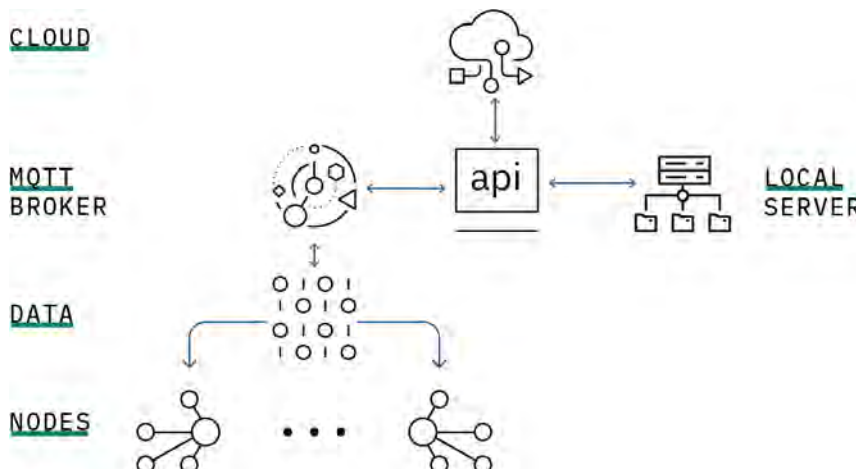


Figure 64: SpEIT network workflow.

The three main classes that the API provides are:

- **SpEIT**. IoT implementation for SpEIT modules. Connect to a SpEIT device through a ESP32 using a MQTT broker.
- **DataLogger**. Handle common SpEIT data acquisition tasks.
- **SpAutomata**. Implementation of an automation class for SpEIT's IoT solution. The class is meant to be used with the multiprocessing python package.

A more in-depth description of the above classes is presented in the Appendix section.

This chapter began by describing the steps involved in the hardware design and went on to present a software implementation to create a basis for the IoT implementation of an EIT network. Together, the SpEIT system, the EIT rhizotron, and the spmqtt package encompass the Smart Rhizotron platform. The next chapter describes the results from the implementation of the concepts presented here.

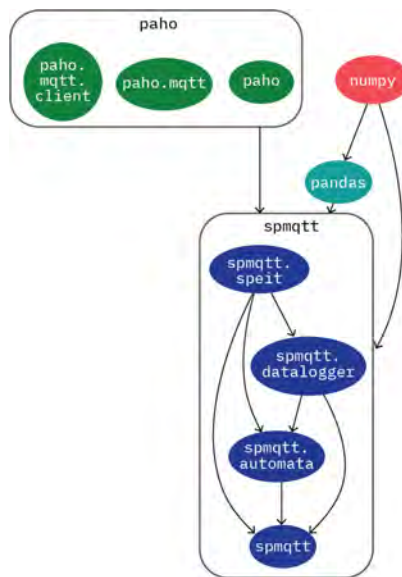


Figure 65: spmqtt hierarchy.

EMPIRICAL FINDINGS AND DISCUSSION

PLANT ROOTS react to their surroundings in complex ways and usually respond quicker than leaves. On that account, there is an expectation within any phenotyping endeavours that they must elucidate on the mechanics behind root growth processes to create new varieties focused on sustainable traits. The previous chapters have laid the theoretical foundation of Electrical Impedance methods and introduced the design of an EIT system focused on researching plant roots non-invasively. The aim of the following experiments is to validate the SpEIT system capabilities and the usefulness of the data acquired for plant root monitoring. The following expands on the research previously conducted by the author of the present work¹. Therefore, the soil preparation approach has been reproduced in this work to enhance the ability of the system to obtain a distinct electrical response from root-soil processes that is different from those seen in the air drying process of soil. In this chapter, three experiments are presented:

1. *Air drying experiment.*
2. *Raphanus sativus (Mooli Minowase) "Japanese Radish".*
3. *Brassica oleracea (Acephala Group) "Dwarf Blue Curled" Kale.*

The first experiment illustrates how the system can be used to track the natural evolution of soil moisture, which often is measured using a single point sensor². The other selection of experiments use plant material from the *Brassica* family considering both a tap and a fibrous RSA. The selection of the plants was based on previous research that explored EIT as a method for the early detection of *Plasmodiophora Brassicae* (commonly referred to as Clubroot), a pathogen that affects the *Brassica* family. The present chapter details the materials, protocols and results used throughout the remainder of the research. First, to understand the changes in the system's electrical response, a basic characterisation of the growing material employed is presented. Next, an overview of the soil preparation protocol is described. Then, a full description of the experiments and how they were conducted is given. Furthermore, due to several practical implications of the system (which are described in the mentioned section) an exploration of multi-ring S/M is presented to justify the protocols employed. Finally, an analysis of the individual results is presented and discussed.

"The observation of roots using phenotyping is central to the discovery of traits beneficial to crops, their incorporation into new cultivars using prebreeding, and to their management using precision agriculture." Saoirse R. Tracy et al. (2019)

¹ Diego D.J. Corona-Lopez et al. "Electrical impedance tomography as a tool for phenotyping plant roots". In: *Plant Methods* 15.1 (2019).

² Peng-Fei Zhao et al. "Electrical imaging of plant root zone: A review". In: *Computers and Electronics in Agriculture* (2019).

6.1 Growth Materials

The experiments presented here were conducted using a SpEIT rhizotron inside a Growth chamber (Fitotron® SGC 120, Weiss Technik®, Loughborough, UK). The lighting conditions inside the chamber offer a photosynthetically active radiation of $\approx 346 \mu\text{mol}^{-2}\text{s}^{-1}$ and $\approx 452 \mu\text{mol}^{-2}\text{s}^{-1}$ for seedlings and older plants respectively. Temperatures and photoperiod cycles were adjusted for each experiment. The rhizotron stood over a weighing plate connected to a precision scale (CCS 150K0.1, Kern®, Balingen, Germany) to continuously measure the gravimetric water content of the experiments. The growing media employed in the following experiments were a commercially available non-professional mixture of black and white peat (Universal Potting Substrate, Van Egmond Potgrond, Netherlands) with an electrical conductivity range of $0.8\text{mS/cm} - 1.5\text{mS/cm}$, a $5.0 - 6.5$ pH range, and added nutrients $120 \text{ N}, 140 \text{ P}, 240 \text{ K} (\text{gr}/\text{cm}^3)$, and a professional sphagnum moss peat based media (Advance Pot & Bedding M3, ICL Levington® Advance, Ipswich, UK) with an electrical conductivity range of $0.355 - 0.435\text{mS/cm}$, a $5.3\text{pH} - 6.0 \text{ pH}$ range, and added nutrients $204 \text{ N}, 140 \text{ P}, 339 \text{ K} (\text{gr}/\text{cm}^3)$. Further to the information provided by the supplier, basic soil characterisation protocols were followed to understand the characteristics of the media.

6.2 Substrate water characterisation

The water availability of soils is one of the key drivers for terrestrial ecosystem productivity, thus, a basic understanding of the soil's water potential is needed to explain some of the effects observed in the following experiments. In order to enhance the ability of the system to distinguish between the soil drying process and root interactions, a mostly homogenous substrate is preferred. Therefore, one must know the water content capabilities of the soil to fill the rhizotron according to a specific Bulk Density (BD). BD describes the volume of soil as it occurs naturally, i.e. it considers the soil, organic matter, and air (Fig. 66) to calculate the total mass of dry soil in a unit bulk volume.

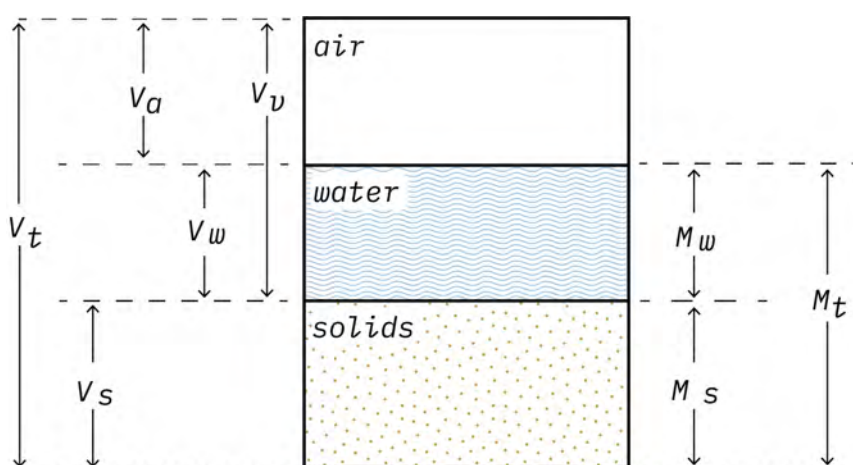


Figure 66: Soil three-phase diagram. The diagram shows what elements are considered part of the total volume (V_t), as well as for the total mass (M_t).

BD is often used as an indicator to determine a good environment for root growth³, as it can be used to describe how compacted a soil is, its structure and water storage capacity⁴. As a rule of thumb, the higher the soil compaction the higher the BD is achieved, which reduces the soil's water holding capacity by reducing the pore volume (i.e. the space between soil particles). Furthermore, the presence of organic content in the soil increases its ability to retain water due to the osmotic potential of its solutes. As mentioned above, the present experiments use peat potting substrates which are commonly used in plant nurseries⁵, as such, peat substrates have distinct properties from the soil found in fields⁶. Due to their porous nature and rich organic content, peat substrates often have bulk densities lower than 0.5 gr/cm³.

Another expression of soil material quality is the amount of water that it can contain, and it can be expressed as different ratios. In literature the most commonly adopted ratio is the weight ratio $w = \text{weight of water} / \text{weight of dry matter}$. Nevertheless, this ratio is not a good reference parameter for peat substrates, which have highly variable specific gravity of solids⁷. A more adequate relationship is the weight ratio $w_{tot} = \text{weight of water} / \text{total weight}$, which ensures that the ratio obtained never exceeds 100%, in contrast with the previous ratio which usually exceeds 100% when analysing peat soils.

Table 9 shows a summary of the volumetric characterisation as a three-phase system for both substrates used in the experiments. For sake of brevity, the Van Egmond Potgrond and Levington® Advance substrates are referred to in this work as S-01 and S-02 respectively. The substrates were characterised with the filling protocol in mind. For this reason, the amounts shown correspond to the quantity of growing media required to fill 2.5 cm of the smart rhizotron following the compaction steps explained in the next section. All experiments employ substrates sieved using a 5 mm rotary soil compost sieve screener (GFJ438, Selections, Dorset, UK) to remove bigger particles of organic content and achieve a homogeneity. The media was further mixed through stirring. Six samples from each substrate were taken and stored in a double zip locked bag, sieved and left sitting on a table for 48 hrs to allow for equal moisture distribution.

QUANTITY	S-01	S-02	UNITS
Total Volume	785.340	785.340	cm ³
Beaker weight	1075.700	1075.700	gr
Soil + Water weight	833.500	950.650	gr
Dry soil weight	299.400	259.600	gr
Water weight	534.100	691.050	gr
BD wet	1.061	1.21041	gr/cm ³
BD dry	0.381	0.33053	gr/cm ³
w	1.783	2.66198	gr/gr
w_{tot}	0.640	0.727	gr/gr
Porosity	68%	88%	—

³ Depending on the bulk density and the type of soil root growth can be limited, e.g. restricted root growth is seen in sandy soils with BD > 1.7 gr/cm³ and clay soils with BD > 1.5 gr/cm³.

⁴ Jr. Lyle M. S. "Surface mine reclamation manual." In: *Surface mine reclamation manual*. (1986).

⁵ This is considered to be due to the large volumes of soil required to fill plant pots and the scarcity of good quality soil. Moreover, peat can hold water up to 20 times its weight. However, the industry is moving towards the use of coir-based substrates to replace peat.

⁶ Neil McKenzie et al. *Soil Physical Measurement and Interpretation for Land Evaluation*. CSIRO Publishing, 2019.

⁷ S. V. Skaven-Haug. "Volumetric relations in soil materials". In: *4th International Peat Congress*. Espoo, Finland, 1972.

Table 9: Substrates' volumetric characterisation required to fill 2.5 cm of the smart rhizotron.

Additionally, soil moisture characterisation curves were obtained using a soil moisture sensor (WET-2, Delta-T Devices LTD, Cambridge, UK) based on Time Domain Reflectometry (TDR). The measurements presented were calibrated according to the substrate used, thus, permittivity (ϵ) measurements were obtained for six soil samples of each substrate in addition to weight measurements at water saturation and dry state⁸. Table 10 shows the calibration coefficients as well as the averaged quantities used to calculate such coefficients. Every manufacturer has specific calibration constants that most often do not perform well for peat substrates⁹, thus, in the present experiments custom calibration coefficients were obtained after the experiment finished and per the specifications of the manufacturer.

QUANTITY	S-01	S-02	UNITS
Avg. weight damp soil	837.200	948.505	gr
Avg. weight dry soil	295.160	257.820	gr
Avg. max. volumetric water content	79.710%	80.893%	--
$b_0 = \sqrt{\epsilon_0}$	2.155	1.786	--
$b_1 = (\sqrt{\epsilon_w} - \sqrt{\epsilon_0})$	4.517	5.479	--

The averaged results are presented in Figs. 67 and 68. The starting point of the curves represent the state of the sieved peat substrates “out of the bag”¹⁰. Once the soil was packed it was put on a weighing scale (PCB8000-1, Kern®, Balingen, Germany) and 10 mL of tap water (0.04 ppt, 8.25 pH, 0.08 mS/cm) was added at 5 min intervals until noticeable water drip was observed. Figs. 67 and 68 show the relationship between the measured soil moisture content (θ) and the electrical conductivity of the pores both of them as function of the dielectric constant. A graphical inspection of the presented result shows the typical response of the dielectric constant when the water content within the substrate increases. The logarithmic fit presented corresponds to the typical behaviour of increased moisture levels in soil¹¹, thus, one can conclude that the calibration coefficients were adequately calculated due to the high degree of accuracy in the fit in both substrates.

⁸ The substrates were oven dried for 24 hrs at 105 degrees according to commonly documented drying procedures to preserve the integrity of the soil(Brendan C. O’Kelly. “Oven-drying characteristics of soils of different origins”. In: *Drying Technology* 23.5 [2005].).

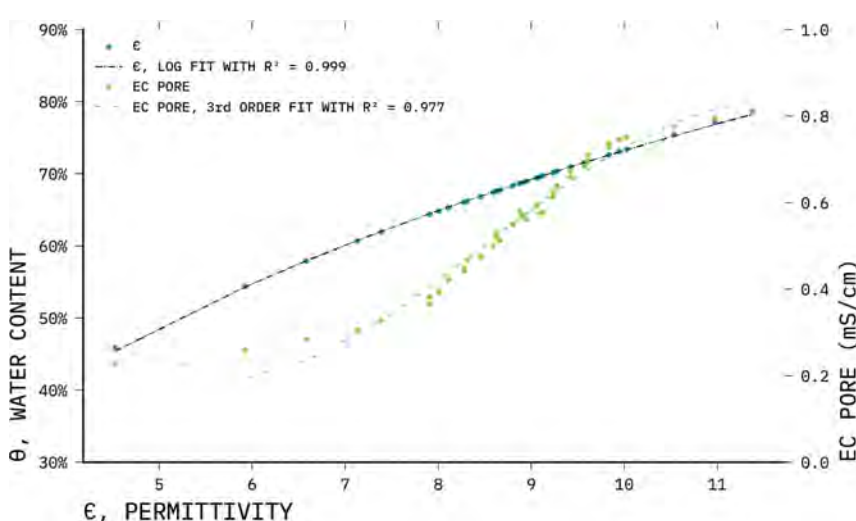
⁹ R. Oleszczuk et al. “Calibration of TDR for moisture determination in peat deposits”. In: *International Agrophysics* 18.2 (2004).

Table 10: Substrate conditions to calibrate the moisture sensor.

¹⁰ Starting with dry peat can hinder the experiment, as once peat is dry it exhibits hydrophobic properties making it challenging to adequately re-wet the substrate.

¹¹ Merja Myllys and Asko Simojoki. “Calibration of time domain reflectometry (TDR) for soil moisture measurements in cultivated peat soils”. In: *Suo* (1996).

Figure 67: S-01 TDR characterisation. The figure shows the change in permittivity and electrical pore conductivity as a function of water content.



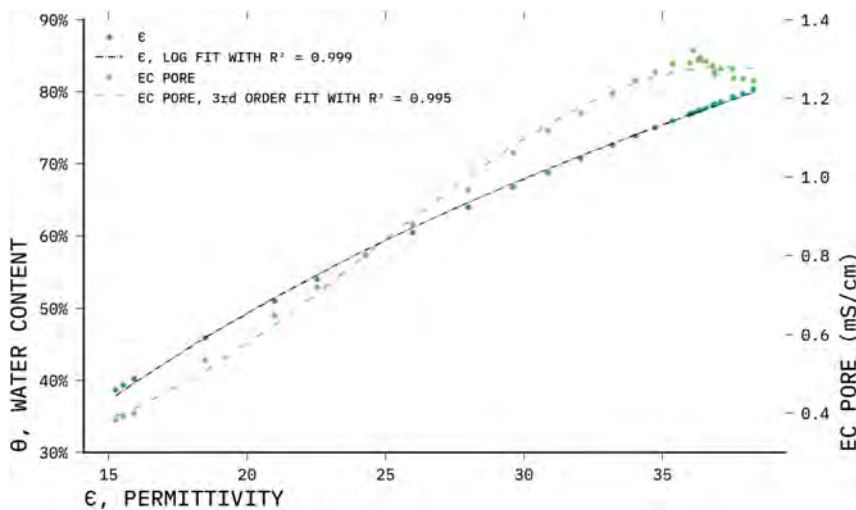


Figure 68: S-02 TDR characterisation. The figure shows the change in permittivity and electrical pore conductivity as a function of water content.

The following table summarises the fitted models for both responses as a function of permittivity:

SUBSTRATE	VARIABLE	MODEL
S-01	EC pore	$(-6.345x^3 + 162.706x^2 - 1226.678x + 3069.324) \times 10^{-3}$
	θ	$(359.091 \ln x - 96.040) \times 10^{-3}$
S-02	EC pore	$(-0.111x^3 + 8.170x^2 - 144.696x + 1092.283) \times 10^{-3}$
	θ	$(459.524 \ln x - 879.488) \times 10^{-3}$

Both substrates under study show a similar response between moisture content and permittivity, however, S-02 presents a higher permittivity range. This is likely due to the higher porosity of S-02 as there are more air-filled cavities where water can travel, thus, a higher variation and magnitude of the dielectric permittivity is expected¹². The electrical conductivity within the pores of the substrates (here referred to as EC pore) increases significantly as the substrates' water content surpasses 50%-60%. This is due to the spaces within the substrates' pore start to fill with water, filling spaces that previously contained air. In this case, S-02 shows higher EC values. This behaviour is expected due to the higher ionic content present in S-02's macronutrients content. As presented in the literature, the EC pore response is best described by a third order polynomial¹³, which in this case offers an accurate fit. However, there are other variables contributing to the difference in electrical conductivity of the pores. One of those variables is the porosity of the substrate, and while Archie's law¹⁴ is often used to describe the relationship between electrical conductivity and porosity, this model is poorly suited to explain the behaviour in peat substrates. Peat substrates exhibit a "dual porosity" which describes self-contained pores where solutes get trapped¹⁵ created by the high-organic content of the substrate.

The substrates were further characterised by obtaining their corresponding impedance spectra. The spectral characterisation was obtained using a 3D printed cubical vessel (Fig. 69) that can hold a volume of 421.88 cm^3 . The vessel has two parts, the main core and its

Table 11: Substrates' characterisation models for water content and EC pore as a function of permittivity change.

¹² Myron Dobson et al. "Microwave Dielectric Behavior of Wet Soil-Part II: Dielectric Mixing Models". In: *IEEE Transactions on Geoscience and Remote Sensing* Ge-23.1 (1985).

¹³ Oleszczuk et al., "Calibration of TDR for moisture determination in peat deposits".

¹⁴ Gustave E Archie et al. "The electrical resistivity log as an aid in determining some reservoir characteristics". In: *Transactions of the AIME* (1942).

¹⁵ Xavier Comas and Lee Slater. "Low-frequency electrical properties of peat". In: *Water Resources Research* 40.12 (2004).

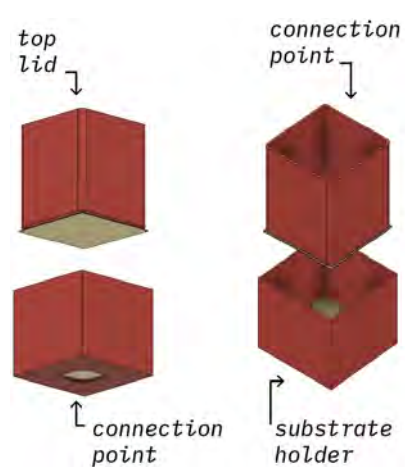


Figure 69: Cubical vessel used for the EIS characterisation in the present work.

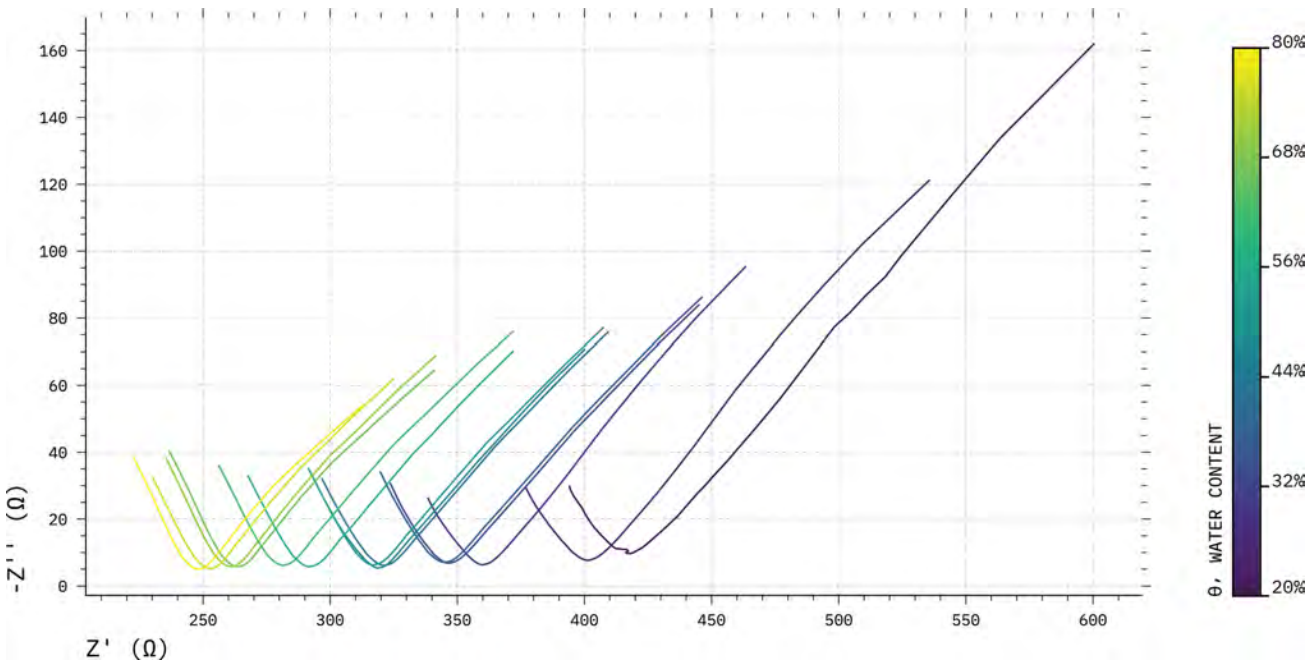


Figure 70: S-01 substrate EIS curves for different water contents. The right side of each curve corresponds to the lower frequencies of the spectral profile.

lid, both have a copper plate attached at the bottom with an aperture to allow for a direct connection to the plate. The vessel was filled with the substrates at $\approx 29.7\%$ and $\approx 38.5\%$ moisture content for S-01 and S-02 respectively. The average achieved “out-of-the-bag” BD was 0.5324 gr/cm^3 for S-01 and 0.5126 gr/cm^3 for S-02. Next, the impedance spectra was measured with a precision LCR meter (4284A, Hewlett Packard, Japan) through a Kelvin clip fixture (TLKB1, BK Precision, China) using a frequency range of $20 \text{ Hz} - 1 \text{ MHz}$. The spectral profiles of different moisture content levels were measured by adding 10 mL of tap water until saturation. Figs. 70 & 71 show the Nyquist plots resulting from the described process¹⁶. The figures follow the traditional naming convention used in EIS studies. The terms of reactance and resistance are referred to as Z'' and Z' respectively.

¹⁶ The plot describes the changes in magnitude of the impedance components from high (left side) to low (right side) frequency.

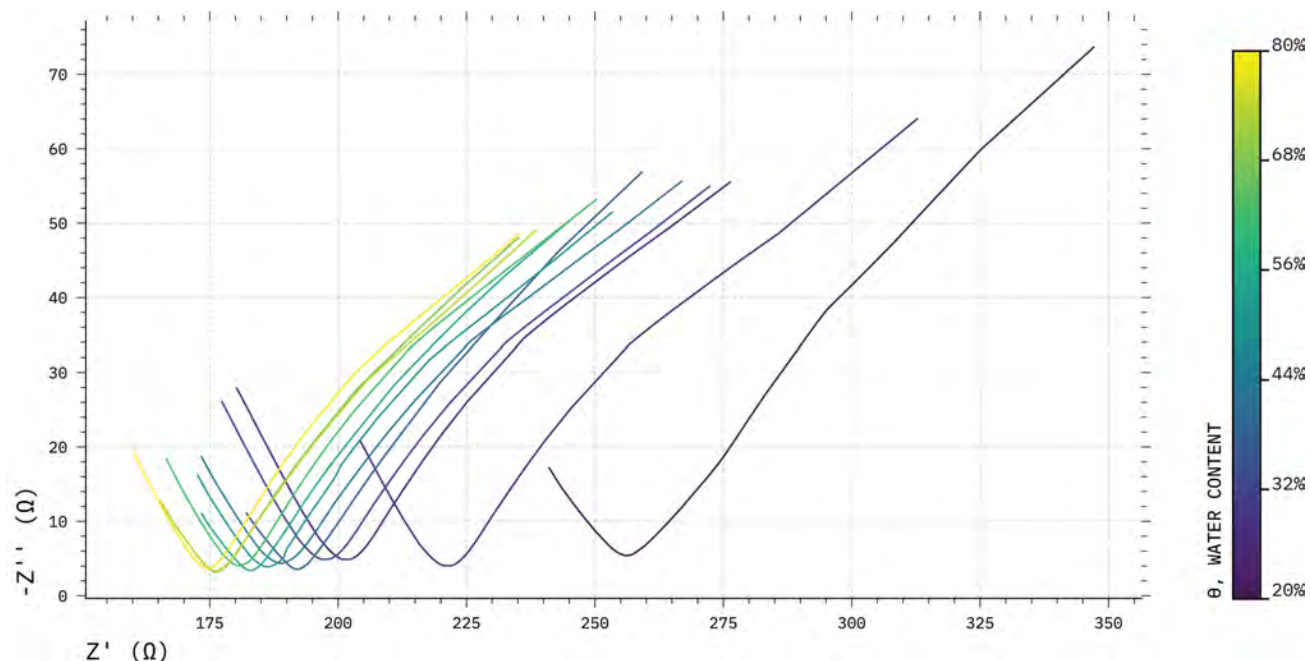


Figure 71: S-02 EIS curves for different water contents. The right side of each curve corresponds to the lower frequencies of the spectral profile.

As expected, the real part of the impedance decreases as the water content increases in both substrates. As more pores are filled with water, more continuous and direct paths will be created for the current to travel from one plate to another. Just as in the previous TDR characterisation, S-02 exhibits a lower level of resistance even when considering their different moisture content starting points. Since the maximum volumetric content that both substrates can reach is quite similar, it is likely that the difference in nutrient content and porosity are the causative agents for the difference in conductivity of both substrates. Furthermore, it can be seen that the initial state of the substrates has a dramatic increase after 10 – 20 mL have been added. The before mentioned behaviour can be explained with the aid of the EC pore results from the previous TDR analysis. As the substrates have a volumetric water content lower than %50, most of the substrate pores will be filled with air with some independent/disconnected pores. Thus, at the start of the experiment one can observe higher resistivity values.

Figs. 72 and 72 shows the individual components of the impedance changes that occur in both substrates as a function of the stimulation frequency for different levels of moisture content. It can be observed that while the resistivity behaves in a similar manner at different moisture contents, it decreases as the frequency increases. These results are in line with the response obtained through traditional resistivity profiling of soil^{17,18}.

Upon inspection of the EIS spectra (taking into consideration both Z' and Z''), one can observe that the resistivity dominates the magnitude of the response. This does not mean that the substrates behave like resistors. Even though, the magnitude of the imaginary component is small, this will introduce a phase shift in the total response that can add up to the shift already introduced by parasitic capacitances within the system multiplexing array (5.0). The behaviour of the imaginary part (Fig. 72 B) is consistent with that of colloid solutions containing electrolytes (e.g. tap water). Hence, a significantly lower reactance is observed¹⁹ at frequencies lower than 1 kHz.

When comparing both substrates' responses and considering their differences in initial moisture contents, S-01 resistivity range is greater than that of S-02 by at least 20% (when taking the third curve of S-01 as the starting point). The same performance is present when looking at the imaginary components of the substrates. S-02 shows no less than 15% less range than S-01. Nevertheless, in both cases the response of the real component always exceeds the variation in the imaginary component. Both substrates see an inversion of the trend that corresponds to the imaginary element at approx. 30 kHz and 20 kHz for S-01 and S-02 respectively.

According to the models presented by Cao et al. (2011)²⁰, the soil substrate is usually modelled as a single resistance. However, it is clear that this simple model does not fit well with the results obtained. The present work takes the electrochemical approach to model the peat

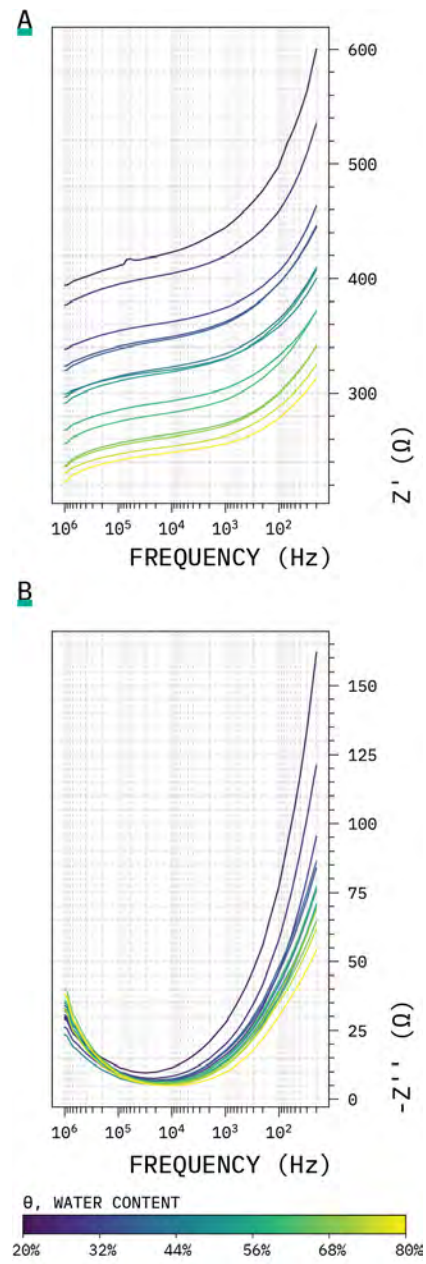


Figure 72: S-01 individual frequency response, where A. shows the resistance and B. displays the reactance at different water levels.

¹⁷ M. Fukue et al. "The micro-structures of clay given by resistivity measurements". In: *Engineering Geology* 54.1-2 (1999).

¹⁸ Samouëlian et al., "Electrical resistivity survey in soil science: A review".

¹⁹ Harry Ozier-Lafontaine and Thierry Bajazet. "Analysis of root growth by impedance spectroscopy (EIS)". in: *Plant and Soil* 277.1-2 (2005).

based substrates used. As Chloupek (1977)²¹ found, EIS methods are highly sensitive to the soil's ionic status, as well as its water content. Moreover, as described by Ozier-Lafontaine and Bajazet (2005)²², the electrical current flows through a path outlined by the soil pores. For this reason, the impedance of the soils is heavily defined by their structure and texture. Hence, a non-linear behaviour is expected when dealing with peat soils²³, as they have peculiar characteristics such as high compressibility, high water retention, presence of organic content, and low density.

Considering the three phasic nature of soil, one can define three main conductive current paths:

1. The pore conductive fluid path.
2. An insulated path created only by peat particles.
3. The interleaved path formed at the interface between soil particles and pore conductive fluid.

The first path acts mainly as an imperfect conductor that typically can be represented as an impedance with negligible reactance, i.e. a resistance²⁴. Furthermore, an additional double layer capacitor can be defined, as the substrate particles act as a dielectric surface that retains the energy transported by an alternate current. Lastly, at the interface between particles and fluid, the fluid's ions will flow towards the diffusion zone²⁵ of the peat-water interface²⁶.

The identification of the conductive paths is the first step to establish an equivalent circuit model of the peat-based substrate (Fig. 74). First, as previously mentioned, the fluid solution is modelled as a resistance R_f in parallel with a capacitive element C_f . Next, one needs to model the interface between the electrode and the substrate. The imperfections of the planar copper plates used as electrodes can create a dispersion effect due to difference in angular frequency between the electrode and the surface of the substrate. Therefore, a Constant Phase Element (CPE) can be used to model the different effects of this layer^{27,28}. CPEs are defined by the following equation $Z_{CPE} = Q_0^{-1}(j\omega)^{-n}$ where Q_0 (units $S \times cm^{-2} \times sec^{-n}$) describes the capacitance of the double layer and n characterises how far from ideal the element is by controlling the phase shift (e.g. $n = 1$ represents an ideal capacitor).

In addition to the before mentioned reactions, it is important to consider the electrochemical effects when an AC signal is applied to an electrolytic solution. One can model the voltage drop at the

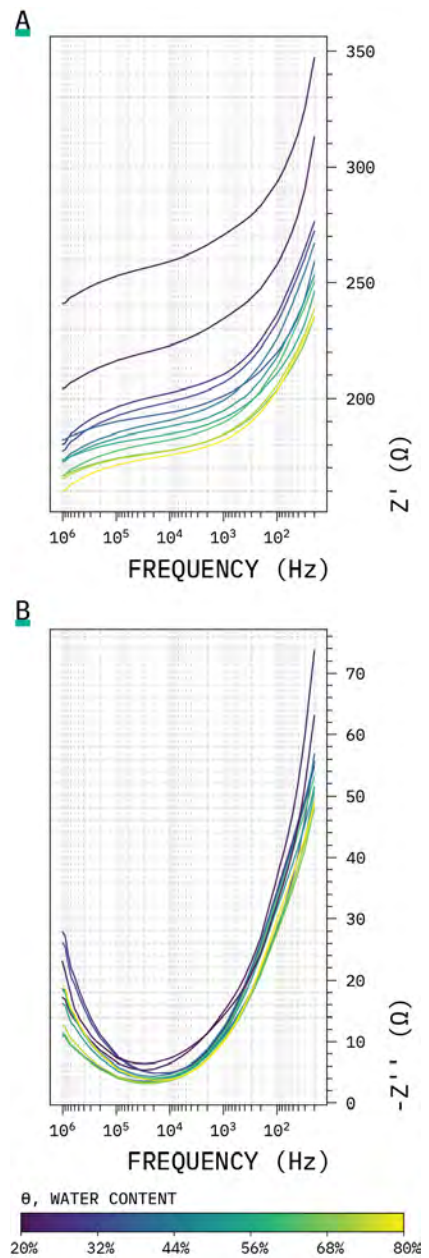


Figure 73: S-02 individual frequency response, where A. shows the resistance and B. displays the reactance at different water levels.

²⁰ Cao et al., "Analysis of the willow root system by electrical impedance spectroscopy".

²¹ Chloupek, "Evaluation of the size of a plant's root system using its electrical capacitance".

²² Ozier-Lafontaine and Bajazet, "Analysis of root growth by impedance spectroscopy (EIS)".

²³ Pengju Han. "Study on Mechanical Properties of Acidic and Alkaline Silty Soil by Electrochemical Impedance Spectroscopy". In: *International Journal of Electrochemical Science* 13 (2018).

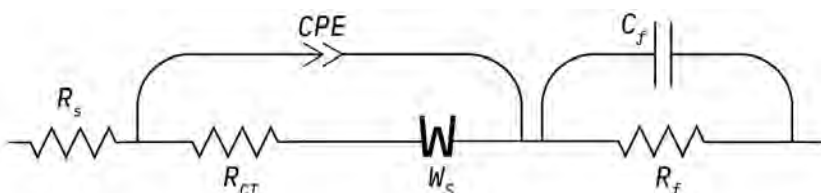


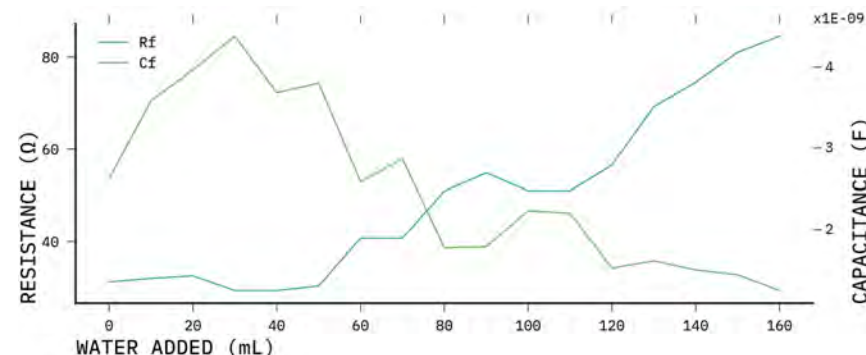
Figure 74: Proposed circuit analogue model for peat substrates

interface between the electrode and electrolyte solution using a resistive element, commonly named as charge-transfer resistance R_{CT} . Furthermore, a Warburg impedance W_s is introduced in series with the R_{CT} to describe the slow diffusion of ions from one part of the cell to the other where concentration gradients build up and relax with the applied AC input. The Warburg element is described by $W_s(\omega) = Z_0(j\omega)^{-1/2} \tanh \sqrt{j\omega}\tau$, where Z_0 (units $\Omega s^{-1/2}$) is the Warburg coefficient and τ is the structural information of the diffusion layer (units s). The model selected for the Warburg impedance is the Finite-length model or Warburg-short²⁹. The latter element is always present at lower frequencies and can be identified as a line with a 45° angle. Therefore, the model shown in Fig. 74 resembles a modified Randles circuit³⁰. Using this model, the frequency dependent impedance can be described using the following equation:

$$(99) \quad Z_{SUS}(\omega) = \frac{R_{CT}\sqrt{j\omega} + W_s \tanh(\sqrt{j\omega}\tau)}{R_{CT}Q_0(j\omega)^{n+1/2} + W_s \tanh(\sqrt{j\omega}\tau) + \sqrt{j\omega}} + R_s + \frac{R_f}{j\omega R_f C_f + 1}$$

The model above is fitted to the spectroscopy data obtained by using non-linear least squares regression with uniform weighting³¹. All EIS curves with different water contents are fitted initially to determine the constant values of the structural elements R_s , and τ . The values obtained are averaged and used as constants for the second fitting process. The found values are $R_s = 5.6\Omega$, $\tau = 160\text{ ms}$, and $R_s = 8.1\Omega$, $\tau = 230\text{ ms}$ for S-01 and S-02 respectively. By fitting the curves with the before-mentioned process, the relationship between the elements of the analogue circuit with respect to the water content was further explored.

Figs. 75 and 76 show the impedance response of the fluid as more water is added to the testing vessel. Both substrates exhibit a small range of impedance values in both their real and imaginary component. Both figures present an upward exponential trend with respect to the resistive element, which starts raising at approximately half the range of the x-axis. The resistivity elements of both substrates share a similar range of values with S-02 being 12.3% above S-01's range. The



²⁴ Juan Bisquert et al. "Doubling Exponent Models for the Analysis of Porous Film Electrodes by Impedance Relaxation of TiO₂ Nanoporous in Aqueous Solution". In: *Journal of Physical Chemistry B* 104.10 (2000).

²⁵ In electrochemistry, this zone is the one that is closer to the electrode's surface, where the concentration of ions is substantially different from that of the bulk material.

²⁶ Samouelian et al., "Electrical resistivity survey in soil science: A review".

²⁷ Pengju Han et al. "Electrochemical Corrosion Behavior of X70 Steel in Sand Soil Contaminated by Copper(II)". In: *Int. J. Electrochem. Sci.* 11 (2016).

²⁸ CPE elements are used in electrochemistry EIS to describe imperfect capacitors. The units of CPE elements are 1s

²⁹ A Warburg short essentially describes a linear diffusion, in the electrode-electrolyte interface, as a homogeneous layer with finite thickness.

³⁰ Xiao-Zi Yuan et al. "EIS Equivalent Circuits". In: *Electrochemical Impedance Spectroscopy in PEM Fuel Cells*. London: Springer London, 2010.

³¹ The optimisation was conducted using the least_squares function from the python package scipy.optimize.

Figure 75: Changes in the fluid components of the analogue circuit model representing the fluid as water content increases in S-01.

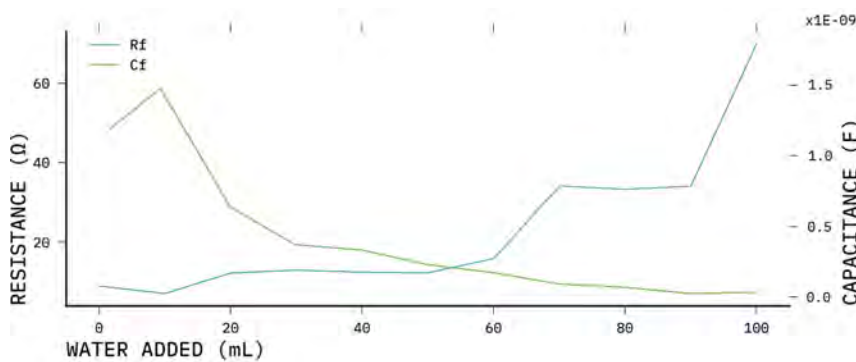


Figure 76: Changes in the fluid components of the analogue circuit model representing the fluid as water content increases in S-02.

maximum resistance value at the saturation point is consubstantial for both substrates with S-01 showing a maximum value 11% higher than that of S-02. In contrast, the imaginary component shows a continuous decline as the water content increases. In S-02 the decline shown behaves exponentially, while in S-01 the trend is more linear. It can be observed that S-02 starts with a higher level of capacitance, at least 10 times that of S-01. However, when reaching 30 mL of added water, the capacitance values become closer to the ones observed in S-01. Furthermore, both substrates' capacitive elements show an initial upward trend until reaching a certain moisture water content, where the trend is inverted. Even though the decline of the imaginary elements tends towards zero, the capacitance present from the beginning of the experiment can be considered significantly small. For this reason, the fluid's impedance magnitude in both cases will mostly be determined by R_f .

The above effects are expected, as the resistance of the liquid can be modelled as a traditional wire as in Eq. 2. However, the behaviour of the capacitive element is more complex. The decline in capacitance is due to the water filling more pores; pores from which some macronutrient ions will interact with the added water, making it more conductive. As a result, the relative permittivity of the water will start decreasing³², and by proxy, the capacitance of C_f will also drop as it is directly proportional to the permittivity value (Eq. 3). The slight increase in capacitance at the beginning of both plots is due to the significant presence of air filled pores that can act as a capacitor in

³² J. B. Hasted et al. "Dielectric Properties of Aqueous Ionic Solutions. Parts I and II". in: *The Journal of Chemical Physics* 16.1 (2004); Nir Gavish and Keith Promislow. "Dependence of the dielectric constant of electrolyte solutions on ionic concentration - a microfield approach". In: 22 (2012).

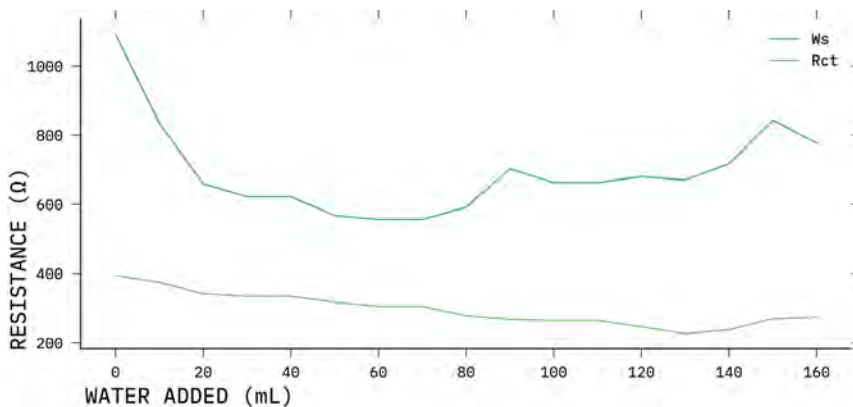


Figure 77: Changes in the Warburg and charge-transfer resistance as the water content increases in S-01.

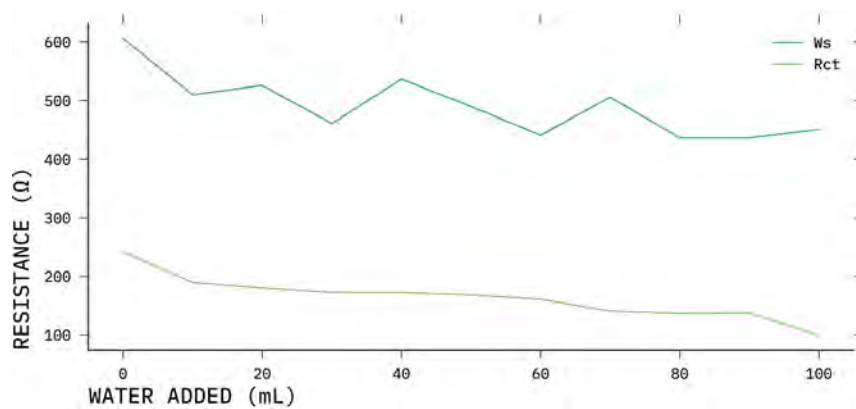


Figure 78: Changes in the Warburg and charge-transfer resistance as the water content increases in S-02.

parallel with the water, however, as the water starts filling the pores the capacitor becomes more homogenous with water becoming its main dielectric component.

Fig. 77 and 78 represent the changes in R_{CT} and the Warburg impedance for S-01 and S0-2 respectively. The charge-transfer resistance can be observed in the original EIS curves. R_{CT} is the point where the imaginary component of the impedance is at its minimum usually tending towards zero. Moreover, as the water content increases one can see that this point shifts slowly. The value of R_{CT} is directly related to the electrolytes present in the substance under study. At higher electrolyte values the charge-transfer location leans towards zero (i.e. the substance under study becomes more conductive). The range of R_{CT} for S-01 is understandably higher due to the lower moisture content at its “out-of-the-bag” condition. Nevertheless, at saturation point the charge-transfer resistance in S-02 is $\approx 30\%$ lower than that of S-01.

In the case of the Warburg magnitude factor, there both substrates show an almost continuous declining trend. While the range of W_s is again larger for S-01, when considering the values after 30 mL of added water, both substrates share a similar range. In S-01 an inverse logarithmic trend is shown at the beginning. This is due to the lack of water needed to transport the electrolytes close to the diffusion layer. Such effect can be explained considering that a higher ability of ions decreases the time in which the diffusion layer will form at the interface. Furthermore, S-01 presents a Warburg magnitude $\approx 40\%$ higher than that of S-02. Both elements’ behaviours corroborate the presence of higher levels of macronutrients in S-02.

Figs 79 and 80 show how the components that describe the CPE change with different water contents. In both substrates, the CPE magnitudes present an exponential upward trend. On the other hand, their corresponding coefficients present a continuous downward trend. S-02 CPE Q_0 presents a lower magnitude with an upward exponential trend, whereas, S-01 magnitude is three orders of magnitude bigger and presents a more linear trend. In general, one should only consider the overall upward or downward trend of the CPE elements as the different soil moisture content of the samples will affect the steepness.

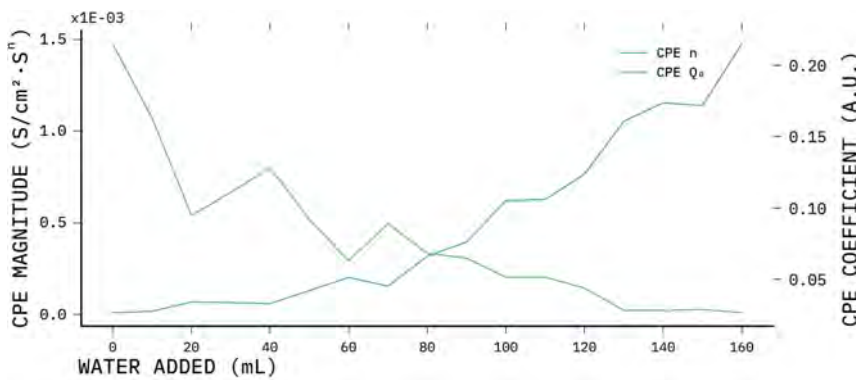


Figure 79: Changes in the CPE characteristics as water content increases in S-01.

Moreover, while the trends of the elements might behave similarly in both substrates, their characteristics are drastically different. The inclusion of the CPE element is to address the imperfections of the copper plates used as electrodes, and their possible non-uniform current distribution. However, this is only an assumption required to fit the data to the model. In other words, while the behaviour of the CPE might not correspond to the behaviour of the assumption made, still the CPE is a crucial tool to model the interaction³³. Following the recommendations of Yuan et al. (2010)³⁴ since the S-01 CPE n has a range between 0.0 – 0.2, (Fig. 79) then the CPE can be understood as a distorted electrode, whose value increases with an increased contact with the liquid as the water content rises. However, in the case of S-02's n , the coefficient has a range of 0.32 – 0.50. This range means that from its starting point up until 70 mL of added water, the CPE element represents a non-static diffusion. After 70 mL, for values below $n = 0.40$, the CPE can describe an inhomogeneous reaction rate at the surface.

From Eq. 99, one can conclude that the behaviour of the substrates is characterised mostly by the R_{CT} and Warburg element. Thus, it is expected to behave mostly as a linear resistor across most frequencies. Nevertheless, the reactance component of the substrates is expected to increase in the presence of low water levels. Furthermore, considering that both impedance elements are directly related to the ionic content of the liquid being introduced, as the liquid travels through the substrate, the nutrients present in it will move with the

³³ Evgenij Barsoukov and J. Ross Macdonald. *Impedance Spectroscopy*. Ed. by Evgenij Barsoukov and J. Ross Macdonald. Wiley, 2005.

³⁴ Yuan et al., "EIS Equivalent Circuits".

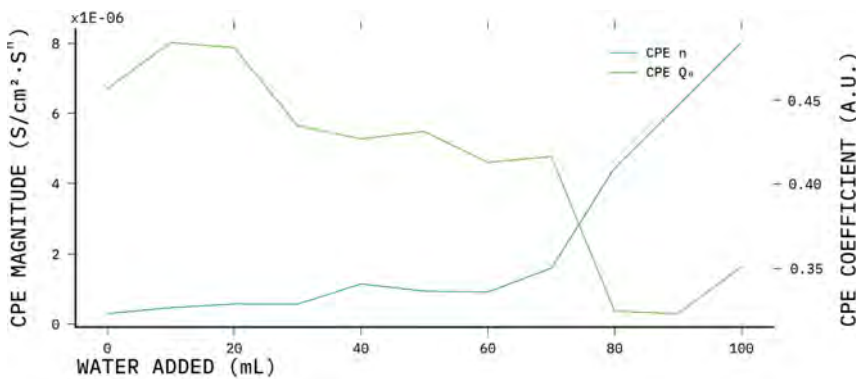


Figure 80: Changes in the CPE characteristics as water content increases in S-02.

fluid, making ions more readily available at certain regions.

The presented characterisation of the substrates' electrical behaviour allows us to explain the effects seen in the following experiments, as water movement in soil is a complex topic.

6.3 Substrate preparation

The present section describes the protocol used to fill the smart rhizotron with the substrates previously characterised. Having a defined protocol improves the repeatability of pot-experiments. Bulk density has been proven to affect RSA development, as well as biomass production³⁵. A preparation protocol not only helps better define subjects of a statistical population but can help improve EIT'S ability of detecting subsoil pathogens, as previous research has demonstrated³⁶. The goal of the protocol is to create a homogenous substrate core that has a similar electrical response at each of its layers.

One caveat of the protocol used in previous research efforts, was the complexity of it, as well as the time required to fill one pot of 18 × 13 cm. For this reason, a new preparation protocol was developed to help overcome the issues of working with peat-based substrates.

6.3.1 Packing protocol

Traditional substrate packing protocols rely on drying the substrate first to achieve a certain BD. However, as mentioned in the previous section, the challenges of working with peat-based substrates is that they can become hydrophobic when at low moisture levels. Therefore, it is impossible to apply the common dry BD protocol. Using a previously developed protocol based on the BSI standard BS EN 12580:2013, homogenous packing was achieved using a peat substrate. Nevertheless, the process requires extensive preparation that allows the soil to settle for at least one-week. Furthermore, the actual filling process could take up to two hours for one pot.

A new preparation and pot-filling protocol was developed to reduce preparation time. The developed protocols take into consideration the wet BD of the substrate (a more adequate measure for peat), and watering from the bottom. The latter avoids a significant movement of nutrients by allowing water to travel using the matric potential that results from the capillary properties of the high porous media³⁷.

Fig. 81 gives an overview of the steps involved in the pot packing protocol. The protocol is divided into two phases: preparation and filling. The first ensures that the media is homogenous by removing big particles of organic content³⁸. Next, the sieved media is put into small individual containers that are then watered until saturation. At the same time, one can start calculating the desired BD by sectioning the vessel into layers. Using the saturated substrate, one layer of the vessel should be filled with a desired compaction³⁹. Once the layer

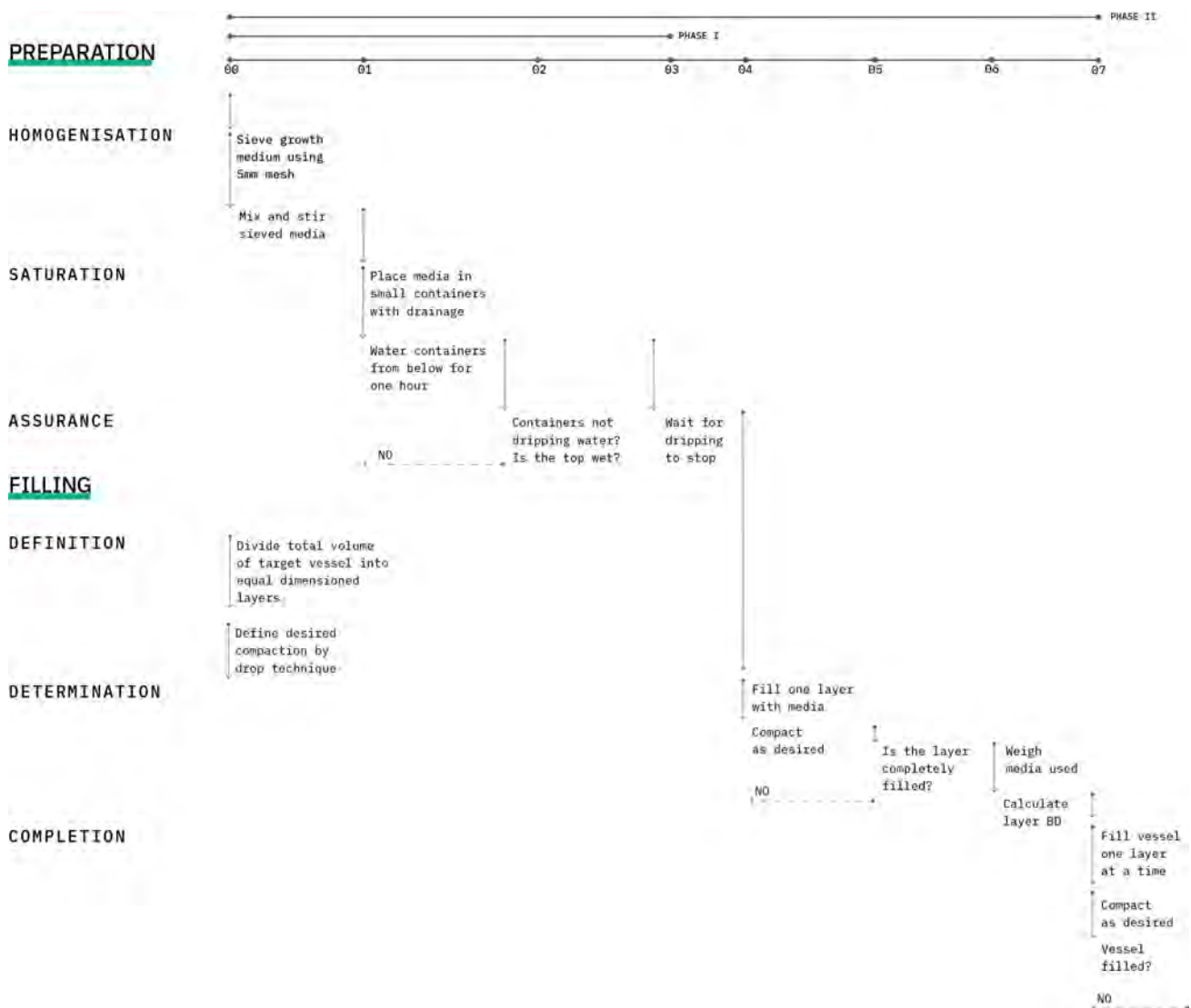
³⁵ R J Stirzaker et al. *Soil structure and plant growth: Impact of bulk density and biopores*. Tech. rep.

³⁶ Corona-Lopez et al., "Electrical impedance tomography as a tool for phenotyping plant roots".

³⁷ If this cannot be achieved due to the height of the vessel employed, a slow introduction of the water can be achieved using a fine sieve or mesh.

³⁸ The sieving of the media is not necessary to carry out EIT experiments, but it greatly improves the resolution of the reconstructions, specially in tdEIT.

³⁹ The compaction method suggested and used throughout this work is to drop a piston or weight, that covers most of the substrate, from a determined height and certain number of times. This ensures the repeatability of the compaction across layers.



is filled, the substrate is weighted to determine the wet BD for one layer, thus, the BD of the whole vessel can be estimated. The repetition of the latter process until the whole vessel is filled corresponds to the second phase of the protocol.

Figure 81: Wet pot packing protocol used in experiments.

6.4 Air drying experiment

The present experiment tracks the evolution of a fully saturated S-01 inside the smart rhizotron left to air dry for fifteen days. The vessel was filled using the protocol previously described and left to settle for one day prior to the measurement acquisition. The vessel was left sitting in a bed of water for twelve hours before the experiment in order to compensate for any water loss during the settling time. S-01 was kept inside the growth chamber at 20° C under a 12h/12h day and night cycle. EIT measurements were taken every 35 minutes⁴⁰. Weight measurements were obtained at the start of each measurement cycle. The frequencies analysed were: 1kHz, 10kHz, and 50kHz. Both planar and square protocols were explored. The frequencies explored

⁴⁰ The first 25 minutes corresponds to the actual data acquisition and the other 10 minutes corresponds to the spacing between acquisition periods.

were selected using the EIS profiles previously obtained. The three frequencies correspond to the linear part, complex inflection point, and complex inversion curve of the EIS profile for S-01. Three frequencies were selected as a compromise between acquisition time and amount of data. The planar arrangement uses S1/M1, and S3/M7. The square protocol employs S1/M1, and S5/M6. All measurements were temperature calibrated and set at 1 mA. The data sets were collected using 64 electrodes from the even ring combination of the smart rhizotron. The reason for such selection was to maximise the system's ability to obtain data since the drying of peat typically shrinks the substrate, pulling it away from the outer edges of the cylinder. A total of 9,000 data sets were obtained, with each protocol having an average of 745 sets per frequency⁴¹. Due to the amount of data, important considerations were taken into account to guarantee the quality of the reconstructions. The considerations were:

1. Implementation of a Multi-ring stimulation strategy.
2. Filtering of erroneous data-sets.
3. Covariance matrix calculation to mitigate for possible reciprocity errors in the data.
4. Robust reconstruction algorithm.

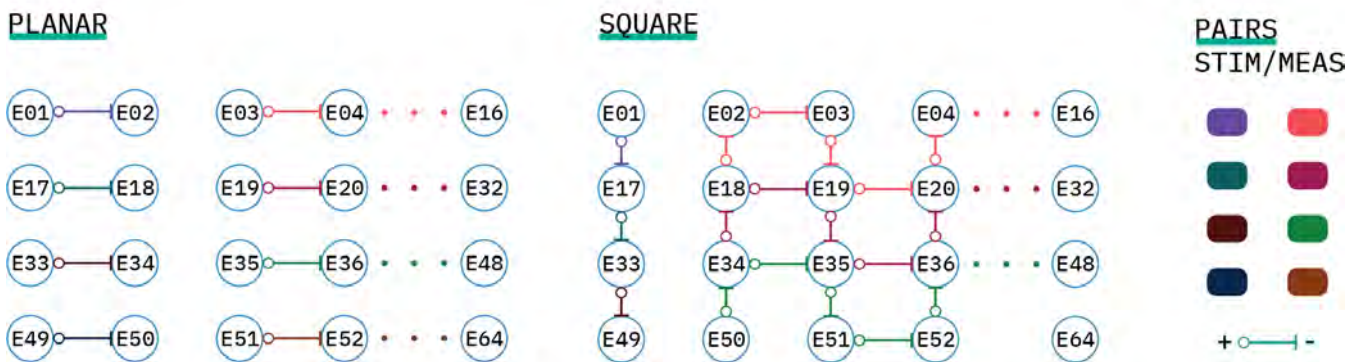
The need for a different stimulation strategy was discovered during initial tests of the vessel functionality. The tests involved obtaining the typical "U-shape" signal signature for each individual ring. The second test was to obtain a complete data set with the previously mentioned protocols. From the results, it became obvious that the non-homogeneous nature of the substrate made the travel of current from high to low positioned electrodes challenging if not impossible. By comparing the data-sets to simulated measurements using FEM modelling, it became apparent that the test data-sets had high levels of reciprocity errors⁴². The errors were particularly high ($\approx 90\%$) when comparing reciprocal measurements from the top and bottom ring in both square and planar strategies. When data agrees with the results from a simulated model then a sensible result can be expected. However, reciprocity errors resulting either from a discontinuity in the electrode, or in this case a lack of current input and a non-homogenous substrate, can create significant data mismatches that will undoubtedly lead to unexpected artefacts in the final image.

The first point to avoid conflating the quality of the data with the results obtained from the reconstruction process, was to develop a multi-ring strategy. The S/M patterns presented so far in this work employ a continuous strategy i.e. all electrodes will interact with each other at some point during the data acquisition⁴³. This not only increases the chances of creating reciprocity errors, but also, having more measurements means increased acquisition and processing times. The multi-ring strategy (Fig. 82) considers independent rings for planar arrangements, and sectioned squares for square arrangements. By having independent rings, in the case of planar arrangements, one can

⁴¹ The average is considered as faulty sets were discarded during the reconstruction process.

⁴² In the context of EIT, reciprocity refers to the principle that Kelvin measurements, under ideal conditions, will be the same if the stimulation and measurement electrodes pairs invert their roles.

⁴³ This can also be understood as having just one ring with 64 electrodes. For instance, if the stimulation is driven through electrode 1 and 2, at some point the protocol will measure between electrodes 63 and 64 (in the case of a S1/M1 strategy).



simplify the acquisition process while ensuring maximum reciprocity. Having independent rings means that the vertical resolution of the 3D reconstructions will be fairly limited, but a guaranteed convergent solution can be achieved. Moreover, this can allow users to dismiss an entire ring when reconstructing data coming from detached electrodes caused by shrinkage of the substrate (particularly at the top of the vessel). The multi-ring square protocols were designed to maintain the vertical resolution of the system while ensuring minimal reciprocity errors. The S/M protocol in this case, obtains data in subsequent square arrangements. The latter means to create an initial square using two rings, then to create another ring using the last ring and the following one, and so on until the last ring is reached.

The multi-ring strategy offers a balanced approach to the amount of acquired data while helping to ensure that reasonable reconstructions can be achieved. However, as with any system, interference in the communication devices can occur, leading to missing information or poorly formatted data. The approach taken in this experiment was to filter out poorly formatted data-sets. Due to the amount of data, only a few data-sets were not considered for reconstruction (less than $\approx 2\%$ per frequency).

The final steps taken to guarantee the quality of the images relate to the reconstruction algorithm. Using the quadratic reciprocity error:

$$(100) \quad \mathbf{e}_n^2 = (y - y_r)^2$$

where y represents the measurements taken and y_r the reciprocity vector, a diagonal weighting matrix was introduced as:

$$(101) \quad \mathbf{W} = e^{-(\mathbf{e}_n^2 / \tau)}$$

The reciprocity vector is constructed by indexing the corresponding reciprocal pair of every measurement. Thus, there is n -th reciprocal errors. Here τ serves as a filtering factor. In other words, final conductivity values with reciprocal errors much greater than τ will be cut-off by \mathbf{W} . In this way, one can automate the detection of faulty electrodes

Figure 82: Multi-ring stimulation and measurement protocols considered for both planar and square arrangements. The figure exemplifies a S1/M1 configuration for both arrangements.

and objectively filter out faulty data⁴⁴.

The reciprocity error works with S/M protocols that use the same skip for both the stimulation and measurement electrodes. However, for patterns using different skips a three-step approach was taken. The reciprocal patterns were used to determine the timing and location of the electrode errors. Then, an initial image reconstruction was performed at the first instance in time when electrode errors started happening. Thirdly, depending on the effect of the faulty electrodes in the final results the measurements from the affected electrodes were removed by zeroing their corresponding elements in \mathbf{W} . The electrodes that incurred faults were E8, E12. If no reciprocity error greater than τ is present, \mathbf{W} is calculated as the inverse covariance of the measurements.

Finally, a robust Gauss-Newton iterative solver was used to guarantee the quality of the final reconstructions⁴⁵. The latter leads to a poor fit of the data and the distribution presented in the image. Therefore, an iterative solution was preferred despite its reliance on calculating the forward solution upon each iteration, since each iteration further improves the final fit of the data. All voltage measurements were normalized using their corresponding current measurement. Planar arrangements consisted of 832 and 768 measurements for S1/M1 and S3/M7 respectively. Square configurations obtained 2784 and 2688 measurements for S1/M1 and S5/M6 respectively.

The hyperparameter (λ) for the reconstructions was computed using the L-curve criterion. The hyperparameter for each data set was computed, and then the final hyperparameter was selected using the median of the samples. Table 12 presents the hyperparameters used for all protocols across the different frequencies. The selection was made to achieve a smooth transition between data sets. Upon examination of the computed hyperparameters, it was noted that the distribution of values was highly skewed. Therefore, rather than using a specific hyperparameter for each data-set, the non normality of the distribution imposed the before-mentioned approach. The criteria to stop was if there was no improvement (differential residual $> 10\%$) in the solution's residual when compared to the previous iteration, and to stop after five iterations. The regularization scheme selected for the reconstructions was the Tikhonov method in order to keep the reconstruction simple and robust. The data was fitted to a FEM model consisting of 5577 elements that represent the inner cylinder⁴⁶ of the smart rhizotron.

⁴⁴ One typical approach is to remove all measurements from the faulty electrodes when performing the reconstruction. While this helps obtain a reasonable reconstruction, it is highly dependent on the expertise of the user and their ability to detect the fault.

⁴⁵ While a one-step solver can be substantially faster, the reciprocal errors expected due to substrate shrinkage can make one-step solvers overestimate conductivity values near faulty electrodes.

⁴⁶ The vessel was filled up to the first ring of electrodes, thus, the model represents an effective height of 37.2 cm.

Table 12: Computed hyperparameters for all S/M protocols.

CONFIGURATION	PROTOCOL	λ AT 1 kHz	λ AT 10 kHz	λ AT 50 kHz
PLANAR	S1/M1	1.472e-04	1.876e-04	2.056e-04
	S3/M7	5.795e-04	5.795e-04	5.795e-04
SQUARE	S1/M1	5.940e-04	7.021e-04	7.021e-04
	S5/M6	5.878e-04	8.106e-04	8.467e-04

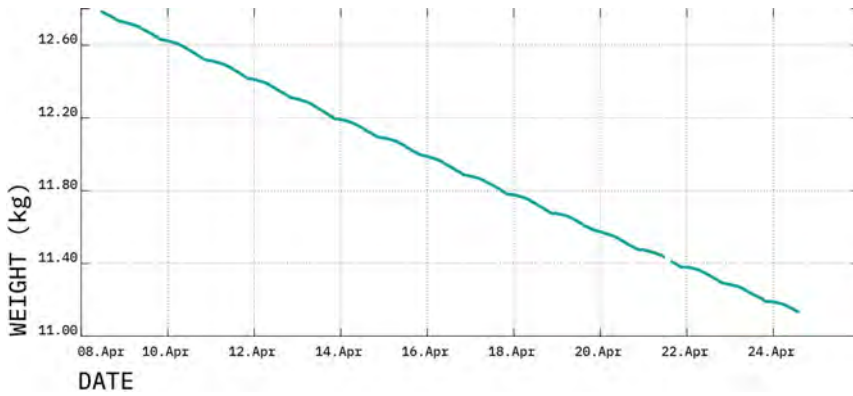


Figure 83: Evolution of S-01's weight across the duration of the experiment.

6.4.1 Results

Fig. 83 shows how the weight of S-01 changed over the duration of the experiment. One can observe a downward trend that corresponds with the drying process of the substrate. The drying process affects the water content inside the vessel in small decrements. For example, a 3% decrease occurs approximately every four days. There is a clear trend that can be used to estimate the volumetric water content of the system in the future. Upon closer inspection of the plot presented, one can observe that the rate of decrease is not entirely linear. The data shows “bumps” at certain points. These anomalies in the linear trend correspond to the night cycle when the lights are off, thus, a decrease in temperature is expected to slow down the drying process of the system. By removing the trend using a moving average approach (Fig. 84), one can observe that the data is non-stationary and that there is seasonality present. The non-stationary nature was confirmed through the Augmented Dickey-Fuller (ADF) test, which corroborates the presence of a unit-root. Further analysis of the data set reveals that the data is heavily autocorrelated.

The seasonal nature of the data is expected due to the day-night cycles. A better model for this type of behaviour can be described using a state space model. The time series was modelled using a Seasonal ARIMA model corresponding to SARIMA(1, 1, 1)(1, 0, 1)₅₀. The seasonal element of 50 was selected as the data corresponding to one day/night cycle contains that amount of data points. The fit was further evaluated through the Ljung-Box chi-square approach, which confirmed that the residuals are not autocorrelated with $p > 0.05$. Moreover, the residuals obtained when comparing the model to the data present a normal Gaussian distribution. The estimated parameters as well as their performance are described in the following table.

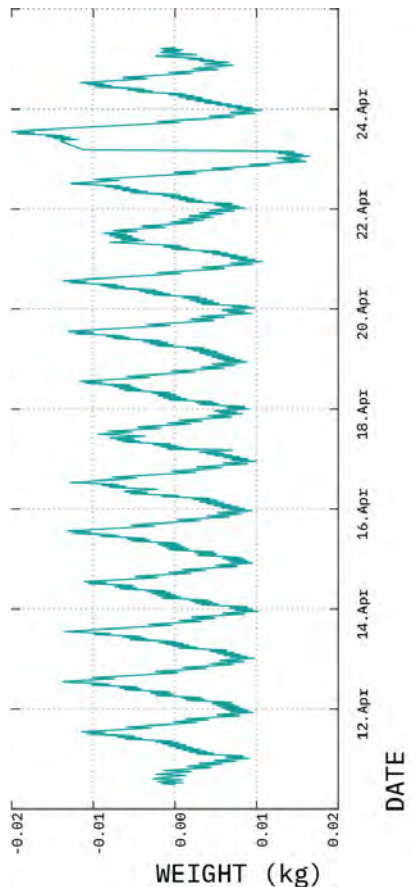


Figure 84: De-trended weight response.

TYPE	COEFFICIENT	STANDARD ERROR	T-STATISTIC	P-VALUE
AR 1	-0.347	0.082	-4.209	0.000
MA 1	-0.359	0.093	-3.840	0.000
SAR 50	0.987	0.010	95.605	0.001
SMA 50	-0.674	0.068	-9.8254	0.000

Table 13: Estimation results for S-01's SARIMA model

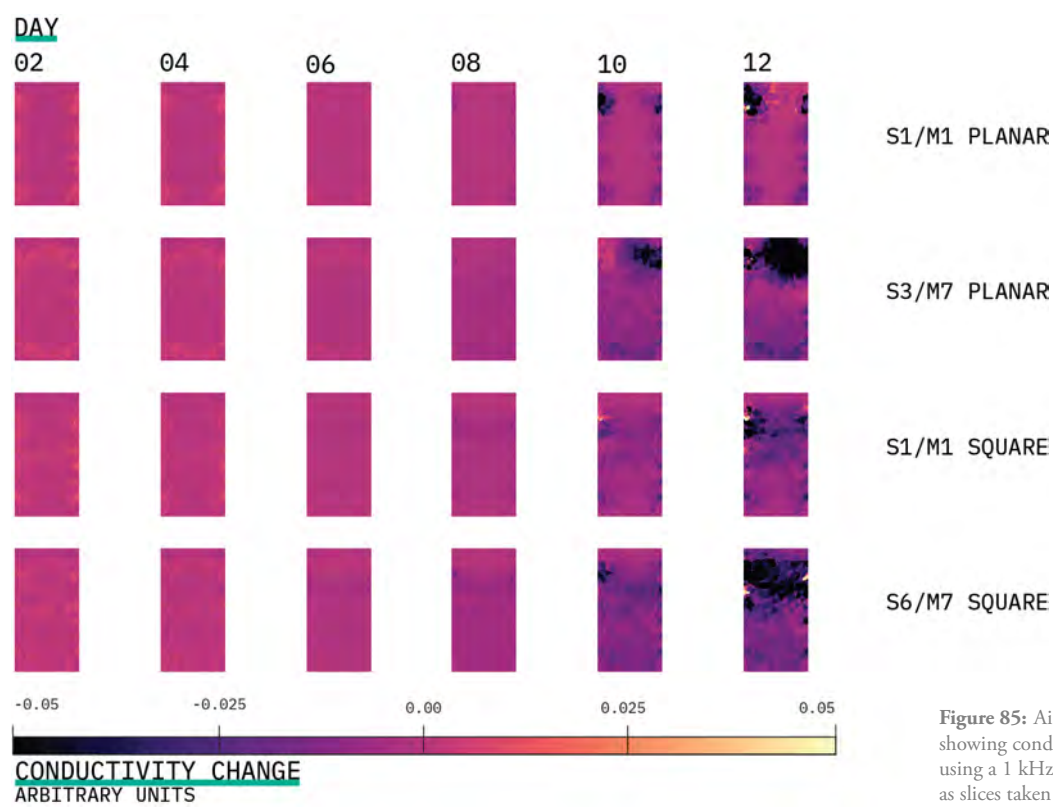
A cross-sectional analysis of the reconstructions is presented near

⁴⁷ Pages 144 and 145

the end of this section⁴⁷. The reference data sets selected were the ones taken at the beginning of the experiment at 9:00 AM on 8th April 2021. The reference point represents the initial acquisition taken before the vessel was left standing still on a bed of water. The vessel was moved to the growth chamber at 18:25, and this corresponds to the initialisation of the weight measurement acquisition. The obtained images represent the subsequent change in admittance from the reference point till the end of the experiment at 11:00 AM on 23rd April 2021. The admittance⁴⁸ changes are presented as their individual parts. Therefore, there is a set of images that correspond to the admittance's real part and another one corresponding to its imaginary part. The reconstructions are shown as vertical and horizontal section planes. The images shown are from the points in time when the night cycle ended⁴⁹.

DATA QUALITY

Observing the reconstructions from Fig. 85, the limitations of the S1M1 planar pattern become immediately apparent. As the sensitivity of this particular configuration is significantly higher near the edges of the system, the reconstruction algorithm maps most conductivity changes to the vicinity of the electrodes. On the other hand, the same version of the protocol under a square arrangement performs significantly better, being able to map small conductivity changes across all elements. Nevertheless, the pattern still presents a certain bias to over/under-estimate values near the edges of the vessel. In contrast, protocols using higher skips show a more evenly spread distribution of the small conductivity changes.



⁴⁸ The term admittance is essentially the inverse of impedance i.e. $Y = 1/Z$. Therefore, the real and imaginary components for admittance are referred to as conductivity and susceptance respectively.

⁴⁹ Thus, they can be understood as the last image of the day/night cycle.

Figure 85: Air-drying experiment reconstructions showing conductivity changes of all protocols using a 1 kHz stimulation. Images presented as slices taken at the centre of the vessel in its y-planes. All slices represent the first frame at the beginning of the day cycle.

As expected, the vertical resolution of planar configurations is limited, and when closer to the last days of the experiment there is a tendency to concentrate most changes to the electrode surface and plane. Furthermore, when comparing planar against square configurations, there is a clear lack of agreement between reconstructions using planar arrangements. The explanation for this is due to the shrinkage of the substrate and how it affects each S/M protocol. For instance the S1/M1 protocol by using adjacent electrode pairs will present more reciprocity errors since having one faulty electrode implies that at least two pairs will contain erratic measurements or greater noise⁵⁰. Moreover, with the filtering of faulty electrodes considered in the reconstruction algorithm, this type of protocol will lack the same level of information that the other protocols present. In the case of protocols with uneven skips such as S3/M7, the effect of faulty electrodes is less pronounced, presenting small artefacts of contrasting amplitudes near the source of the fault. These errors can be further examined when analysing the pseudosection of the raw data in relation to the forward model.

Pseudo-sections of raw data are commonly used in geophysics to further examine its behaviour. Fig. 85 shows the pseudo-section of the difference between the reference data set and the data from day 10 when a high reciprocity error was detected. Considering polar coordinates, the before-mentioned representation angle shows the average location of all electrodes for a specific measurement, and the radius can be understood as the separation between electrodes and the surface of the vessel⁵¹. The average magnitude of the difference data is expressed through its colour map. In Fig. 86 a strong contrasting measurement can be observed at $(-0.135, -0.360)$. The location of this contrast takes place between electrodes E8 through E10. Presenting a high voltage value can be interpreted as a loose connection between the electrode and the substrate. However, it is important to note that the position of the data set in the pseudo-section's grid has a certain level of randomness, and should not be treated as an image reconstruction. Even so, by visualising EIT data in this way, users can quickly detect inconsistencies associated with conductivity anomalies, or faulty electrodes. Thus, adjacent protocols, by having a greater sensitivity near the edges of the vessel, can be used to track small changes in the vicinity of the electrode that can lead to errors caused by electrode movement, loose contact with the substrate, and complete detachment from the substrate.

Square configurations show an enhanced level of agreement with respect to their final reconstructions. The key difference between both protocols is the sensitivity⁵². Since S5/M6 has a higher sensitivity in the centre, one can expect a more accurate distribution of the data across the centre of the vessel. While similar conductivity maps can be observed in both square protocols, akin to the planar S1/M1 the adjacent square protocol tends to image significant conductivity changes towards the edges of the vessel. Nevertheless, this does not mean that

⁵⁰ For example, if the faulty electrode is E1, then all the measurements taken with pairs E1-E2 and E16-E1 will contain errors.

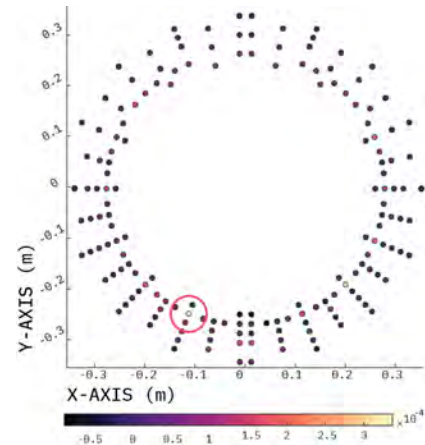


Figure 86: Pseudo-section representing the difference in voltage magnitude between the reference and the electrode fault time-point. The detected fault is circled in red.

⁵¹ The method visualises and sorts data into a colour coded two-dimensional grid. The plot does not represent a reconstruction of the data.

⁵² The sensitivity analysis of different skip protocols was explored in Chapters 2 and 3.

adjacent protocols should be avoided. In the present work, adjacent protocols are used as a tool to track electrode faults. The next analysis is focused on the reconstructions obtained with square configurations enhanced through an adequate selection of \mathbf{W} , aided by the previous analysis of the data from planar configurations.

RECONSTRUCTION ANALYSIS

The overall evolution of the drying process with respect to a reference time-point at field capacity conditions can be observed in Fig. 87, and a more detail cross-examination is presented in Figs. 88 & 89.

Conductivity and susceptance decrements are indicated by darker colours. During the first six days, an increase in conductivity can be observed. The iso-volumes presented in Fig. 87 represent the decremental change in the range of the minimum change at the end of the experiment and 1% of that value, i.e. a range from $-5 - 0.05$.

The conductivity changes during day two show a limited reduction of conductivity at the top and bottom of the vessel. However, as seen from Figs. 88 & 89, during this period there are slight increases in conductivity in most of the vessel.

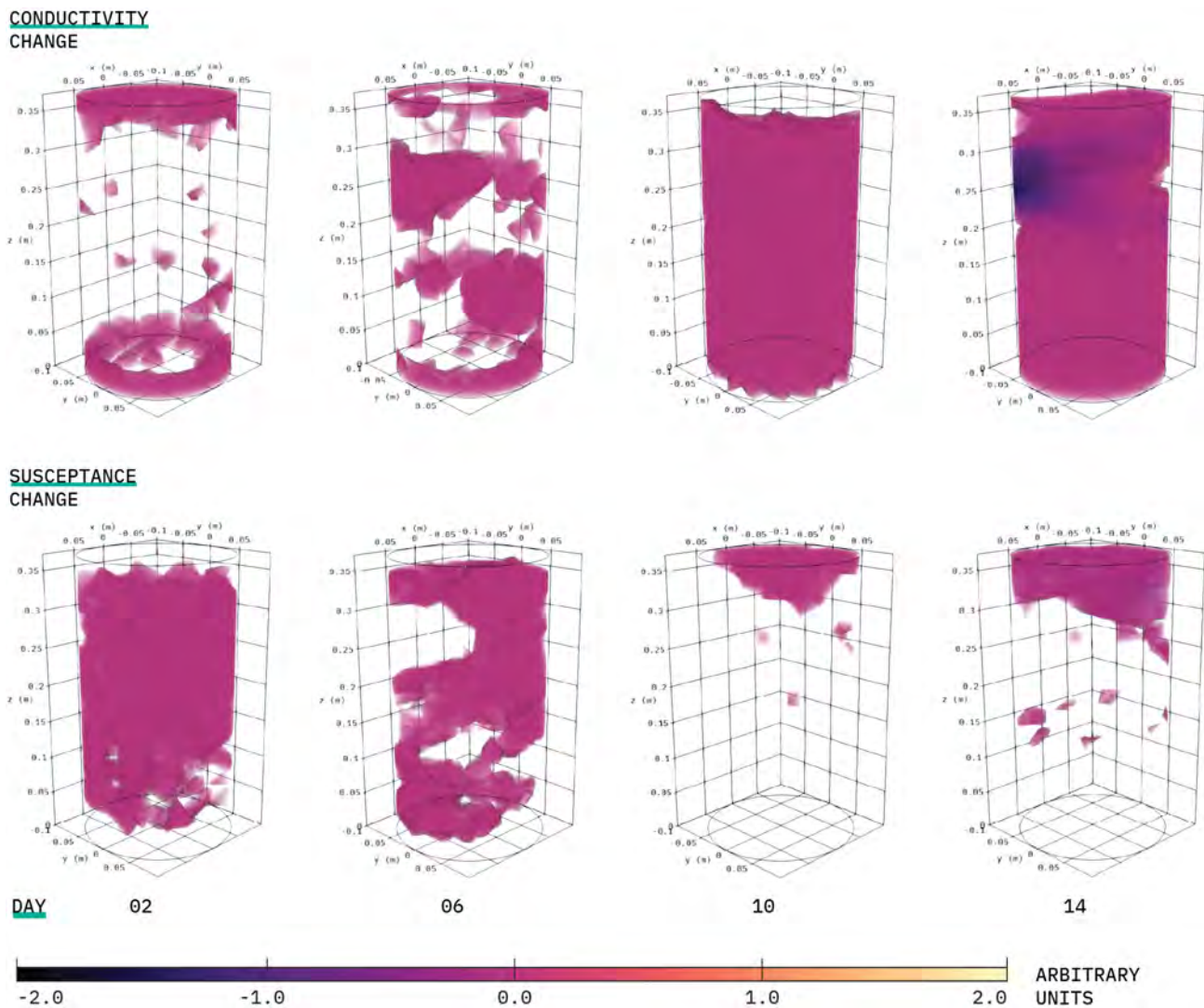


Figure 87: S-01's conductivity and susceptance changes at 10 kHz presented as 3D iso-volumes for the most representative days.

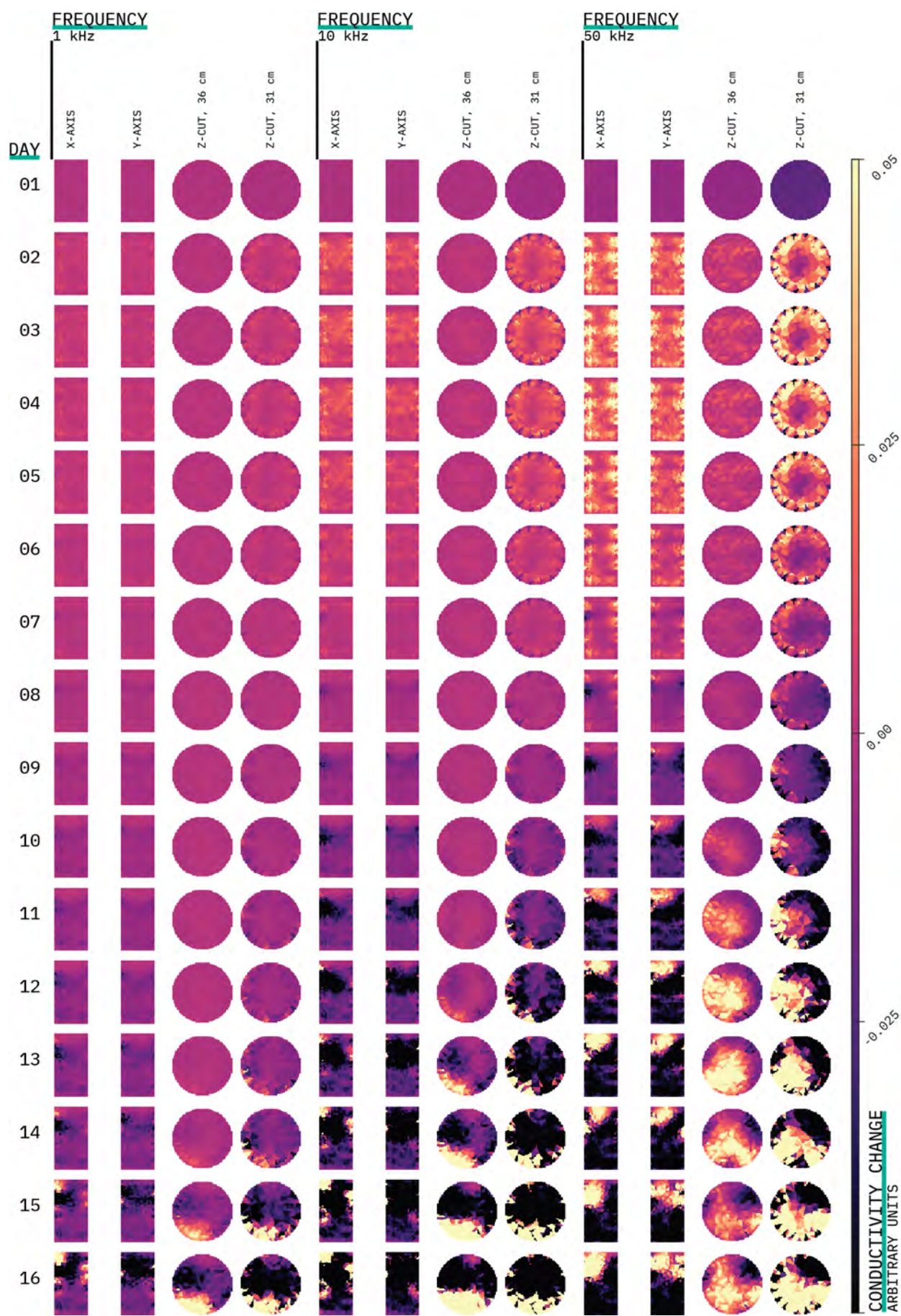


Figure 88: S-01's conductivity changes at different frequencies. Slice views at specific axes.

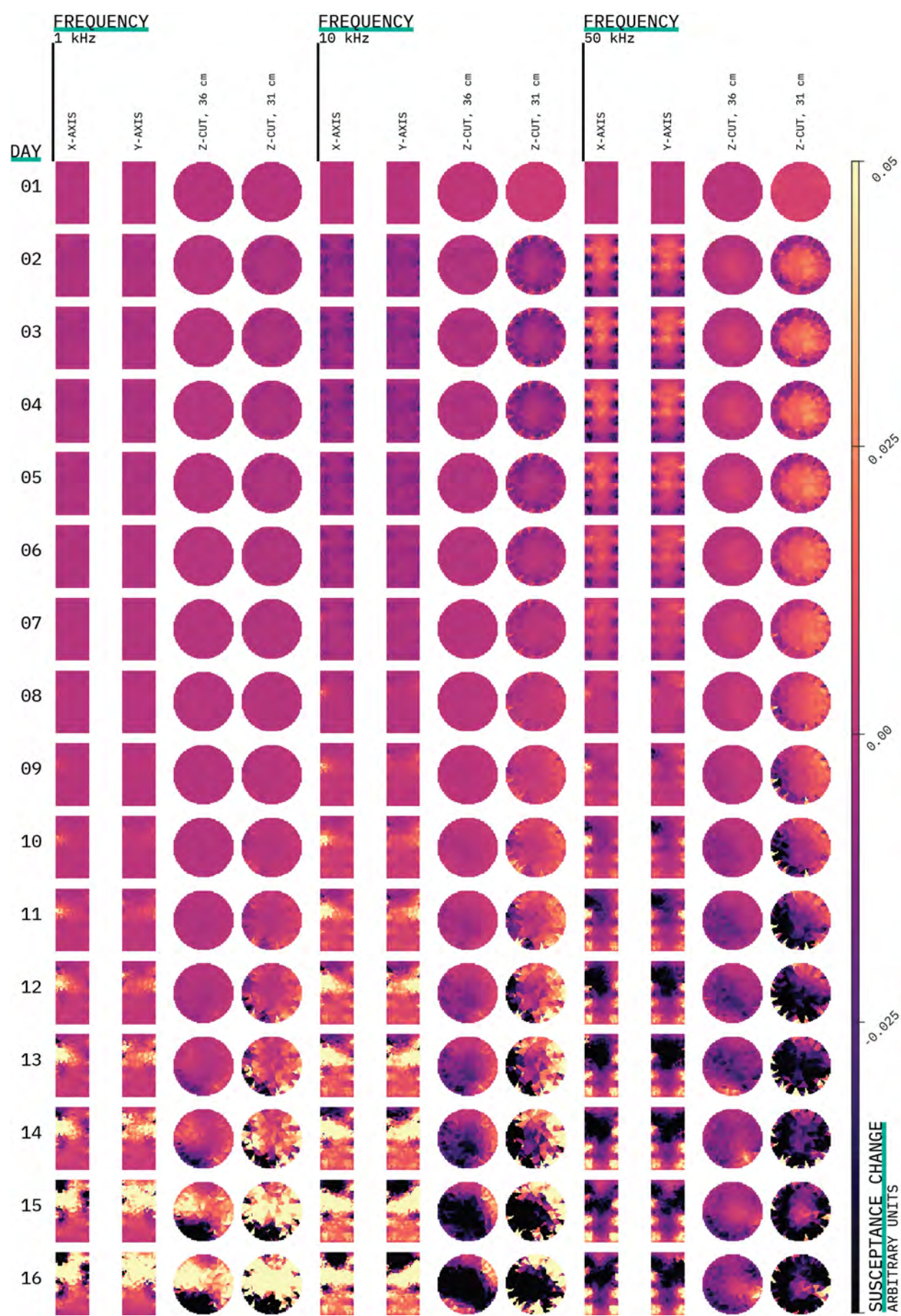


Figure 89: S-01's susceptance changes at different frequencies. Slice views at specific axes.

As the drying process advances, conductivity starts decreasing in specific parts of the vessel. At day ten, one can observe that most of S-01 has experienced a reduction in its conductivity. By day 14, the S-01 shows significant reductions in conductivity at its top, particularly between 20 cm to 30 cm height. The susceptance changes, on the other hand, behave almost inversely to the conductivity changes. Negative changes in the susceptance are prominent during the first days of the experiment. The changes are only observable at S-01's top corner $\{[-0.10, 0.05], [-0.10, 0.05], [22, 37.25]\}$ near the end of the trial.

Both changes reflect well the behaviour previously explored with the EIS analysis. Conductivity decreases almost linearly at high water content levels. Using the BD calculated previously (Table 9) and the weight data for the experiment (Fig. 83), it can be inferred that the water content decreases by approximately 20% at the end of the experiment, which is still within the range of high water content. On the other hand, the susceptance, being the inverse of the reactance, is expected to decrease in the presence of increased levels of water content. Therefore, in this case the susceptance reconstructions can be understood as the “negative” space of the conductivity changes. Hence, susceptance changes can be seen as the positive water movement within the vessel.

Figs. 88 & 89 show the effect of frequency in the reconstructions. The figures present cross-sectional cuts of the vessel taken at the centre and at 36 cm & 31.38 cm for vertical and horizontal cuts respectively. In general, admittance changes manifest a higher response at higher frequencies. For this reason, we can reiterate the point that the reconstructions follow the behaviour explored with the EIS analysis, in which at higher frequencies the substrate presents higher levels of conductivity. Furthermore, the EIS behaviour is further corroborated by the images obtained at 50 kHz. At 1 kHz, the electrical response of S-01 still falls within the linear part of its EIS curve. Near 10 kHz, S-01 is approximately at the valley of the EIS curve. At 50 kHz, while there is still a decrease in conductivity, the susceptance response is past the valley of the EIS curve, presenting an upward trend. A comparison between the intensity of admittance changes of different frequencies is explored in Table 14. The ratios presented in Table 14 are calculated by computing the sum of all elements and then calculating their corresponding moving average, using a window of 50 elements to account for the seasonal nature of the ratios⁵³.

The non-stationary behaviour was also evaluated by testing the presence of the unit root through an ADF test ($p > 0.05$). One can observe that the moving average remains mostly linear at two intervals; thus, the moving average range is reported for the interval encompassing day 1 to day 7, and from day 8 till day 15.

Examining the results presented in the previous table, one can notice that the ratios of the admittance's real component decrease as the drying process takes place. As expected, the conductivity ratios be-

⁵³ Most likely due to the effects of the night/day cycle.

TIME	RATIO	REAL	IMAGINARY
Days 01-07	50 kHz / 10 kHz	03.957 - 04.725	00.211 - 00.329
	50 kHz / 01 kHz	10.006 - 12.3665	01.979 - 02.396
	10 kHz / 01 kHz	02.528 - 02.617	06.362 - 07.251
Days 08-15	50 kHz / 10 kHz	01.980 - 00.274	-00.080 - -00.343
	50 kHz / 01 kHz	06.632 - 01.852	-00.386 - -00.679
	10 kHz / 01 kHz	02.528 - 06.817	04.615 - 01.981

Table 14: Seasonal moving average intensity ratios for individual admittance's components between reconstruction's frequencies at different stages of the experiment.

tween high and lower frequencies remain considerably large during the experiment. However, the ratio between 50 kHz and 10 kHz decreases considerably at the end of the experiment. A reasonable explanation for this, is the fact that the reconstructions at 50 kHz present heavy outliers⁵⁴ during the start of day 11. The susceptance ratios increase slightly during the initial duration of the experiment, and decrease during the remaining days of the experiment. Overall, the behaviour of the ratios is inline with S-01's EIS profile, except for the particular case of the 50 kHz ratios at later stages of the experiment.

The present work further dissects the results obtained by subdividing the VOI into three VOIs that correspond to the areas covered by each square arrangement involved. The VOIs cover the complete diameter of the FEM and have the following height ranges: bottom $0 < z < 12.42$ cm, middle $12.42 < z < 24.83$ cm, and top $24.83 < z < 37.25$ cm. The magnitude and phase angle of the VOIs was computed. Based on the exploration of the distributions of admittance magnitude change ($|\Delta Y|$) and phase change (ΔY°) values for each VOI, the adequate average was selected. Fig. 90 exemplifies the nature of the distribution at three instances in time. All distributions presented a significant level of positive skewness; progressively heavier tails were found as the duration of the experiment increased. Therefore, due to the heavy outlier found, the average selected was the median.

Fig. 91 shows the admittance average changes, represented as magnitude and phase, over the analysed frequencies across all VOIs. As

⁵⁴ An in depth exploration of this is presented later on this section

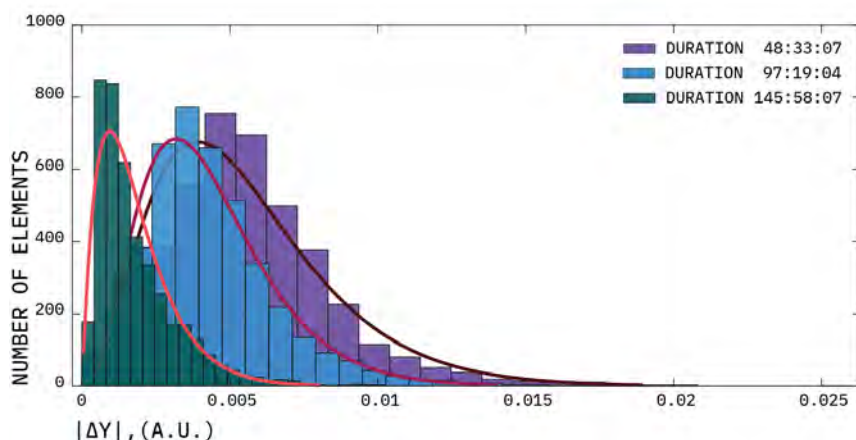


Figure 90: Histograms of the admittance change magnitude of all FEM elements. The histograms correspond to three different instances in time. N=25 and 5577 elements

explored previously, for both 1 kHz (Fig. 91 A) and 10 kHz (Fig. 91 B) in terms of magnitude one can expect them to behave similarly with the only difference being their amplitude. The magnitude in both cases is significantly influenced by the admittance's real part. At 50 kHz (Fig. 91 C) it can be noted that the magnitude's intensity is larger than the other frequencies. According to the EIS profile, the conductivity at this frequency is higher, which explains the increased magnitude values. Most magnitude changes present a similar trend, corresponding to that of a 3rd order polynomial. On the other hand, phase changes present a sigmoid growth in most cases, particularly at 1 kHz and 10 kHz. In the 50 kHz case, VOIs present a sigmoid decrease except for the bottom VOI, which shows a sigmoid increase. The seasonality of the day/night cycle is present in all graphs, which like the previously presented weight analysis, can be detected as the cyclical "bumps".

By removing the seasonality from the magnitude change associated with the complete VOI, the stationary points of the cubical trend can be identified. The first stationary point is found between times 50:30:15–50:59:34, which correspond to the first local maximum and turning point. The second stationary point can be found between times 176:22–176:51, where the local minimum is located. The inflection points at which the trend changes its concavity are located between times 109:01–109:30. Similarly, removing the seasonality from the complete VOI's phase change reveals a logistic trend. The inflection points of the logistic trend are located between the same time-points as in the magnitude's trend⁵⁵. It is at these inflection points where the conductivity starts presenting more decremental changes as indicated by the change of the phase's sign. The top VOI experiences a higher positive gradient after its inflection point. This can also be observed in the reconstructions, where the vessel presented significant changes at its top. Furthermore, as previously analysed, the middle and bottom VOI present a slower change over time. In particular, when compared against each other, the bottom VOI seems to be less affected by seasonality. However, upon closer inspection of the data, seasonality is still present within the lower regions of the vessel.

We can observe that for the top VOI's phase, its trend at 1 kHz shows a slower rise, and at 10 kHz it fluctuates between positive and negative phase changes. Here this phase change can be understood as an indicator of the type of conductivity change that dominates that VOI. The results from the 50 kHz stimulation are quite notable as the phase changes are relatively small before the inflection point. After the inflection point, the phase change decreases slowly in both the complete and top VOI. However, the bottom VOI shows a similar behaviour to that of the other frequencies. In the case of the middle VOI, one can observe a rapid rise followed by a quick fall during the inflection point. The behaviour is due to the VOI having two different opposite changes at its top and bottom. Furthermore, at time-point 273 : 46 one can notice that the magnitude tails become noisier for all VOIs except the bottom one.

⁵⁵ Such behaviour is expected due to the inherent correlation between the admittance's real and imaginary parts.

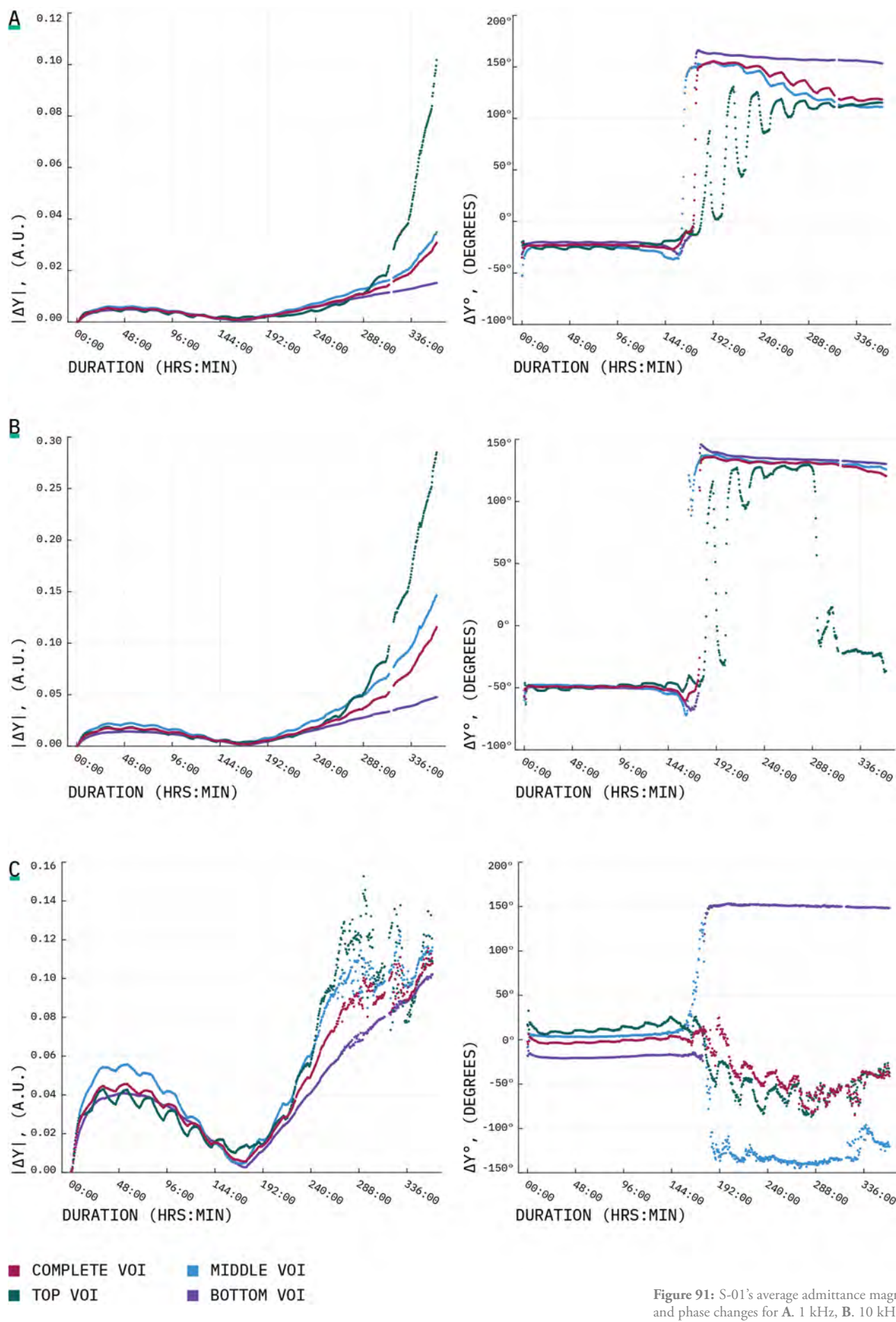


Figure 91: S-01's average admittance magnitude and phase changes for A. 1 kHz, B. 10 kHz, and C. 50 kHz.

The before-mentioned behaviour is likely due to two facts: 1. The effects of noise are more noticeable at higher frequencies, 2. In the presence of a region with high levels of water content, that region will become considerably more conductive at higher frequencies; thus, the electrical current will prefer that path of travel, decreasing the overall sensitivity across all the VOI⁵⁶. Furthermore, the lack of change in the phase for higher frequencies is expected as described by the EIS curves previously presented. At frequencies near the inflection point of the admittance's imaginary part, the intensity of the susceptance does not vary significantly with water content.

Using the complete VOI, the admittance changes were fitted to a SARIMA(3, 2, 0)(0, 1, 0)₅₀ model. The computed coefficients for the models over the analysed frequencies are summarised in Table 15.

FREQUENCY	TYPE	COEFFICIENT	STANDARD ERROR	T-STATISTIC	P-VALUE
01 kHz	AR 1	-0.766	0.012	-59.902	0.000
	AR 2	-0.521	0.015	-33.980	0.001
	AR 3	-0.198	0.015	-13.013	0.001
	RSS	0.0005	--	--	--
10 kHz	AR 1	-0.805	0.011	-70.005	0.000
	AR 2	-0.454	0.013	-33.675	0.001
	AR 3	-0.212	0.013	-16.042	0.006
	RSS	0.001	--	--	--
50 kHz	AR 1	-1.130	0.018	-60.494	0.000
	AR 2	-0.841	0.021	-38.442	0.002
	AR 3	-0.291	0.013	-22.019	0.002
	RSS	0.0 09	-	-	-

⁵⁶ In turn, this creates more outliers in the final reconstruction

Table 15: Coefficient estimation for S-01's SARIMA model for admittance magnitude changes

All models pass the Ljung-Box chi-square approach ($p > 0.05$). The models can accurately forecast future values with the data acquired through the experiment. When considering the residual sum of squares (RSS), one can notice that the goodness of fit decreases with frequency. The estimated values are inversely proportional to the frequency, except for AR 2. The latter coefficient increases when going from 1 kHz to 10 kHz but decreases at 50 kHz. This effect, in conjunction with the decrease in the RSS, is anticipated due to the stochastic nature of the data at later stages of the experiment particularly at 50 kHz. It is clear from the complexity of the models that the correlation between magnitude changes and the volumetric water content loss (presented in this work as weight loss) is expected to be low. For this reason, the distance correlation between the individual admittance components was computed. Table 16 summarises the strength of the relationship between conductivity and susceptance with water content loss due to the air-drying process. The results summarised in Table 16 show that there is a strong correlation⁵⁷ between admittance's individual components and water loss. The above correlations can be used to determine the areas of most activity within a drying process. In this case, most of the VOIs present a high correlation coefficient except

⁵⁷ In contrast with the usual Pearson Correlation, a distance correlation does not test for linear relationship between variables but rather their dependence whether linear or not.

FREQUENCY	VARIABLE	C-VOI	T-VOI	M-VOI	B-VOI
01 kHz	Conductivity	0.977	0.913	0.978	0.975
	Susceptance	0.958	0.767	0.964	0.965
10 kHz	Conductivity	0.968	0.876	0.969	0.969
	Susceptance	0.974	0.687	0.967	0.968
50 kHz	Conductivity	0.974	0.564	0.969	0.970
	Susceptance	0.842	0.915	0.905	0.965

Table 16: Distance correlation between VOI admittances changes and water content loss over different frequencies. C = complete, T = top, M = middle, and B = bottom.

for the top VOI. In the top VOI, one can notice moderate correlation values. Therefore, one can conclude that this region of the volume presents abnormal changes and can expect higher levels of variance within this particular VOI. Additionally, due to the strong correlations found, this is indicative that the relationship between variables can be further simplified. Using the model most employed in geophysics for relating water content to electrical resistivity values⁵⁸ as a starting point, the relationship between water loss and conductivity changes was fitted to the following equation:

$$(102) \quad w = \left[\frac{\Delta\sigma + b}{a} \right]^2 + c$$

where w represents the weight associated with the water content of the substrate, $\Delta\sigma$ represents the change in conductivity with respect to a starting point. Lastly a, b and c represent fitting parameters. Fig. 92 shows the above model fitted to the complete VOI conductivity change for the 1 kHz stimulation. The fitted model does not consider the initial measurements that correspond to time-points at which the vessel was left sitting on a water bed. The computed fitting parameters were $a = 0.026$, $b = 0.027$, and $c = 11.010$. Even though the model does not account for the seasonality effect of the day/night cycle nor the initial sharp increase in conductivity at the beginning, the model has an acceptable fit (root-mean-squared error (RMSE) = 0.022).

⁵⁸ S. Garré et al. "Three-Dimensional Electrical Resistivity Tomography to Monitor Root Zone Water Dynamics". In: *Vadose Zone Journal* 10.1 (2011).

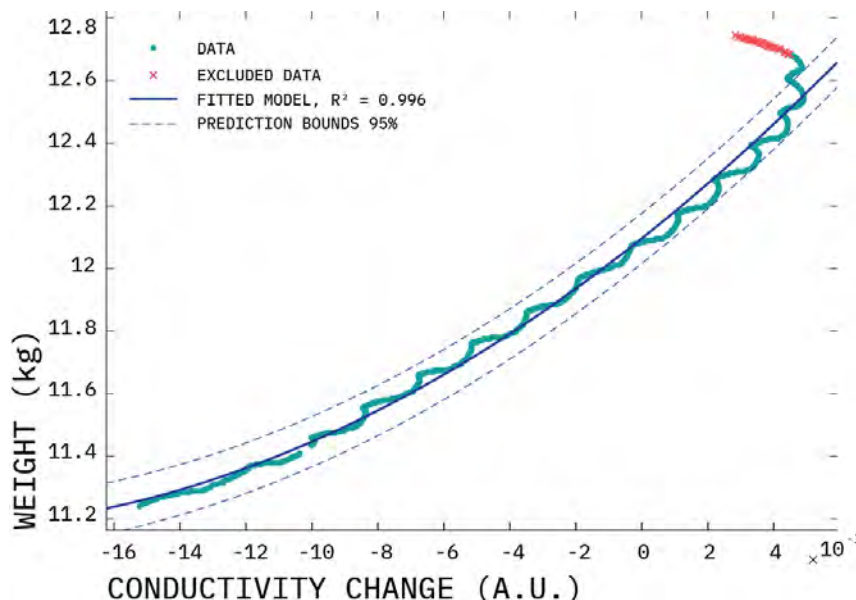


Figure 92: Model fitting for weight loss versus total conductivity change across the vessel for a 1 kHz stimulation signal.

6.4.2 Discussion

Water flow in soils is not a straight-forward process, and it can be more complex when dealing with soils in which their volume changes with their corresponding water content. Water movement is known to travel in “fingers” rather than in blocks due to the porous nature of the substrate. Furthermore, water dynamics are governed by soil water potential⁵⁹, and as such water storage in soil plays a crucial role in the movement process as water content is directly related to water potential⁶⁰. Water flows from high to low water potentials. Therefore, difference in the potential energy gradient is what dictates how water is redistributed and stored in soil. Soil water potential is the sum of four components: matric⁶¹, gravitational⁶², osmotic⁶³, pressure⁶⁴. In soil the matric potential is the most important component that will dominate water flow. The present work considers the free water at the soil surface as the reference point for the water potential.

The images obtained not only represent a change in water content, but also can be used to describe the water flow within the soil, which can be further explained through the effects of water potential. Since S-01 was left 1 day to settle before the experiments, this study considers that S-01 would be closer to field capacity conditions⁶⁵. Close to field conditions, soil water potential is approximately -33 kPa. Such small potential arises due to the soil drying process, which creates a suction force that allows soil to retain water. From the magnitude graphs and initial reconstructions, a significant increase in conductivity is observed. Such an increase is due to the vessel sitting on a bed of water before initialising the weight measurements. The increase in conductivity represents water moving from a high potential (0 kPa from free water) to lower potential. Close to field conditions, water retained in micropores is not affected by gravity forces, thus, water retention will be dominated by the soil matric potential, which in turn will make water flow against gravity due to capillary forces.

The difference in time before starting the weight measurements was approximately 9 hours. We can observe the conductivity increase until 50 hours into the experiment. Nevertheless, the increase in conductivity is mostly experienced along the edges of the vessel and the top middle section of the vessel. The top surface clearly displays small conductivity decreases on the edges, and small increases at its centre. These changes are the result of the evaporation process taking place. According to the weight measurements, the rate of evaporation is approximately 105 gr per day. As previously discussed, the rate is different depending on the night/day cycle. The difference in rates is due to the temperature exerted by the light tubes in the growth chamber⁶⁶. The change in rate was captured by both the weight and EIT measurements. Furthermore, temperature measurements from the main processing unit corroborate the temperature fluctuations (Fig. 93). The slow water evaporation process is limited by upward movement of water to the soil’s surface. This process can be observed until day six of the experiment.

⁵⁹ Soil water potential describes how tightly water is bound to the soil or plant material. Water potential represents the amount of energy required to separate water from the material. Thus, water potential is usually negative. A zero-water potential corresponds to a pool of pure water.

⁶⁰ L. A. Richards. “Capillary conduction of liquids through porous mediums”. In: *Journal of Applied Physics* 1.5 (1931).

⁶¹ Describes the binding of the water to a surface

⁶² Describes the potential depending on the gravitational field, i.e. it depends on the position with respect to a reference point.

⁶³ Represents the dilution of solutes dissolved in water

⁶⁴ Physical pressure hydrostatic or pneumatic applied to the water

⁶⁵ S-01 could not be at saturation point. Near saturation, water potentials are close to zero. In saturation, the direction of water potential is downward and would lead to water dripping from the soil.

⁶⁶ The location of the temperature sensor inside the growth chamber is one of the limitations. While the growth chamber can achieve an overall temperature inside, it cannot detect and compensate for areas with a different temperature profile.

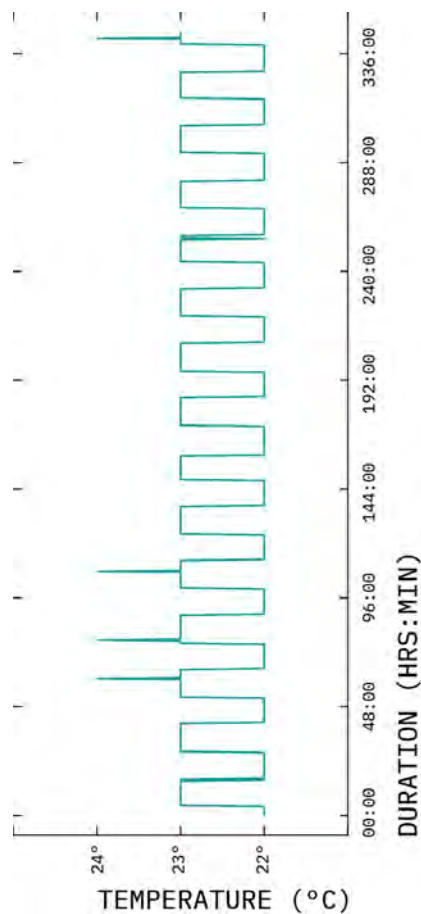


Figure 93: Logged processor temperature changes for the duration of the experiment.

At day seven, decreases in conductivity start to become obvious, particularly slightly below the surface level. Small conductivity increases can be observed at the surface layer. As the drying process carries on, it can be noted that the redistribution of conductivity is more active at the middle and top layers. Since the evaporation at surfaces is balanced by the upward water movement, this decrease in conductivity is expected, however, the results show that this process is not uniform. A significant decrease in conductivity occurs at the middle edge of the vessel, and this decrease progresses first along the middle layer and then below this layer. This can be easily observed at higher frequencies. Knowing that the permittivity is linearly related to water content, one can use the susceptance as an indicator for areas with higher water content. Therefore, the susceptance reconstructions show that as the experiment progresses there is a high redistribution of water content at one of the vessel's edges. By the end of the experiment, we observe that the middle and top edges start to have significant decreases near the edges. Furthermore, this was visually corroborated at the end of the experiment, when one of the vessel edges was exhibiting low shrinkage.

The ability of ERT to evaluate moisture content and water flow is often analysed in geophysics at both field scale and container scale. This study presents the benefits of EIT as a small-scale approach with high temporal resolution. The measurements acquired show that EIT can detect small changes in conductivity at small intervals of time. This enables us to track the variability in soil moisture and how water moves through the substrate. Admittedly, this experiment has its limitations. A key limitation was the lack of complementary measurements that could corroborate moisture content at different levels, as well as the soil water potential. Nonetheless, one of the key advantages of EIT is the use of spatial analysis, which can allow users to obtain valuable insights from admittance measurements. This is a clear advantage over traditional single point moisture measurements. However, the degree of expertise required to obtain sensible images can be a detractor for such an approach. The present work describes different steps taken to ensure not only the quality of the reconstructions, but to remove the uncertainty of the obtained images. Furthermore, the present work proposes a new multi-ring approach that enhances the vertical resolution of the images while preserving a high temporal resolution. In addition, the researcher recommends profiling the substrate used through EIS at different moisture contents. The use of an EIS profile can remove the uncertainty of the meaning of the images. Particularly, at higher frequencies where conductivity and susceptance stop being inversely proportional. The researcher also recommends analysing the imaginary part of the data. Many EIT studies often only report the real part of the measurements, however, valuable information can be extracted from the susceptance or reactance. In this case, it was used to corroborate the effects at different frequencies along the EIS profile, and to further evaluate the redistribution of water content.

6.5 *Raphanus sativus*

The experimental data presented in this section corresponds to measurements taken to track the RSA development of a Japanese Minowase Daikon (*Raphanus sativus*) (Radish (Mooli) Mino Early F1, Johnsons Seeds, UK). Daikon is a type of radish from the *brassica* family that is often used as a decoy crop to reduce clubroot spores. One daikon seed was planted close to the centre on the left top region of the smart rhizotron at a 1.5 cm depth using the S-02 substrate at $\text{BD} = 1.210 \text{ gr/cm}^3$. The plant subject was grown under a 16h/8h day/night photoperiod at 18° C . Before the experiment began, S-02 was brought to saturation and left to settle for 24 hours. Occasional watering from the top was conducted. The watering regime was selected to ensure that S-02 would not drop below 85% of its weight measured at the start of the experiment. EIT and weight measurements were obtained for 28 days at 30 minute intervals. The frequencies explored in this experiment were: 500 Hz, 1 kHz, 10 kHz, 25 kHz, 40 kHz, and 50 kHz. Square S1/M1 measurements were taken to account for any faulty electrodes. On average, 1106 frames per frequency were obtained. The main measurements used for the analysis and image reconstructions were the ones obtained using a S5/M6 protocol. The reference frame for all time-difference reconstructions was the one obtained at time-point 5th July 2021 15:20. The last dataset was taken on 2nd August 15:30. The reconstruction process for the data is identical to the one described in the previous section. The hyperparameters computed are summarised in Table 17.

FREQUENCY	S1/M1 λ	S5/M6 λ
500 Hz	3.043e-04	2.620e-04
01 kHz	5.025e-04	5.864e-04
10 kHz	7.021e-04	1.586e-04
25 kHz	7.593e-04	1.342e-04
40 kHz	7.021e-04	1.342e-04
50 kHz	7.021e-04	1.342e-04

Table 17: Computed hyperparameters used to reconstruct images of the *Raphanus sativus* subject.

6.5.1 Results

Fig. 94 shows the mass changes from the experiment at different time-points. A linear decrease can be observed during the first nine days of the experiments. As in the previous experiment, the effects of the day/night cycle are present, however, they are less pronounced due to a shorter night photoperiod. The seedling sprout was out of the soil by day two, and no significant changes to the decrease in weight were observed. Fig. 94 exhibits multiple peaks, corresponding to the irrigation instances, and Table 18 summarises these events. Before the first significant irrigation event, a steady linear decrease of 0.032% ($R^2 = 0.988$) of the current weight every 30 minutes can be observed.

In order to obtain the underlying trend of the decrease, the peaks corresponding to the water irrigation events were removed⁶⁷.

⁶⁷ The present work considers that variations in water density are insignificant as water was added at room temperature.

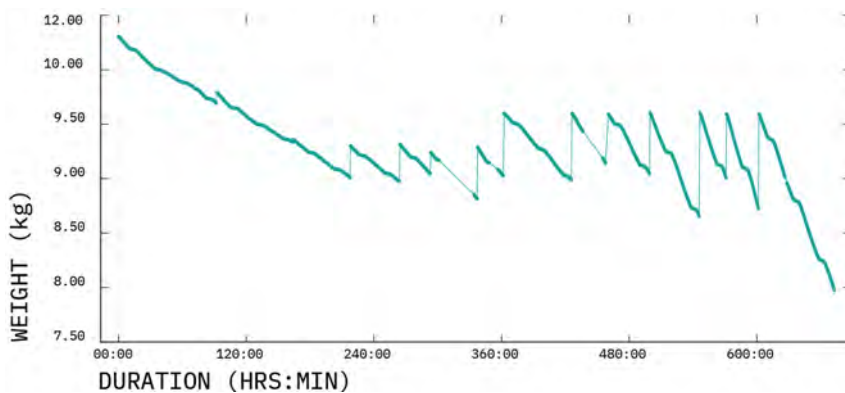


Figure 94: Mass evolution for the *Raphanus sativus* subject.

EVENT	ELAPSED TIME (HRS:MIN:SEC)	WATER ADDED (GR)
01	092:42:25	095
02	164:18:39	025
03	218:03:39	290
04	264:29:56	340
05	293:32:13	195
06	337:32:36	475
07	362:22:59	575
08	426:06:20	610
09	460:28:12	450
10	500:08:16	560
11	546:22:30	950
12	571:30:36	585
13	601:53:41	865

Table 18: Irrigation events for the *Raphanus sativus* subject.

Since the data set lacks points where the acquisition failed due to power outages⁶⁸, missing data points were added using forecasted values obtained from two SARIMA models.

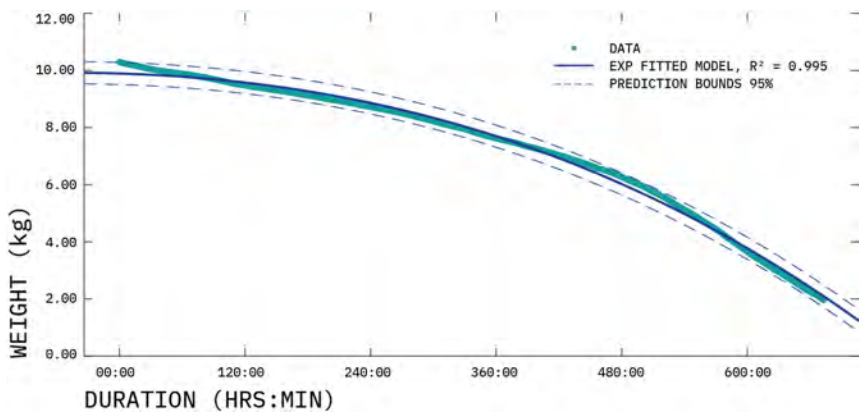
⁶⁸ Data points are missing between intervals 301:04–334:13, 348:28–356:42, 435:34–455:03.

The first SARIMA(1,1,1)(1,1,0)₃₉ was used to complete the first two intervals missing due to their proximity. The second model fitted was a SARIMA(1,1,0)(2,1,0)₃₉ that corresponds to the last missing intervals on day 18 of the experiment. Both models' residuals present a normal Gaussian distribution and exhibit no autocorrelation (Ljung-Box chi-square $p > 0.05$). The data without the irrigation instances was further modelled as a SARIMA(2,2,1)(0,1,1)₃₉. Again, the residuals for this model did not show significant autocorrelation as corroborated through a Ljung-Box chi-square test ($p > 0.05$). The coefficients for the latter model are summarised in Table 19:

TYPE	COEFFICIENT	STANDARD ERROR	T-STATISTIC	P-VALUE
AR 1	-0.390	0.058	-06.714	0.001
AR 2	-0.160	0.039	-04.044	0.002
MA 1	-0.342	0.061	-05.618	0.001
SMA 1	-0.867	0.014	-60.101	0.000
RSS	0.012	—	—	—

Table 19: Coefficient estimation for *Raphanus sativus* mass changes SARIMA model.

The final model was smoothed to account for the seasonality effects using its seasonal moving average, thus, Fig. 95 presents the overall downward trend during the experiment. The data was fitted to an



exponential concave decline function ($SSE = 28.847$, $R^2 = 0.995$, $RMSE = 0.1494$). The function is described by:

$$(103) \quad y = Asym + (RO - Asym) \exp^{(-x \cdot DR)}$$

where⁶⁹ $Asym = 00:10:00$, $DR = 00:01:28$ and $RO = 02:10:24$. The model used is the one proposed by Fonzo et al. (2013)⁷⁰ for rapid decline dynamics, where $Asym$ can be understood as the first horizontal asymptote, RO represents the first seasonal intercept, and DR represents the decay rate of the model. The models presented illustrate how the decline process accelerates as the RSA develops. The decline's slope starts to increment between times 337:00 and 362:00; the latter is corroborated by the irrigation event table, where during these and later events the amount water required to stay within the 85% criteria also increased. By the end of the experiment, the subject's main tap root was 15.25 cm in height, with a 4.5 cm top diameter and 0.975 cm bottom diameter (Fig. 96). The fresh mass weight with foliage was 401.20 gr, and 120.5 gr for the main RSA. At the end of the experiment, approximately 1.5 cm of the main tap root was above the soil.

Figure 95: *Raphanus sativus* mass decrease fitted model.

⁶⁹ In order to fit the model to actual time stamps, a conversion to UNIX time was made, and then reverted to time-points.

⁷⁰ Martina Di Fonzo et al. "A new method for identifying rapid decline dynamics in wild vertebrate populations". In: *Ecology and Evolution* 3.7 (2013).



Figure 96: A. *Raphanus sativus* at the end of the experiment, B. and its main RSA.

RECONSTRUCTION ANALYSIS

Reconstructions of the admittance changes for different frequencies over a 28-day period were obtained. For the sake of brevity, the present work shows the most representative subsets of images that reflect the changes on the substrate due to the root development of the *Raphanus sativus* subject. The next figure (Fig. 97) shows the most significant decremental changes in admittivity (expressed as individual components) from day 14 until day 26. The changes are presented as iso-volumes⁷¹ that represent the range of values from the minimum/-maximum⁷² value at that time-point to 10% of that value. Volumes were computed through the sizes of the FEM cells involved in the selected changes. Table 20 presents the calculated volumes as for the shown reconstructions.

DAY	CONDUCTIVITY VOLUME (cm ³)	SUSCEPTANCE VOLUME (cm ³)
14	369.653	339.816
18	448.222	352.817
22	761.209	478.583
26	883.736	860.763

⁷¹ Cross-sectional images are presented near the end of this section.

⁷² Minimum in the case of conductance values, and maximum for susceptance values.

Table 20: Volumes computed from the reconstructions selected at 10 kHz

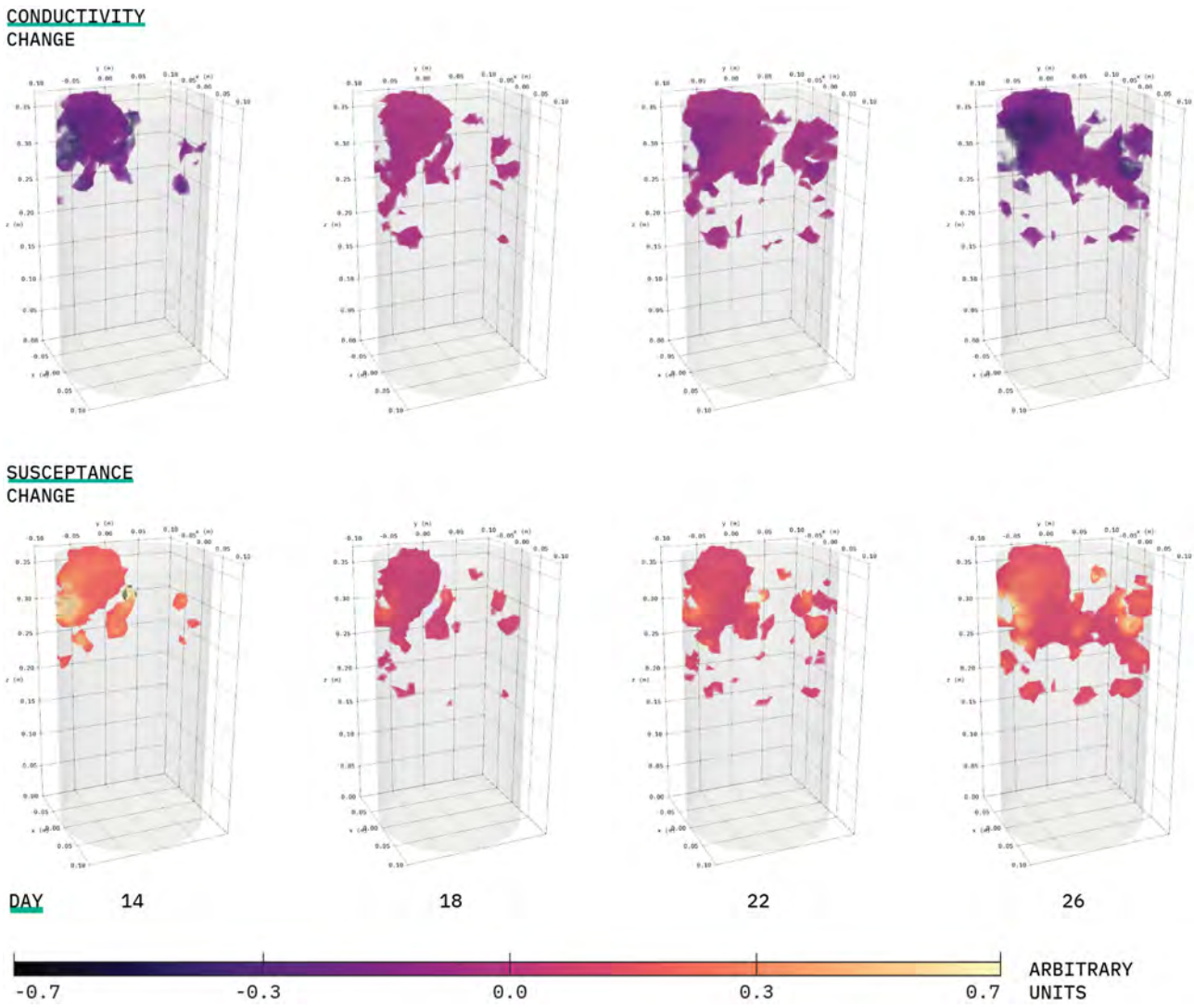


Figure 97: *Raphanus sativus* conductivity and susceptance changes at 10 kHz presented as iso-volumes.

Using the latter criteria, conductivity changes have $\approx 7.5\%$ more volume than the reconstructions obtained through the susceptance. Despite the fact that the reconstructions presented at day 14 show higher levels of change⁷³ the criteria selected are able to highlight the main changes near the subject under study.

Figs. 98 & 99 show cross-sectional cuts of the vessel's conductivity and susceptance distribution map at regions that present significant changes near the subject under study. The figures show the admittance changes every two days at the beginning of the day cycle. As expected, the intensity of the changes is dictated mainly by the stimulation frequency. However, while similar conductivity changes can be tracked between 10 kHz and 40 kHz, at 500 Hz the changes when a significant amount of water loss has occurred are almost insignificant. For instance, by day 14 a clear region where most negative changes occur starts to be more distinguishable. Furthermore, the changes at 500 Hz occur predominantly at near the centre of the vessel, and they localize near the end of the experiment at the lower left quadrant (z-axis cuts). In the case of the higher frequencies, the tendency towards negative conductivity changes is progressive on the same lower bottom quadrant (z-axis cuts) for the duration of the experiment. Nevertheless, by day 28 one can observe a region of high conductivity next to the most negative changes. This region is present in all frequencies, however, at 40 kHz the size of the region appears to be greater than in the other regions.

Fig. 99 shows the susceptance changes for the same cross-sectional cuts and frequencies mentioned above. Similar to the air-drying experiment, the susceptance changes seem to act as a "negative" of the conductance changes, particularly at 500 Hz and 10 kHz. The images at 40 kHz present small susceptance increases, which do not appear to reflect the intensity of conductivity changes at the time-points. During the last 4 days of the experiment, one can observe that the susceptance changes appear to have the same distribution as the conductivity changes. On the other hand, the distribution of susceptance changes at 500 Hz and 10 kHz appears to be similar with a higher rate of change for the former frequency. Moreover, the region where most changes occur is slightly smaller than the ones observed in the conductivity changes. Such effect was mentioned in the previous computation of the volume on the region of interest in the 3D iso-volume exploration.

As in the previous experiment, looking at the EIS profile of the substrate can help understand why such discrepancies between frequencies happen. At low frequencies, we can notice that the admittance's behaviour will most likely be influenced by the conductivity, since the reactance values do not change significantly with water content. However, at the higher frequencies one can expect the susceptance to contribute more to the total admittance change since at these frequencies the reactance is lower. Furthermore, frequencies that are located after the inflection point (as in the case of 40 kHz) we observe that the susceptance will differ greatly depending on the water content.

⁷³ The effect is due to the image being taken before the first significant irrigation event.

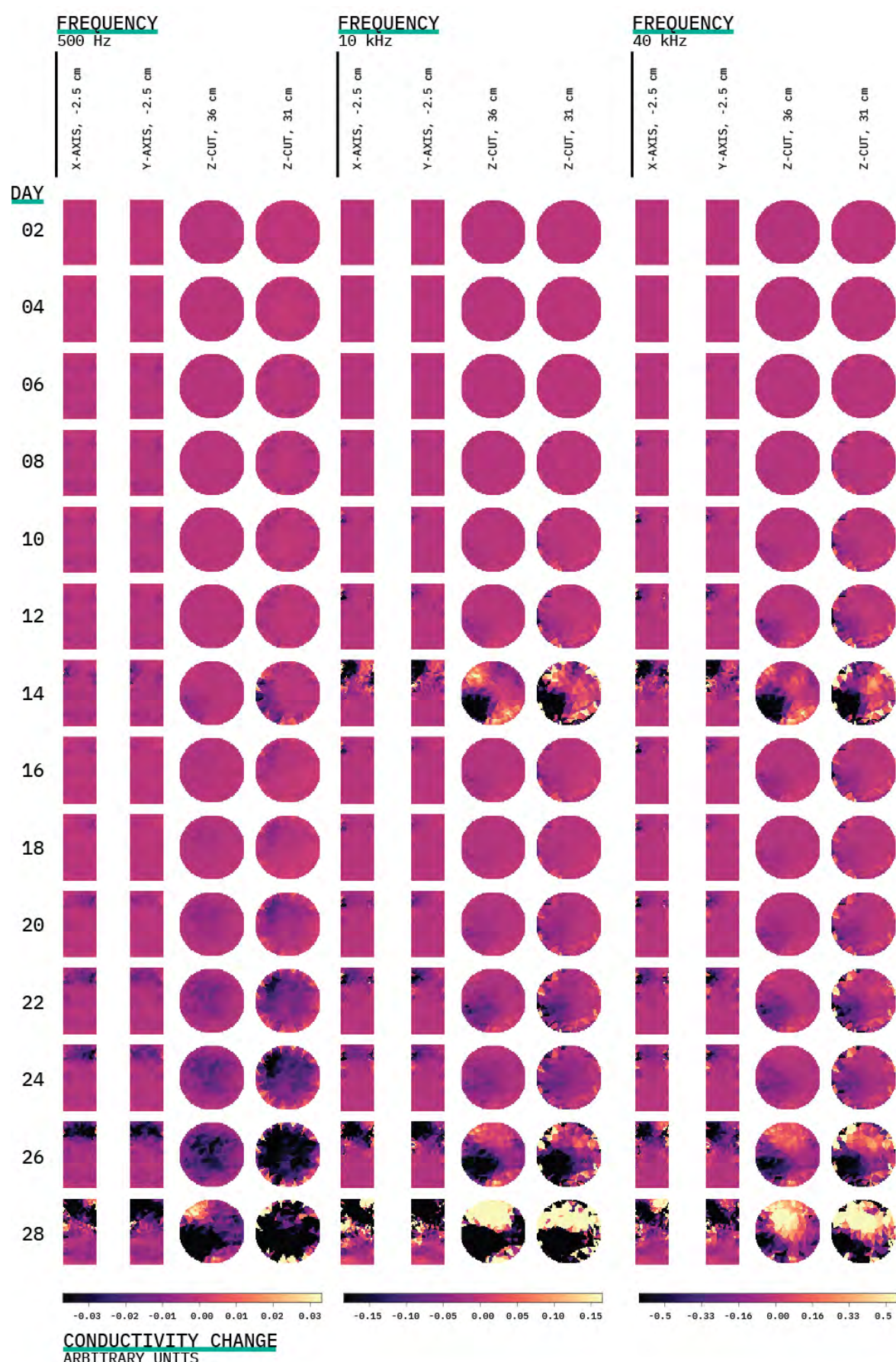


Figure 98: *Raphanus sativus* conductivity changes at different frequencies. Slice views at specific axes.

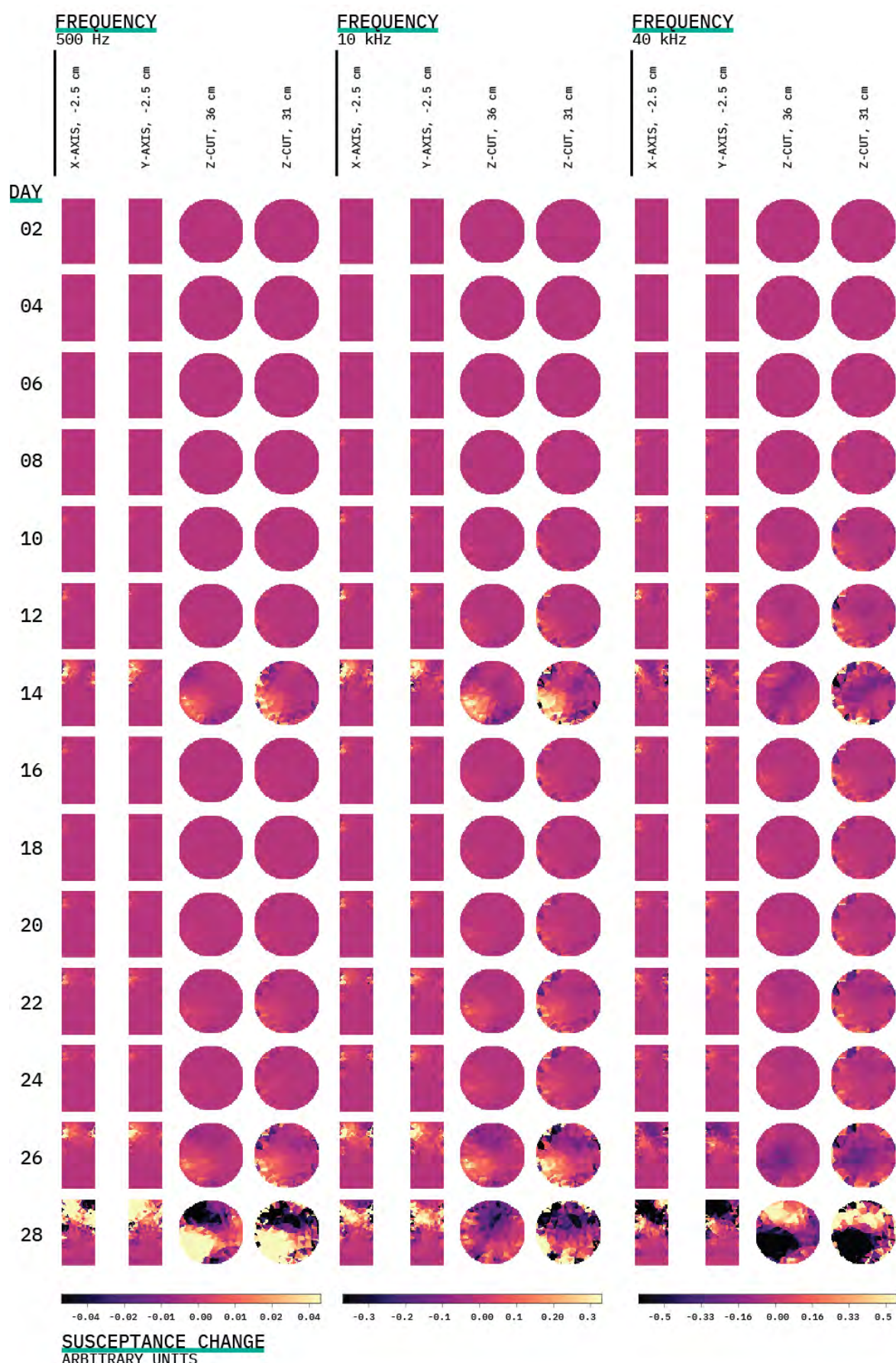


Figure 99: *Raphanus sativus* susceptibility changes at different frequencies. Slice views at specific axes.

Similar to the previous section, a more in depth analysis was conducted through the analysis of different VOIs. The same VOIs as the past section were used in the following analysis. Additionally, an extra VOI was analysed based on the concept of EZ presented in the previous chapter. The EZ was selected from the data sets corresponding to the beginning of the last complete day/night cycle near the time-point 638:00. It was extracted using the previously described criteria, thus, the VOI related to the EZ tracks the changes in that zone for the duration of the experiment. For sake of brevity, only three frequencies are reported⁷⁴. The frequencies selected were 500 Hz, 10 kHz, and 40 kHz. Since changes in admittance vary greatly over time, the results presented are subdivided into three periods: 00:00–220:00 (Fig. 100), 220:00–480:00 (Fig. 101), and 480:00–672:00 (Fig. 102). The average selected for the following results is the median⁷⁵ of the elements involved in each VOI.

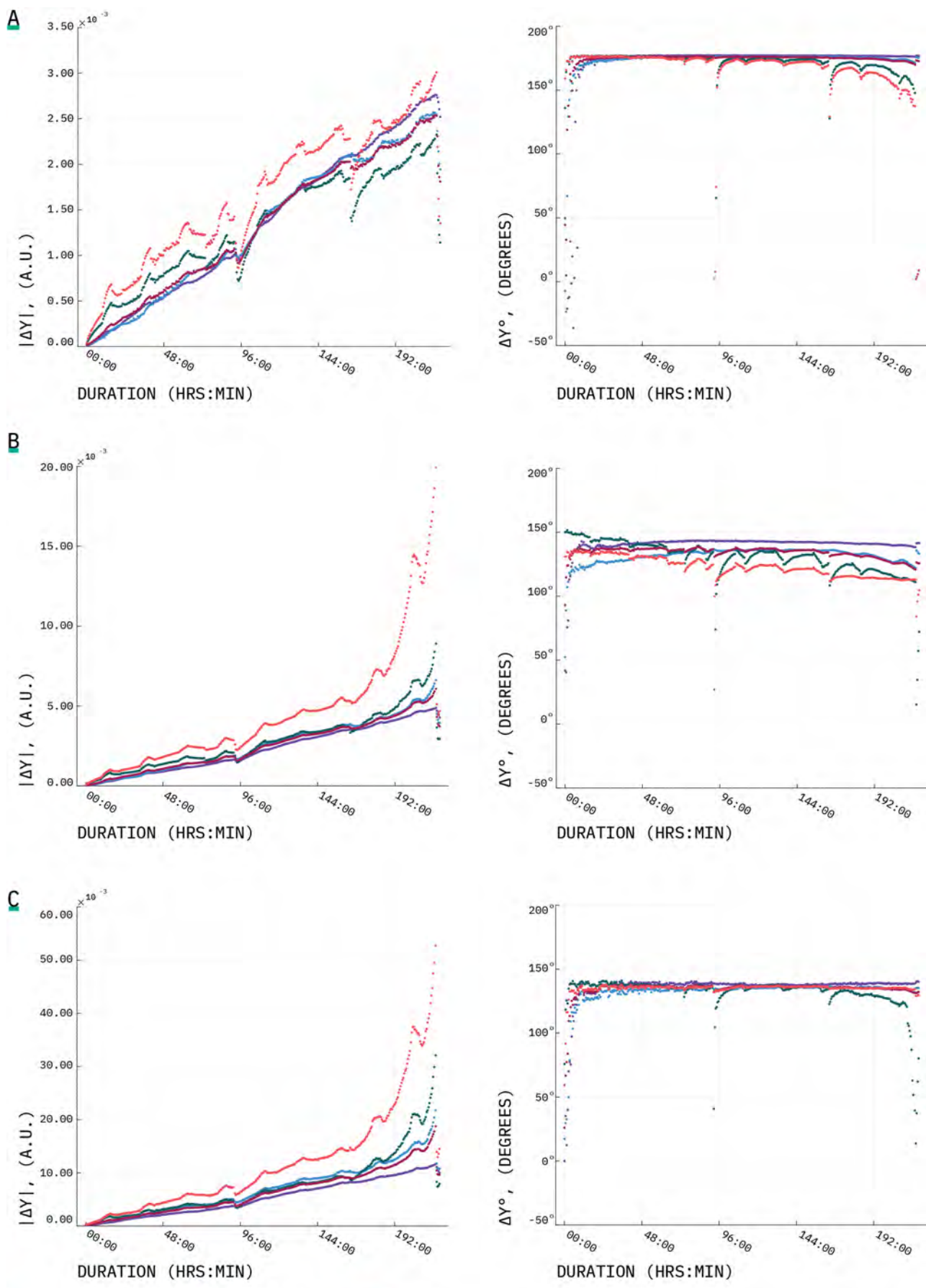
A linear increase in the admittance magnitude is observed during the first days of the experiment across all the VOIs (Fig. 100). As expected, the intensity is different depending on the magnitude. At higher frequencies, the magnitude of the changes is higher. The effects of the photoperiod cycle can be observed in all VOIs. Nevertheless, its effects are more easily observed in the VOIs close to the top of the vessel. The EZ VOI shows a slightly more pronounced change rate than the other VOIs. At duration 167:47 an inflection point is observed where the rate of change increases significantly, specially in the top and EZ VOI for the 10 kHz and 40 kHz frequencies. In the case of the 500 Hz frequency, one can observe that at the same time-point there is a sharp decrease in the top and EZ VOI. The sharp decreases observed at 500 Hz can be explained through the EIS profile, where at lower frequencies the change in moisture content has a higher impact on the admittance of the system, particularly in the real component. Looking at the phase changes, most VOI present small changes that also present the effects of the night/day cycle. While a downward decrease in phase is observable at 500 Hz in the top and EZ VOI, at 40 kHz the EZ VOI seems to remain almost constant.

Fig. 101 presents the results corresponding to the experiment's second time period. These results highlight the increased rate of change after the subject under study is past its seedling stage, where true leaves are clearly visible⁷⁶. The starting point of the results presented in this figure differs greatly to the ending point of the previous figure due to the first significant irrigation taking place at 218:03. Therefore, one can expect the total admittance change to be closer to zero. This returning to zero effect can be observed at every irrigation event. In the case of magnitude changes, one can observe that the most significant changes occur at the EZ VOI. The increase in the rate of change can be seen at the first and second irrigation period during this time interval. For instance, at 40 kHz from the beginning of the experiment to the point before the first irrigation, there is a 5.8% increase that happened over a 44 hour period.

⁷⁴ The selection of the frequencies was based on S-02's profile to maximise the difference between them.

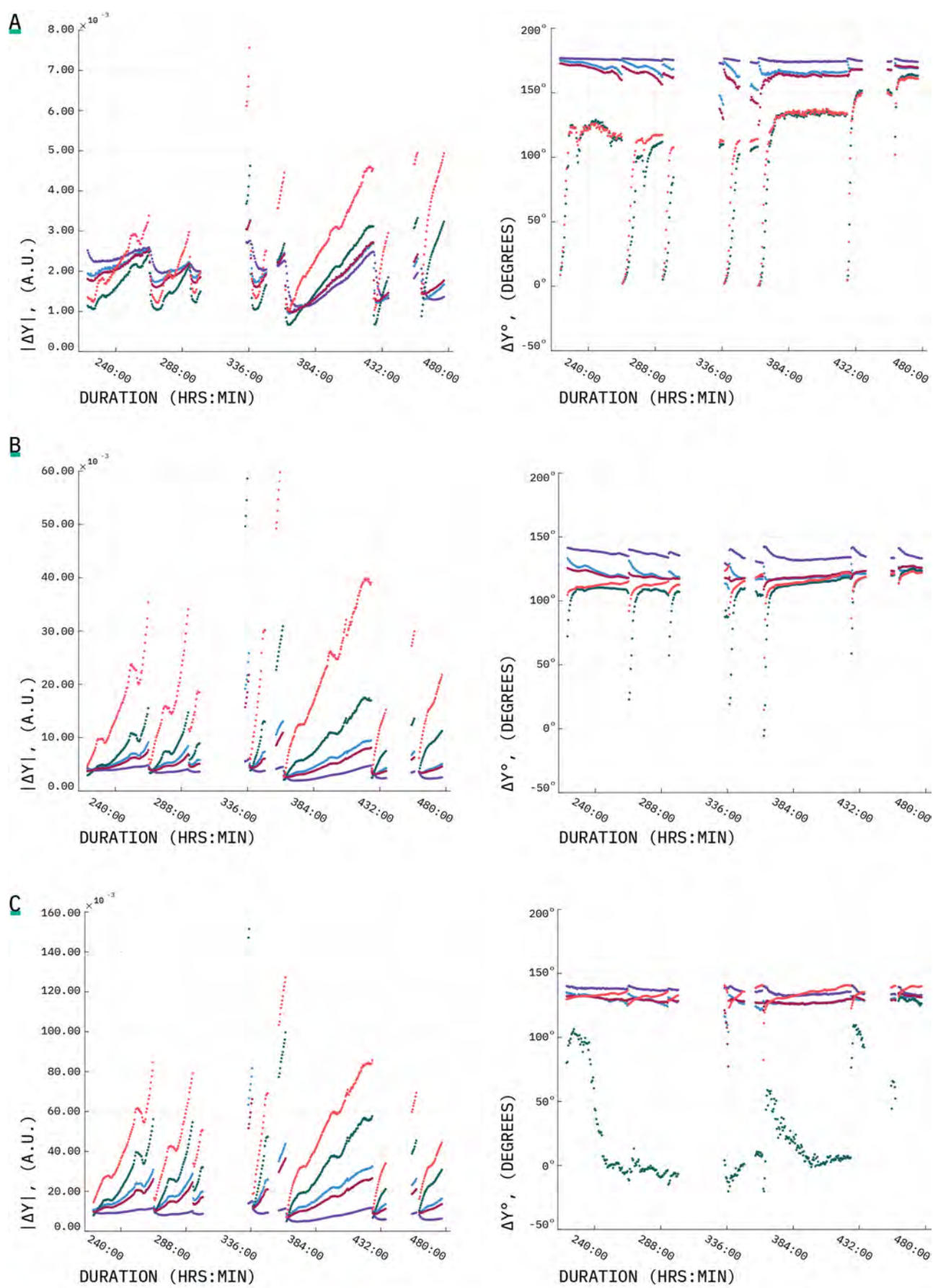
⁷⁵ As in the previous section, the elements involved exhibit skewness in their distribution.

⁷⁶ The subject under study presented only cotyledons up until day seven of the experiment, when a small true leaf was identified.



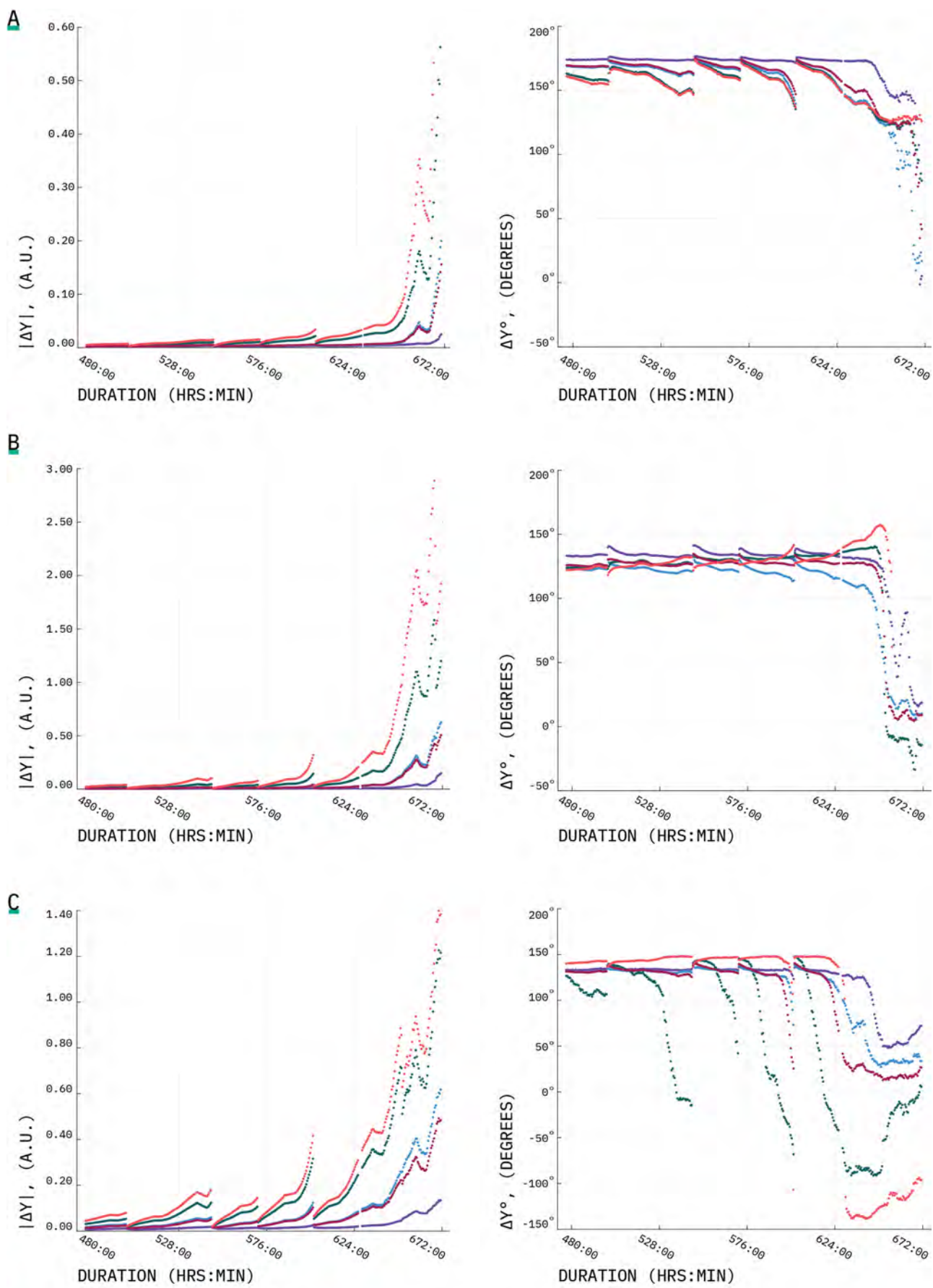
■ COMPLETE VOI	■ MIDDLE VOI	■ EZ VOI
■ TOP VOI	■ BOTTOM VOI	

Figure 100: *Raphanus sativus* average admittance magnitude and phase changes over the time period 00:00–220:00 at A. 500 Hz, B. 10 kHz, and C. 40 kHz.



■ COMPLETE VOI ■ MIDDLE VOI ■ EZ VOI
 ■ TOP VOI ■ BOTTOM VOI

Figure 101: *Raphanus sativus* average admittance magnitude and phase changes over the time period 220:00–480:00 at A. 500 Hz, B. 10 kHz, and C. 40 kHz.



■ COMPLETE VOI	■ MIDDLE VOI	■ EZ VOI
■ TOP VOI	■ BOTTOM VOI	

Figure 102: *Raphanus sativus* average admittance magnitude and phase changes over the time period 480:00–672:00 at A. 500 Hz, B. 10 kHz, and C. 40 kHz.

A similar increase can be seen over 28 hours between the first and second irrigation. The rate of change continues to increase as the experiment goes on. Observing the phase changes, the effect of the irrigation can be easily recognised, particularly at the top and EZ VOI using 500 Hz and 10 kHz. At 40 kHz the phase changes are similar in intensity for all VOIs except the top VOI, which shows an unusual behaviour that is only present during this time interval. Nevertheless, while the phase changes show similar intensities, both 10 kHz and 40 kHz present an upward trend at the EZ VOI.

During the last time interval (Fig. 102), the admittance magnitude rate of change increases significantly for all frequencies. By the end of the experiment, the top and EZ VOI experience changes are almost 100 times greater than their starting points. Furthermore, 28 hours before the end of the experiment, the bottom VOI starts showing more noticeable changes. At 500 Hz, most phase changes are similar in both intensity and behaviour except for the bottom VOI, which remains mostly constant. At 10 kHz, only the EZ VOI exhibits an upward behaviour. The results from this frequency show a sharp decrease at 646:35 for all VOIs except for the EZ VOI, which presents an even sharper decrease two hours after. Finally, the phase changes from the 40 kHz frequency present small downward changes except for the top VOI, which exhibits a significant downward trend. In the case of the EZ VOI, it presents a slight linear upward trend up until the timestamp 552:31, when it appears to behave more steadily. Similar to the 10 kHz results, the EZ and top VOI experience a sharp decrease at 620:12 and 602:25 respectively.

There is a clear correlation between the mass losses and the changes in admittance. For brevity's sake, this study analyses the correlation using the most representative frequency in this experiment, 10 kHz. To enhance the ability to discern the type of correlation, the relationship between variables was taken at intervals corresponding to each irrigation event. The variables compared are the average magnitude of the complete FEM and the weight data. In this case, the seasonality was not removed. Both quantities were normalised through:

$$(104) \quad x' = \frac{x - \mu}{\max(x) - \min(x)}$$

where x' represents the normalised data, and μ is the average of the data being normalised. Both sets of data use the median as the average. The relationship between mass loss and admittance changes before the first major irrigation event are summarised in Table 21.

EVENTS	D-CORR	COEFF 1	SSE	R^2	RMSE
00-01	0.993	-72.510E-03	9.100E-03	0.988	7.800E-03
01-02	0.988	-51.119E-03	8.721E-03	0.977	8.416E-03

The relationship corresponding to the time period from the beginning of the experiment to 218:00 is mostly linear. For this reason, a

Table 21: Linear relationship between mass losses and admittance magnitude changes at 10 kHz for the first two irrigation events.

1st order polynomial was fitted to the data. The 1st order coefficient corresponding to the slope of the decrease is shown in Table 22, as well as the sum squared errors, R^2 and the root mean squared error. The distance correlation during this period reveals a strong relationship between both phenomena. The slope intensity decreases during events 1 and 2. This can be explained by using the temperature information. Upon inspection of the main system temperature data, it was noticed that before the first irrigation event the temperature inside the growth chamber was 1°C higher. Temperature readings became stable after the first irrigation event.

When reaching the third irrigation event, the nature of the relationship between variables shows a power-law dependency, $y(x) = kx^n$. Table 22 summarises the evolution of the coefficients involved in the power dependency. In Table 22, coefficients one and two correspond to k and n respectively. Here n can be understood as the rate of decay. While one could expect the rate of decay to continue to decrease even further as the experiment continues, the results show that this is not the case. However, the duration between irrigation periods should be taken into consideration. For instance, the duration between events 2 and 3 is 52:35 and the duration between events 3 and 4 is 46:26. Nevertheless, from the event interval 7-8 the rate of decay decreases constantly. In the last interval, one can observe a drop in the R^2 value of the fit. The reason for this is that by the time-point 658:00 a more complex behaviour can be observed, thus, not only the fit but also the reconstructions should be cautiously analysed.

EVENTS	D-CORR	COEFF 1	COEFF 2	SSE	R ²	RMSE
02-03	0.983	31.37E-03	-558.312E-03	2.210E-03	0.981	5.214E-03
03-04	0.975	73.712E-03	-401.714E-03	1.103E-03	0.980	4.308E-03
04-05	0.946	93.312E-03	-357.005E-03	0.990E-03	0.976	4.822E-03
05-06	0.976	144.717E-03	-268.816E-03	1.278E-03	0.988	8.201E-03
06-07	0.950	187.805E-03	-218.012E-03	3.304E-03	0.945	10.320E-03
07-08	0.980	89.280E-03	-382.807E-03	11.510E-03	0.986	9.482E-03
08-09	0.978	69.340E-03	-440.102E-03	1.202E-03	0.990	7.229E-03
09-10	0.981	67.180E-03	-455.400E-03	3.505E-03	0.991	6.929E-03
10-11	0.984	39.940E-03	-528.901E-03	19.310E-03	0.985	14.902E-03
11-12	0.980	68.680E-03	-505.700E-03	13.210E-03	0.995	5.360E-03
12-13	0.965	73.674E-03	-520.514E-03	17.546E-03	0.996	5.647E-03
13--	0.847	86.907E-03	-523.151E-03	97.140E-03	0.892	27.119E-03

Table 22: Power-law between mass losses and admittance magnitude changes at 10 kHz for eleven irrigation events.

6.5.2 Discussion

The results presented show that EIT can serve as a tool to track the development of the RSA. Its high temporal resolution enhances the ability of the system to monitor small effects resulting from the root-soil interactions. In this case, since a different substrate was used, one can expect to have a different effect on the overall rate of evaporation. However, as previously discussed, in order to understand the admit-

tance changes, it is important to keep track of any external events. For instance, before the first major irrigation event one can observe two different rates of decrease, which could be explained by looking at the information supplied in the temperature logs of the main EIT system. Considering that at early stages the seedling will not contribute significantly to the evapotranspiration process, we can only expect to see a linear decrease in conductivity such as that in the previous experiment. However, increases in the rate of change start to be noticeable at the VOI around day 4, and clearly observable by day 7. These trend changes are more visible at higher frequencies.

The present work does not fully explore the possibility of frequency difference EIT, but it is clear that the difference of admittance at different frequencies can improve the identification of the RSA. For this reason, the importance of acquiring the EIS profile of the growth substrate cannot be ignored. The profile can enhance our understanding of the images obtained, which can enhance discernment between roots and the effects of roots. This is not to say that EIT can detect individual roots, but in this case, considering that the RSA was taproot based, one could expect it to be more easily distinguishable due to its size. While the effects of the growing RSA are easily understood in terms of decreases in conductivity in certain areas due to the displacement of the soil by the roots, the susceptance changes should be interpreted more cautiously. For example, an unexpected susceptance profile by the end of the experiment that does not follow the previous trend can be observed. It is also important to note, that due to the intensity of the changes computed at the end of the experiment, the reconstructions might benefit from taking a different reference point to avoid admittance hot-spots and artefacts such as the ones observed in the final images.

The present study proposes the use of EZ based on a specific selection criterion. Typically, reconstruction using a regularization scheme such as Tikhonov's will present an amount of ringing (i.e. the reconstruction of any intrusion or admittance change is not going to present highly defined edges). Thus, by selecting an EZ as regions where the values do not fluctuate greatly, one can ensure that the tracking of most elements affected by the main RSA and avoid artefacts. The EZ in this case was selected once the experiment was over, and all images were analysed. This approach has the potential to further calculate the volume of the main taproot by analysing the FEM cell sizes. However, in this experiment the volume does not completely reflect the final fresh mass. Such calculation could be enhanced by using a higher resolution FEM. In the present work, the mesh used is always finer towards the edge of the vessel, thus, a more uniform and finer mesh could enhance the ability of the system to accurately track the volume of tap RSAs. The results highlight the importance of analysing the changes pertaining to the imaginary part of the admittance. The results from the susceptance changes appear to have a higher potential to track the shape of the RSA. However, one of the limitations of the

present work is the lack of any other verification tool that can help interpret the results. Notwithstanding this limitation, the study shows that EIT is a suitable tool to track the development of RSA at different stimulation frequencies under different irrigation regimes.

6.6 *Brassica oleracea var. acephala*

The RSA development of a Kale “Dwarf Blue Curled Vates” (*Brassica oleracea* variety *acephala*, Premier Seeds Direct, UK) was monitored through both EIT and continuous weight measurements for 43 days. Kale is one of the most grown cruciferous species that exhibits a moderate to high resistance to clubroot. As mentioned earlier, the use of EIT can aid breeding programmes by helping understand the peculiarities involved in the RSA development of such an important crop. The subject was planted in its seed stage at 1 cm depth inside a vessel filled with the growing substrate S-01 with a BD = 1.061 gr/cm³. The conditions for growing were a 20° C constant temperature and a 16h/8h day/night cycle. The growing substrate was left to settle for one day before the planting of the seed. Irrigation was dictated by the weight of the vessel. The criterion for irrigation was to not let the total mass drop below 85% of its starting weight. The frequencies, stimulation patterns, and reconstruction process is the same as the one used in the previous experiment. The average number of data frames collected at each frequency was 1890. The images and results reported correspond to the S5/M6 protocol using the data set from time-point 19th-May-2021 13:05 as a reference. The following table lists the hyperparameters used for the reconstructions.

FREQUENCY	S1/M1 λ	S5/M6 λ
500 Hz	6.424E-04	1.586E-04
01 kHz	6.424E-04	1.342E-04
10 kHz	7.021E-04	1.342E-04
25 kHz	7.021E-04	1.586E-04
40 kHz	7.021e-04	1.586E-04
50 kHz	7.021e-04	1.586E-04

Table 23: Computed hyperparameters used to reconstruct images of the *Brassica oleracea* subject.

6.6.1 Results

The mass changes monitored through the scale are shown in Fig. 103. A summary of the irrigation events is presented in Table 24. During the first days of the experiment, one can observe the typical linear behaviour associated with the natural water evaporation at the surface of the substrate. It is important to note that at time-point 566:20 the growth chamber's temperature control started to malfunction and continued until 632:50. During this period, the temperature inside the chamber started to rise above 20° C reaching almost 45° C at certain points (Fig. 104). When the fault was detected, the system was migrated to a different growth chamber in which the lighting system was adapted to supply approx. $346\mu\text{mol}^{-2}\text{S}^{-1}$.

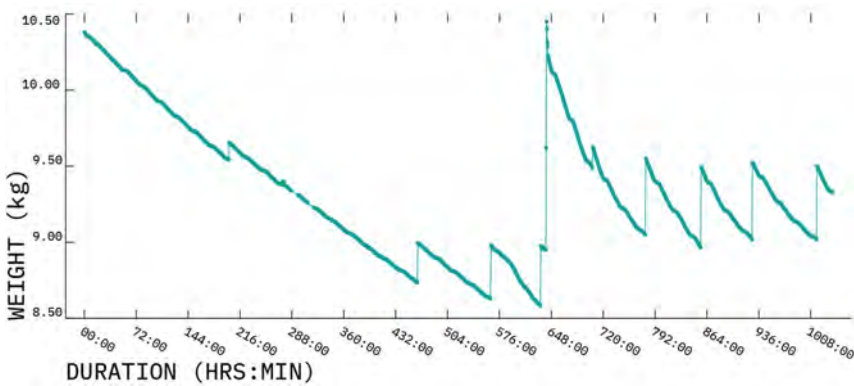


Figure 103: *Brassica oleracea* mass changes during a 43 day period.

EVENT	ELAPSED TIME (HRS:MIN:SEC)	WATER ADDED (GR)
01	201:18:46	110
02	275:11:23	020
03	462:35:27	260
04	564:45:07	350
05	633:22:56	390
06	640:50:46	670
07	641:27:09	830
08	706:03:34	135
09	779:10:30	500
10	855:51:05	530
11	927:04:27	500
12	1016:34:13	480

Table 24: *Brassica oleracea* experiment irrigation events.

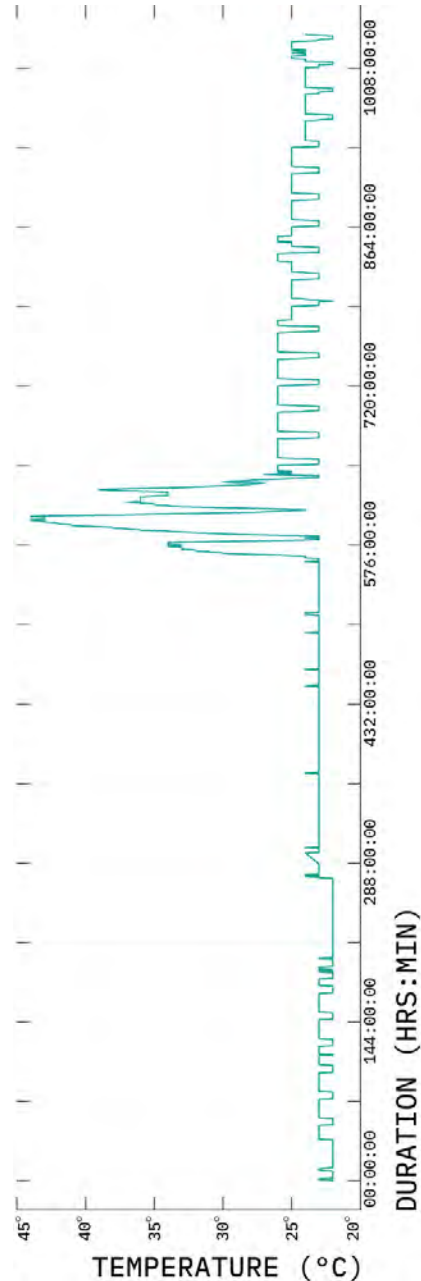


Figure 104: Logged processor temperature changes for the *Brassica oleracea* experiment.

To compensate for the significant water loss, the subject was irrigated (event 05). However, due to the temperature variations, the scale needed to be recalibrated. Therefore, it was decided to bring the growing substrate to saturation. The latter is reflected in irrigation events 6 and 7. This explains how during the first eight hours after event 7, there is an exponential decrease due to the excess of water dripping from below. Similar to the previous experiment, by smoothing the irrigation events the mass losses trend can be simplified to ease the modelling process. The mass losses without irrigation spikes and the overall trend is illustrated in Fig. 105. The trend was fitted to an exponential model $y = a \exp^{bx}$ with $a = -10.167$, and $b = 0.030$. Here b can be understood as the rate of decay. While the goodness of fit is relatively high ($R^2 = 0.989$, SSE = 58.280, RMSE = 0.176), it can be observed that after the re-saturation of the substrate, the decay rate is significantly different from the mostly linear trend before this event. Moreover, such fit does not consider the effects of seasonality, thus, the data was fitted to two SARIMA models. The first SARIMA(1, 1, 0)(0, 1, 1)₄₅ models the seasonal, mostly linear decay at the beginning of the experiment. The second model is a SARIMA(1, 1, 0)(1, 1, 0)₄₅ that corresponds to the mass loss behaviour for the remainder of the experiment after the heat stress event. The autocorrelation of both models' residuals was evaluated through a Ljung-Box chi-square test exhibiting no significant autocorrelation ($p > 0.05$).

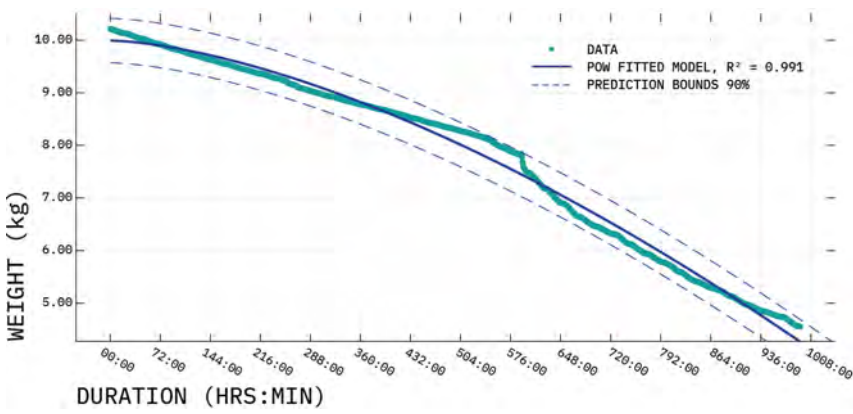


Figure 105: *Brassica oleracea* mass losses fitted model.

The coefficients for each model are presented in the following table:

EVENTS	TYPE	COEFFICIENT	STANDARD ERROR	T-STATISTIC	P-VALUE
01-05	AR 1	-0.510	0.014	-35.071	0.000
	SMA 1	-0.810	0.013	-59.048	0.000
06-12	AR 1	-0.142	0.038	-3.670	0.002
	SAR 1	-0.491	0.031	-15.477	0.001

Table 25: Estimation results for the SARIMA models of the *Brassica oleracea* experiment.

At the end of the experiment, the subject under study was removed from the growth substrate. Fig. 106 shows the foliage and the main RSA (without finer and deep roots) by the end of the experiment. The total fresh mass by the end of the experiment was 19 gr (14.10 gr corresponding to foliage, and 4.9 gr to the main RSA) with the main RSA presenting approximately 15.9 cm in length.

RECONSTRUCTION ANALYSIS

The distribution of the admittance changes inside the vessel were obtained for a 48-day period. In this case, the analysis of the cross-sectional cuts of the reconstructions is presented first. The admittance's

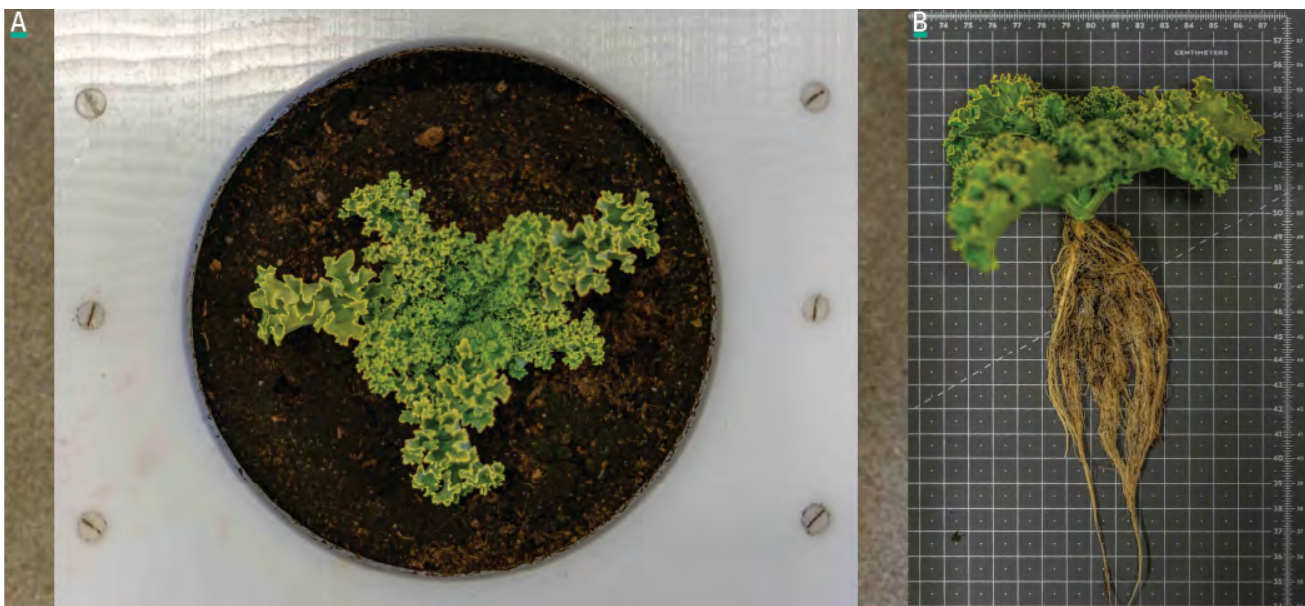


Figure 106: A *Brassica oleracea* at the end of the experiment, and B its main RSA.

real and imaginary distribution components are presented in Figs. 107 & 108 respectively. The results correspond to the following frequencies: 500 Hz, 10 kHz, and 40 kHz. The slices presented represent cuts taken at the central x-axis, central y-axis, z-axis at 36 cm, and z-axis at 27.77 cm. In this case, the slices selected correspond to regions where the most significant changes were observed. Furthermore, the cross-sectional images show the admittance changes every three days. The images correspond to the beginning of the day photoperiod.

Upon initial inspection of the results, one can notice that the effect of the frequency mainly affects the intensity of the changes, particularly during the first 12 days. An increase in conductivity can be observed at the top centre of the vessel from day 3 to 12 at 500 Hz and 40 kHz. On the other hand, at 10 kHz the increase in conductivity can only be observed by day 15. At the latter time-point, negative conductivity changes can be observed below the region of increased conductivity. The negative changes are easily observed in the z-axis cut at height 27.77 cm. The above-mentioned pattern can be observed as the experiment carries on, where a clear region of increased conductivity can be detected at the centre top area and low conductivity changes can be located below this area.

It is worth noting that at 40 kHz the increased conductivity extends further in depth (≈ 8.25 cm), and a clear high intensity centre appears to be constant across all images after day 9. As in previous experiments, the susceptance changes (Fig. 108) behave as negatives at low frequencies, but at 40 kHz the response is similar to that of the conductivity changes. Nevertheless, the depth of the central positive susceptance change is lower (≈ 3.25 cm). For this reason, it can be seen that at 30 the susceptance changes are predominantly negative in the z-axis cut at 27.77 cm. In both cases, during day 27 a decrease in the intensity of the changes at the top of the vessel can be seen. At this time-point, the re-saturation of the vessel had occurred approximately eight hours prior. Interestingly, while the intensity of the conductivity changes does vary from frequency to frequency, the susceptance changes at this time-point show a similar response across all frequencies. The re-saturation of the vessel would in theory bring the measurements close to the reference point, thus, one can be certain that the variations at this stage are due to the processes involved in the subject's root development.

Due to the complexity involved in the redistribution of the admittance's maps, the simple approach to determine the EZ presented in the previous section would not correctly track the changes corresponding to the main RSA. Consequently, a k-means⁷⁷ approach was used to define the reconstructions' EZs. The elements constituting the FEM were grouped into three clusters. The k number was selected by evaluating multiple k-means cluster combinations through the computation of the silhouette's coefficients⁷⁸.

⁷⁷ The k-means algorithm organises data points into a set of k clusters defined by centroids. The data-partition is based in the minimisation of the sum of squared distances between each data point and its closest centroid.

⁷⁸ Peter J. Rousseeuw. "Silhouettes: A graphical aid to the interpretation and validation of cluster analysis". In: *Journal of Computational and Applied Mathematics* 20.C (1987).

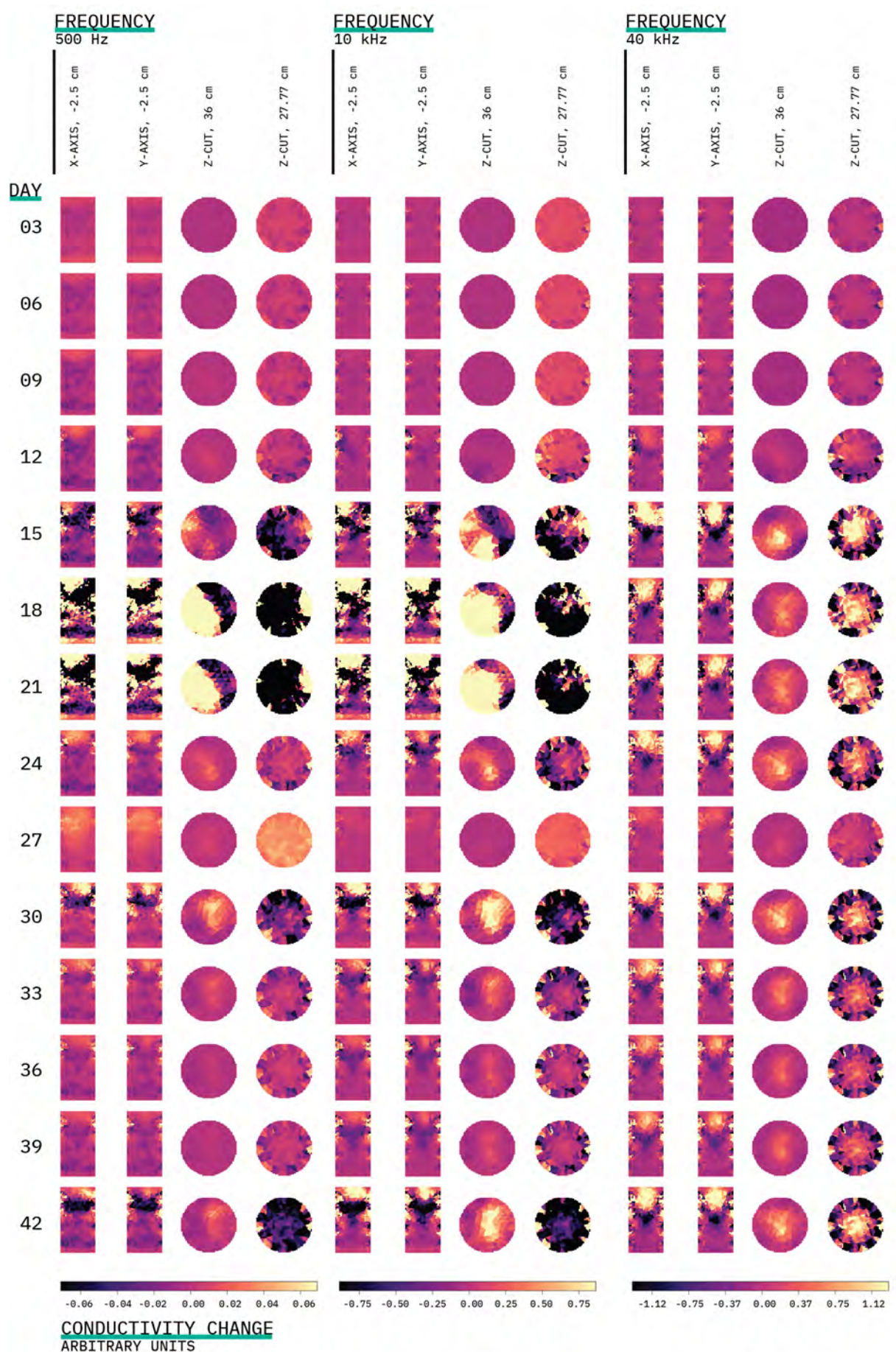


Figure 107: *Brassica oleracea* conductivity changes at different frequencies. Slice views at specific axes.

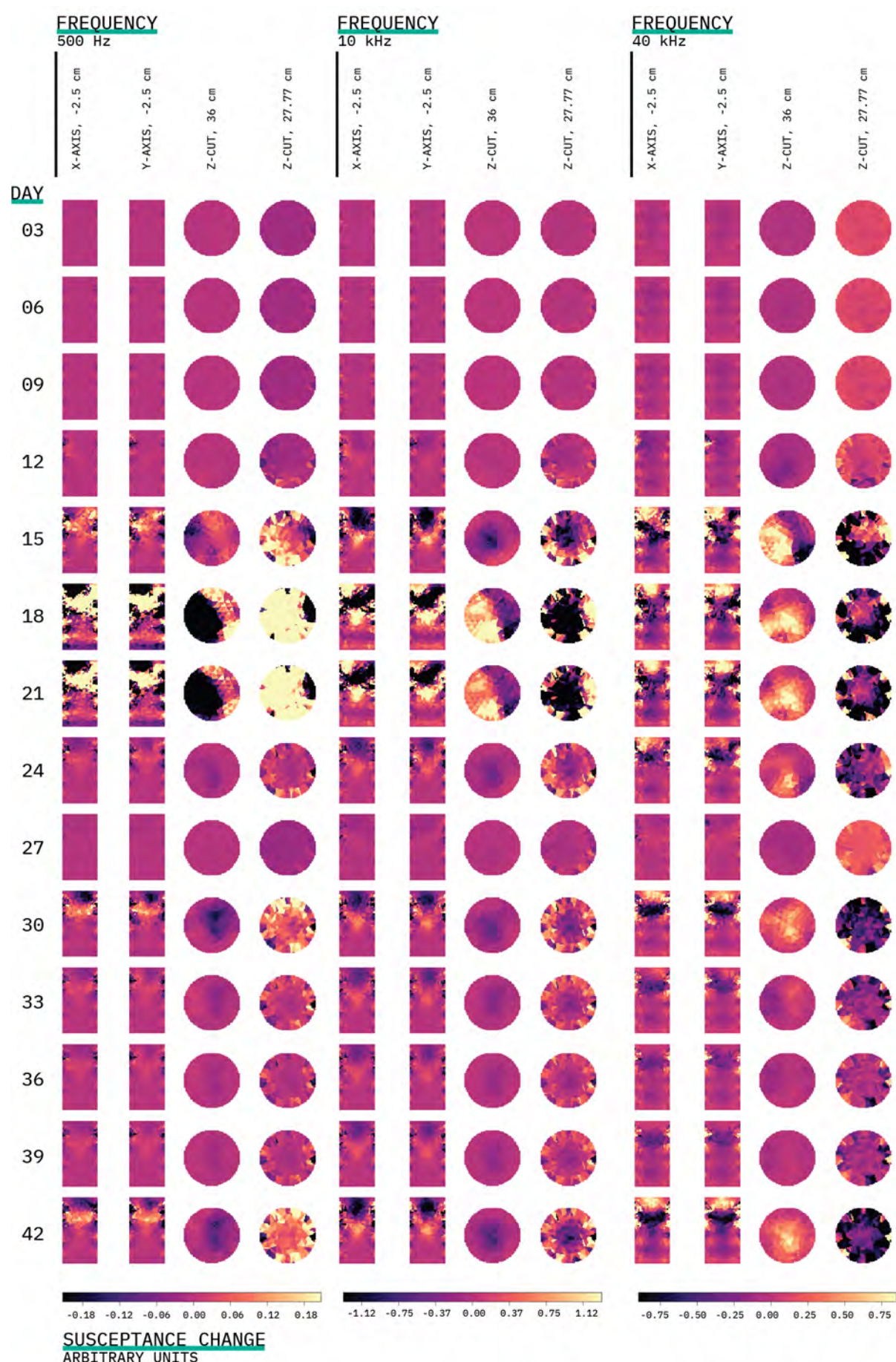


Figure 108: *Brassica oleracea* susceptibility changes at different frequencies. Slice views at specific axes.

The elements constituting the FEM were grouped into three clusters. Fig. 109 shows the silhouette coefficient for each cluster combination tested. From the results presented in Fig. 109, it can be observed that the optimal number of clusters is 3 as it corresponds to the highest value. The k-means approach implemented in the present work uses a k-means++ algorithm to initialise the cluster centroid positions. The distance metric used for the minimisation of the sum of point-to-centroid lengths is the L1 norm, which corresponds to using the median of a cluster as the centroid for its respective points. Furthermore, to enhance the final result 50 replicates, each with a different initial clusters centroids, were computed. From the replicates, the final solution selected was the one with the lowest sum of point-to-centroid distances. The iso-volumes presented in Fig. 110, show how this approach can help filter zones of interest. For the sake of brevity, the figure shows the conductivity changes of the data acquired using a 10 kHz stimulation frequency.

The 3D representations show how during the first days of the experiment a decrease in conductivity is present across most of the vessel. It is not until later stages of the experiment that the shape of a constant volume starts to appear. While the results from day 21 show a volume with increased conductivity, the centre of such incremental changes moves from location $y \approx -0.05$ to $y \approx 0.015$ when get-

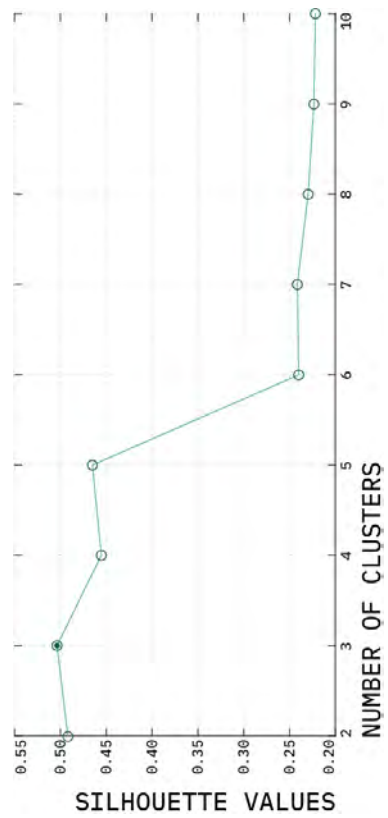


Figure 109: Silhouette coefficients to find the optimal number of clusters.

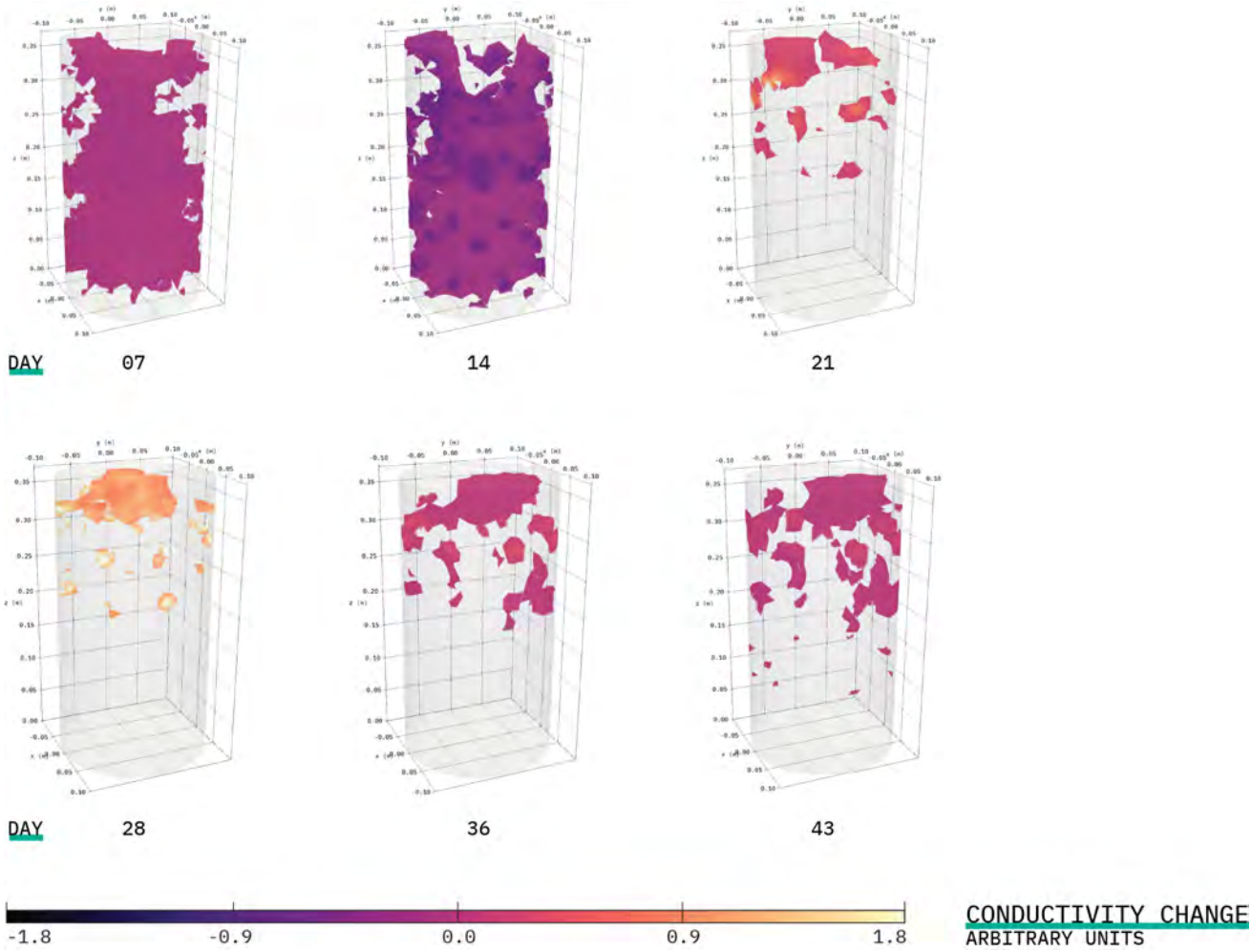


Figure 110: *Brassica oleracea* clustered conductivity changes at 10 kHz presented as iso-volumes.

ting closer to the final days of the experiment. As in the exploration of the cross-sectional images, during day 28 a significant increase in conductivity can be observed at the top centre of the vessel. The final two reconstructions show that there is still an increase in conductivity in this region, although the intensity is less than that of day 27.

Additional to the visual exploration of the reconstructions, a more in depth analysis is presented below. Fig. 111 shows the conductivity⁷⁹ changes and admittance phase changes corresponding to each of the clusters for the total duration of the experiment. Since the groups mostly represent high, average and low conductivity changes, here the clusters are referred to as top, middle, and bottom cluster. The average of the cluster (i.e. its centroid) is reported.

The conductivity changes presented show that the k-means approach works adequately by separating the conductivity changes into three primary categories. The conductivity results presented at each frequency show that there is almost an equilibrium between positive and negative changes. Similar to the previous experiment, one of the main differences between frequencies is the intensity of the change. At 500 Hz a clear upward trend starts to appear at duration 354:42. This point is clearer at higher frequencies, with the exception being that at 40 kHz the starting point of the upward trend can be observed at 240:00. Due to the intensity of the changes at 40 kHz, the effects of irrigation events can easily be identified. During irrigation events, the centroid of the changes becomes closer to zero. In the case of the low frequency results, it can be observed that after the re-saturation event, the changes in conductivity remain close to zero. However, when looking individually at the periods in between irrigation events, the trends persist⁸⁰. Before the re-saturation event, we can observe that between irrigation events 3-5 the conductivity changes exponentially. Between events 4 and 5 (i.e. during the heat stress incident) an increase in the rate of growth/decay can be noted. The latter is difficult to identify at 40 kHz. After the re-saturation event, the rate of change diminishes significantly, and the trends observed appear to be almost linear. In the 40 kHz case, the conductivity changes become more stable after the re-saturation; in turn, this eases the identification of the trends.

The results from the phase changes show a different behaviour at each frequency. At low frequency (500 Hz), the phase changes show small differences up until duration 360:00. When reaching this time-point, both the middle and top EZs decrease sharply towards 50°. Moreover, during irrigation events it can be observed that the phase change of the middle EZ increases and decreases abruptly. However, after irrigation event 10, this EZ decreases slowly and more linearly. The top EZ remains at a negative phase change upon getting closer to duration 360:00, except for the time corresponding to the re-saturation event. The effects of the different irrigation events can also be observed in the phase changes as sudden peaks. Interestingly, at 10 kHz the phase changes show distinct responses that can be easily separated from one another.

⁷⁹ Since the clusters were determined using the real component of the admittance, the conductivity is reported rather than the admittance's magnitude as in previous experiments.

⁸⁰ Essentially, this would be akin to the exploration presented in the previous experiment, where individual graphs were plotted between irrigation periods.

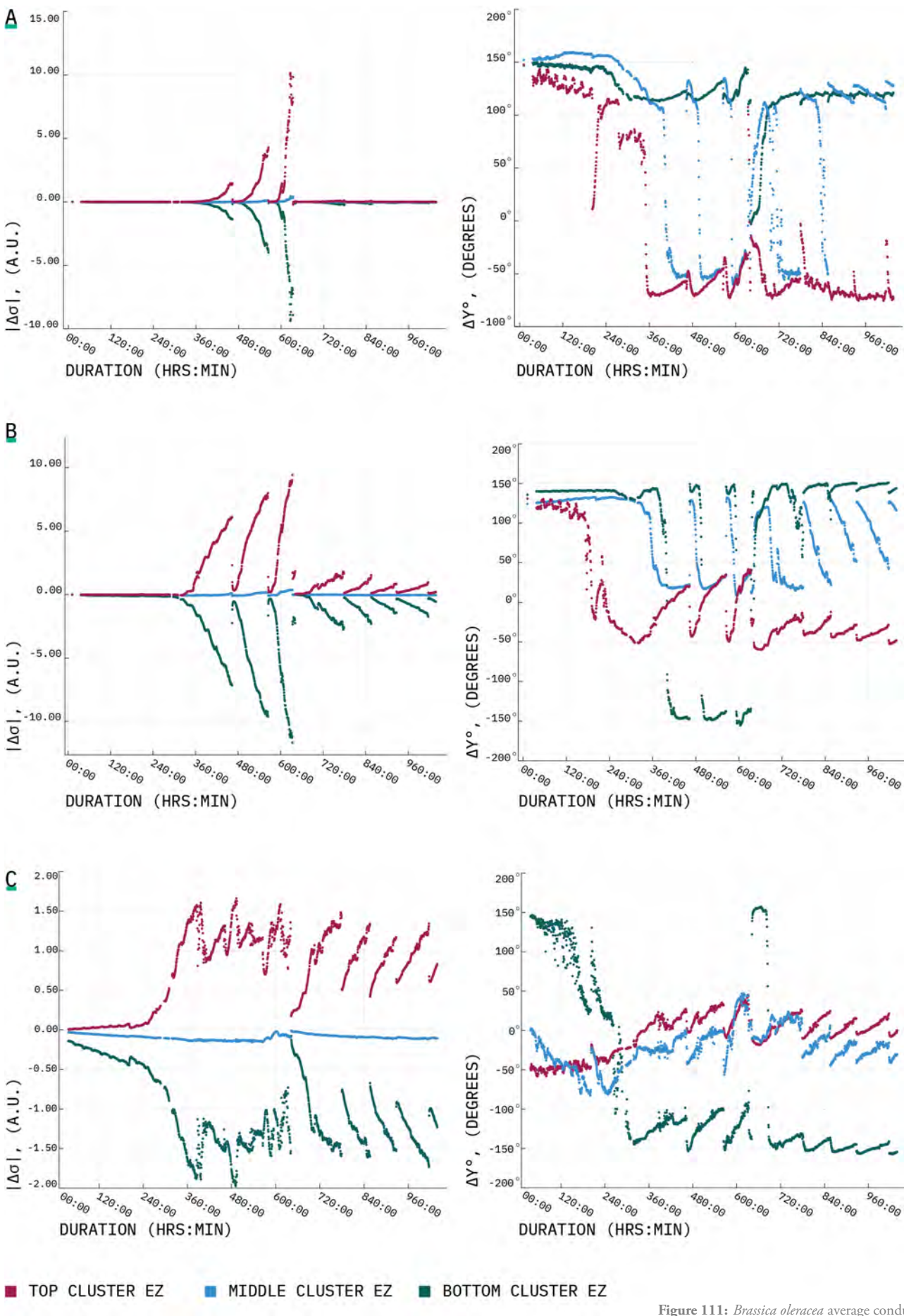


Figure 111: *Brassica oleracea* average conductivity and phase changes over A. 500 Hz, B. 10 kHz, and C. 40 kHz.

For instance, it can be seen that the middle EZ always presents a downward trend that remains between the range of 150° and 25° . In the 40 kHz case, the only line that shows a distinct behaviour is the one corresponding to the bottom EZ, which also presents a higher range, going from 150° to -150° .

Since the 10 kHz frequency shows a clear distinction between phase changes and more constant trends for the duration of the experiment, this work further explores the relationship of its admittance changes with the mass losses recorded. The relationship between the latter variables is explored between irrigation events. Table 26 summarises the dependence between these variables evaluated through their corresponding distance correlation. All variables were normalised through Eq. 104. The results show that there is a strong dependence between admittance changes and the mass fluctuations. It can be observed that the conductivity changes show a greater correlation than the phase changes. As expected, during the first irrigations events the top EZ has a lower dependence with the mass changes. It is after event 3 that one can notice higher correlation coefficients for both the top and bottom EZ. On the other hand, the middle EZ shows the lowest correlation coefficients, particularly between events 11-12. Even though there is a dependence between mass losses and phase changes, their interaction can be more challenging to model due to the significant changes that the phase experiences at certain events (Fig. 111). These results demonstrate that there is a clear relationship between the admittance changes and the actual mass within the vessel.

EVENTS	VARIABLE	TOP D-CORR	MIDDLE D-CORR	BOTTOM D-CORR
00-01	Conductivity	0.726	0.990	0.970
	Phase	0.738	0.978	0.807
01-02	Conductivity	0.774	0.959	0.848
	Phase	0.794	0.692	0.535
02-03	Conductivity	0.961	0.615	0.966
	Phase	0.933	0.941	0.832
03-04	Conductivity	0.973	0.940	0.980
	Phase	0.955	0.765	0.878
04-05	Conductivity	0.966	0.907	0.969
	Phase	0.939	0.775	0.872
05-07	Conductivity	0.930	0.913	0.951
	Phase	0.938	0.930	0.932
07-08	Conductivity	0.842	0.762	0.848
	Phase	0.910	0.832	0.775
08-09	Conductivity	0.968	0.552	0.986
	Phase	0.982	0.875	0.799
09-10	Conductivity	0.876	0.513	0.911
	Phase	0.893	0.959	0.478
10-11	Conductivity	0.861	0.597	0.895
	Phase	0.861	0.923	0.572
11-12	Conductivity	0.943	0.471	0.964
	Phase	0.940	0.959	0.961
12--	Conductivity	0.941	0.881	0.941
	Phase	0.939	0.945	0.939

Table 26: Distance correlation between mass losses and admittance magnitude changes at 10 kHz for all irrigation events. Admittance changes are presented as conductivity and phase changes.

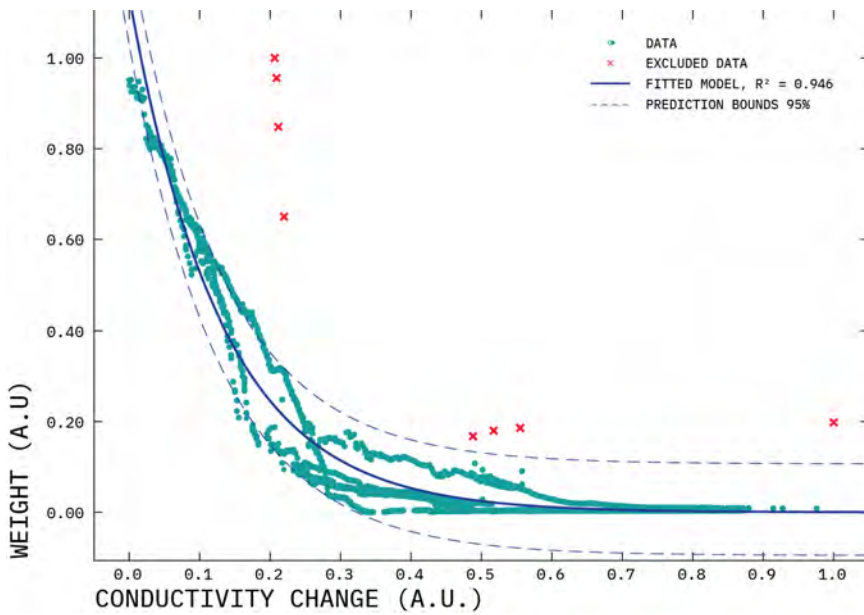


Figure 112: *Brassica oleracea* relationship between normalised weight and conductivity changes, and its fitted model.

Unlike the previous experiment, the present experiment did not suffer from unexpected disconnections that might create several missing data points, thus, this section presents the fitting of a model that considers all conductivity and mass⁸¹. Fig. 112 presents the relationship between normalised conductivity changes and mass losses. The interaction is modelled using an exponential model $y = a \exp^{bx}$ with $a = 1.136$, and $b = -7.651$ with an acceptable goodness of fit ($R^2 = 0.946$, SSE = 5.064, RMSE = 0.053).

6.7 Discussion

Detecting the effects of fibrous plant roots with electrical methods is considered to be quite challenging⁸². The present work shows that a better identification of root effects can be achieved through a combination of EIS profiling and EIT's high temporal resolution. Undoubtedly, the evolution of the admittance changes shows a complex behaviour that makes the identification of the main RSA more challenging. For this reason, this study employs one of the most common techniques used in computational statistics (k-means clustering) to separate the elements of the reconstructions into VOIs where key interactions take place. While this work does not further explore other common dissection techniques, the researcher acknowledges that the use of such techniques can help overcome some of the limitations of EIT. As in the previous experiment, the experimentation using different frequencies can help identify certain aspects or processes of the RSA. It was noticed that at 40 kHz there was a more consistent central region of high conductivity changes. The results using multiple frequencies hint at the potential of frequency-difference EIT, which can be further enhanced with the natural high temporal resolution of the technique. As expected, there is a strong correlation between the weighted mass and the changes observed in admittance distribu-

⁸¹ In contrast to fitting different models at different time ranges.

⁸² Amato et al., “Multi-electrode 3D resistivity imaging of alfalfa root zone”.

tion. Surprisingly, the images obtained show a consistent increase in conductivity at the top of the vessel. This increase can be understood as a combination of root exudates and water uptake. The increase in conductivity is interesting, as such an increase is even higher than when irrigation occurs. During such irrigation events, the infiltration of water appears to lower the conductivity of these regions and at the same time to bring the regions that lost conductivity back to their initial state. Nevertheless, even by re-saturating the substrate the high conductivity at the top persists. This effect might help identify the central tap root. The results differ from the expected behaviour from our previous research on *P. Brassicae*, where the effects of the RSA were observed as negative conductivity changes. However, it is worth noting that in that instance the substrate was kept under a bed of water at most times. Nevertheless, the location and shape of the changes leads us to the conclusion that what is being observed in the reconstruction is indeed the main RSA. The nature of the changes can only be speculated on at this stage, due to a lack of replicates and an additional tool to define a ground truth. One natural conclusion would be that what is being observed is water and nutrient uptake, as the clustering and images show that the negative and positive changes occur in a balanced manner. Another explanation could be that such conductivity changes are due to root exudates, since the irrigation events seem to decrease the intensity of the high conductivity changes. It is known that roots have different life stages, and their functions change over time, however, there is a lack of literature regarding the electrical characterisation of root processes.

The method shows a high potential to monitor different interactions. Hence, there is a need to understand in depth the underlying effects of different root processes to completely understand what is being imaged. Notwithstanding this limitation, the results demonstrate the prospect of using multiple approaches to model such interactions. For instance, a simple approach such as subdividing the FEM into multiple VOIs can be considered when there is a clear expectation that the RSA will significantly modify the shape of the substrate. In the case of the *Raphanus sativus*, the main tap root was expected to displace the growing substrate in a substantial manner, creating discontinuities in the substrate's structure. On the other hand, in an herbaceous root system, such as the one from the *Brassica oleracea*, certain displacement of the substrate would be expected, however, due to the small diameter of most roots such an effect would be hard to identify, particularly at early stages of the subject's development. In this case, changes taking place in the soil manifested in different regions of the vessel, thus, an approach based on clustering provided a more objective way to identify certain regions based on the changes exhibited.

The lack of replicates in the present study makes it difficult to infer a clear relationship between admittance changes, root biomass, RSA and root-soil processes. Nevertheless, this study shows that a better understanding of the reconstructions can be achieved through EIS

profiling of the growing substrate at different moisture levels. An additional method would need to be incorporated along EIT to correctly relate the changes observed in the reconstructions to their respective root-soil interaction. The latter in addition to multiple replicates can finally demonstrate the potential of EIT as a high-throughput phenotyping tool.

CONCLUDING REMARKS

WHILE OFTEN HIDDEN, plant roots play a crucial role in modifying the behaviour of ecosystems. The purpose of the present research is to propose a variation of a traditional geophysics technique as a modern plant phenotyping tool that has the potential to bridge the current gaps in root research. The study of root traits is challenging, not only due to the inherent inaccessibility when using traditional growing substrates such as soil, but also due to the lack of standardisation and metrics to evaluate both root traits and root-soil interactions¹. Undoubtedly, this is no easy task as roots present a vast amount of diversity in their structures and properties. The use of electrical imaging to monitor the physical and biological process of roots is not new, however, more often than not, root studies employing electrical imaging rely on ERT and absolute reconstructions. The latter combination can create more uncertainty about what is being imaged, as reconstructions rely on assumptions about the resistivity properties of the substrate under study.

The present work's original contribution to knowledge is the development of an EIT system optimised for high-throughput root studies, and a methodology that enhances the interpretation of the images reconstructed. This study expands on the work previously published, where the main focus of the research was the use of EIT for pathogen detection and on maximising the potential of the technique for more general root studies.

After revising the benefits of several technologies to study roots, and the specification of modern phenotyping platforms, an EIT system enabled for IoT usage was developed. The design of the system considered the current state of the art where EIT is predominantly used i.e. medical and industrial fields. Such fields often focus on two-dimensional reconstructions, thus, studies trying to enhance the vertical resolution of 3D reconstructions is limited. The research presented took into consideration the advance presented by the medical community^{2,3} and extends this knowledge by exploring how different stimulation protocols affect the sensitivity of the measurement procedure, and how they perform under the presence of noise when reconstructing images. The benefits of the system and methodology developed were demonstrated through three experiments under a controlled environment scenario. The challenges imposed by the nature of the substrates led to the creation of a multi-ring stimulation strategy, and a soil preparation-packaging protocol. The former reduces the probability of encountering reciprocal errors where the measurement

"Holistic rhizosphere science has the potential to substantially increase understanding of plant-soil systems and provide guidance for pressing issues of the 21st century, such as agricultural sustainability and environmental change" York et al., 2016

¹ Gregoire Freschet et al. "A starting guide to root ecology: Strengthening ecological concepts and standardizing root classification, sampling, processing and trait measurements". In: *Hal-02918834* August (2020).

² Andy Adler et al. "Electrical impedance tomography in 3D using two electrode planes: characterization and evaluation 3D EIT image reconstruction with GREIT Bartomiej Grychtol, Beat Müller and Andy Adler - Adjacent stimulation and measurement patterns considered harmful Elec". In: *Physiol. Meas* 37 (2016).

³ Wagenaar and Adler, "Electrical impedance tomography in 3D using two electrode planes: characterization and evaluation".

is different when taken in the opposite configuration. Moreover, it enhances the temporal ability of the system⁴ when using more than 32 electrodes while retaining the vertical improvements of the stimulation protocols explored. The soil-packing protocol presented builds on the methodology previously developed⁵ and presents a more efficient protocol that is better suited for peat-based substrates. Next, different approaches to the analysis of the acquired data were presented. Due to the high temporal nature of the method, the effects of day/night photoperiods could be detected across all experiments. These effects were corroborated by the weight measurements taken at the same time. The present work also illustrates the importance of doing preliminary EIS profiling of the growth substrates at different moisture contents. Such profiling greatly improves the understanding of the data being imaged, particularly when analysing the imaginary component of the data. Finally, the experiments show that there is a strong correlation between fluctuations in mass and EIT data, which hints at the possibility of linking EIT data to biomass development.

The use of electrical imaging is predominant in field studies; this explains why the use of a geophysical survey technique, such as ERT, is the most common method. One of the most recent advances in this field is the combination of ERT with Mise-à-la-Masse approaches⁶. Both imaging methods help image different root interactions, nevertheless, the method becomes more invasive since a physical connection must be made through the stem. Furthermore, this type of approach is again limited by the use of DC based current sources and the use of traditional stimulation protocols. While these types of approaches demonstrate that RSAs and root zone water dynamics can be monitored through their electrical properties, these methods do not fully explore the possibilities of characterising such properties using more than resistivity and under a spectrum of stimulation frequencies. The experimental results shown in this work demonstrate that exploring the same process under different stimulation frequencies can enhance the ability of the system to detect root development, and water/nutrient uptake. The experimental achievements presented here demonstrate that there is value in exploring the electrical characteristics of roots, and that further developments in this area can create an accessible tool well suited for high-throughput root phenotyping.

7.1 Limitations

One clear limitation of this work is the lack of an alternative tool to help better interpret the reconstructions. In particular, in the first instance an additional method such as X-ray imaging would be preferable to define a ground truth. A current study⁷ shows the effectiveness of using ERT alongside X-ray to describe water infiltration in soil columns. Typically, ERT studies using soil columns rely on the use of TDR probes at certain points of the column to corroborate what is being imaged or to evaluate moisture content. Either would help

⁴ In the case of planar arrangements the acquisition time was reduced by ≈ 5 times when compared to a typical 64 planar acquisition. For square arrangements the acquisition was twice as fast as a complete square protocol.

⁵ Corona-Lopez et al., “Electrical impedance tomography as a tool for phenotyping plant roots”.

⁶ Benjamin Mary et al. “Time-lapse monitoring of root water uptake using electrical resistivity tomography and mise-à-la-masse: a vineyard infiltration experiment”. In: *Soil* 6.1 (2020).

⁷ Mihai O. Cimpoiașu et al. “Hydrodynamic characterization of soil compaction using integrated electrical resistivity and X-ray computed tomography”. In: *Vadose Zone Journal* 20.4 (2021).

corroborate the veracity of the images, however, it remains unclear how many of the root-soil interactions could be explained through combining these approaches. Root interactions are not only structural, and the biophysical processes occurring in the movement of water through soil and root involves chemical processes. Root exudates can change the chemistry of the soil in proximity to the roots, however, the exploration of how these would affect the electrical properties of the soil is still unknown. Therefore, this is one of the key limitations of this study. While changes in impedance can be correlated to mass changes, it still can not be determined how many of these changes are due to chemical processes occurring in the rhizosphere. Future research should focus on filling such knowledge gaps and methodology through multidisciplinary collaborations.

Additionally, the lack of a complementary method hindered the exploration of the reconstruction on finer meshes. The reconstruction method used in the experimental work prioritised robustness. Since the algorithm selected relies on the computation of the forward problem upon each iteration, the reconstruction of a finer mesh would be more computationally expensive and would require specialised hardware. The use of such an algorithm also imposed restrictions on the type of mesh used. As the algorithm re-computes the forward solution upon each iteration, the selection of the mesh is required to be finer to present a more accurate calculation of the Jacobian matrix.

Besides the aforementioned limitations, the lack of replicates in the experimental section is an obvious drawback. To fully demonstrate the utility of the system for phenotyping studies, the system should not only show the robustness of its IoT capabilities, but should also prove that it can reliably measure with small variability the same process in a population under study.

7.2 Future work

As an evolving project, the results from this work and the understanding of its limitations provide evidence for the amount of research which could compliment the findings presented. A short list of further research identified by the author is as follows:

- Electrical characterisation of root interactions. EIS is commonly used in electrochemical studies to model complex chemical interaction. Applying this approach to study the effects of root exudates would greatly improve the understanding of the images being generated through EIT.
- Demonstrate EIT full capabilities as a phenotyping platform. The high-temporal resolution of EIT is able to detect subtle changes that can lead to the characterisation of root systems. However, this should be explored in a phenotyping environment under controlled conditions using an adequate population size.
- Explore the effects of non-similar skips. While the exploration of

stimulation protocols was presented, the effects of non-reciprocity were not studied. Non-reciprocity was achieved using non-similar skips (e.g. S5/M6), and most often converged faster than stimulation patterns using similar skips (e.g. S1/M1).

- Study plant seedlings using EIT. The resolution of EIT system is often limited by the diameter of the vessel being imaged. The findings presented hint at the possibility of using smaller vessels that can help study plants during their seedling stages with a higher resolution.
- Exploration of temporal frequency difference EIT. The results presented in the experimental chapter of this work show that different electrical responses occur at different frequencies. These responses not only vary in intensity, but also show unexpected trends. Such responses are typically used in EIT to create a clear distinction between the background and elements of interest.

Undoubtedly, the challenges that our food supply chain faces today require the efforts of multiple disciplines. The results of this study aim to move forward such efforts by providing a tool and methodology to study plant roots under a different light.

APPENDIX

What follows is a detailed explanation of the use and implementation of the classes from the spmqtt package developed in this work.

SPEIT CLASS

The SpEIT class is the base of the spmqtt package. It inherits some methods found in the class “`mqtt_client.Client`” from the Paho package. The class allows the user to search for SpEIT systems within a MQTT server, connect to a specific device, and send commands to it. A name for the client must be provided as per MQTT specifications, as well as the IP and port of the MQTT broker⁸. To create an instance (referred to as node in this work) one can use:

```
from spmqtt.speit import SpEIT
node = SpEIT(client_name='PyConsole', broker=('192.168.1.5', 1883),
              log=True, animation=False)
```

The methods and parameters available to the user are summarized in the following table:

⁸ The user can enable an internal event logger and animation progress sequences to aid in debugging.

Listing 4: SpEIT node instantiation through the spmqtt API.

Table 27: Methods available to the SpEIT class.

NAME	SYNOPSIS	DESCRIPTION	OUTPUT
show_speits	show_speits - []	Start the look-up process to find all the available SpEIT devices in the MQTT server	Array containing a list of SpEIT devices
open	open - device	Main method to establish a connection with a specified SpEIT device. The device name should be its unique ID	Boolean connection flag
send	send - cmd [with_response]	The method formats the command with the appropriate encoding and delimiter. If the <code>with_response</code> flag is active, the API will lock until it receives a response from the node	Decoded data sent from SpEIT
data	data - [clean]	Data container setter and getter method. The container serves as a buffer for formatted data acquired from the <code>eit</code> command. If the <code>clean</code> flag is active, the API will clear the container manually	Decoded data sent from SpEIT
message	message - [clean]	Message container setter and getter method. The container serves as a buffer for non-formatted data acquired from SpEIT. If the <code>clean</code> flag is active, the API will clear the container manually	Non-Decoded data sent from SpEIT
received	received - []	Getter method for the data acquisition completion flag. For external use. Once the method is called the flag is cleared.	Boolean received flag
restart_node	restart_node - [re_connect]	Restart node in use. Both the gateway and SpEIT connected. If the <code>re_connect</code> flag is active, the API will wait until connection with the node is re-established.	NULL
restart_all	restart_all - []	Restart all nodes in the network	NULL

The usual interaction is illustrated in the following minimal working example:

```

1  if __name__ == '__main__':
2      """
3          speit.py Module test
4          """
5
6
7      node = SpEIT(client_name='Test', animation=True)
8      node.loop_start()
9      speits = node.show_speits()
10     node.open(input('Choose device: '))
11
12     try:
13         cmd = input('\rEnter command >_ ')
14         node.send(cmd, with_response=True)
15         data = node.data
16         print(f'Acquired data:\n{data}')
17         node.data = True
18         print(node.data)
19         del node
20         break
21
22     except KeyboardInterrupt:
23         print("exiting...")
24         node.disconnect()
25         node.loop_stop()

```

Listing 5: Exemplification of the spmqtt API typical use.

Internally, the SpEIT class handles all the subscriptions and connection callbacks from the MQTT broker. Once an instance is created, the system analyses the current topics on the MQTT server to determine the availability of each Wi-Fi module and SpEIT node. The before-mentioned process starts the data flow with the broker, and in order to maintain such flow, the loop method has to be called. Once the user selects a SpEIT to establish a connection with, the client API runs a process to first check the availability of the device within the network, then determines which Wi-Fi modules can connect to it according to their RSSI, and finally starts the connection process using the Wi-Fi module with the best connection signal. As the connection with the SpEIT device is established, the Wi-Fi module sends a message to the topic, corresponding to its status to inform all subscribers that the Wi-Fi module and SpEIT are being controlled by a specific spmqtt client. Next, the Wi-Fi module creates a new subset of topics corresponding to the SpEIT device connected, one for the client to send commands, and another one to receive the data.

In our type of application, data reliability is more crucial than the speed at which the user receives the data, thus, the Wi-Fi module can identify the commands associated with EIT measurements, and once it receives one it starts the acquisition process in three steps. First, it allocates memory in a virtual SSD. Next, it transmits the command to the SpEIT module and stores the incoming data in the SSD. The data is transmitted to the MQTT broker once the complete frame is stored in the SSD.

The Wi-Fi module handles the rigorous connection process to

SpEIT's BLE module. Once a device is selected, it establishes a testing connection. Using the testing connection, the Wi-Fi module first reads all the services available in the BLE module. Once it finds the transparent UART service, it then reads its characteristics. If within the characteristics the module finds the TX channel, then the Wi-Fi module secures the connection and subscribes to the notifications of that service. The process will trigger an acknowledgement signal from the BLE module to the core of the SpEIT board, and in turn it will start its initialisation process and run its calibration protocols. Finally, the status messages corresponding to SpEIT's initialisation process will be sent back to the Wi-Fi module and back to the MQTT server to find its way to the user.

The complexity of achieving a stable and reliable connection with a combination of BLE and Wi-Fi is what prompted the creation of this API. Nevertheless, dealing with the data received can be a laborious process that can be easily automated, and thus, the next class was designed to ease this process.

DATALOGGER CLASS

The aim of the class is to automate the most common data acquisition tasks when using SpEIT devices. Thus, the class is mainly a data formatter to create useful and readable data. The class is based on the concept of pandas Dataframes⁹. The logger requires a node to control, thus, the user can create multiple instances to acquire data from multiple nodes. During the logger instantiation, the connection is checked to re-ensure that the device is still present. The code needed to create a Datalogger consists of:

```

1 from spmqtt.speit import Datalogger
dlog = Datalogger(speit_node=node, freq='1'k, elec_n=8,
                  elec_n=8,
                  inj_sk=1, meas_sk=1,
                  ring_offset_size=32,
                  square=False)

```

⁹ Pandas is an open-source package, built on top of numpy, that helps analyse and manipulate tabular data.

Listing 6: Exemplification of the DataLogger instantiation.

The object takes the common parameters needed to run the 'eit' command. Depending on the type of S/M configuration, the user needs to specify either the ring offset (planar arrangement) or the ring size (square arrangement). An overview of the methods available to the class is presented in Table. 28. There are two types of acquisition methods, single and reference. As its name states, the single method acquires one data-frame, whereas the reference function takes multiple data-frames and averages them. When calling the data acquisition methods from the class, a temperature calibration per data frame is acquired to ensure the consistency between frames. If needed, the user can add metadata elements to the data-frames, such as the name of SpEIT system, gateway, and temperature. If required, the user can save the data as a csv file.

NAME	SYNOPSIS	DESCRIPTION	OUTPUT
get_data	get_data - [meta]	Acquire a single data-frame. If desired, the method can add meta-data to the frame. The method returns a pandas data-frame	Formatted data in a pandas DataFrame object
get_reference	get_reference - n_frames [meta]	Acquire a reference data-frame. The method takes multiple frames. The method creates both a pandas reference frame containing all acquired frames, and a calculated single frame comprised of the mean of all frames. If desired the method can add meta-data to the frame	Formatted data in a pandas DataFrame object
save_df	save_df - frame - file_name [experiment]	Save data-frames as csv files. The user can add an extra metadata field called experiment. Options for frame parameter : 'data_df', 'mean_df', 'ref_df'	csv file containing the desired data-frame

Table 28: Methods available to the DataLogger class.

The above-described classes work well when dealing with some pots, and in the scenario when the user desires to control systems manually. However, when working with a considerable amount of rhizotron, manual data acquisition becomes a laborious and difficult process. This is the reason behind the design of the final class of the spmqtt package.

SP AUTOMATA CLASS

The SpAutomata class is designed to automate the data acquisition process of multiple SpEIT devices. Its aim is to create multiple clients that can run on different processor cores of the target server. At initialisation, the object opens a specified SQLite database, or creates a new one based on the devices connected to the SpEIT network. The database operates as a to-do list, that is meant to be accessed by multiple SpAutomatas to acquire the data for all SpEITs in the database. Furthermore, the class handles the storing of the data acquired in folder files by first using the SpEIT device name, then using the date of the experiment, and finally storing the file according to the specified name or by the time of acquisition. An example of how to instantiate and use the class follows:

```
from spmqtt.speit import SpAutomata
automaton = SpAutomata(sp_database=database, rebuild=True, freq=frequency,
elec_n=electrodes,
inj_sk=Injection_skip,
meas_sk=measurement_skip,
square=square_strategy,
ring_offset_size=offset)
```

Listing 7: Exemplification of the SpAutomata instantiation.

The class only provides the following method (Table. 29):

NAME	SYNOPSIS	DESCRIPTION	OUTPUT
start	start - acquisition_method [file_name] [n_frames]	Start automatic acquisition process	SQLite database & csv data-frames

Table 29: Methods available to the SpAutomata class.

BIBLIOGRAPHY

- Adler, Andy and Alistair Boyle. "Electrical Impedance Tomography". In: *Wiley Encyclopedia of Electrical and Electronics Engineering*. Wiley, May 2019, pp. 1–16. doi: [10.1002/047134608X.W1431.pub2](https://doi.org/10.1002/047134608X.W1431.pub2).
- "Electrical Impedance Tomography: Tissue Properties to Image Measures". In: *IEEE Transactions on Biomedical Engineering* 64.11 (Nov. 2017), pp. 2494–2504. issn: 0018-9294. doi: [10.1109/tbme.2017.2728323](https://doi.org/10.1109/tbme.2017.2728323).
- Adler, Andy, Pascal Olivier Gaggero, and Yasheng Maimaitijiang. "Adjacent stimulation and measurement patterns considered harmful". In: *Physiological Measurement* 32.7 (2011), pp. 731–744. issn: 09673334. doi: [10.1088/0967-3334/32/7/s01](https://doi.org/10.1088/0967-3334/32/7/s01).
- Adler, Andy, Pascal Olivier Gaggero, Yasheng Maimaitijiang, John H Arnold, Richard Bayford, and Justin Wagenaar. "Electrical impedance tomography in 3D using two electrode planes: characterization and evaluation 3D EIT image reconstruction with GREIT Bartomiej Grychtol, Beat Müller and Andy Adler - Adjacent stimulation and measurement patterns considered harmful Elec". In: *Physiol. Meas* 37 (2016).
- Adler, Andy and Robert Guardo. "Electrical impedance tomography: Regularized imaging and contrast detection". In: *IEEE Transactions on Medical Imaging* 15.2 (1996), pp. 170–179. issn: 02780062. doi: [10.1109/42.491418](https://doi.org/10.1109/42.491418).
- Adler, Andy and William R B Lionheart. "Uses and abuses of EIDORS: an extensible software base for EIT." In: *Physiological Measurement* 27.5 (May 2006), S25–s42. issn: 0967-3334. doi: [10.1088/0967-3334/27/5/s03](https://doi.org/10.1088/0967-3334/27/5/s03).
- Adler, Andy et al. "GREIT: a unified approach to 2D linear EIT reconstruction of lung images". In: *Physiological Measurement* 30.6 (June 2009), S35–s55. issn: 0967-3334. doi: [10.1088/0967-3334/30/6/s03](https://doi.org/10.1088/0967-3334/30/6/s03).
- Alexandratos, N. and Bruinsma, J. "World Agriculture Towards 2030/2015: The 2012 Revision". In: *World Agriculture* (2012).
- Amato, Mariana, Bruno Basso, Giuseppe Celano, Giovanni Bitella, Gianfranco Morelli, and Roberta Rossi. "In situ detection of tree root distribution and biomass by multi-electrode resistivity imaging". In: *Tree Physiology* 28.10 (2008), pp. 1441–1448. issn: 0829318x. doi: [10.1093/treephys/28.10.1441](https://doi.org/10.1093/treephys/28.10.1441).
- Amato, Mariana, Giovanni Bitella, Roberta Rossi, José A. Gómez, Stella Lovelli, and João J Ferreira Gomes. "Multi-electrode 3D resistivity imaging of alfalfa root zone". In: *European Journal of Agronomy* 31.4 (Nov. 2009), pp. 213–222. issn: 11610301. doi: [10.1016/j.eja.2009.08.005](https://doi.org/10.1016/j.eja.2009.08.005).
- Archie, Gustave E et al. "The electrical resistivity log as an aid in determining some reservoir characteristics". In: *Transactions of the AIME* (1942).
- Arifuzzaman, Muhammad, Atena Oladzadabbasabadi, Phillip McClean, and Mukhlesur Rahman. "Shovelomics for phenotyping root architectural traits of rapeseed/canola (*Brassica napus L.*) and genome-wide association mapping". In: *Molecular Genetics and Genomics* 294.4 (Apr. 2019), pp. 985–1000. issn: 16174623. doi: [10.1007/s00438-019-01563-x](https://doi.org/10.1007/s00438-019-01563-x).
- Atkinson, Jonathan A., Michael P. Pound, Malcolm J. Bennett, and Darren M. Wells. "Uncovering the hidden half of plants using new advances in root phenotyping". In: *Current Opinion in Biotechnology* 55 (Feb. 2019), pp. 1–8. issn: 18790429. doi: [10.1016/j.copbio.2018.06.002](https://doi.org/10.1016/j.copbio.2018.06.002).
- Aylmore, L. A.G. "Use of Computer-Assisted Tomography in Studying Water Movement Around Plant Roots". In: *Advances in Agronomy* 49.C (Jan. 1993), pp. 1–54. issn: 00652113. doi: [10.1016/s0065-2113\(08\)60792-0](https://doi.org/10.1016/s0065-2113(08)60792-0).
- Bao, Yun et al. "Plant roots use a patterning mechanism to position lateral root branches toward available water". In: *Proceedings of the National Academy of Sciences of the United States of America* (2014). issn: 10916490. doi: [10.1073/pnas.1400966111](https://doi.org/10.1073/pnas.1400966111).
- Barber, Stanley A. *Soil nutrient bioavailability : a mechanistic approach*. Wiley, 1995, p. 414. isbn: 9780471587477.
- Barsoukov, Evgenij and J. Ross Macdonald. *Impedance Spectroscopy*. Ed. by Evgenij Barsoukov and J. Ross Macdonald. Wiley, Apr. 2005, Sect. 2.2. isbn: 9780471647492. doi: [10.1002/0471716243](https://doi.org/10.1002/0471716243).
- Barthel, Andreas, Thomas Nacke, and Dieter Frense. "Interfacing the AD5933 for bio-impedance measurements with front ends providing galvanostatic or potentiostatic excitation Related content Electrodes-the challenge in electrical characterization of biological material". In: *Journal of Physics: Conference Series* 407 (). doi: [10.1088/1742-6596/407/1/012019](https://doi.org/10.1088/1742-6596/407/1/012019).

- Basso, Bruno, Mariana Amato, Giovanni Bitella, Roberta Rossi, Alexandra Kravchenko, Luigi Sartori, Lucila M. Carvalho, and João Gomes. "Two-Dimensional Spatial and Temporal Variation of Soil Physical Properties in Tillage Systems Using Electrical Resistivity Tomography". In: *Agronomy Journal* 102.2 (2010), p. 440. ISSN: 1435-0645. DOI: 10.2134/agronj2009.0298.
- Bebber, Daniel P., Timothy Holmes, David Smith, and Sarah J. Gurr. "Economic and physical determinants of the global distributions of crop pests and pathogens". In: *New Phytologist* 202.3 (May 2014), pp. 901–910. ISSN: 14698137. DOI: 10.1111/nph.12722.
- Bell, John B., A. N. Tikhonov, and V. Y. Arsenin. "Solutions of Ill-Posed Problems." In: *Mathematics of Computation* 32.144 (Oct. 1978), p. 1320. ISSN: 00255718. DOI: 10.2307/2006360.
- Bera, Tushar Kanti, Sampa Bera, Kalyan Kar, and Shubha Mondal. "Studying the Variations of Complex Electrical Bio-Impedance of Plant Tissues During Boiling". In: *Procedia Technology* 23 (2016), pp. 248–255. ISSN: 22120173. DOI: 10.1016/j.protcy.2016.03.024.
- Besson, A., I. Cousin, A. Samouëlian, H. Boizard, and G. Richard. "Structural heterogeneity of the soil tilled layer as characterized by 2D electrical resistivity surveying". In: *Soil and Tillage Research* 79.2 (Dec. 2004), pp. 239–249. ISSN: 01671987. DOI: 10.1016/j.still.2004.07.012.
- Bisquert, Juan, Germà Garcia-Belmonte, Francisco Fabregat-Santiago, Noemí S. Ferriols, Peter Bogdanoff, and Ernesto C. Pereira. "Doubling Exponent Models for the Analysis of Porous Film Electrodes by Impedance. Relaxation of TiO₂ Nanoporous in Aqueous Solution". In: *Journal of Physical Chemistry B* 104.10 (Mar. 2000), pp. 2287–2298. ISSN: 15206106. DOI: 10.1021/jp993148h.
- Blancaflor, Elison B. "Regulation of plant gravity sensing and signaling by the actin cytoskeleton". In: *American Journal of Botany* (2013). ISSN: 00029122. DOI: 10.3732/ajb.1200283.
- Böhm, Wolfgang. *Methods of studying root systems*. Vol. 33. New York: Springer-Verlag, 1979, pp. 1–188. ISBN: 038709329x.
- Bolaños, J. and G O Edmeades. "Eight cycles of selection for drought tolerance in lowland tropical maize. II. Responses in reproductive behavior". In: *Field Crops Research* 31.3-4 (1993), pp. 253–268. ISSN: 03784290. DOI: 10.1016/0378-4290(93)90065-u.
- Borsic, A. and A. Adler. "A primal-dual interior-point framework for using the L1 or L2 norm on the data and regularization terms of inverse problems". In: *Inverse Problems* (2012). ISSN: 02665611. DOI: 10.1088/0266-5611/28/9/095011.
- Borsic, Andrea. "Regularisation Methods for Imaging from Electrical Measurements by Andrea Borsic". In: July (2002), pp. 1–165.
- Bradford, Neil and David A. Wolfe. *Governing regional economic development: Innovation challenges and policy learning in Canada*. Vol. 6. 2. 2013, pp. 331–347. ISBN: 9789251305713. DOI: 10.1093/cjres/rst006.
- Braun, Fabian, Martin Proenca, Josep Sola, Jean Philippe Thiran, and Andy Adler. "A Versatile Noise Performance Metric for Electrical Impedance Tomography Algorithms". In: *IEEE Transactions on Biomedical Engineering* 64.10 (Oct. 2017), pp. 2321–2330. ISSN: 15582531. DOI: 10.1109/tbme.2017.2659540.
- Brown, B H. "Electrical impedance tomography (EIT): a review BH Brown Electrical impedance tomography (EIT): a review". In: (). ISSN: 0309-1902. DOI: 10.1080/0309190021000059687.
- Brown, Kathleen and Jonathan Lynch. "Whole-Plant Adaptations to Low Phosphorus Availability". In: *Plant-Environment Interactions, Third Edition*. 2006. DOI: 10.1201/9781420019346.ch8.
- Burgess, T, J McComb, G Hardy, and I Colquhoun. "Influence of low oxygen levels in aeroponics chambers on eucalypt roots infected with Phytophthora cinnamomi". In: *Plant Disease* 82.4 (1998), pp. 368–373. ISSN: 01912917. DOI: Doi10.1094/Pdis.1998.82.4.368.
- Calderón, Alberto P. "On an inverse boundary value problem". In: *Computational and Applied Mathematics* 25.2-3 (2006), pp. 133–138. ISSN: 1807-0302. DOI: 10.1590/s0101-82052006000200002.
- Cao, Yang, Tapani Repo, Raimo Silvennoinen, Tarja Lehto, and Paavo Pelkonen. "An appraisal of the electrical resistance method for assessing root surface area". In: *Journal of Experimental Botany* 61.9 (May 2010), pp. 2491–2497. ISSN: 00220957. DOI: 10.1093/jxb/erq078.
- "Analysis of the willow root system by electrical impedance spectroscopy". In: *Journal of Experimental Botany* 62.1 (Jan. 2011), pp. 351–358. ISSN: 0022-0957. DOI: 10.1093/jxb/erq276.
- Cassiani, G., J. Boaga, D. Vanella, M. T. Perri, and S. Consoli. "Monitoring and modelling of soil-plant interactions: The joint use of ERT, sap flow and eddy covariance data to characterize the volume of an orange tree root zone". In: *Hydrology and Earth System Sciences* 19.5 (May 2015), pp. 2213–2225. ISSN: 16077938. DOI: 10.5194/hess-19-2213-2015.
- Cassiani, Giorgio, Jacopo Boaga, Matteo Rossi, Mario Putti, Giuseppe Fadda, Bruno Majone, and Alberto Bellini.

- "Soil-plant interaction monitoring: Small scale example of an apple orchard in Trentino, North-Eastern Italy". In: *Science of the Total Environment* 543 (2016), pp. 851–861. issn: 18791026. doi: 10.1016/j.scitotenv.2015.03.113.
- Celano, G., A. M. Palese, A. Ciucci, E. Martorella, N. Vignozzi, and C. Xiloyannis. "Evaluation of soil water content in tilled and cover-cropped olive orchards by the geoelectrical technique". In: *Geoderma* 163.3–4 (2011), pp. 163–170. issn: 00167061. doi: 10.1016/j.geoderma.2011.03.012.
- Čermák, Jan, Radek Ulrich, Zdenek Stančk, Jan Koller, and Ludek Aubrecht. "Electrical measurement of tree root absorbing surfaces by the earth impedance method: 2. Verification based on allometric relationships and root severing experiments". In: *Tree Physiology* 26.9 (Sept. 2006), pp. 1113–1121. issn: 0829318x. doi: 10.1093/treephys/26.9.1113.
- Cheney, M., D. Isaacson, J. C. Newell, S. Simske, and J. Goble. "NOSER: An algorithm for solving the inverse conductivity problem". In: *International Journal of Imaging Systems and Technology* 2.2 (1990), pp. 66–75. issn: 08999457. doi: 10.1002/ima.1850020203.
- Cheney, Margaret and David Isaacson. "Distinguishability in Impedance Imaging". In: *IEEE Transactions on Biomedical Engineering* 39.8 (1992), pp. 852–860. issn: 15582531. doi: 10.1109/10.148393.
- Chloupek, O. "The relationship between electric capacitance and some other parameters of plant roots". In: *Biologia Plantarum* 14.3 (May 1972), pp. 227–230. issn: 00063134. doi: 10.1007/bf02921255.
- Chloupek, Oldrich. "Evaluation of the size of a plant's root system using its electrical capacitance". In: *Plant and Soil* 48.2 (Nov. 1977), pp. 525–532. issn: 0032079x. doi: 10.1007/bf02187258.
- Christie, C. B. and M. A. Nichols. "Aeroponics - A production system and research tool". In: *Acta Horticulturae* 648.648 (Feb. 2004), pp. 185–190. issn: 05677572. doi: 10.17660/ActaHortic.2004.648.22.
- Cimpăoiașu, Mihai O., Oliver Kuras, Paul B. Wilkinson, Tony Pridmore, and Sacha J. Mooney. "Hydrodynamic characterization of soil compaction using integrated electrical resistivity and X-ray computed tomography". In: *Vadose Zone Journal* 20.4 (July 2021). issn: 1539-1663. doi: 10.1002/vzj2.20109.
- Comas, Xavier and Lee Slater. "Low-frequency electrical properties of peat". In: *Water Resources Research* 40.12 (Dec. 2004). issn: 00431397. doi: 10.1029/2004wr003534.
- Corona-Lopez, Diego D.J., Sarah Sommer, Stephen A. Rolfe, Frank Podd, and Bruce D. Grieve. "Electrical impedance tomography as a tool for phenotyping plant roots". In: *Plant Methods* 15.1 (Dec. 2019), p. 49. issn: 17464811. doi: 10.1186/s13007-019-0438-4.
- Corwin, D. L. and S. M. Lesch. "Apparent soil electrical conductivity measurements in agriculture". In: *Computers and Electronics in Agriculture* 46.1–3 Spec. Iss. (2005), pp. 11–43. issn: 01681699. doi: 10.1016/j.compag.2004.10.005.
- Costa, Corrado, Ulrich Schurr, Francesco Loreto, Paolo Menesatti, and Sébastien Carpentier. *Plant phenotyping research trends, a science mapping approach*. Jan. 2019. doi: 10.3389/fpls.2018.01933.
- Cui, Xi Hong, Jin Chen, Jin Song Shen, Xin Cao, Xue Hong Chen, and Xiao Lin Zhu. "Modeling tree root diameter and biomass by ground-penetrating radar". In: *Science China Earth Sciences* (2011). issn: 16747313. doi: 10.1007/s11430-010-4103-z.
- Dalton, F. N. "In-situ root extent measurements by electrical capacitance methods". In: *Plant and Soil* 173.1 (June 1995), pp. 157–165. issn: 0032-079x. doi: 10.1007/bf00155527.
- Dias, Teresa, Angela Dukes, and Pedro M. Antunes. "Accounting for soil biotic effects on soil health and crop productivity in the design of crop rotations". In: *Journal of the Science of Food and Agriculture* (2014). issn: 10970010. doi: 10.1002/jsfa.6565.
- Dietrich, Ralf C., Anthony G Bengough, Hamlyn G Jones, and Philip J White. "A new physical interpretation of plant root capacitance". In: *Journal of Experimental Botany* 63.17 (Oct. 2012), pp. 6149–6159. issn: 00220957. doi: 10.1093/jxb/ers264.
- Dix, R. L. and J. E. Weaver. "Prairie Plants and Their Environment: A Fifty-Year Study in the Midwest". In: *Journal of Range Management* (1969). issn: 0022409x. doi: 10.2307/3896202.
- Dobson, Myron, Fawwaz Ulaby, Martti Hallikainen, and Mohamed El-rayes. "Microwave Dielectric Behavior of Wet Soil-Part II: Dielectric Mixing Models". In: *IEEE Transactions on Geoscience and Remote Sensing* Ge-23.1 (Jan. 1985), pp. 35–46. issn: 0196-2892. doi: 10.1109/tgrs.1985.289498.
- Doran, John W. and Michael R. Zeiss. "Soil health and sustainability: Managing the biotic component of soil quality". In: *Applied Soil Ecology* (2000). issn: 09291393. doi: 10.1016/s0929-1393(00)00067-6.
- Downie, Helen, Nicola Holden, Wilfred Otten, Andrew J. Spiers, Tracy A. Valentine, and Lionel X. Dupuy. "Transparent Soil for Imaging the Rhizosphere". In: *PLoS ONE* 7.9 (Sept. 2012). Ed. by Malcolm Bennett, e44276. issn: 19326203. doi: 10.1371/journal.pone.0044276. arXiv: e44276.
- Dusschoten, Dagmar van, Ralf Metzner, Johannes Kochs, Johannes A. Postma, Daniel Pflugfelder, Jonas Bühl, Ulrich Schurr, and Siegfried Jahnke. "Quantitative 3D

- analysis of plant roots growing in soil using magnetic resonance imaging". In: *Plant Physiology* 170.3 (Jan. 2016), pp. 1176–1188. ISSN: 15322548. DOI: [10.1104/pp.15.01388](https://doi.org/10.1104/pp.15.01388).
- Ellis, Tim W., Wayne Murray, Kelyn Paul, Laimonis Kavalieris, Jim Brophy, Chris Williams, and Manuel Maass. "Electrical capacitance as a rapid and non-invasive indicator of root length". In: *Tree Physiology* 33.1 (Jan. 2013), pp. 3–17. ISSN: 0829318X. DOI: [10.1093/treephys/tps115](https://doi.org/10.1093/treephys/tps115).
- Eyüboğlu, B Murat. "An interleaved drive electrical impedance tomography image reconstruction algorithm". In: *Physiological Measurement* 17.4a (Nov. 1996), A59–a71. ISSN: 0967-3334. DOI: [10.1088/0967-3334/17/4a/009](https://doi.org/10.1088/0967-3334/17/4a/009).
- Fan, Junliang, Alexander Scheuermann, Adrien Guyot, Thomas Baumgartl, and David A. Lockington. "Quantifying spatiotemporal dynamics of root-zone soil water in a mixed forest on subtropical coastal sand dune using surface ERT and spatial TDR". In: *Journal of Hydrology* 523 (Apr. 2015), pp. 475–488. ISSN: 00221694. DOI: [10.1016/j.jhydrol.2015.01.064](https://doi.org/10.1016/j.jhydrol.2015.01.064).
- Fisher, Matthew C., Daniel A. Henk, Cheryl J. Briggs, John S. Brownstein, Lawrence C. Madoff, Sarah L. McCraw, and Sarah J. Gurr. "Emerging fungal threats to animal, plant and ecosystem health". In: *Nature* 484.7393 (Apr. 2012), pp. 186–194. ISSN: 00280836. DOI: [10.1038/nature10947](https://doi.org/10.1038/nature10947). arXiv: Nihms150003.
- Fitter, Alastair, Lisa Williamson, Birgit Linkohr, and Ottoline Leyser. "Root system architecture determines fitness in an <i>Arabidopsis</i> mutant in competition for immobile phosphate ions but not for nitrate ions". In: *Proceedings of the Royal Society of London. Series B: Biological Sciences* 269.1504 (Oct. 2002), pp. 2017–2022. ISSN: 0962-8452. DOI: [10.1098/rspb.2002.2120](https://doi.org/10.1098/rspb.2002.2120).
- Fonzo, Martina Di, Ben Collen, and Georgina M. Mace. "A new method for identifying rapid decline dynamics in wild vertebrate populations". In: *Ecology and Evolution* 3.7 (July 2013), pp. 2378–2391. ISSN: 2045-7758. DOI: [10.1002/ece3.596](https://doi.org/10.1002/ece3.596).
- Freschet, Gregoire et al. "A starting guide to root ecology: Strengthening ecological concepts and standardizing root classification, sampling, processing and trait measurements". In: Hal-02918834 August (2020), p. 291.
- Fukue, M., T. Minato, H. Horibe, and N. Taya. "The micro-structures of clay given by resistivity measurements". In: *Engineering Geology* 54.1-2 (Sept. 1999), pp. 43–53. ISSN: 00137952. DOI: [10.1016/s0013-7952\(99\)00060-5](https://doi.org/10.1016/s0013-7952(99)00060-5).
- Garbout, Amin et al. "The use of PET/CT scanning technique for 3D visualization and quantification of real-time soil/plant interactions". In: *Plant Soil* 352 (2012), pp. 113–127. DOI: [10.1007/s11104-011-0983-8](https://doi.org/10.1007/s11104-011-0983-8).
- Garré, S., M. Javaux, J. Vanderborght, L. Pagès, and H. Vereecken. "Three-Dimensional Electrical Resistivity Tomography to Monitor Root Zone Water Dynamics". In: *Vadose Zone Journal* 10.1 (Feb. 2011), pp. 412–424. DOI: [10.2136/vzj2010.0079](https://doi.org/10.2136/vzj2010.0079).
- Gavish, Nir and Keith Promislow. "Dependence of the dielectric constant of electrolyte solutions on ionic concentration - a microfield approach". In: 22 (Aug. 2012). DOI: [10.1103/PhysRevE.94.012611](https://doi.org/10.1103/PhysRevE.94.012611). arXiv: 1208.5169.
- Gibert, Dominique, Florence Nicollin, Bruno Kergosien, Paul Bossart, Christophe Nussbaum, Agnès Grislin-Mouëzy, Frédéric Conil, and Nasser Hoteit. "Electrical tomography monitoring of the excavation damaged zone of the Gallery 04 in the Mont Terri rock laboratory: Field experiments, modelling, and relationship with structural geology". In: *Applied Clay Science* 33.1 (June 2006), pp. 21–34. ISSN: 01691317. DOI: [10.1016/j.clay.2006.03.008](https://doi.org/10.1016/j.clay.2006.03.008).
- Glick, Bernard R. "Phytoremediation: Synergistic use of plants and bacteria to clean up the environment". In: *Biotechnology Advances* (2003). ISSN: 07349750. DOI: [10.1016/s0734-9750\(03\)00055-7](https://doi.org/10.1016/s0734-9750(03)00055-7).
- Goff, E. S. and D. D. Mayne. *First principles of agriculture / by Emmet S. Goff and D.D. Mayne ; introduction by W.D. Hoard*. New York : American Book Co., 1904. DOI: [10.5962/bhl.title.40175](https://doi.org/10.5962/bhl.title.40175).
- Graham, B. M. and A. Adler. "Objective selection of hyperparameter for EIT". In: *Physiological Measurement* 27.5 (May 2006), S65–79. ISSN: 09673334. DOI: [10.1088/0967-3334/27/5/s06](https://doi.org/10.1088/0967-3334/27/5/s06).
- Gregory, P. J. and P. Hinsinger. "New approaches to studying chemical and physical changes in the rhizosphere: An overview". In: *Plant and Soil* 211.1 (1999), pp. 1–9. ISSN: 0032079X. DOI: [10.1023/a:1004547401951](https://doi.org/10.1023/a:1004547401951).
- Greve, A. K., R. I. Acworth, and B. F J Kelly. "3D cross-hole resistivity tomography to monitor water percolation during irrigation on cracking soil". In: *Soil Research* 49.8 (2011), pp. 661–669. ISSN: 1838675X. DOI: [10.1071/sr11270](https://doi.org/10.1071/sr11270).
- Grimnes, Sverre and Ørjan Grøttem Martinsen. *Bioimpedance and Bioelectricity Basics*. 2008. ISBN: 9780123740045. DOI: [10.1016/b978-0-12-374004-5.x0001-3](https://doi.org/10.1016/b978-0-12-374004-5.x0001-3). arXiv: 9809069v1 [arXiv:gr-qc].
- Grosse, Constantino and Mónica Cecilia Tirado. "Low-frequency dielectric spectroscopy of colloidal suspensions". In: *Journal of Non-Crystalline Solids*. Vol. 305. 1-3. July 2002, pp. 386–392. DOI: [10.1016/s0022-3093\(02\)01133-x](https://doi.org/10.1016/s0022-3093(02)01133-x).

- Grychtol, Bartłomiej and Andy Adler. "FEM electrode refinement for electrical impedance tomography". In: *Proceedings of the Annual International Conference of the IEEE Engineering in Medicine and Biology Society, EMBS. 2013.* ISBN: 9781457702167. doi: [10.1109/embc.2013.6611026](https://doi.org/10.1109/embc.2013.6611026).
- Guo, Li, Jin Chen, Xihong Cui, Bihang Fan, and Henry Lin. *Application of ground penetrating radar for coarse root detection and quantification: A review.* 2013. doi: [10.1007/s11104-012-1455-5](https://doi.org/10.1007/s11104-012-1455-5).
- Hadamard, J. *Sur les problèmes aux dérivées partielles et leur signification physique.* Vol. 13. Princeton University, 1902, pp. 49–52.
- Haling, Rebecca E., Lawrie K. Brown, A. Glyn Bengough, Iain M. Young, Paul D. Hallett, Philip J. White, and Timothy S. George. "Root hairs improve root penetration, root-soil contact, and phosphorus acquisition in soils of different strength". In: *Journal of Experimental Botany* (2013). ISSN: 00220957. doi: [10.1093/jxb/ert200](https://doi.org/10.1093/jxb/ert200).
- Han, Pengju. "Study on Mechanical Properties of Acidic and Alkaline Silty Soil by Electrochemical Impedance Spectroscopy". In: *International Journal of Electrochemical Science* 13 (Nov. 2018), pp. 10548–10563. ISSN: 14523981. doi: [10.20964/2018.11.19](https://doi.org/10.20964/2018.11.19).
- Han, Pengju, Ruizhen Xie, Naiming Lin, and Bin He. "Electrochemical Corrosion Behavior of X70 Steel in Sand Soil Contaminated by Copper(II)". In: *Int. J. Electrochem. Sci* 11 (2016), pp. 9491–9507. doi: [10.20964/2016.11.07](https://doi.org/10.20964/2016.11.07).
- Hansen, Per Christian. "Analysis of Discrete Ill-Posed Problems by Means of the L-Curve". In: *SIAM Review* (1992). ISSN: 0036-1445. doi: [10.1137/1034115](https://doi.org/10.1137/1034115).
- "Regularization Tools version 4.0 for Matlab 7.3". In: *Numerical Algorithms* 46.2 (2007), pp. 189–194. ISSN: 10171398. doi: [10.1007/s11075-007-9136-9](https://doi.org/10.1007/s11075-007-9136-9).
- Harper, J. L., M. Jones, and N. R. Sackville Hamilton. "The evolution of roots and the problems of analysing their behaviour". In: *Plant root growth* (1991).
- Hartmann, Anton, Michael Rothbäller, and Michael Schmid. "Lorenz Hiltner, a pioneer in rhizosphere microbial ecology and soil bacteriology research". In: *Plant and Soil*. Vol. 312. 1-2. Springer Netherlands, Nov. 2008, pp. 7–14. ISBN: 0032-079x. doi: [10.1007/s11104-007-9514-z](https://doi.org/10.1007/s11104-007-9514-z).
- Hassouni, K., S. Alahmad, B. Belkadi, A. Filali-Maltouf, L. T. Hickey, and F. M. Bassi. "Root System Architecture and Its Association with Yield under Different Water Regimes in Durum Wheat". In: *Crop Science* 58.6 (Nov. 2018), pp. 2331–2346. ISSN: 0011-183X. doi: [10.2135/cropsci2018.01.0076](https://doi.org/10.2135/cropsci2018.01.0076).
- Hasted, J. B., D. M. Ritson, and C. H. Collie. "Dielectric Properties of Aqueous Ionic Solutions. Parts I and II". In: *The Journal of Chemical Physics* 16.1 (Dec. 2004), p. 1. ISSN: 0021-9606. doi: [10.1063/1.1746645](https://doi.org/10.1063/1.1746645).
- Heimmer, Don H. and Steven L. De Vore. "Near-Surface, High Resolution Geophysical Methods for Cultural Resource Management and Archaeological Investigations". In: *Science and Technology in Historic Preservation.* 2000. doi: [10.1007/978-1-4615-4145-5_3](https://doi.org/10.1007/978-1-4615-4145-5_3).
- Hochholdinger, Frank, Woong June Park, Michaela Sauer, and Katrin Woll. *From weeds to crops: Genetic analysis of root development in cereals.* 2004. doi: [10.1016/j.tplants.2003.11.003](https://doi.org/10.1016/j.tplants.2003.11.003).
- Holder, David. "Electrical Impedance Tomography: Methods, History and Applications". In: *Medical Physics* 32.8 (2005), pp. 2731–2731. ISSN: 00942405. doi: [10.1118/1.1995712](https://doi.org/10.1118/1.1995712).
- Hruska, Jiri, Jan Cermák, and Svatopluk Sustek. "Mapping tree root systems with ground-penetrating radar". In: *Tree Physiology* 19.2 (1999), pp. 125–130. ISSN: 0829318X. doi: [10.1093/treephys/19.2.125](https://doi.org/10.1093/treephys/19.2.125). arXiv: [1007.5074](https://arxiv.org/abs/1007.5074).
- Isaac, Marney E. and Luke C.N. Anglaaere. "An in situ approach to detect tree root ecology: Linking ground-penetrating radar imaging to isotope-derived water acquisition zones". In: *Ecology and Evolution* 3.5 (2013), pp. 1330–1339. ISSN: 20457758. doi: [10.1002/ece3.543](https://doi.org/10.1002/ece3.543).
- Jahnke, Siegfried et al. "Combined MRI-PET dissects dynamic changes in plant structures and functions". In: *Plant Journal* (2009). ISSN: 09607412. doi: [10.1111/j.1365-313X.2009.03888.x](https://doi.org/10.1111/j.1365-313X.2009.03888.x).
- Johnson, M. G., D. T. Tingey, D. L. Phillips, and M. J. Storm. "Advancing fine root research with minirhizotrons". In: *Environmental and Experimental Botany* 45.3 (June 2001), pp. 263–289. ISSN: 00988472. doi: [10.1016/s0098-8472\(01\)00077-6](https://doi.org/10.1016/s0098-8472(01)00077-6).
- Judd, Lesley A, Brian E Jackson, and William C Fonteno. "Advancements in Root Growth Measurement Technologies and Observation Capabilities for Container-Grown Plants". In: *Plants* 4 (2015), pp. 369–392. ISSN: 2223-7747. doi: [10.3390/plants4030369](https://doi.org/10.3390/plants4030369).
- Kac, Mark. "Can One Hear the Shape of a Drum?" In: *The American Mathematical Monthly* (1966). ISSN: 00029890. doi: [10.2307/2313748](https://doi.org/10.2307/2313748).
- Kendall, W. A., G. A. Pederson, and R. R. Hill. "Root size estimates of red clover and alfalfa based on electrical capacitance and root diameter measurements". In: *Grass and Forage Science* 37.3 (Sept. 1982), pp. 253–256. ISSN: 0142-5242. doi: [10.1111/j.1365-2494.1982.tb01604.x](https://doi.org/10.1111/j.1365-2494.1982.tb01604.x).

- Köckenberger, W. "Nuclear magnetic resonance micro-imaging in the investigation of plant cell metabolism." In: *Journal of experimental botany* 52.356 (Apr. 2001), pp. 641–652. issn: 0022-0957. doi: 10.1093/jexbot/52.356.641.
- Lee, Jin Fa and Romanus Dyczij-Edlinger. "Automatic mesh generation using a modified delaunay tessellation". In: *IEEE Antennas and Propagation Magazine* 39.1 (1997), pp. 34–45. issn: 10459243. doi: 10.1109/74.583517.
- Liu, Xiuwei, Xuejun Dong, and Daniel I. Leskovar. *Ground penetrating radar for underground sensing in agriculture: A review*. 2016. doi: 10.1515/intag-2016-0010.
- Lobet, Guillaume, Xavier Draye, and Claire Périlleux. "An online database for plant image analysis software tools". In: *Plant Methods* 9.1 (2013), pp. 1–7. issn: 17464811. doi: 10.1186/1746-4811-9-38.
- López, Bernat, Santiago Sabaté, and Carlos Gracia. "An inflatable minirhizotron system for stony soils". In: *Plant and Soil* 179.2 (Feb. 1996), pp. 255–260. issn: 0032079x. doi: 10.1007/bf00009335.
- Lucas, Tamara and Richard Horton. *The 21st-century great food transformation*. Feb. 2019. doi: 10.1016/s0140-6736(18)33179-9.
- Lyle M. S., Jr. "Surface mine reclamation manual." In: *Surface mine reclamation manual*. (1986).
- Lynch, James M, Melissa J Brimecombe, and Frans AAM De Leij. "Rhizosphere". In: *eLS*. Chichester, UK: John Wiley & Sons, Ltd, Aug. 2001. isbn: 9780470015902. doi: 10.1038/npg.els.0000403.
- Lynch, Jonathan P. *Root phenes that reduce the metabolic costs of soil exploration: Opportunities for 21st century agriculture*. Sept. 2015. doi: 10.1111/poe.12451.
- "Roots of the Second Green Revolution". In: *Australian Journal of Botany* 55.5 (Sept. 2007), p. 493. issn: 0067-1924. doi: 10.1071/bt06118.
- Lynch, Jonathan P. and Tobias Wojciechowski. *Opportunities and challenges in the subsoil: Pathways to deeper rooted crops*. 2015. doi: 10.1093/jxb/eru508.
- Margo, C., J. Katrib, M. Nadi, and A. Rouane. "A four-electrode low frequency impedance spectroscopy measurement system using the AD5933 measurement chip". In: *Physiological Measurement* 34.4 (Apr. 2013), pp. 391–405. issn: 09673334. doi: 10.1088/0967-3334/34/4/391.
- Mary, Benjamin, Feras Abdulsamad, Ginette Saracco, Laurent Peyras, Michel Vennetier, Patrice Mériaux, and Christian Camerlynck. "Improvement of coarse root detection using time and frequency induced polarization: from laboratory to field experiments". In: *Plant and Soil* 417.1-2 (May 2017), pp. 243–259. issn: 15735036. doi: 10.1007/s11104-017-3255-4.
- Mary, Benjamin, Luca Peruzzo, Jacopo Boaga, Nicola Cenni, Myriam Schmutz, Yuxin Wu, Susan S. Hubbard, and Giorgio Cassiani. "Time-lapse monitoring of root water uptake using electrical resistivity tomography and mise-à-la-masse: a vineyard infiltration experiment". In: *Soil* 6.1 (Mar. 2020), pp. 95–114. issn: 2199-398x. doi: 10.5194/soil-6-95-2020.
- Mathieu, Laura, Guillaume Lobet, Pierre Tocquin, and Claire Périerreux. "Rhizoponics": A novel hydroponic rhizotron for root system analyses on mature *Arabidopsis thaliana* plants". In: *Plant Methods* 11.1 (Jan. 2015), p. 3. issn: 17464811. doi: 10.1186/s13007-015-0046-x.
- McKenzie, Neil, Keppel Coughlan, and Hamish Cresswell. *Soil Physical Measurement and Interpretation for Land Evaluation*. CSIRO Publishing, Feb. 2019. doi: 10.1071/9780643069879.
- McMichael, B. L., D. R. Upchurch, and H. M. Taylor. "Transparent wall techniques for studying root growth and function in soil". In: *Journal of Plant Nutrition* 15.6-7 (June 1992), pp. 753–762. issn: 15324087. doi: 10.1080/01904169209364360.
- Meister, Robert, M. S. Rajani, Daniel Ruzicka, and Daniel P. Schachtman. *Challenges of modifying root traits in crops for agriculture*. 2014. doi: 10.1016/j.tplants.2014.08.005.
- Mendrinna, Amelie and Staffan Persson. "Root hair growth: It's a one way street". In: *F1000Prime Reports* 7 (Feb. 2015). issn: 20517599. doi: 10.12703/p7-23.
- Metzner, Ralf, Anja Eggert, Dagmar van Dusschoten, Daniel Pflugfelder, Stefan Gerth, Ulrich Schurr, Norman Uhlmann, and Siegfried Jahnke. "Direct comparison of MRI and X-ray CT technologies for 3D imaging of root systems in soil: potential and challenges for root trait quantification". In: *Plant Methods* 11.1 (2015), p. 17. issn: 1746-4811. doi: 10.1186/s13007-015-0060-z.
- Michot, Didier, Yves Benderitter, Abel Dorigny, Bernard Nicoullaud, Dominique King, and Alain Tabbagh. "Spatial and temporal monitoring of soil water content with an irrigated corn crop cover using surface electrical resistivity tomography". In: *Water Resources Research* 39.5 (May 2003), n/a–n/a. issn: 00431397. doi: 10.1029/2002wr001581.
- Miguel, Magalhaes Amade, Johannes Auke Postma, and Jonathan Paul Lynch. "Phene Synergism between Root Hair Length and Basal Root Growth Angle for Phosphorus Acquisition". In: *Plant Physiology* 167.4 (Apr. 2015), pp. 1430–1439. issn: 0032-0889. doi: 10.1104/pp.15.00145.
- Mirtaheri, Peyman, Sverre Grimnes, and Ørjan G. Martinsen. "Electrode polarization impedance in weak NaCl aqueous solutions". In: *IEEE Transactions on Biomedical Engineering* 52.12 (Dec. 2005),

- pp. 2093–2099. ISSN: 00189294. DOI: [10.1109/tbme.2005.857639](https://doi.org/10.1109/tbme.2005.857639).
- Molden, David. *Water for food water for life: A Comprehensive assessment of water management in agriculture*. Routledge, July 2013, pp. 1–645. ISBN: 9781849773799. DOI: [10.4324/9781849773799](https://doi.org/10.4324/9781849773799).
- Mooney, S. J., T. P. Pridmore, J. Helliwell, and M. J. Bennett. *Developing X-ray computed tomography to non-invasively image 3-D root systems architecture in soil*. 2012. DOI: [10.1007/s11104-011-1039-9](https://doi.org/10.1007/s11104-011-1039-9).
- Murai, Tadakuni and Yukio Kagawa. “Electrical Impedance Computed Tomography Based on a Finite Element Model”. In: *IEEE Transactions on Biomedical Engineering* Bme-32.3 (Mar. 1985), pp. 177–184. ISSN: 0018-9294. DOI: [10.1109/tbme.1985.325526](https://doi.org/10.1109/tbme.1985.325526).
- Myllys, Merja and Asko Simojoki. “Calibration of time domain reflectometry (TDR) for soil moisture measurements in cultivated peat soils”. In: *Suo* (1996). ISSN: 00395471.
- Neumann, Günter, Timothy S. George, and Claude Plassard. “Strategies and methods for studying the rhizosphere—the plant science toolbox”. In: *Plant and Soil* 321.1–2 (2009), pp. 431–456. ISSN: 0032079x. DOI: [10.1007/s11104-009-9953-9](https://doi.org/10.1007/s11104-009-9953-9).
- Nissinen, A., L. M. Heikkilä, V. Kolehmainen, and J. P. Kaipio. “Compensation of errors due to discretization, domain truncation and unknown contact impedances in electrical impedance tomography”. In: *Measurement Science and Technology* 20.10 (Sept. 2009), p. 13. ISSN: 13616501. DOI: [10.1088/0957-0233/20/10/105504](https://doi.org/10.1088/0957-0233/20/10/105504).
- Nocedal, J and S Wright. *Numerical optimization*. 2006. ISBN: 0387987932.
- O’Kelly, Brendan C. “Oven-drying characteristics of soils of different origins”. In: *Drying Technology* 23.5 (2005), pp. 1141–1149. ISSN: 07373937. DOI: [10.1081/drt-200059149](https://doi.org/10.1081/drt-200059149).
- Oerke, E. C. “Crop losses to pests”. In: *Journal of Agricultural Science* 144.1 (Feb. 2006), pp. 31–43. ISSN: 00218596. DOI: [10.1017/s0021859605005708](https://doi.org/10.1017/s0021859605005708).
- Oleszczuk, R., T. Brandyk, T. Gnatowski, and J. Szatyłowicz. “Calibration of TDR for moisture determination in peat deposits”. In: *International Agrophysics* 18.2 (2004), pp. 145–151. ISSN: 02368722.
- Oliveira, J. T., L. Martins, R. Picciuchi, P. B. Malafaya, R. A. Sousa, N. M. Neves, J. F. Mano, and R. L. Reis. “Gellan gum: A new biomaterial for cartilage tissue engineering applications”. In: *Journal of Biomedical Materials Research - Part A* 93.3 (June 2010), pp. 852–863. ISSN: 15493296. DOI: [10.1002/jbm.a.32574](https://doi.org/10.1002/jbm.a.32574).
- Ozier-Lafontaine, Harry and Thierry Bajazet. “Analysis of root growth by impedance spectroscopy (EIS)”. In: *Plant and Soil* 277.1–2 (Dec. 2005), pp. 299–313. ISSN: 0032079x. DOI: [10.1007/s11104-005-7531-3](https://doi.org/10.1007/s11104-005-7531-3).
- Paez-Garcia, Ana, Christy M. Motes, Wolf Rüdiger Scheible, Ruijin Chen, Elison B. Blancaflor, and Maria J. Monteros. *Root traits and phenotyping strategies for plant improvement*. June 2015. DOI: [10.3390/plants4020334](https://doi.org/10.3390/plants4020334).
- Pallant, Eric, Richard A. Holmgren, George E. Schuler, Kimberly L. McCracken, and Barbara Drbal. “Using a fine root extraction device to quantify small diameter corn roots (>0.025 mm) in field soils”. In: *Plant and Soil* 153.2 (June 1993), pp. 273–279. ISSN: 0032-079x. DOI: [10.1007/bf00013000](https://doi.org/10.1007/bf00013000).
- Pantazi, X. E., D. Moshou, and A. A. Tamouridou. “Automated leaf disease detection in different crop species through image features analysis and One Class Classifiers”. In: *Computers and Electronics in Agriculture* 156 (Jan. 2019), pp. 96–104. ISSN: 01681699. DOI: [10.1016/j.compag.2018.11.005](https://doi.org/10.1016/j.compag.2018.11.005).
- Passioura, J. B. “Phenotyping for drought tolerance in grain crops: when is it useful to breeders?” In: *Functional Plant Biology* 39.11 (Nov. 2012), p. 851. ISSN: 1445-4408. DOI: [10.1071/fp12079](https://doi.org/10.1071/fp12079).
- Passioura, John B. “Viewpoint: The perils of pot experiments”. In: *Functional Plant Biology* 33.12 (2006), p. 1075. ISSN: 1445-4408. DOI: [10.1071/fp06223](https://doi.org/10.1071/fp06223).
- Paya, Alexander M., Jesse L. Silverberg, Jennifer Padgett, and Taryn L. Bauerle. “X-ray computed tomography uncovers root–root interactions: Quantifying spatial relationships between interacting root systems in three dimensions”. In: *Frontiers in Plant Science* (2015). ISSN: 1664462x. DOI: [10.3389/fpls.2015.00274](https://doi.org/10.3389/fpls.2015.00274).
- Pena, Antonio Ansede. “Final Degree Thesis A Feasibility Study of the Suitability of an AD5933-based Spectrometer for EBI Applications”. In: *Analyzer* (2009). ISSN: 0257-5655.
- Penrose, R. “A generalized inverse for matrices”. In: *Mathematical Proceedings of the Cambridge Philosophical Society* 51.3 (July 1955), pp. 406–413. ISSN: 0305-0041. DOI: [10.1017/s0305004100030401](https://doi.org/10.1017/s0305004100030401).
- Pflugfelder, Daniel, Ralf Metzner, Dagmar Dusschoten, Rüdiger Reichel, Siegfried Jahnke, and Robert Koller. “Non-invasive imaging of plant roots in different soils using magnetic resonance imaging (MRI)”. In: *Plant Methods* (2017). ISSN: 17464811. DOI: [10.1186/s13007-017-0252-9](https://doi.org/10.1186/s13007-017-0252-9).
- Pinton, Roberto, Zeno Varanini, and Paolo Nannipieri. *The Rhizosphere: Biochemistry and Organic Substances at the Soil-Plant Interface*. 2nd. Crc Press, 2019, pp. 1–472. ISBN: 9780367389123.
- Pliquett, Uwe. “Bioimpedance: A review for food processing”. In: *Food Engineering Reviews* 2.2 (June

- 2010), pp. 74–94. ISSN: 18667910. doi: 10.1007/s12393-010-9019-z.
- Polydorides, Nicholas. "Image reconstruction algorithms for soft field tomography". In: (2002), p. 262.
- Polydorides, Nick and William R.B. B Lionheart. "A Matlab toolkit for three-dimensional electrical impedance tomography: A contribution to the Electrical Impedance and Diffuse Optical Reconstruction Software project". In: *Measurement Science and Technology* 13.12 (Dec. 2002), pp. 1871–1883. ISSN: 09570233. doi: 10.1088/0957-0233/13/12/310.
- Postic, François and Claude Doussan. "Benchmarking electrical methods for rapid estimation of root biomass". In: *Plant Methods* 12.1 (Dec. 2016), p. 33. ISSN: 17464811. doi: 10.1186/s13007-016-0133-7.
- Postma, Johannes Auke, Annette Dathe, and Jonathan Paul Lynch. "The optimal lateral root branching density for maize depends on nitrogen and phosphorus availability". In: *Plant Physiology* (2014). ISSN: 15322548. doi: 10.1104/pp.113.233916.
- Pound, M. P., A. P. French, J. A. Atkinson, D. M. Wells, M. J. Bennett, and T. Pridmore. "RootNav: Navigating Images of Complex Root Architectures". In: *Plant Physiology* 162.4 (Aug. 2013), pp. 1802–1814. ISSN: 0032-0889. doi: 10.1104/pp.113.221531.
- Rajkai, K. "Electrical capacitance of roots in relation to plant electrodes, measuring frequency and root media". In: *Acta Agronomica Hungarica* 53.2 (Aug. 2005), pp. 197–210. ISSN: 0238-0161. doi: 10.1556/AAgr.53.2005.2.8.
- Rellán-Álvarez, Rubén et al. "GLO-Roots: An imaging platform enabling multidimensional characterization of soil-grown root systems". In: *eLife* 4.August2015 (Aug. 2015). ISSN: 2050084x. doi: 10.7554/eLife.07597.
- Repo, Tapani, Yang Cao, Raimo Silvennoinen, and Harry Ozier-Lafontaine. "Electrical Impedance Spectroscopy and Roots". In: *Measuring Roots*. Berlin, Heidelberg: Springer Berlin Heidelberg, 2012, pp. 25–49. doi: 10.1007/978-3-642-22067-8\2.
- Repo, Tapani, Janne Laukkonen, and Raimo Silvennoinen. "Measurement of the tree root growth using electrical impedance spectroscopy". In: *Silva Fennica* 39.2 (2005), pp. 159–166. ISSN: 00375330.
- Repo, Tapani, Tarja Lehto, and Leena Finér. "Delayed soil thawing affects root and shoot functioning and growth in Scots pine." In: *Tree physiology* 28.10 (Aug. 2008), pp. 1583–1591. ISSN: 0829-318x. doi: 10.1093/treephys/28.10.1583.
- Repo, Tapani, M. I.N. Zhang, Aija Ryypö, Elina Vapaavuori, and Sirkka Sutinen. "Effects of freeze-thaw injury on parameters of distributed electrical circuits of stems and needles of scots pine seedlings at different stages of acclimation". In: *Journal of Experimental Botany* 45.6 (1994), pp. 823–833. ISSN: 00220957. doi: 10.1093/jxb/45.6.823.
- Richard, Cecile A.I., Lee T. Hickey, Susan Fletcher, Raeleen Jennings, Karine Chenu, and Jack T. Christopher. "High-throughput phenotyping of seminal root traits in wheat". In: *Plant Methods* 11.1 (Mar. 2015), p. 13. ISSN: 17464811. doi: 10.1186/s13007-015-0055-9.
- Richards, L. A. "Capillary conduction of liquids through porous mediums". In: *Journal of Applied Physics* 1.5 (Nov. 1931), pp. 318–333. ISSN: 01486349. doi: 10.1063/1.1745010.
- Robinson, D. "Integrated Root Responses to Variations in Nutrient Supply". In: *Nutrient Acquisition by Plants*. 2005. doi: 10.1007/3-540-27675-0\3.
- Rossi, Roberta, Alessio Pollice, Gianfranco Bitella, Rocco Bochicchio, Amedeo D'antonio, Alaa Aldin Alromeed, Anna Maria Stellacci, Rosanna Labella, and Mariana Amato. "Soil bulk electrical resistivity and forage ground cover: Nonlinear models in an alfalfa (*Medicago sativa* L.) case study". In: *Italian Journal of Agronomy* 10.4 (Dec. 2015), pp. 215–219. ISSN: 11254718. doi: 10.4081/ijoa.2015.647.
- Rousseeuw, Peter J. "Silhouettes: A graphical aid to the interpretation and validation of cluster analysis". In: *Journal of Computational and Applied Mathematics* 20.C (Nov. 1987), pp. 53–65. ISSN: 0377-0427. doi: 10.1016/0377-0427(87)90125-7.
- Saengwilai, Patompong, Xiaoli Tian, and Jonathan Paul Lynch. "Low crown root number enhances nitrogen acquisition from low-nitrogen soils in maize". In: *Plant Physiology* (2014). ISSN: 15322548. doi: 10.1104/pp.113.232603.
- Samouëlian, A., I. Cousin, A. Tabbagh, A. Bruand, and G. Richard. "Electrical resistivity survey in soil science: A review". In: *Soil and Tillage Research* 83.2 (Sept. 2005), pp. 173–193. ISSN: 01671987. doi: 10.1016/j.still.2004.10.004. arXiv: arXiv:1011.1669v3.
- Sato, Ethel Mendocilla, Hussein Hijazi, Malcolm J. Bennett, Kris Vissenberg, and Ranjan Swarup. "New insights into root gravitropic signalling". In: *Journal of Experimental Botany* 66.8 (Apr. 2015), pp. 2155–2165. ISSN: 1460-2431. doi: 10.1093/jxb/eru515.
- Savary, Serge, Laetitia Willocquet, Sarah Jane Pethybridge, Paul Esker, Neil McRoberts, and Andy Nelson. "The global burden of pathogens and pests on major food crops". In: *Nature Ecology and Evolution* 3.3 (Mar. 2019), pp. 430–439. ISSN: 2397334x. doi: 10.1038/s41559-018-0793-y.
- Schöberl, Joachim. "An advancing front 2D/3D-mesh generator based on abstract rules". In: *Computing and*

- Visualization in Science* 1.1 (July 1997), pp. 41–52. ISSN: 14330369. doi: 10.1007/s007910050004.
- Schuurman, J J and M A J Goedewaagen. “Methods for the examination of root systems and roots.” In: *Methods for the Examination of Root Systems and Roots*. (1965), 86 pp. doi: 10.2136/ssaj1965.03615995002900050007x.
- Schwab, Klaus. “The Fourth Industrial Revolution: what it means and how to respond”. In: *World Economic Forum* (2016). ISSN: 13489216.
- Schwan, H. P. “Electrode polarization impedance and measurements in biological materials.” In: *Annals of the New York Academy of Sciences* 148.1 (Feb. 1968), pp. 191–209. ISSN: 0077-8923. doi: 10.1111/j.1749-6632.1968.tb20349.x.
- “Linear and nonlinear electrode polarization and biological materials”. In: *Annals of Biomedical Engineering* 20.3 (May 1992), pp. 269–288. ISSN: 00906964. doi: 10.1007/bf02368531.
- Schwan, H. P., G. Schwarz, J. Maczuk, and H. Pauly. “On the low-frequency dielectric dispersion of colloidal particles in electrolyte solution”. In: *Journal of Physical Chemistry* 66.12 (1962), pp. 2626–2635. ISSN: 00223654. doi: 10.1021/j100818a066.
- Seagar, A D. “Probing With Low Frequency Electric Currents”. In: *Electrical Engineering* PhD (1983).
- Seoane, Fernando, Javier Ferreira, Juan José Sánchez, and Ramon Bragós. “An analog front-end enables electrical impedance spectroscopy system on-chip for biomedical applications”. In: *Physiological Measurement* 29.6 (June 2008), S267–s278. ISSN: 0967-3334. doi: 10.1088/0967-3334/29/6/s23.
- Skaven-Haug, S. V. “Volumetric relations in soil materials”. In: *4th International Peat Congress*. Espoo, Finland, 1972.
- Smit, AL, E George, and J Groenwold. “Root Methods”. In: *Root Methods*. 2000, pp. 235–271. ISBN: 978-3-642-08602-1. doi: 10.1007/978-3-662-04188-8.
- Somersalo, Erkki, Margaret Cheney, and David Isaacson. “Existence and Uniqueness for Electrode Models for Electric Current Computed Tomography”. In: *SIAM Journal on Applied Mathematics* 52.4 (1992), pp. 1023–1040. ISSN: 0036-1399. doi: 10.1137/0152060.
- Stevens, William Chase. *Plant anatomy from the standpoint of the development and functions of the tissues, and handbook of microtechnic*. 2011. doi: 10.5962/bhl.title.24774.
- Stirzaker, R J, J B Passioura, and Y Wilms. *Soil structure and plant growth: Impact of bulk density and biopores*. Tech. rep.
- Stout, Darryl G., John W. Hall, and Neil B. McLaughlin. “In vivo plant impedance measurements and characterization of membrane electrical properties: The influence of cold acclimation”. In: *Cryobiology* 24.2 (Apr. 1987), pp. 148–162. ISSN: 00112240. doi: 10.1016/0011-2240(87)90017-4.
- Stover, Daniel B., Frank P. Day, John R. Butnor, and Bert G. Drake. “Effect of elevated CO₂ on coarse-root biomass in Florida scrub detected by ground-penetrating radar”. In: *Ecology* 88.5 (2007), pp. 1328–1334. ISSN: 00129658. doi: 10.1890/06-0989.
- Subbarao, Guntur Venkata et al. *Suppression of soil nitrification by plants*. 2015. doi: 10.1016/j.plantsci.2015.01.012.
- Tanaka, Natsuki, Mariko Kato, Rie Tomioka, Rie Kurata, Yoichiro Fukao, Takashi Aoyama, and Masayoshi Maeshima. “Characteristics of a root hair-less line of *Arabidopsis thaliana* under physiological stresses”. In: *Journal of Experimental Botany* 65.6 (Apr. 2014), pp. 1497–1512. ISSN: 1460-2431. doi: 10.1093/jxb/eru014.
- Taylor, H. M., D. R. Upchurch, and B. L. McMichael. “Applications and limitations of rhizotrons and minirhizotrons for root studies”. In: *Plant and Soil* 129.1 (Dec. 1990), pp. 29–35. ISSN: 0032079x. doi: 10.1007/bf00011688.
- Tepfer, D. *Root methods, a handbook*. Vol. 160. 4. Springer, 2001, p. 755. ISBN: 978-3-642-08602-1. doi: 10.1016/s0168-9452(00)00440-4.
- Thompson, M. V. “Root-Gel Interactions and the Root Waving Behavior of *Arabidopsis*”. In: *Plant Physiology* 135.3 (July 2004), pp. 1822–1837. ISSN: 0032-0889. doi: 10.1104/pp.104.040881. arXiv: 3543011390.
- Tollner, E. W. “X-ray computed tomography applications in soil ecology studies”. In: *Agriculture, Ecosystems and Environment* 34.1-4 (Feb. 1991), pp. 251–260. ISSN: 01678809. doi: 10.1016/0167-8809(91)90112-b.
- Trachsel, Samuel, Shawn M. Kaeppler, Kathleen M. Brown, and Jonathan P. Lynch. “Shovelomics: High throughput phenotyping of maize (*Zea mays* L.) root architecture in the field”. In: *Plant and Soil* (2011). ISSN: 0032079x. doi: 10.1007/s11104-010-0623-8.
- Tracy, Saoirse R., Kerstin A. Nagel, Johannes A. Postma, Heike Fassbender, Anton Wasson, and Michelle Watt. *Crop Improvement from Phenotyping Roots: Highlights Reveal Expanding Opportunities*. Jan. 2020. doi: 10.1016/j.tplants.2019.10.015.
- Tsutsumi, Daizo. “Study on Root System Development by Modeling Approach”. PhD thesis. Kyoto: Kyoto University, 2003, p. 141. doi: 10.14989/doctor.k10236.
- Tufte, Edward R. *Beautiful Evidence*. 1st Editio. Lcc: Graphics Press, 2006. ISBN: 0-9613921-7-7.

- Tufte, Edward R. *Visual Explanations*. Cheshire, Connecticut: Graphics Press, 1997, p. 156. ISBN: 0-9613921-2-6.
- Uga, Yusaku et al. "Control of root system architecture by DEEPER ROOTING 1 increases rice yield under drought conditions". In: *Nature Genetics* 45.9 (Sept. 2013), pp. 1097–1102. ISSN: 10614036. DOI: 10.1038/ng.2725.
- Urban, Josef, Raphael Bequet, and Raphael Mainiero. "Assessing the applicability of the earth impedance method for in situ studies of tree root systems". In: *Journal of Experimental Botany* 62.6 (Mar. 2011), pp. 1857–1869. ISSN: 00220957. DOI: 10.1093/jxb/erq370.
- Vanella, D., G. Cassiani, L. Busato, J. Boaga, S. Barbagallo, A. Binley, and S. Consoli. "Use of small scale electrical resistivity tomography to identify soil-root interactions during deficit irrigation". In: *Journal of Hydrology* 556 (Jan. 2018), pp. 310–324. ISSN: 00221694. DOI: 10.1016/j.jhydrol.2017.11.025.
- Vaughan, Martha M, Dorothea Tholl, and James G Tokuhisa. "An aeroponic culture system for the study of root herbivory on *Arabidopsis thaliana*". In: *Plant Methods* 7.1 (2011), p. 5. ISSN: 1746-4811. DOI: 10.1186/1746-4811-7-5.
- Vauhkonen, Päivi J., Marko Vauhkonen, Tuomo Savolainen, and Jari P. Kaipio. "Static three-dimensional electrical impedance tomography". In: *Annals of the New York Academy of Sciences*. Vol. 873. 1 Electrical Bi. Blackwell Publishing Ltd, Apr. 1999, pp. 472–481. ISBN: 0362-028X (Print). DOI: 10.1111/j.1749-6632.1999.tb09496.x.
- Vermeulen, Sonja J., Bruce M. Campbell, and John S.I. Ingram. "Climate Change and Food Systems". In: *Annual Review of Environment and Resources* 37.1 (Nov. 2012), pp. 195–222. ISSN: 1543-5938. DOI: 10.1146/annurev-environ-020411-130608.
- Wagenaar, Justin and Andy Adler. "Electrical impedance tomography in 3D using two electrode planes: characterization and evaluation". In: *Physiological Measurement* 37.6 (June 2016), pp. 922–937. ISSN: 0967-3334. DOI: 10.1088/0967-3334/37/6/922.
- Wahba, Grace and Yonghua Wang. "When is the optimal regularization parameter insensitive to the choice of the loss function?" In: *Communications in Statistics - Theory and Methods* 19.5 (Jan. 1990), pp. 1685–1700. ISSN: 0361-0926. DOI: 10.1080/03610929008830285.
- Walker, John M. "Electrical A. C. resistance and capacitance of *Zea Mays L*". In: *Plant and Soil* 23.2 (Oct. 1965), pp. 270–274. ISSN: 0032-079x. DOI: 10.1007/bf01358354.
- Walter, Achim et al. "Dynamics of seedling growth acclimation towards altered light conditions can be quantified via GROWSCREEN: A setup and procedure designed for rapid optical phenotyping of different plant species". In: *New Phytologist* 174.2 (Apr. 2007), pp. 447–455. ISSN: 0028646x. DOI: 10.1111/j.1469-8137.2007.02002.x.
- Wang, Jun bang, Xiu juan Zhang, and Chu Wu. "Advances in experimental methods for root system architecture and root development". In: *Journal of Forestry Research* 26.1 (Mar. 2015), pp. 23–32. ISSN: 19930607. DOI: 10.1007/s11676-015-0017-0.
- Wasson, A. P., R. A. Richards, R. Chatrath, S. C. Misra, S. V.Sai Prasad, G. J. Rebetzke, J. A. Kirkegaard, J. Christopher, and M. Watt. *Traits and selection strategies to improve root systems and water uptake in water-limited wheat crops*. 2012. DOI: 10.1093/jxb/ers111.
- Werban, Ulrike, Said Attia al Hagrey, and Wolfgang Rabbel. "Monitoring of root-zone water content in the laboratory by 2D geoelectrical tomography". In: *Journal of Plant Nutrition and Soil Science* 171.6 (Dec. 2008), pp. 927–935. ISSN: 14368730. DOI: 10.1002/jpln.200700145.
- West, L. J., D. I. Stewart, A. M. Binley, and B. Shaw. "Resistivity imaging of soil during electrokinetic transport". In: *Engineering Geology* 53.2 (1999), pp. 205–215. ISSN: 00137952. DOI: 10.1016/s0013-7952(99)00034-4.
- Whalley, W.R. R. et al. "Methods to estimate changes in soil water for phenotyping root activity in the field". In: *Plant and Soil* 415.1-2 (June 2017), pp. 407–422. ISSN: 0032-079x. DOI: 10.1007/s11104-016-3161-1.
- Whitmee, Sarah et al. *Safeguarding human health in the Anthropocene epoch: Report of the Rockefeller Foundation-Lancet Commission on planetary health*. Nov. 2015. DOI: 10.1016/s0140-6736(15)60901-1.
- Willett, Walter et al. "Food in the Anthropocene: the EAT–Lancet Commission on healthy diets from sustainable food systems". In: *The Lancet* 393.10170 (Feb. 2019), pp. 447–492. ISSN: 1474547x. DOI: 10.1016/s0140-6736(18)31788-4.
- Yin, Xuefeng, Jianjun Zhang, and Xiaofang Wang. "Sequential injection analysis system for the determination of arsenic by hydride generation atomic absorption spectrometry". In: *Fenxi Huaxue*. Vol. 32. 10. 2004, pp. 1365–1367. ISBN: 9788578110796. DOI: 10.1017/cbo9781107415324.004. arXiv: arXiv:1011.1669v3.
- York, Larry M., Andrea Carminati, Sacha J. Mooney, Karl Ritz, and Malcolm J. Bennett. "The holistic rhizosphere: integrating zones, processes, and semantics in the soil influenced by roots". In: *Journal of Experimental Botany* 67.12 (June 2016), pp. 3629–3643. ISSN: 0022-0957. DOI: 10.1093/jxb/erw108.
- Yorkey, T. J. and J. G. Webster. "A comparison of impedance tomographic reconstruction algorithms". In: *Clinical*

- Physics and Physiological Measurement* 8.4a (Nov. 1987), pp. 55–62. ISSN: 01430815. doi: [10.1088/0143-0815/8/4a/007](https://doi.org/10.1088/0143-0815/8/4a/007).
- Yuan, Xiao-Zi, Chaojie Song, Haijiang Wang, and Jiujun Zhang. “EIS Equivalent Circuits”. In: *Electrochemical Impedance Spectroscopy in PEM Fuel Cells*. London: Springer London, 2010, pp. 139–192. doi: [10.1007/978-1-84882-846-9\4](https://doi.org/10.1007/978-1-84882-846-9_4).
- Zampieri, M., A. Ceglar, F. Dentener, and A. Toreti. “Wheat yield loss attributable to heat waves, drought and water excess at the global, national and subnational scales”. In: *Environmental Research Letters* 12.6 (June 2017), p. 064008. ISSN: 17489326. doi: [10.1088/1748-9326/aa723b](https://doi.org/10.1088/1748-9326/aa723b).
- Zappala, Susan, Stefan Mairhofer, Saoirse Tracy, Craig J. Sturrock, Malcolm Bennett, Tony Pridmore, and Sacha J. Mooney. “Quantifying the effect of soil moisture content on segmenting root system architecture in X-ray computed tomography images”. In: *Plant and Soil* 370.1-2 (Sept. 2013), pp. 35–45. ISSN: 0032079x. doi: [10.1007/s11104-013-1596-1](https://doi.org/10.1007/s11104-013-1596-1).
- Zhang, Yuzhou, Guanghui Xiao, Xiaojuan Wang, Xixi Zhang, and Jiří Friml. “Evolution of fast root gravitropism in seed plants”. In: *Nature Communications* 10.1 (Dec. 2019), pp. 1–10. ISSN: 20411723. doi: [10.1038/s41467-019-11471-8](https://doi.org/10.1038/s41467-019-11471-8).
- Zhao, Peng-Fei et al. “Electrical imaging of plant root zone: A review”. In: *Computers and Electronics in Agriculture* (2019). ISSN: 0168-1699. doi: [10.1016/j.compag.2019.105058](https://doi.org/10.1016/j.compag.2019.105058).
- Zhu, Jinming, Paul A. Ingram, Philip N. Benfey, and Tedd Elich. “From lab to field, new approaches to phenotyping root system architecture”. In: *Current Opinion in Plant Biology* 14.3 (June 2011), pp. 310–317. ISSN: 13695266. doi: [10.1016/j.pbi.2011.03.020](https://doi.org/10.1016/j.pbi.2011.03.020).
- Zhu, Shiping, Chunlin Huang, Yi Su, and Motoyuki Sato. “3D ground penetrating radar to detect tree roots and estimate root biomass in the field”. In: *Remote Sensing* 6.6 (2014), pp. 5754–5773. ISSN: 20724292. doi: [10.3390/rs6065754](https://doi.org/10.3390/rs6065754).